Molecular Cloud Structure in the Star-forming Region W43

Inaugural-Dissertation

zur
Erlangung des Doktorgrades
der Mathematisch-Naturwisschenschaftlichen Fakultät
der Universität zu Köln

vorgelegt von

Philipp Christoph Carlhoff
aus Krefeld

Köln 2013

Berichterstatter:	Prof. Dr. Peter Schilke Prof. Dr. Jürgen Stutzki
Tag der mündlichen Prüfung:	16. Januar 2014

Für Flora

"The world is full of magical things
patiently waiting for our wits to grow sharper."

Bertrand Russell

Abstract

In the struggle toward an understanding of the process of star formation it is one of the most important tasks to study the initial properties of the cold and dense interstellar medium. Stars are known to form in dense molecular clouds, but it is not yet fully understood how they from from the neutral gas that permeates the Galaxy. Therefore, it is crucial to fully understand the creation process of molecular clouds.

Colliding flows are a possible explanation for this process. This class of models considers streams of warm, diffuse, and atomic hydrogen gas that stream into each other. Fluctuations of the gas at the collision area create regions of higher density and lower temperature, where molecules can form.

W43 is one of the largest molecular cloud complexes in the Milky Way with a total gas mass of several $10^6\ M_\odot$. Prior investigations have identified it as one of the largest and most luminous star-forming regions in the Galaxy. This is most probably due to its exceptional position, which is assumed to be at the junction point of the Galactic spiral arms and the bar. At this location, gas is piled up, because the elliptical orbits in the bar and the circular orbits in the spiral arms interfere. Therefore, W43 poses an excellent laboratory to study the formation of molecular clouds.

This thesis aims at characterizing the W43 star-forming region. The distribution of molecular clouds, their velocity structure, and physical properties are analyzed and the origin of a single filament is studied in detail.

The first part of this work describes the project W43 HERO (W43 Hera/EmiR Observations) that has been initiated to observe the large scale distribution of ^{13}CO (2–1) and C^{18}O (2–1) in the W43 complex with the IRAM 30m telescope. These molecular emission lines provide information of the medium dense molecular gas ($n \approx 10^3$ cm^{-3}) in the complex. While ^{13}CO (2–1) traces the more diffuse, widespread gas in the clouds, C^{18}O (2–1) is used to depict the denser central clumps of the clouds.

We analyze the velocity structure of our data and align our findings with velocity models of the spiral arms in the Galaxy. We thus confirm the position of W43 near the tangential point in the Scutum arm, which is situated near the tip of the elongated bar. This point has a distance of 6 kpc from the Sun.

We then derive the optical depth, the excitation temperature, and the H_2 column density of the gas from our observations. The total mass of medium dense molecular clouds in the W43 complex is found to be $1.9 \times 10^6\ M_\odot$. An estimation of the shear parameter of the cloud complex provides the insight that it is massive enough to withstand the shear forces generated by the motions of gas streams in the Galaxy. Mass estimations are in agreement with those taken from *Herschel* dust emission maps.

Plots of the probability distribution functions of the H_2 column density, derived from *Herschel* and the IRAM 30m data, are created. Both show a log-normal distribution on lower masses and power-law deviation on the high-mass end of the function. This is commonly associated with the influence of star formation. The slope of the CO power-law tail is less steep than that derived from dust emission. We could have found an efficient tool, that only traces the gas that collapses into a protostar.

In the second part of this thesis we pick one single filament in the W43 complex and analyze it in detail. Additional observations have been carried out to complement the IRAM 30m dataset. In particular, there are observations of CO (6–5) from the APEX telescope, [C II] from the *Herschel* satellite, [C I], observed with NANTEN2, and the CARMA observations of HCN (1–0), HCO^+ (1–0), and N_2H^+ (1–0).

We use the radiative transfer code RADEX to estimate the temperature and density of the molecular gas. The best solution is a kinetic temperature around 30 K and a density of $\sim 10^4$ cm^{-3}. We then study the origin of the ionized carbon which we have observed with *Herschel*. This species is often discussed in the framework of static photon-dominated regions (PDRs). The physical conditions are studied with the program KOSMA-τ, which yields a very high UV-field, necessary for the creation of the observed data. A comparison with typical UV-tracers results in the insight that this radiation strength is unrealistically high. Thus, the creation of C^+ by a static PDR is implausible and a different mechanism has to be the origin.

We find it more likely that the [C II] emission traces the transition zone between the initial atomic gas and the molecular cloud which forms from it. We would thus witness the dynamic formation of a young molecular filament.

We conclude that W43 is indeed one of the most massive and important molecular cloud complexes in the Galaxy and that colliding flows are a possible explanation for its formation.

Zusammenfassung

Den Ausgangszustand des kalten, dichten interstellaren Mediums zu verstehen ist einer der wichtigsten Aspekte, um den Prozess der Sternentstehung zu erklären. Es ist bekannt, dass Sterne in dichten Molekülwolken entstehen, es ist jedoch noch nicht vollständig verstanden, wie diese aus dem neutralen Gas, das die Galaxie durchdringt, entstehen. Deshalb ist es entscheidend, den Entstehungsprozess dieser Molekülwolken nachzuvollziehen.

Kollidierende Gasströme sind eine mögliche Erklärung dieses Prozesses. Diese Klasse von Modellen betrachtet Ströme warmen, diffusen, atomaren Wasserstoffgases, die ineinander fließen. Fluktuationen des Gases innerhalb der Kollisionsfläche erzeugen Regionen erhöhter Dichte und niedrigerer Temperatur, in denen Moleküle enstehen können.

W43 ist einer der größten molekularen Wolkenkomplexe in der Milchstraße mit einer Gesamtmasse von mehreren 10^6 $M_\odot$. Vorausgehende Untersuchungen haben es als eine der größten und leuchtkräftigsten Sternenstehungsregionen in der Galaxie identifiziert. Der Grund dafür ist wahrscheinlich die außergewöhnliche Position, welche am Treffpunkt der galaktischen Spiralarme und dem Balken vermutet wurde. Da sich dort die elliptischen Orbits des Balkens und die kreisförmigen Orbits in den Spiralarmen überlagern, wird an diesem Punkt Gas angehäuft. Daher bietet W43 exzellente Bedingungen, um die Entstehung von Molekülwolken zu studieren.

Ziel dieser Arbeit ist es, die Sternenstehungsregion W43 zu charakterisieren. Die Verteilung der Molekülwolken, ihre Geschwindigkeitsstruktur und physikalischen Eigenschaften werden analysiert und der Ursprung eines einzelnen Filaments genauer untersucht.

Der erste Teil dieser Arbeit beschreibt das Project W43 HERO (W43 Hera/EmiR Observations), das begonnen wurde, um die Verteilung von ^{13}CO (2–1) und C^{18}O (2–1) im W43 Komplex mit dem IRAM 30m Teleskop zu beobachten. Diese Molekülemissionslinien liefern Informationen über das molekulare Gas mittlerer Dichte ($n \approx 10^3$ cm^{-3}) im Komplex. Das weiter ausgedehnte, diffusere Gas wird durch ^{13}CO (2–1) beobachtet, wohingegen C^{18}O (2–1) genutzt wird um die etwas dichteren, zentralen Klumpen innerhalb der Wolken darzustellen.

Wir analysieren die Geschwindigkeitsstruktur unserer Daten und vergleichen unsere Ergebnisse mit Geschwindigkeitsmodellen der Spiralarme in der Galaxie.

Auf diese Weise können wir die Position von W43 in der Nähe des Tangentialpunktes im Scutum-Arm bestätigen, welcher sich nahe der Spitze des verlängerten Balkens befindet. Dieser Punkt hat eine Entfernung zur Sonne von 6 kpc.

Wir leiten danach die optische Tiefe, die Anregungstemperatur und die H_2 Säulendichte des Gases von unseren Beobachtungen ab. Die Gesamtmasse des molekularen Gases mittlerer Dichte im W43 Komplex beträgt $1.9 \times 10^6\ M_\odot$. Eine Abschätzung des Scherungs-Parameters der Wolke erlaubt die Einsicht, dass diese massereich genug ist, um den Scherkräften zu widerstehen, welche durch die Bewegung der Gasströme in der Galaxie erzeugt werden. Die Masseschätzung stimmt mit den Werten überein, die wir aus *Herschel* Staubemissionskarten erhalten haben.

Abbildungen der Wahrscheinlichkeitsverteilungsfunktionen der H_2 Säulendichte, abgeleitet von *Herschel* und IRAM 30m Daten, werden erzeugt. Beide zeigen eine logarithmische Normalverteilung bei niedrigen Massen und eine Abweichung in Form eines Potenzgesetzes bei hohen Massen. Dies wird normalerweise mit dem Einfluss der Sternenstehung in Verbindung gebracht. Die Steigung des CO Potenzgesetzes ist weniger steil als diejenige, die aus der Staubemission abgeleitet wurde. Möglicherweise haben wir eine effiziente Methode gefunden, nur jenes Gas zu erkennen, welches zu einem Protostern kollabiert.

Im zweiten Teil der Arbeit suchen wir ein spezielles Filament im W43 Komplex heraus und analysieren es im Detail. Zusätzliche Beobachtungen wurden durchgeführt, um das IRAM 30m Datenset zu vervollständigen. Im Einzelnen sind dies Beobachtungen von CO (6–5) mit dem APEX Teleskop, [C II] vom *Herschel* Satelliten, [C I], beobachtet mit NANTEN2 und die CARMA Beobachtungen von HCN (1–0), HCO^+ (1–0) und N_2H^+ (1–0).

Wir verwenden den Strahlungstransportcode RADEX, um die Temperatur und Dichte des molekularen Gases zu bestimmen. Die besten Lösungen sind eine kinetische Temperatur von etwa 30 K und eine Dichte von $\sim 10^4$ cm^{-3}. Daraufhin analysieren wir den ionisierten Kohlenstoff, welchen wir mit *Herschel* beobachtet haben. Dieses Element wird häufig im Rahmen von statischen photonendominierten Regionen (PDRs) diskutiert. Die physikalischen Bedingungen werden mit dem KOSMA-τ-Programm untersucht, welches ergibt, dass ein sehr starkes UV-Feld nötig wäre, um die beobachteten Daten zu erzeugen. Ein Vergleich mit typischen UV-Tracern zeigt, dass dieses Strahlungsfeld unrealistisch stark ist. Daher ist die Erzeugung von C^+ durch eine statische PDR unplausibel und ein anderer Mechanismus muss als Ursprung dienen.

Es erscheint uns wahrscheinlicher, dass die [C II] Strahlung die Übergangszone markiert, welche zwischen urpsrünglichem atomarem Gas und der Molekülwolke, welche sich daraus entwickelt, befindet. Somit würden wir Zeuge der dynamischen Entstehung eines jungen molekularen Filaments.

Wir schließen, dass W43 in der Tat einer der massereichsten und wichtigsten Molekülwolkenkomplexe in der Galaxie ist und eine mögliche Erklärung seiner Entstehung in der Theorie kollidierender Gasströme zu finden ist.

Contents

Chapter 1

Introduction

Throughout the history of mankind, observations of the sky have played an important role. Even the earliest human tribes used the stars for navigation, calculation of times, and an inspiration for their mythology. When humanity started to became agricultural, determining times from observations of the sun and the nightly sky became so important, that it got a central part of everyday life in form of holidays, rites, and traditions. Astronomy can thus be considered one of the first sciences (although we cannot use this word in its modern meaning).

For millennia, people could only use their eyes to watch the sky. And although great progress was made in the description of planets, stars, comets, and nebulae, this covered only a fraction of the information that is transported to us through space. Even with the invention of the first lenses and telescopes, that drastically improved the accuracy of observations, still, only the visible light was accessible to us.

Only in the 19th century, the works of Maxwell (1873) made clear that light had to be considered as an electromagnetic wave and that it was only a small window of the complete electromagnetic spectrum. These electromagnetic waves were discovered by Hertz (1887) with his newly built antennas. The unit of frequency, in oscillations per second, was named after him. The first actual astronomical observations in the radio wavelengths were conducted by Jansky (1933), operating at wavelengths of 14.6 m. Astronomers discovered that these wavelengths (and others, up to the infrared regime) mainly trace the interstellar medium (ISM), clouds of gas and dust that fill the space between the stars.

Many processes in the ISM can be studied with the help of radiation in the millimeter and sub-millimeter wavelengths (several ten μm to a few mm). Instrumentation of telescopes for this range is not only technically demanding, but includes fundamentals of physics that are just about to be understood. This is the reason this field has flourished only in the last decades. With better receivers and more computing power, larger and more detailed maps with higher spectral resolution became possible, fueling increasing insight into the physical

processes. Figure 1.1 shows the Atacama Large Millimeter/submillimeter Array (ALMA), the newest and most advanced interferometer, which operates in the submm/mm range.

Over the time, a completely new astronomical field was established, the study of the ISM and the process of star formation. This process is not only interesting by itself, but also has an important impact on the ISM through feedback effects. Stars were found to emerge from molecular gas clouds (e.g. McKee and Ostriker 2007). They have to be cold and dense for stars to be able to form. Until today, it is not fully understood how these clouds develop, as the initial gas in the Galaxy is warm and atomic. The process of molecular cloud formation is therefore one of the crucial recent subjects of investigation in radio astronomy.

Fig. 1.1: Night sky over the ALMA telescope in the Atacama desert, Chile. Credits of image: C. Malin, European Southern Observatory (ESO).

To understand this formation process, the structure of giant molecular clouds (GMCs) needs to be studied. It was found that these molecular clouds show a fractal distribution of gas over several orders of magnitude (Stutzki et al. 1998). Theoretical models and recent observations show that filamentary shapes form at certain scales and that star-forming cores grow along these filaments (e.g. Banerjee et al. 2009; André et al. 2010). It is therefore important to analyze the mechanisms that create them. Especially, the transition phase between atomic and molecular clouds requires attention.

One of the most prominent star-forming regions in our Galaxy, besides the Galactic center, is the GMC W43. This region is located in the Galactic plane at 30° Galactic longitude, in the constellation Aquila. Figure 1.2 shows the position of W43 on the sky. This region was identified as one of the most massive and most luminous cloud complexes in the Galactic plane by Nguyen Luong et al. (2011). It harbors a cluster of OB-stars that recently formed in this region and fuels further star formation. W43 is assumed to be located at the junction point

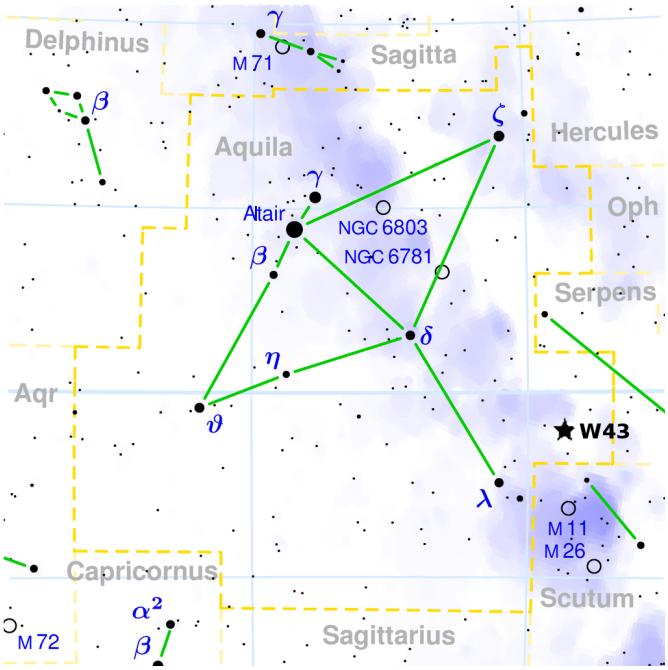

Fig. 1.2: Position of W43 in the Aquila constellation. Credits of image: Wikipedia.org.

of the Galactic spiral arms and the bar, which is a distinguished position in the Galaxy, where different classes of orbits intersect and colliding mass is piled up.

The goal of this thesis is to characterize the molecular clouds located in the star-forming region W43 and clarify the process of their formation. Large scale maps of the medium density molecular clouds in W43, observed with the IRAM 30m, are described and analyzed. We study the velocity structure of this cloud complex and determine its physical properties. One single filament is then investigated in more detail.

Observations of ionized and atomic carbon as well as high-density tracers are presented. They allow to characterize the transition zone between atomic and molecular clouds. We study the origin of the ionized carbon emission and try to find out whether it has a dynamic origin. This would be a hint at the dynamic formation process of this filament.

1.1 Structure of this work

We now give a short overview of the structure of this thesis. After this introduction, in chapter 2, we explain some theoretical backgrounds, needed for our project. Star and molecular cloud formation are discussed in Sect. 2.1.1 and 2.1.3. The spiral arm structure of the Milky Way is explained in Sect. 2.1.5, while Sect. 2.1.6 introduces the W43 molecular cloud complex and gives an overview

of previous research related to it. Finally, some technical descriptions of astronomical observation fundamentals are given in Sect. 2.2.

The project itself consists of two main parts, the large scale CO observations of the W43 complex and their analysis and the detailed small scale investigation of one filament, using complementary observations. Chapter 3 describes the CO observations, taken with the 30m telescope that is operated by the Institut de Radioastronomie Millimétrique (IRAM), while in chapter 4 we analyze the velocity structure of the CO dataset and describe the position of W43 in the Galaxy. We then derive physical properties of the W43 region in chapter 5 and compare our data to far-infrared and submillimeter dust emission maps. Is there any similarity between molecular line emission and dust continuum maps? The findings of these three chapters have been published in Carlhoff et al. (2013).

From this dataset we then choose one filament and analyze it in detail. Chapter 6 gives an overview of the additional observations with the *Herschel* Space Observatory (HSO), the Atacama Pathfinder Experiment (APEX), the Combined Array for Research in Millimeter-wave Astronomy (CARMA), and NANTEN2. The information gathered from these datasets is then given in chapter 7, where, apart from the exact size and velocity structure of the filament, we determine its temperature and density. We finally investigate the origin of ionized carbon emission. Is the filament a typical photodissociation region/photon-dominated region (PDR) or do we need a different explanation? And what does this reveal about the transition phase between atomic and molecular gas?

To finish the thesis, a summary and conclusion of the results is given in chapter 8. It also contains an outlook on open questions and possibilities for future research. A short description of several important sources can be found in Appendix A, while plots of all sources are shown in Appendix B.

Chapter 2

Theoretical backgrounds

In this chapter, we discuss some of the astrophysical fundamentals that pose the physical background of this work. In section 2.1 we give a short introduction to the theory of star formation, which role molecular clouds play, and how they form. We give an overview of the Galactic structure and introduce the W43 star-forming region. Then, we want to describe some technical details of astronomical observations that were used during the data collection for this project. Basics of single-dish and interferometer telescopes are explained in Sect. 2.2 together with the background of molecular emission lines that are used to study the properties of the ISM.

2.1 Astrophysical backgrounds

2.1.1 Star formation

Star formation is one of the most important processes in Galaxies. At this point, we explain the basics of this process as it strongly influences the energy balance of the ISM on all scales through feedback effects. Especially the formation of high-mass stars ($M \gtrsim 8\ M_\odot$) has a crucial impact on its surroundings and is thus relevant for this thesis. Although many steps of the formation process are understood by now (McKee and Ostriker (2007) give a good overview), there are still important open questions.

It has been known for a long time that the formation processes of high- and low-mass stars differ strongly (Herbig 1962). These two types of stars are distinguished by the Kelvin-Helmholtz timescale

$$\tau_{\mathrm{KH}} = \frac{G\,M^2}{R\,L}, \tag{2.1}$$

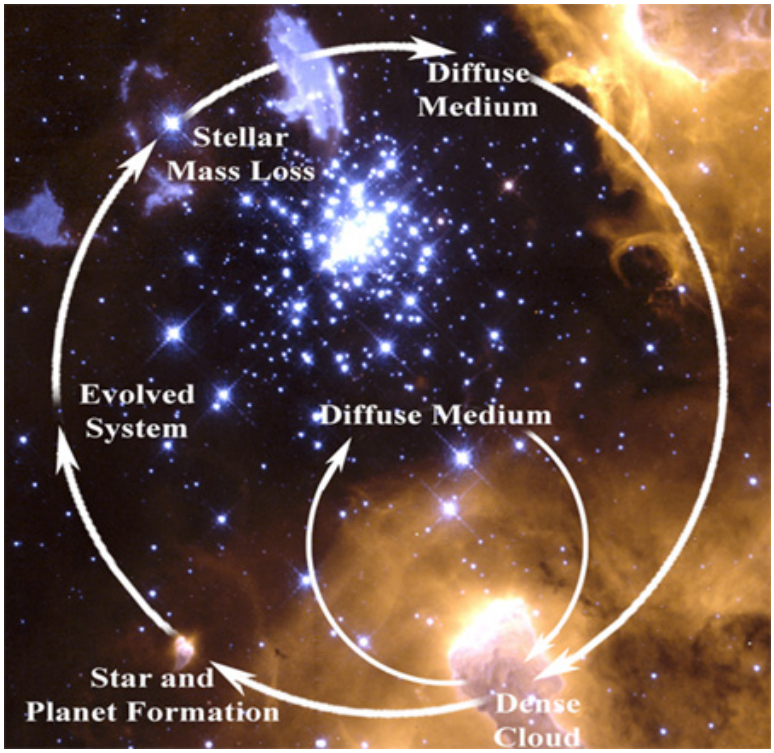

Fig. 2.1: Cycle of star formation. Credits: National Aeronautics and Space Administration (NASA).

where M, R, and L are the mass, radius, and luminosity of the star, respectively. It denotes the time needed for gravitational collapse of the star, decelerated by its radiation. The formation of low-mass stars takes on the order of τ_{KH}, while the formation of high-mass stars takes longer.

Mezger and Smith (1977) noted that high-mass and low-mass stars seem to form in different locations. OB stars (hot and luminous high mass stars) primarily form in molecular clouds complexes of large masses. These complexes are called GMCs and are usually found in the spiral arms of Galaxies. Although they only take up a small part of the volume of the ISM, GMCs contain an important part of the total molecular gas mass. Individual cloud complexes show masses of at least $10^4\ M_\odot$, but are usually on the order of 10^5 –$10^6\ M_\odot$ (Williams et al. 2000). We discuss the formation of these molecular clouds in Sect. 2.1.3.

The final mass of the formed star depends strongly on the mass of the initial cores. As usually groups of stars form in the same region, it is possible to measure the distribution of these stars. This initial mass function (IMF) measures the mass of the stars at the point where they enter the main sequence and is usually given as a probability distribution function (PDF). The IMF has first been

described by Salpeter (1955) and has the characteristic form

$$\xi(m)\Delta m = \xi_0 \left(\frac{m}{M_\odot}\right)^{-2.35} \left(\frac{\Delta m}{M_\odot}\right), \tag{2.2}$$

where $\xi(m)\Delta m$ is the number of stars with masses between m and $m+\Delta m$. This function ranges to a maximum stellar mass of 10 $M_\odot$. It has later been refined by Kroupa (2001), who introduced an IMF that shows a turnover at low masses (cf. dot-dashed line in Fig. 2.2) and Chabrier (2003), who used a smoother function (cf. dashed line in Fig 2.2).

Inside the molecular clouds, regions of higher density lead to the formation of cores. Cores are defined to be smaller, colder, and denser regions of molecular clouds that are gravitationally bound. Typically, their size ranges from below 0.1 pc to nearly 1 pc, having a temperature between 10 and 15 K and masses of a few to a few hundred $M_\odot$ (Benson and Myers 1989). Assuming a uniform, stationary, isothermal gas with perturbations of length scale λ, these are stable if the thermal energy of the gas can balance its gravity. Jeans instability occurs for large mass accumulations, i.e., when the perturbations are larger than the Jeans length

$$\lambda_\mathrm{J} = \sqrt{\frac{\pi\, c_s^2}{G\, \rho_0}}, \tag{2.3}$$

with the density ρ_0 and the local sound speed c_s.

In the last years, it became more and more clear that filaments play a crucial role in the process of star formation. Several studies, especially the results from the HSO, have shown that cores form along filaments (Molinari et al. 2010; André et al. 2010; Schneider et al. 2012; Palmeirim et al. 2013). The details of filamentary structure and their formation are described in Sect. 2.1.4.

In analogy to the IMF, a similar description for the mass of molecular clouds (Williams and McKee 1997; Rosolowsky 2005) can be found, where a major fraction of the mass is found in the larger clouds (Stark and Lee 2006). The combination of this mass-size relation and the mass distribution of molecular clouds explains the fractal structure of observations of these clouds (Stutzki et al. 1998), and vice versa. The same is true for embedded high density molecular cores, for which a distribution, a core mass function (CMF), can be given (Lada et al. 2007; Onishi et al. 2002). The distribution of clouds and cores usually shows a shape similar to the IMF, with a power-law tail on the high-mass end (Stutzki and Guesten 1990; Könyves et al. 2010), but with a different spectral index.

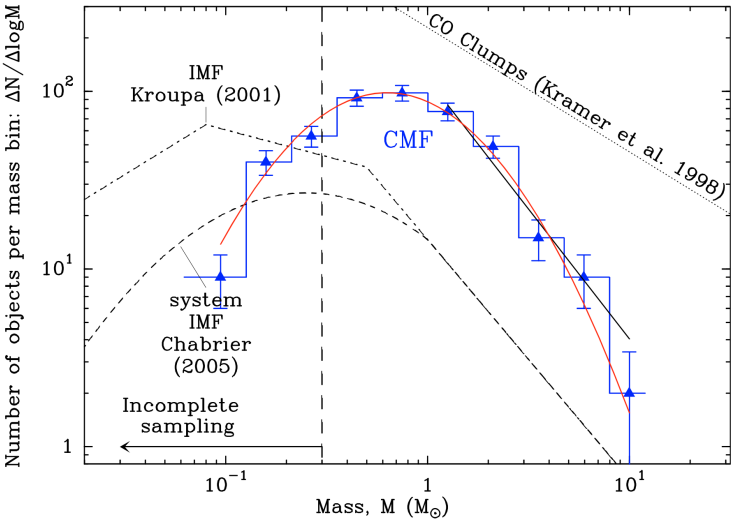

Fig. 2.2: Shift between IMF and CMF from Könyves et al. (2010).

This similarity of the IMF and the CMF implies that the mass of the cores directly determines the mass of the resulting stars. Also, the star formation rate (SFR), the amount of mass formed to stars in a certain time, depends directly on the clouds density (see e.g. Kennicutt 1998). However, the IMF is shifted to lower masses (Matzner and McKee 2000), which means that only a fraction of the initial cloud's gas mass is transformed into a core and only a fraction of this core actually forms a star (see Fig. 2.2). The respective efficiencies are found to rely on the density of the cloud, thus the denser a molecular cloud is, the more of its mass will be forming stars later (e.g. Burkert and Hartmann 2013). Usually, the efficiency is quite low; Myers et al. (1986) find a value of 2 %, Evans et al. (2009) one between 3 and 6%. The Schmidt-Kennicutt Law,

$$\Sigma_{\mathrm{SFR}} = (2.5 \pm 0.7) \times 10^{-4} \left(\frac{\Sigma_{\mathrm{gas,disk}}}{M_\odot \,\mathrm{pc}^{-2}} \right)^{1.4 \pm 0.15} M_\odot \,\mathrm{kpc}^{-2}\,\mathrm{yr}^{-1}, \tag{2.4}$$

however, found in Kennicutt (1998), is often used to describe the star formation rate in a galaxy.

From here on, we describe the low-mass star formation process, which is quite well known, and describe differences to high-mass star formation later. Cores tend to collapse due to the gravity of the enclosed mass. The time-scale of this collapse, the free-fall time,

$$f_{\mathrm{ff}} = \sqrt{\frac{3\,\pi}{32\,G\rho}} = 1.37 \times 10^6 \sqrt{\frac{10^3\,\mathrm{cm}^{-3}}{n_{\mathrm{H}}}}\,\mathrm{year}, \tag{2.5}$$

describes the collapse of a pressure-free, spherical cloud of density ρ, parameterized to the number density of hydrogen n_{H}. However, its kinetic energy, the presence of magnetic fields, and turbulences work against gravity and provide stability for the core (see e.g. Larson 2003). This increases the collapse timescale. A core is called magnetically supercritical when its magnetic field is too low to keep the core stable, which will result in the collapse of the core. The collapsed core is then called a protostar.

During the collapse, angular momentum and magnetic field play important roles. The angular momentum that is still left in the core is usually orders of magnitudes higher than that in the later star. It can result in the formation of a binary system (Bodenheimer 1978) or will form a rotating protostellar disk surrounding the protostar (Hayashi et al. 1982; Toomre 1982). The amount of magnetic flux trapped in the initial core will also mostly drop by a factor of 10^4 to 10^8 (Nakano 1983), possibly through ambipolar diffusion, which moves the charged particles (only a small fraction of the gas) out of the neutral gas. This diffusion of the magnetic flux could be efficient enough for clump densities of $n > 2 \times 10^6$ cm^{-3} (Draine 2011, p. 461). Crutcher et al. (2009) find that most cores are magnetically subcritical.

The initial hydrostatic core, or star embryo, is very small (a few AU) and has little mass ($\sim$0.01 $M_\odot$) as found by Low and Lynden-Bell (1976). However, accretion from the surrounding diffuser cloud can still increase the mass of the protostar. This is called Bondi-Hoyle accretion (Hoyle and Lyttleton 1939; Bondi 1952). Most matter will first accrete onto the disk surrounding the protostar. These disks have typical sizes of a few 100 AU (Vorobyov 2011) and lifetimes τ of several Myr with a relationship of $\tau \sim 1/M$ (Hernández et al. 2007). The dynamics in the disk, assuming its material is somewhat viscous, transport angular momentum outward (Lynden-Bell and Pringle 1974), which allows the material to finally fall onto the protostar and increase its mass.

But not all matter in the disk is funneled onto the protostar. Magnetic winds drive great parts of the disk mass toward the center, but then create jets that are directed away from the protostar, perpendicular to the disk. These jets guide ionized and molecular gas back into the ISM, which is seen as bipolar outflows in observations (e.g. Edwards et al. 1993). One example is shown in Fig. 2.3.

At a mass of about 0.2 $M_\odot$, deuterium burning sets in, which stabilizes the star and keeps it from further collapsing. It usually accretes more mass, up to a certain radius (about 4 $R_\odot$ for a star of 1 $M_\odot$, see Stahler et al. 1980), when the surrounding mass reservoir is used up and accretion does not play a role anymore. From here on, the low-mass star follows the usual evolution.

There are certain differences in the evolution of high-mass stars of masses larger than 8 $M_\odot$, although many details are not yet understood. See also Beuther et al. (2007) for a review. High-mass stars often form in clusters, where several cores are embedded in a molecular cloud (Klessen and Burkert 2001), mostly along filaments (André et al. 2010; Molinari et al. 2010, see

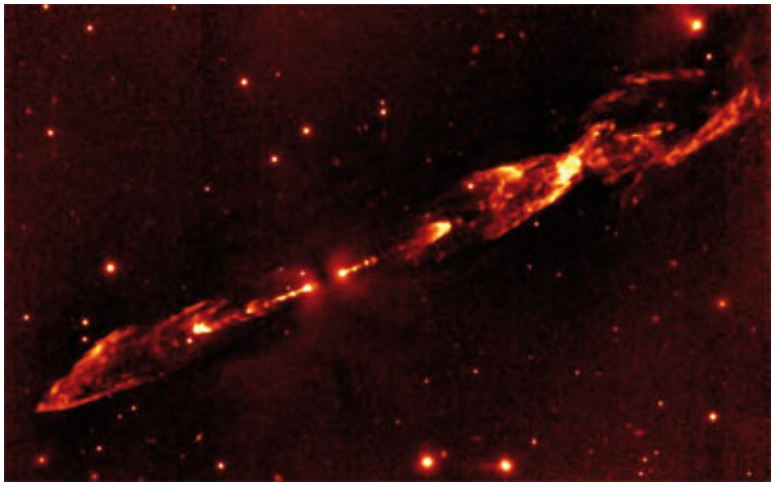

Fig. 2.3: Protostellar jet observed at 2.12 μm with the Infrared Astronomical Satellite (IRAS). H_2 emission of the object HH212 as described in Zinnecker et al. (1997).

also Sect. 2.1.4). In these clusters, protostars form from accretion and mergers, which leads to growth (e.g. Bonnell et al. 2003). The final mass is essentially determined by the mass of the formation environment and not by the single cores mass. The most massive stars will form in the center of the cluster. As larger cores accrete the most mass and eat away the molecular clouds in their vicinity, the model is also called competitive accretion model.

In contrast, in the monolithic collapse model, single high mass stars of up to 140 $M_\odot$ can form from turbulent cores (Kuiper et al. 2010). The mass of the initial clump limits the stars final mass. This model is basically a scaled-up low-mass star formation model, where a disk forms early and mass outflows transport radiation away and allow further accretion of mass.

High mass stars form from cores with masses above the Jeans mass, which Evans (e.g. 1999) stated, can have densities of more than 10^7 cm^{-3} and temperatures of more than 100 K. They are so massive that they already start nuclear fusion during the accretion process, which leads to feedback effects. This feedback was first thought to stop accretion so that stars could not become more massive than a few tens of $M_\odot$ (Wolfire and Cassinelli 1987). However, the formation of jets that transport radiation to the outside should increase accretion and allow for higher masses (Banerjee and Pudritz 2007).

The radiation of high-mass stars ionizes the surrounding molecular gas and creates H II regions[1]. Depending on size and density, these regions are called ultra compact H II regions (UCHIIs), with densities of >10^4 cm^{-3} and sizes of <0.1 pc, or hyper compact H II regions (HCHIIs), that can have densities >10^6 cm^{-3} and sizes of <0.05 pc, according to Kurtz (2005) and Hoare et al. (2007). This radiation can disrupt GMCs and return their matter back to the dif-

[1] This is the spectroscopic notation of ionized hydrogen.

fuse ISM (McKee and Ostriker 2007). From there, the cycle of molecular cloud formation and star formation can begin anew (see also Fig. 2.1).

2.1.2 Interstellar medium

As already mentioned in Sect. 2.1.1, our Galaxy does not only contain stars, but also a huge amount of gas and dust (which account for $\sim 10 - 15\%$ of the total mass of the Galaxy) that fills the space in-between them. The fraction of mass found in gas form is usually much higher in young galaxies (Popping et al. 2013), as only a fraction of the mass could be transformed into stars, yet. We call this phase the ISM, which includes all material that is gravitationally bound to galaxies, except for the stars (and dark matter). In contrast, the intergalactic medium (IGM) identifies the phase between galaxies.

The ISM is composed of several parts (see Table 2.1, values taken from Ferrière 2001; Draine 2011): molecular clouds, the neutral gas, ionized gas, and dust. The ISM gas mainly consists of hydrogen and helium that have been created shortly after the big bang. All higher elements have been formed by nucleosynthesis in stars.

(1) Phase	(2) Temperature	(3) Density	(4) Volume fraction
	[K]	[cm^{-3}]	[%]
Molecular gas	10-20	10^2-10^6	1
CNM	50-100	20-50	1-5
WNM	6000	0.5	10-20
WIM	6000	0.5	20-50
HIM	10^6	10^{-4}	30-70

Table 2.1: Different phases of the ISM and their properties.

Molecular gas is the coldest and densest part of the ISM and only takes up a small fraction of its volume (see Table 2.1 for detailed values). However, the hydrogen in the molecular gas still contains 18% of the total hydrogen mass of the ISM, due to its high density. The total molecular hydrogen mass in the Milky Way is found to be $8.4 \times 10^8\ M_\odot$. This phase is the most important one in the context of this work and the formation of molecular clouds from the neutral gas is described in more detail in Sect. 2.1.3.

The neutral atomic part of the ISM consists of neutral hydrogen and is warmer and diffuser than the molecular clouds. It consists of two phases of different temperature and density that can coexist in pressure equilibrium, due to the bistable nature of the neutral gas. This model is described by Field et al. (1969) and refined by Wolfire et al. (1995). The phases are called the cold neutral medium (CNM), which has medium temperature and density, and the warm

neutral medium (WNM), which has higher temperature and lower density. The CNM and WNM account for about a fifth of the volume of the ISM. The total mass of the H I is $2.9 \times 10^9\ M_\odot$, which is equivalent to 60% of the total hydrogen mass in the ISM gas. Parts of the WNM are ionized by X-rays and cosmic rays and form the warm ionized medium (WIM) that has the same density and temperature structure as the WNM.

Shock fronts in the WNM induce the transition to the CNM. Usually, these shock fronts are unstable and thermally fragmented (Koyama and Inutsuka 2002). Therefore, also the CNM is very fragmented, as seen in several simulations (e.g. Audit and Hennebelle 2005; Heitsch et al. 2005).

McKee and Ostriker (1977) extended the two-phase model by a third component, the hot ionized medium (HIM), which is heated by supernovae and reaches very high temperatures and low densities (Gent et al. 2013). It fills the remaining space of the ISM. The warm and hot ionized hydrogen contributes 23% ($1.1 \times 10^9\ M_\odot$) of the total hydrogen mass, contained in the ISM of the Galaxy.

Finally, dust plays an important role in the ISM. It was found that dust emission correlates quite well with the emission from molecular clouds (Bohlin 1975). Dust consists of grains that are mainly composed of graphites, silicates, or water ice (Ferrarotti and Gail 2006; Voshchinnikov and Henning 2010; Sirono 2013). Mathis et al. (1977) could reconstruct the size distributions of these grains from dust extinction curves. They found a power-law for the distribution of radius a,

$$N(a)\mathrm{d}a \propto a^{-3.5}\mathrm{d}a, \tag{2.6}$$

in the range of 0.005-1 μm (a newer distribution can be found in Casuso and Beckman 2010). On the low-end of the size scale, polycyclic aromatic hydrocarbons (PAHs) (Leger and Puget 1984; Lebouteiller et al. 2011) are the bridge between dust grains and organic macro-molecules. Dust grains can form in the cool atmosphere of red giants and planetary nebulae (Woolf and Ney 1969; Salpeter 1976), as well as in the ISM itself (Dwek and Scalo 1980).

There is much more gas than dust found in the ISM. The typical gas-to-dust mass ratio is on the order of 100, but can be even higher in some regions (Frisch and Slavin 2003; Parkin et al. 2012). The temperature of the interstellar dust is found to be between 10 and 30 K in most regions (Planck Collaboration et al. 2011; Galametz et al. 2012).

It is important to note that dust aids in the creation of molecules. H_2 molecules have to mainly form on grain surfaces (Hollenbach and Salpeter 1971; Charnley and Rodgers 2009) and dust helps to shield the molecules from photodissociation by UV radiation (Shull and Beckwith 1982). It can also be destroyed by shocks and release contained atoms and molecules to the gas phase (Seab 1987; Van Loo et al. 2013). SiO is a typical tracer for these shocks, because it

is released from the destroyed dust grains (Schilke et al. 1997). Therefore, dust acts as an important reservoir for many elements, especially Mg, Si, Fe, but also a good fraction of carbon (80%) and oxygen (15%) are contained in dust (Kim et al. 1994; Dwek et al. 1997). It also plays a crucial role in heating and cooling mechanisms of molecular clouds, as described by Watson (1972), Burke and Hollenbach (1983), or Xilouris et al. (2012).

Therefore, dust emission and absorption observations can be interesting tools to gather information on molecular clouds and their properties. We will utilize this later in this work.

2.1.3 Molecular cloud formation

As discussed in Sect. 2.1.1, stars form in molecular clouds that are part of the ISM. We will now describe how these clouds form from the diffuse atomic gas, as introduced in Sect. 2.1.2. Observationally, carbon monoxide is often used to trace molecular clouds, as cold molecular hydrogen is hard to detect, due to its missing permanent electric dipole moment (see Sect. 2.2.4, where the physics of molecular emission lines is explained in more detail). CO in contrast, is easy to detect and sufficiently well mixed with hydrogen to use it as a proxy for molecular cloud observations.

Williams et al. (1995) discovered an anti-correlation between CO and H I emission in the Rosette nebula. They concluded that atomic and molecular clouds are related but mutually exclusive. The atomic hydrogen forms a halo around the molecular clouds and fills the inter-cloud medium. However, Li and Goldsmith (2003) also find H I in molecular clouds.

As molecular clouds show a large level of turbulence, we can assume this energy to originate from the initial atomic clouds. Continuous accretion of molecular gas from the surrounding H I probably drives turbulence (Klessen and Hennebelle 2010; Goldbaum et al. 2011).

For nearly ten years, theoreticians have now produced models of the molecular cloud formation. One class of models describes the interaction of colliding flows (also called converging flows). There have been calculations by different groups, for example, published in Audit and Hennebelle (2005); Vázquez-Semadeni et al. (2007); Hennebelle et al. (2008); Heitsch et al. (2008); Banerjee et al. (2009).

These models base on two flows of warm atomic hydrogen gas that stream toward each other. The principle setup is depicted in Fig. 2.4. The turbulences at the impact region let the WNM collapse into CNM clouds in which molecular clouds can associate.

Of course, this setup is very simplistic and is most probably not found in reality in this way. The simulation of specific star-forming regions is nearly impossible

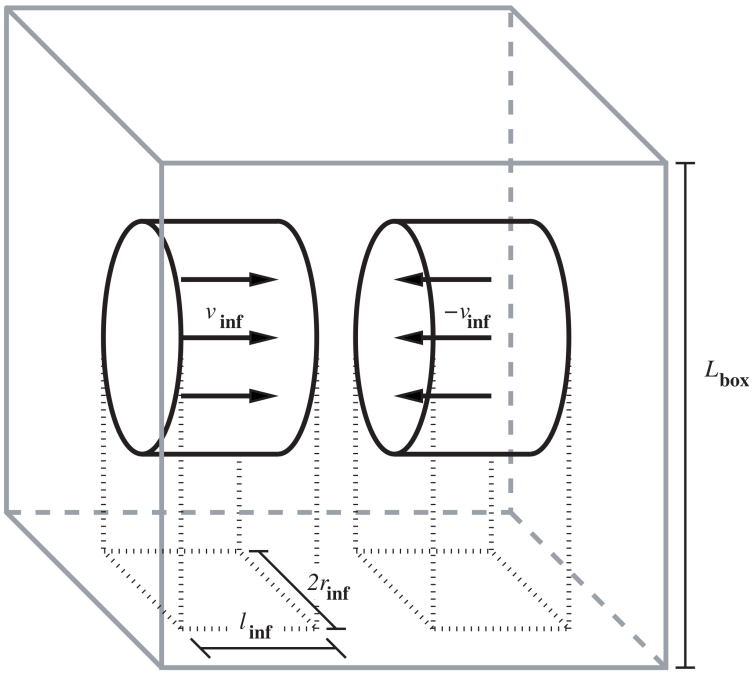

Fig. 2.4: Colliding flows model from Vázquez-Semadeni et al. (2007).

at the moment, as exact starting values for the models have to be found. Still, modeling has made important progress in the last years and can explain molecular cloud formation, at least in principle.

The structure of the molecular clouds is usually very complex and follows the structure of the CNM. The clumps are bounded by the WNM, which provides a confining pressure.

It is possible that star formation already sets in, while the cloud is still accreting (Vázquez-Semadeni et al. 2007). Different tools have been developed to distinguish between quiescent and star-forming clouds. One possibility is the use of PDFs of the H_2 column density (see Kainulainen et al. 2009) that we also use in our analysis later. This method creates a histogram of the column density data and analyzes the resulting shape. Quiescent regions are found to have a log-normal distribution, while star-forming regions show a power-law excess at the high-mass tail of the function (Klessen 2000; Schneider et al. 2012).

Another technique is the calculation of the Δ-variance, developed by Stutzki et al. (1998); Ossenkopf et al. (2008b,a). It is a measure for the characteristic scale in a dataset. It can measure typical widths of filaments but can also provide information on the form of turbulence in a cloud and therefore star formation activity (Rowles and Froebrich 2011).

Most models of molecular clouds have in common that parts of the clouds arrange in filamentary structures. This is an important result, as it is known from

observations that star-forming cores are found along these filaments. Therefore, we will now discuss these structures and their development in more detail.

2.1.4 Filamentary structure

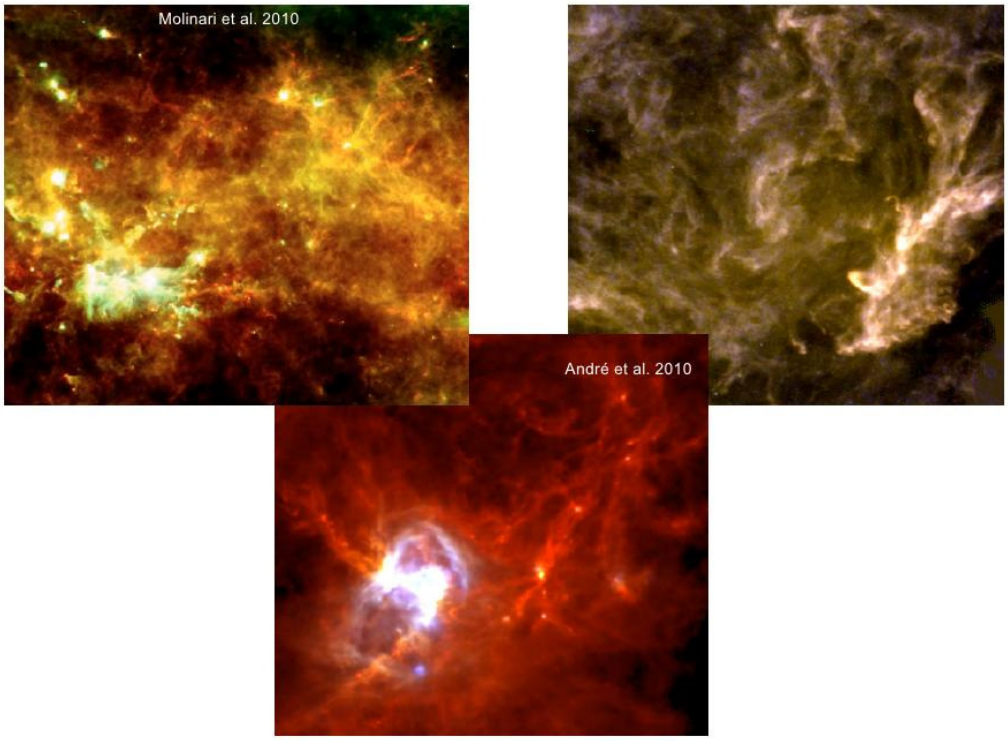

Fig. 2.5: Examples of filaments in observations. **Left:** *Molinari et al. (2010), showing infrared dark clouds (IRDCs) in the Galactic plane at 59° Galactic longitude Herschel infrared Galactic Plane Survey (Hi-GAL) map.* **Center:** *Aquila field from the* Herschel *Gould Belt Survey as described in André et al. (2010).* **Right:** *Polaris field from the same project.*

As mentioned above, filaments are pervasive in recent observations of molecular lines and dust emission (André et al. 2010; Molinari et al. 2010; Schneider et al. 2010). But also earlier observations show these objects (e.g. Dutrey et al. 1991). Here, filaments are defined as coherent, elongated structures that are seen in emission or absorption. Figure 2.5 shows a few examples of filaments observed with the HSO. The typical filament in these observations has a width of 0.1 pc, as measured by Arzoumanian et al. (2011), but the definition of what exactly is called a filament can change. These values stem from dust total power maps that average out possible sub-structure. Additional velocity information and high spatial resolution show that large filamentary clouds can often be broken down into smaller filaments (e.g. Hacar et al. 2013).

Again, as mentioned above, filaments are also found recurrently in the mod-

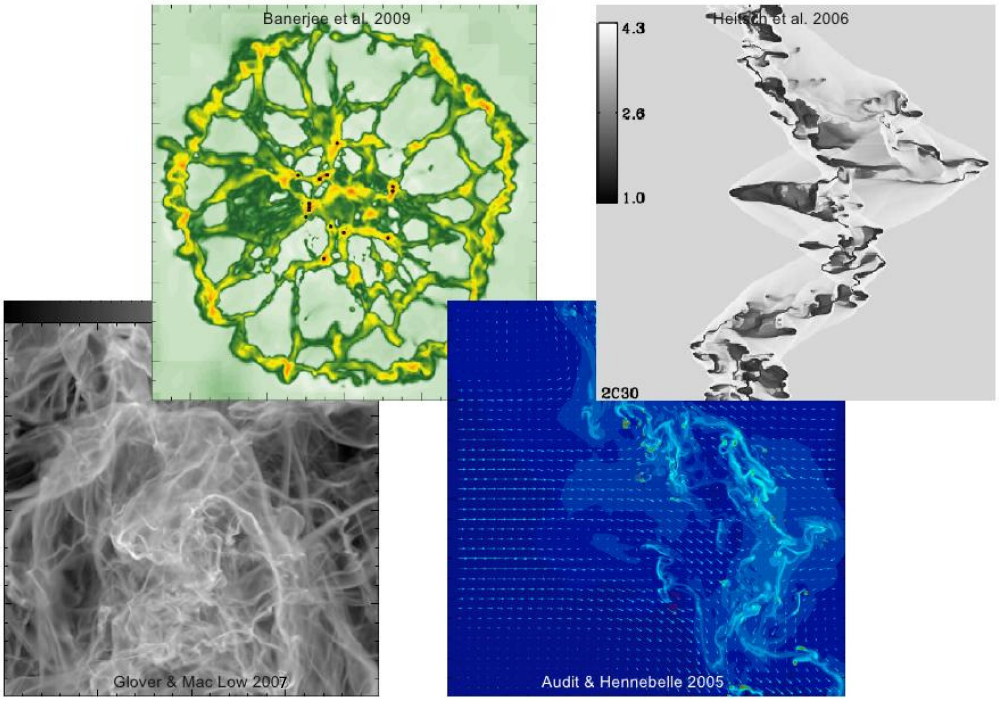

Fig. 2.6: Examples of filaments in simulations. **Left:** *Model from Glover and Mac Low (2007), three-dimensional hydrodynamics with self-gravitation and non-equilibrium chemistry.* **Center left:** *3D colliding flows model using weakly magnetized magneto-hydrodynamics (MHD) simulations (Banerjee et al. 2009).* **Center right:** *2D purely hydrodynamical model from Audit and Hennebelle (2005).* **Right:** *Pure hydrodynamics 3D model, as presented in Heitsch et al. (2006).*

els of molecular cloud formation: Padoan et al. (2001); Audit and Hennebelle (2005); Heitsch et al. (2006); Glover and Mac Low (2007); Hennebelle et al. (2008); Nakamura and Li (2008); Inoue and Totani (2009); Vázquez-Semadeni et al. (2011); this is a non-exhaustive list of works. There are three fundamental processes that can play a role in filament formation: gravity, turbulences, and magnetic fields. Each of the mentioned simulations takes one or more of these into account.

Models based on pure gravity can create filaments from fragmentation of sheets of gas. Self-gravity enhances anisotropies in the mass distribution, thus, somewhat elongated clouds will soon collapse to filaments (Myers 2009), which will further break down and form cores along them (Ostriker 1964; Fiege and Pudritz 2000). In MHD turbulence models, the filamentary structure can be induced by turbulence (Padoan et al. 2001). Including gravity, these initial structures can be selected and further enhanced by gravity, creating cores (Hennebelle and Chabrier 2008). Magnetic fields can add stability to filaments.

It is yet unclear which specific setup of turbulence, MHD, and gravity is most realistic. Until now, it is not possible to actually distinguish between different

models using observations. More advances in models and observations are needed for this purpose.

2.1.5 Structure of the Milky Way

Making statements about the structure of the Milky Way is inherently complicated, since the Solar system is located inside the Galaxy. We have to try and reproduce the distribution of matter by observing the velocity structure of the visible radiation. Via the relative velocities of stars and clouds it is possible to create a model of the Galaxy. A comparison with extragalactic observations of similar galaxies can help to verify this model.

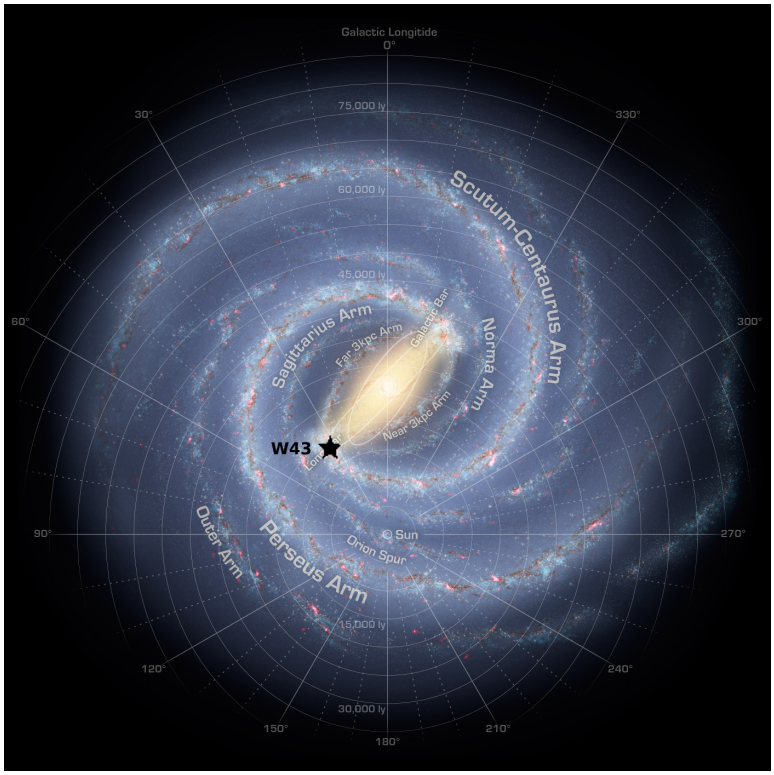

Fig. 2.7: Artists view of the Galaxy. The assumed location of W43, the object of interest in this work, is marked by the black star. Credits: R. Hurt, Caltech.

Basically, it has been known for decades that our Galaxy is a spiral galaxy. It was discovered later that, to be more precise, it has to be considered a barred spiral galaxy (Chen et al. 1996). Many single observations of different parts of the Galaxy and at different wavelengths have been carried out to determine the number, shape and angle of the spiral arms. Meta-studies of dozens of studies from the years 1980 to 2005 are given in Vallée (1995, 2002, 2005) and in Vallée (2008) a simple model of our Galaxy is designed. Figure 2.7 shows a face-on view of the Milky Way, created by an artist, according to the models.

Our Galaxy consists of a flat, nearly circular disk that contains spiral arms and surrounds the Galactic center. Beside the stars, it contains large amounts of dust, atomic, and molecular gas (Levine et al. 2006). A bulge surrounds the inner few kpc spherically and extends above and below the disk. Sometimes, it is rather described as an elliptical pseudo-bulge. Disk and bulge are again embedded into the spherical Galactic halo that contains mostly old stars, but hardly any molecular gas or dust. The size of the halo is roughly defined by the distances of our neighboring dwarf galaxies, the Large and Small Magellanic Clouds (Connors et al. 2006).

The center of the Galaxy, about 8.5 kpc remote from the Sun, contains a super-massive black hole that is found to have a mass of $\sim 3 - 4.5 \times 10^6\ M_\odot$ (Genzel et al. 2000; Ghez et al. 2008). The diameter of the Galaxy is usually given as $\sim$30 kpc, in which it contains a total mass of about $10^{12}\ M_\odot$, the height of the disk is approximately 0.3 kpc (Rix and Bovy 2013).

It is debated (see Nishiyama et al. 2005) whether the center of the Galaxy contains not only a single bar, but two separate bars, the regular Galactic bar and the elongated bar. The assumed lengths of the bars are typically 3 kpc (Rodríguez-Fernández and Combes 2008). Scientists usually agree that four Galactic spiral arms exist (Churchwell et al. 2009), which connect to the tips of the bars. One set of arms, the Perseus and the Scutum-Centaurus arm, are brighter and wider, while the other set, the Norma or Outer arm and the Carina-Sagittarius arm, are fainter and smaller. These arms wind around the Galactic center in logarithmic outward spirals. Additionally, there are two weak arms that are called the near and the far 3-kpc arm that connect both ends of the elongated bar with each other (Rodríguez-Fernández 2011). Finally, several spurs, or arm fragments, can be found in-between the main spiral arms, one of which is the Orion-Cygnus spur that contains the Sun.

There is a fundamental difference between the spiral arms region and the bars. Stars and matter in both regions orbit the Galactic center but their orbits differ. Orbits in the spiral arms are circular (Lin and Shu 1964; Lynden-Bell and Kalnajs 1972; Gómez et al. 2013), whereas elliptical orbits are found in the bars (e.g. Binney 1982; Sanders et al. 1983; Pichardo et al. 2004). The spiral arms are thought to form due to waves of increased density that move outward from the Galactic center. In this model the inter-arm medium would move in and out of the arms, where it is compressed. This increased density would initiate the formation of molecular gas and finally star-formation would set in (e.g. Moore et al. 2012; Eden et al. 2013).

Although stars and gas at all Galactic radii rotate around the center, the rotation velocity changes with the radius. This rotation curve is an important tool for the calculation of distances in the Milky Way and is therefore strongly debated. Rotation speed in the central part of the Galaxy roughly rises linearly with the radius. Outside the bar, the rotation curve is mostly flat, which means that rotation does not depend on the distance toward the Galactic center (see e.g. Clemens 1985; Reid et al. 2009). These observed velocities contradict the

amount of mass that can actually be detected. According to the observed distribution of mass, the rotation curve should decrease for larger radii (Rubin et al. 1980, describe this phenomenon in extragalactic galaxies). The hypothesis of dark matter tries to explain this lack of mass by postulating the existence of hitherto undetectable mass. This question touches some of the fundamentals of physics and is still not answered to date.

The presumed location of the W43 star-forming region, the region of interest in this thesis, is shown by the black star in Fig. 2.7.

2.1.6 The W43 star-forming region

The region at 30° Galactic longitude in the Galactic plane was first identified by Westerhout (1958), who listed it in his catalog as W43. About 10 years ago, this object was identified as one of the most active star-forming regions in the Galaxy (Motte et al. 2003). It was shown to be heated by a cluster of Wolf-Rayet and OB stars (Lester et al. 1985; Blum et al. 1999) and Motte et al. were the first to consider it as a Galactic mini-starburst region.

The name W43 was initially used for the single cloud (G030.8+0.02) that is known today as W43-Main. Nguyen Luong et al. (2011) characterized the complex by analyzing Very Large Array (VLA) H I emission (Stil et al. 2006) and the ^{12}CO (1–0) (Dame et al. 2001) and ^{13}CO (1–0) (Jackson et al. 2006) Galactic plane surveys. They concluded that W43-Main and G29.96-0.02 (also called W43-South) should be considered as a single giant connected complex.

From the position in the Galactic plane and its radial velocity, Nguyen Luong et al. (2011) concluded that W43 is located at the junction point of the Galactic long bar and the Scutum spiral arm at 6 kpc relative to the Sun (see black marker in Fig. 2.7). The kinematic distance ambiguity, arising from the Galactic rotation curve, gives relative distances for W43 of $\sim$6 and $\sim$8.5 kpc for the near and the far kinematic distance, respectively. Although there have been other distances adopted by other authors (e.g. Pandian et al. 2008), most publications (Pratap et al. 1999; Anderson and Bania 2009; Russeil et al. 2011) favor the near kinematic distance. In Sect. 4.4 we will confirm this distance determination.

This position in the Galaxy makes W43 a very interesting object for studying the formation of molecular clouds. Despite its distance, it is possible to analyze the details of this cloud, due to its large spatial scale of $\sim$150 pc and the large amount of gas at high density (see Nguyen Luong et al. 2011). As discussed above, this junction point in the Galactic plane is an ideal laboratory to study the circumstances of molecular cloud formation.

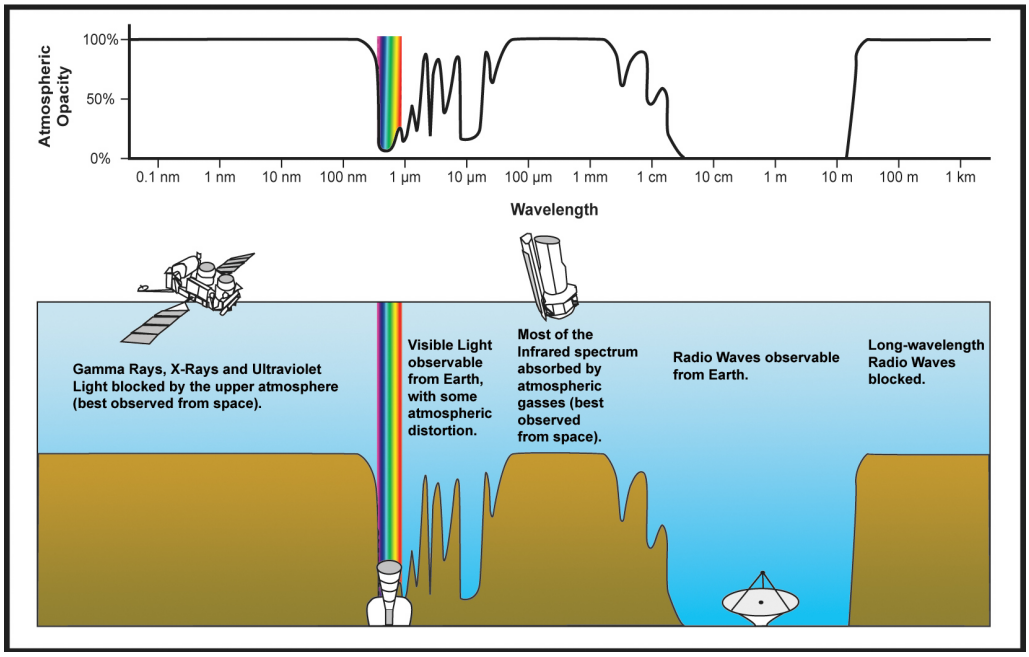

Fig. 2.8: Transmission of the atmosphere. Credits of image: NASA/Infrared Processing and Analysis Center (IPAC).

2.2 Submm/mm-Astronomy

The spectral window of a few mm (about 100–350 GHz) has become one of the most used in radio astronomy in the last decades. Higher frequencies in the sub-millimeter regime (up to a few THz) are more complicated to observe, but improved telescopes and receivers have begun to make this part of the spectrum available to astronomy. These frequency ranges are especially important for research of the ISM. Many molecular emission line transitions fall in these spectral windows. In contrast to lower radio frequencies, the atmosphere is not completely transparent at these frequencies (cf. Fig. 2.8). The higher the frequency, the more radiation is absorbed, mostly by water vapor. Due to this characteristic of the atmosphere, submm/mm telescopes need to be located as high as possible at places as dry as possible. A very good location is the Atacama desert in Chile (ALMA, APEX, NANTEN2). To further reduce the atmospheric absorption, telescopes are also mounted on planes (Stratospheric Observatory For Infrared Astronomy (SOFIA)), balloons (Stratospheric Terahertz Observatory (STO)), and of course satellites (HSO). Unfortunately, the better the conditions, the more costly and complicated the operations are.

We use a variety of telescopes in our work that operate at these frequencies. We will hence give a short introduction into the functionality of radio telescopes.

2.2.1 Radio telescopes

For an exhaustive description of the technical background in this and the next subsections see, for example, Wilson et al. (2009). Single-dish antennas, the most common type of telescopes used in radio astronomy, usually consist of a circularly symmetric paraboloid dish (or mirror), although sometimes dipole antennas are used for very low frequencies (e.g. in the Low-Frequency Array (LOFAR) and in future in the Square Kilometre Array (SKA)). The incoming radiation from the sky is reflected to a secondary mirror, which focuses the signal into the optics of the telescope and finally into the receiver.

The beam pattern of a telescope is the Fourier transform of the shape of the aperture (in optical astronomy, the aperture is just a disk and the beam pattern therefore the square of the Bessel function). In radio astronomy, this pattern is refraction limited and depends on the exact geometry of the telescope. The beam pattern of a parabolic telescope is basically a Gauss function, convolved with the disk of the main mirror, which leads to a beam pattern with a strong Gaussian maximum in boresight and smaller off-axis maxima, so-called side lobes, induced by the cutoff of the Gaussian at the edges. Additionally, the shadowing of the secondary mirror, its suspension legs in the main beam, and the reflection of the beam onto the secondary mirror, add further changes to the final beam pattern. It can only be numerically determined, but the central maximum usually still remains mostly Gaussian.

The distribution of intensities on the sky is convolved with this beam pattern and the integral is then fed into the receiver. This means that information of more than one point on the sky goes into the signal, which can be a problem, when observing extended emission. The weighting is determined by the beam pattern. Side lobes (typically on the order of 10 to 20 dB) can be reduced by only illuminating the inner part of the main dish, however, this tapering reduces sensitivity and resolution of the telescope.

The half power beam width (HPBW) of a radio telescope depends on the details of the beam pattern and the tapering, but can be fitted by the formula

$$\Delta\theta_{\mathrm{HPBW}} = (1.02 + 0.0135\,T_e)\frac{\lambda}{D}, \tag{2.7}$$

from Goldsmith (1996), with the wavelength λ, the diameter of the primary mirror D, and the edge taper T_e in dB. Two points on the sky can still be distinguished if they are separated by this angle. This means that the resolution increases with the telescope size and with the frequency. To regain the full information of the distribution of emission on the sky, filtered by the beam, the spatial sampling of observations has to be below $\lambda/2D$ (Nyquist sampling).

Unfortunately, higher frequencies require a higher accuracy of the telescope surface so that it still acts as a mirror. The root mean square (rms) deviation

of the surface has to be on the order of $\lambda/20$. Therefore, in order to observe the same level of detail, we need larger telescopes, but with less accuracy of the surface, at low frequencies and smaller dishes with high surface accuracy at high frequencies.

For example, the Effelsberg telescope operates at frequencies between 0.4 and 86 GHz, has a diameter of 100 m and a surface accuracy of 0.5 mm, which is a great achievement for this antenna size. In contrast, the Cerro Chajnantor Atacama Telescope (CCAT) will use frequencies between 150 GHz and $\sim$1.5 THz. It will will have a diameter of 25 m and a surface accuracy of less than 10 μm, an extremely demanding technical requirement.

2.2.2 Receivers used in radio astronomy

The radiation from the sky, that has been focused by the antenna, needs to be amplified, filtered by direction, frequency, and polarization, and converted to an electrical signal to be usable. These different steps are done by receivers that convert the electromagnetic radiation into electrical voltage, amplify it, and nowadays mostly convert it to digital information.

Different receiver designs serve different purposes in radio astronomy. For a high sensitivity of continuum observations over a large bandwidth, bolometers are often used. They measure the temperature change of an absorber, induced by the absorption of photons. This temperature change can be used to determine the energy of the absorbed radiation. Bolometers do not preserve the spectral information, phase, or polarization of the detected photons. Bolometers are best used for total power measurements, where they can be extremely sensitive. They can be combined with spectrometers or polarizing devices in front of them to regain this information but loose sensitivity that way. These measurements are more complicated and the resolution is limited with these devices.

Heterodyne receivers are widely-used for high resolution spectroscopic observation. Their advantage over bolometers is that they preserve frequency information through the filtering process. These receivers amplify and then convert the signal from the sky to a lower frequency, by mixing it with a pure sine-wave from a local oscillator (LO). This synthesizer signal is shifted by a few percent from the sky signal (usually a few GHz). The resulting mixed signal has a lower frequency, that still contains all the astronomical information and can then be filtered and further amplified. Superconductor-insulator-superconductor (SIS) junctions are nowadays often used as mixers, as they provide a good spectral resolution and large bandwidth (several GHz). However, from frequencies on the order of THz, SIS mixers suffer from losses. At this range hot electron bolometer (HEB) mixers have the advantage of a lower noise level, but only have a limited bandwidth of a few MHz.

Heterodyne receivers have the advantage of mostly preventing feedback effects during the amplification of the signal. Without the frequency conversion

(homodyne receivers), it is possible that amplified signal leaks back into the initial signal. In addition, these receivers are easier to tune to the desired frequency by changing the LO signal. Finally, it is more complicated to build amplifiers that work at very high frequencies. This can be circumvented by amplifying the lower frequency in heterodyne receivers.

The part of the receiver that works at sky frequency is usually called frontend, while the part that works at the down-converted frequency is called a backend. Frontends can consist of one (single-pixel receivers) or several (array receivers) mixers. Arrays can observe several positions on the sky simultaneously, which is efficient if an observation includes many points or complete maps.

Spectrometers are backends that resolve the spectral information of the signal. There are several ways of doing so. One possibility are acusto-optical spectrometers (AOSs), where the signal is converted to an acoustic signal and fed into a special crystal (Bragg-cell), whose refraction behavior is changed. A laser, pointed at the cell, is deflected depending on the frequency of the incoming signal and then reaches a matrix of charge-coupled devices (CCDs) that pick up the laser at different positions. Thus, the Bragg-cell acts as a natural Fourier transformation of the input signal. Fourier-transform spectrometers (FTSs) digitize the time dependent signal and transform it to a spectrum using raw computing power. These spectrometers are becoming the new standard, since computers have become fast enough to provide enough bandwidth and resolution.

For spectrometers, the sensitivity ΔT that can be reached depends on the systems noise temperature T_{sys}, the desired spectral resolution $\Delta\nu$, and the observing time t:

$$\frac{\Delta T}{T_{\mathrm{sys}}} \propto \frac{1}{\sqrt{\Delta\nu\, t}}. \tag{2.8}$$

The needed observing time can be quite large (sometimes hours or more), therefore, the receiver needs to be as stable as possible, but will rarely reach a stability of more than a few minutes. Both, the total gain and differences along the spectral axis will change over time. Therefore, observations often need to be split up into shorter observations, with gain calibrations conducted in-between.

In addition, the instability of the atmosphere has to be taken into account. It will usually change on the order of minutes and can be dealt with, by observing not only the astronomical target (on-position), but also a nearby blank position on the sky (off-position). The difference of both spectra is therefore the desired signal, adjusted for atmospheric and receiver effects. This position switching method is used when observing single positions on the sky. For large objects, the on-the-fly (OTF) method is more efficient. Here, several positions are consecutively observed while the telescopes slews across the sky and share one common off-position. This is the observational technique which is most often used in this work.

2.2.3 Interferometer telescopes

As discussed above, the angular resolution of a telescope at a fixed wavelength linearly depends on the telescope size. This, of course, cannot be increased infinitely, due to technical reasons. A way to increase the resolution is to use two or more telescopes and combine them. Using two telescopes with a distance D will yield the same resolution of a single telescope of diameter D. Still, the collecting area of two small telescopes is much smaller than that of a big one, thus, the sensitivity is lower, too. Also, the distance determines the maximum scale of the intensity distribution that can still be observed. It decreases with larger D.

An interferometer does not receive a signal at each telescope individually, but rather the cross correlation of the radiation field at both antennas, including its phase. The wavefront arriving at the telescopes is the Fourier transform of the spatial image on the sky. The pair of antennas, also called a baseline, produce the mutual coherence function, or visibility. For N antennas, we receive a total of $N(N-1)/2$ baselines. Aperture synthesis is the name for the recovery of the physical intensity distribution on the sky, as a large single-dish telescope would observe it, from the visibilities of a telescope array.

Each visibility of one antenna pair is located at a point in the uv-plane, the Fourier transformed xy-plane of the sky, determined by the relative location of the two antennas. For a good reconstruction of the intensity image, the uv-plane needs to be covered as completely as possible. Therefore, more antennas in different relative distances improve the quality of the final image. Long observation times also help, as the sky rotates over the array and further fills the uv-plane.

As mentioned, the larger scale emission is filtered out by very wide antenna configurations. Therefore, a combination of long and short baselines is required to combine the information of different size scales. ALMA, for example, uses an extra interferometer of smaller antennas, the Atacama Compact Array (ACA) to provide short spacings. Still, the origin of the uv-plane can never be covered, as a baseline of length zero cannot be achieved. This neglects widespread emission that fills the complete field-of-view of the array. Ideally, additional data of a single-dish telescope is used to complement interferometric observations.

2.2.4 Molecular emission lines

As stated before in Sect. 2.1.1, molecular clouds play an important role in the process of star formation. To understand the physical conditions of these clouds, astronomical observations of them have to be carried out. For details on this topic, see for example Draine (2011); Hänsel and Neumann (1995).

Molecules can either be observed in emission or absorption, where we need background sources that shine through the cloud of interest. For both cases,

certain quantum-mechanical energy states of the molecule have to be excited, either by photons, collision with other molecules, or through radiative excitation. There are several classes of transitions between states that can either emit or absorb a photon, leading to a detection. The frequency ν of the photon is given by the energy difference of the two states, $\Delta E = h\nu$.

Typically, we distinguish between rotational, vibrational, and electronic transitions. Purely rotational transitions need the least energy and can therefore be observed in the submm/mm wavelength regime. These transitions are changes in the angular momentum J of the molecule, where usually only changes of $\Delta J = \pm 1$ are allowed. Most of the transitions observed in this work are rotational transitions, where the notation ^{13}CO (2–1) describes the rotational transition (J=2$\rightarrow$1) of the ^{13}CO molecule. This notation will be used throughout this work without further notice, from here on. Molecules need a permanent electric dipole moment for the electromagnetic waves to be able to couple to the angular momentum. Without a dipole moment, molecules cannot be observed in purely rotational transitions.

Rotational energy states of two-atomic molecules are often observed, since these molecules are important in the physics of the ISM. The energy states depend on the rotational level J: $\Delta E \propto J(J+1)$. Therefore, the energy difference between two neighboring levels, which determines the frequency of the emitted photon, is directly proportional to J. The emission lines for upper $J = 1, 2, 3...$ are thus equidistant in frequency and are easy to recognize in observed spectra.

Vibrational transitions need much more energy than the rotational ones. They are therefore observed in the infrared. The respective energy states describe vibration of atoms of the molecule in different directions. The specific degrees of freedom are defined by the geometry of the molecule. Finally, electronic transitions change the energy states of the electrons orbiting the molecule. Exciting electrons needs more energy than changing rotational or vibrational states and are typically observed in the optical and UV regime.

The major fraction of molecular clouds consists of molecular hydrogen. Unfortunately, H_2 is a symmetric molecule and has no constant electric dipole moment, and therefore no observable rotational transitions. Vibrational emission of H_2 is observable, but to excite these states, a high kinetic energy of the gas, and therefore a high temperature, is needed. As we are especially interested in cold molecular gas, H_2 cannot be observed directly.

After H_2, CO is the second-most abundant molecule in the ISM. It is very stable, with a dissociation energy of 11.2 eV, and only UV-photons between this energy and the ionization energy of atomic hydrogen (13.6 eV) can destroy it (higher frequency photons are quickly absorbed by the more abundant hydrogen). Therefore, once CO has formed, it is rarely dissociated. Its relative abundance is typically 10^{-5}, i.e. one CO molecule in 10^5 H_2 molecules, but this value varies in different locations of the Galaxy. All other molecules are even less abundant, although more than 150 have been identified to date. Most of these contain

H, C, O, or N atoms, but also Na, Mg, S, and Si can occur.

As CO has a small dipole moment, the molecule can be rotationally excited at low temperatures and densities. It is a linear diatomic molecule and therefore distributes its complete radiated energy to few lines that are therefore strong and easy to recognize (in contrast to "weeds", such as methanol, that have many different lines). It is found in most molecular clouds and is thus often used as a substitution for H_2 observations. Although it is much less abundant than H_2, CO emission becomes optically thick quite easily in dense or large clouds. It is thus used to trace the very expanded, diffuse molecular clouds (e.g. Dame et al. 2001).

The opacity τ is a measure of how deep we are able to see into a cloud. A cloud is optically thick ($\tau \gg 1$), when emission of its molecules is absorbed again by molecules of the same relative velocity. We can thus only observe the surface of an optically thick cloud. On the other hand, if a cloud is optically thin ($\tau \ll 1$), we are able to completely see through it. This is described by the integral equation of radiative transfer,

$$I_\nu(\tau_\nu) = I_\nu(0)\mathrm{e}^{-\tau_\nu} + \int_0^{\tau_\nu} \mathrm{e}^{-(\tau_\nu - \tau')} S_\nu \mathrm{d}\tau', \tag{2.9}$$

which describes the detected intensity $I_\nu(\tau_\nu)$ at a frequency ν, that results in the initial intensity $I_\nu(0)$ of a background source being absorbed by traveling through a cloud of opacity τ_ν, which for its part emits with the source function S_ν.

A way to circumvent this, is to use other molecules that are less abundant. Using isotopologues of CO is effective, as it combines a lower abundance with similar physical properties than those of CO. CO, or $^{12}C^{16}O$ combines the two stable and most common isotopes ^{12}C and ^{16}O. ^{13}CO is the CO isotopic molecule, where the ^{12}C is replaced by the less common ^{13}C. The usual ratio of CO to ^{13}CO is 60:1. This isotopologue is adequate to trace the mid density molecular clouds. For even denser molecular clouds we can use $C^{18}O$ or $C^{17}O$, where the ^{16}O is replaced by an ^{18}O or ^{17}O atom. $C^{18}O$ is a factor of 500 less abundant than CO, while $C^{17}O$ is even less abundant by another factor of 3. These isotopologues are used for the analysis of dense molecular clumps. All isotopic ratios vary across the Galaxy and can be found in Wilson and Rood (1994).

CO rotational observations only cover a density range of about 10^2 cm^{-3} to 10^4 cm^{-3} in the millimeter and submillimeter domain. For higher densities, other molecules need to be used, for example NH_3, H_2O, HCO^+, or SiO. As different molecules have varying electronic dipole moments, different densities and temperatures are needed to provide enough energy to excite them. A single transition of one molecule cannot determine temperature or density, exactly. The larger the ensemble of observed lines, the better the physical conditions can be constrained (see e.g. Evans 1999, for an overview of tracers of physical conditions).

2.2.5 Fine-/Hyperfine structure lines

Apart from rotational molecular lines, we will also discuss observations of certain atomic and ionic transitions in this work. In detail we observed lines of atomic carbon (C I or C) and ionized carbon (C II or C^+) [2]. The transitions discussed here are classically forbidden, which means that under lab conditions the excited state is collisionally de-excited so quickly that no emission can be measured. Only in the very diffuse gas of the ISM these lines can be detected. Forbidden lines are marked by square brackets, e.g. [C II].

The energy states of these lines are somewhat complicated, so we will describe them in detail here. See again Draine (2011) for the physical background of this section.

Atomic carbon has six electrons that occupy the ground configuration $1s^2 2s^2 2p^2$, two electrons in the $1s$ orbital, two in the $2s$ orbital, and two in the $2p$ orbital, which are the three orbitals of least energy. The $2p$ sub-shell is only partially filled.

Energy levels of atoms and ions in the ground state are determined by the quantum numbers L, the total orbital angular momentum of the electrons, the total spin angular momentum of the electrons S, and the total electronic angular momentum J. The configuration of the electrons is written in the spectroscopic notation: ${}^{2S+1}\mathcal{L}_J$, where $\mathcal{L} = S, P, D, F...$ for $L = 0, 1, 2, 3...$. The two electrons in the $2p$ orbital can be arranged in three ways, where the wave-function is antisymmetric (Pauli exclusion principle), which are ${}^3P$, ${}^1D$, and ${}^1S$. The configuration with the lowest energy is ${}^3P$ ($L = 1$ and $S = 1$).

As J is the vectorial sum of L and S, there is more than one potential value for J, when both other numbers are nonzero. This different configurations have different energies, due to spin-orbit coupling and result in the so-called fine structure. In our case of C I, the ${}^3P$ configuration splits up into three levels: ${}^3P_0$, ${}^3P_1$, and ${}^3P_2$. This results in two possible fine structure transitions in the ground state:

$$ {}^3P_2 \rightarrow {}^3P_1 \text{ and } {}^3P_1 \rightarrow {}^3P_0. $$

The second transition is the one that we observed and describe later in this thesis. We will use the short notation [C I] (1–0) sometimes, which will always refer to this fine structure transition.

The carbon ion C^+ has five electrons in the $1s^2 2s^2 2p^1$ ground configuration. The lowest energy orbital is the ${}^2P$ sub-shell ($L = 1$ and $S = 1/2$), so there are two possible values for $J = L + S$: $3/2$ and $1/2$. This results in one fine structure transition in the ground state:

[2] The spectroscopic ionization notation (e.g. C I for atomic carbon and C II for ionized carbon) and the notation C/C^+ is used synonymously throughout this work to identify the species. When discussing the specific line, [C I] and [C II] are used, respectively, to denote a forbidden transition.

$^2P_{3/2} \rightarrow {}^2P_{1/2}$.

Another phenomenon can be observed for atoms with an nonzero nuclear spin. Interaction of the electrons with the nuclear spin leads to a further splitting of the fine structure lines. This is called hyperfine splitting and can, for example, be observed in the hydrogen atom. It is also found in the N_2H^+ molecule that is used in this work. It is a linear molecule, whose electrons are all paired. The electric quadrupole moments of the nitrogen nuclei interact with the molecular electric field gradient and split the ($J = 1 \rightarrow 0$) line into seven hyperfine components (Caselli et al. 1995).

2.2.6 Line profile and Doppler effect

Observed line profiles of certain transitions are no δ-function, but depend on macroscopic and microscopic processes that broaden the line and give it a specific shape. The most fundamental effect is the natural broadening. The frequency of a transition is given by the difference of the two involved energy states by $\Delta E = h\nu$. These energy differences are not exactly fixed but, have a small energy spread, due to the Heisenberg uncertainty principle: $\Delta E \Delta\tau \leq \hbar/2$, where $\Delta\tau$ is the lifetime of the excited state. This natural line shape is a Lorentz distribution (also Cauchy distribution). In case of collisions with other particles this natural emission process can be interrupted and the lifetime of the excited states will be reduced. This pressure broadening leads to a broader Lorentz line shape.

Additionally, thermal motion of the particles has an influence. A gas in thermal equilibrium shows a Maxwell distribution of energies that results in a Gaussian profile. In combination with pressure broadening, the observed line will be a Voigt function (see Rybicki and Lightman 1979; Wilson et al. 2009).

Macroscopic effects also influence the line shape, especially large scale gas streams, which shift the line, or parts of it. From the frequency ν of an observed line, we can conclude the radial velocity Δv between the emitting gas and the observer via the Doppler effect,

$$\frac{\Delta v}{c} = \frac{\nu - \nu_0}{\nu_0}, \tag{2.10}$$

measured in $\mathrm{km\,s^{-1}}$, where ν_0 is the rest frequency of the transition. The distribution of velocities in the gas then leads to a broadening of the measured line, called Doppler broadening. Outflow, infall, and rotation of gas are typical processes which can be recognized in the line profile. Another line broadening effect is turbulence, but the resulting line profile can be more complicated than

the before mentioned effects. Even though the velocity distribution of an incompressible turbulent gas is Gaussian, the line profile can deviate due to optical depth effects (Silant'ev et al. 2006) or shocks.

Chapter 3

Large scale CO observations of W43

We now present the results of the W43 Hera/EmiR Observations (W43 HERO) project, large scale observations of molecular clouds in the W43 region with the IRAM 30m telescope. In this chapter we describe the technical part of this project, the telescope setup, the details of the observations, and the data reduction. We present the resulting maps at the end of this chapter in Sect. 3.4. In Chapter 4 we then analyze the velocity structure of the obtained data and determine the position of the W43 complex in the Galaxy. Finally, in Chapter 5 we study the physical properties of W43. These three chapters have been published in Carlhoff et al. (2013).

The project W43 HERO was initiated by Frédérique Motte (CEA, Saclay) and Peter Schilke (Universität zu Köln). Its goal is to give a complete characterization of the molecular clouds of medium density ($\sim 10^3$–10^4 cm^{-3}). To achieve this, large scale maps of the complete complex with a size of $\sim 1^\circ \times 1.4^\circ$ had to be taken. A high spatial and spectral resolution was necessary to be able to analyze the distribution of the clouds in detail.

3.1 Contribution of co-authors

This project and the publication in Carlhoff et al. (2013) is a collaboration with several colleagues. The concept of the project was prepared by Frédérique Motte, Peter Schilke, and several other members of the W43 consortium, amongst others, Nicola Schneider, Quang Nguyen Luong, and Frederic Schuller. The preparation of the setup and the observing scripts for the CO observations were done by myself, with the help of Peter Schilke, Carsten Kramer, and Robert Simon; the observations were then conducted by Quang Nguyen Luong and myself.

In the next step, I mainly worked on the data reduction with support from Peter Schilke and Quang Nguyen Luong. The analysis that is given in the next two chapters was done by me in most parts, of course, with comments and suggestions from all co-authors. Additionally, Quang Nguyen Luong provided the *Herschel* excitation temperature and H_2 column density maps in Fig. 5.8 that were used in the analysis in Sect. 5.5.4. Nicola Schneider, finally, contributed the plot of the column density histogram in Fig. 5.9 and part of its interpretation in Sect. 5.6. All other figures and steps of analysis were created by me.

3.2 The observations

3.2.1 Observed lines

For this project we used emission lines of the carbon monoxide isotopologues ^{13}CO and C^{18}O. Carbon monoxide is a diatomic molecule and is easily excited due to its low electric dipole moment. As we are interested in the cold molecular gas, we wanted to observe low rotational transitions of these species. See Sect. 2.2.4 for more details on molecular emission lines. Notation throughout the next chapters will be in the form of ^{13}CO (2–1), denoting the rotational transition (J=2$\rightarrow$1) of ^{13}CO, without vibrational excitation (v=0).

As described in Sect. 2.2.4, cold H_2 cannot be observed directly, due to its symmetry. We therefore used CO as a tracer of molecular clouds, as it is the second most abundant molecule and easily excited, so even diffuse clouds can be traced with it. In fact, CO is so abundant that it becomes optically thick, soon, in molecular clouds of typical size. This is why we used ^{13}CO and C^{18}O which are less abundant. These isotopologues let us trace the mid-density clouds (^{13}CO) and the denser central parts (C^{18}O).

3.2.2 The IRAM 30m telescope

The following data have been observed with the 30m telescope, operated by IRAM[1] (see Fig. 3.1). This telescope is located on Pico Veleta, in the Sierra Nevada near Granada, Spain, at an altitude of 2850 m. With its dish size of 30 m it is one of the most sensitive radio telescopes in the mm wavelength regime. Its heterodyne and bolometer receivers operate at 3, 2, 1, and 0.9 mm wavelengths. The observations of our project have been conducted between November 2009 and March 2011.

[1] http://www.iram-institute.org/

Fig. 3.1: Photo of the IRAM 30m telescope on Pico Veleta, Spain. Credits: IRAM.

3.2.3 Telescope setup

We simultaneously observed the molecular emission lines ^{13}CO (2–1) and C^{18}O (2–1) at 220.398684 GHz and 219.560358 GHz, respectively. Smaller regions around the two main cloud complexes were additionally observed in high-density tracers, such as HCO$^+$ (3–2), H^{13}CO$^+$ (2–1), N_2H^+ (1–0), and C^{34}S (2–1). This part of the project is not discussed here and will we published by Nguyen Luong et al. in prep.

This survey spans the whole W43 region, which includes the two main clouds, W43-Main and W43-South, and several smaller clouds in their vicinity. It covers a rectangular map with a size of $\sim$1.0 $\times$ 1.4 degrees (RA$\times$Dec). This translates to spatial dimensions of $\sim$105 $\times$ 145 pc, given an estimated distance of about 6 kpc to the source (see Sect. 4.4). The center of the map lies at 18:46:54.4 -02:14:11 (EQ J2000). The HPBW of the ^{13}CO and C^{18}O observations is 11.7″[2], which corresponds to 0.34 pc at this distance.

For the observations, we used the Heterodyne Receiver Array (HERA) of the IRAM 30m (Schuster et al. 2004). It consists of 3 $\times$ 3 pixels, separated by 24″, and has two polarizations, which point at the same location on the sky. This gave us the possibility of observing both CO isotopologues in one pass, where we observed one line per polarization. The Instrument HERA can be tuned in the range of 215 to 272 GHz and has a receiver noise temperature of about 100 K at 220 GHz. Typically, the system temperature of the telescope was in the range of 300 to 400 K during our observations.

We used the Versatile Spectrometer Array (VESPA) autocorrelator as back-

[2] http://www.iram.es/IRAMES/mainWiki/Iram30mEfficiencies

end, which was set to a spectral resolution of 80 kHz per channel with a bandwidth of 80 MHz. This translates to a resolution of 0.15 km s^{-1} and a bandwidth of $\sim$160 km s^{-1}, of which $\sim$100 km s^{-1} are usable. The bandwidth was set to cover the velocity range of 30 km s^{-1} to 130 km s^{-1} to cover the complete W43 complex.

In the original proposal, it was planned to take under-sampled OTF maps with a noise level of 0.5 K as an overview of the complex. A sampling of about one data dump per beam should have saved time to be able to cover the complete region. On the other hand, we would thus have missed a good part of the information about the distribution of the emission. Shortly before beginning our observations, we therefore decided to switch to a fully Nyquist-sampled OTF mapping mode to gain the full information. In order to cope with the assigned observing time, we increased the scanning speed, which resulted in a lower sensitivity (see Sect. 3.3). Still, we expected it to be good enough to detect most of the extended molecular emission in W43. In the end, this strategy turned out to be successful.

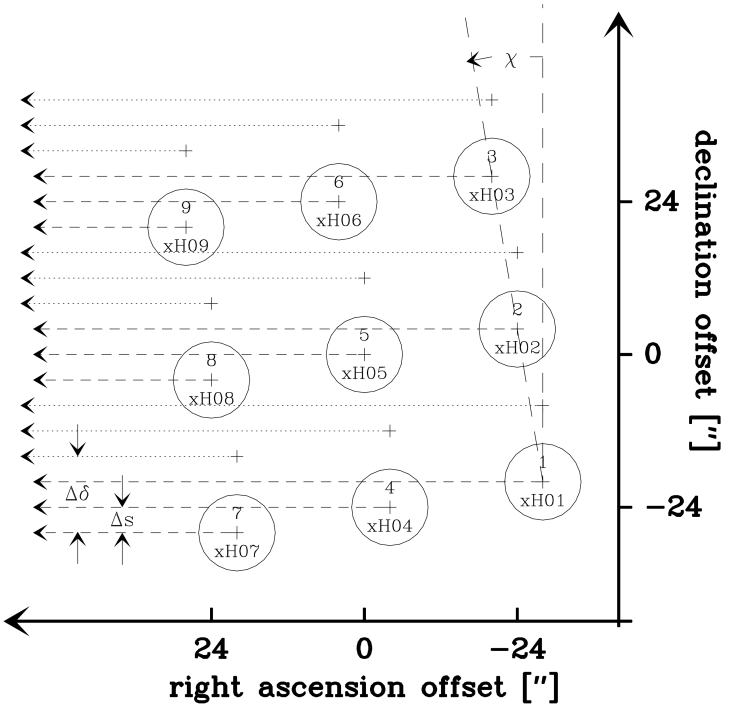

Fig. 3.2: Plot of the HERA coverage.

We used an OTF mapping mode to cover 10′ ×10′ tiles, taking about 20 minutes each. To achieve the right distance between scan lines, HERA was tilted by 9.5°, and using two interweaved coverages of the array. This pattern is demonstrated in Fig. 3.2. Each tile was observed in two orthogonal scanning directions to reduce striping in the results. The tiles uniformly cover the whole region. A total of $\sim$3 million spectra in both CO lines were received that way,

taking a total observation time of nearly 80 hours.

Calibration scans, pointing, and focus were done on a regular basis to assure a correct calibration later. Calibration scans were done every 10 minutes and a pointing every 60 to 90 minutes. A focus scan was done every few hours, with more scans performed around sunset and sunrise, as the atmosphere was less stable then. For the pointing, we used G34.3, a strong nearby UCHII region. The calibration was conducted with the Multichannel Imaging and Calibration Software for Receiver Arrays (MIRA) package, which is part of the Grenoble Image and Line Data Analysis Software (GILDAS)[3] bundle. We expect the flux calibration to be accurate within error limits of $\sim 10\%$.

3.2.4 Data reduction

The raw data were processed using the Continuum and Line Analysis Single-dish Software (CLASS) package, part of the GILDAS software, while the analysis of the processed maps was conducted with the Grenoble Graphic (GreG) package. The steps taken for data reduction included flagging of bad data (e.g., noise levels that are too high or platforms that could not be removed), platform removal in the spectra, baseline subtraction, and gridding to create three dimensional data cubes. About 10 percent of the data had to be flagged, due to excessive platforming or strong noise.

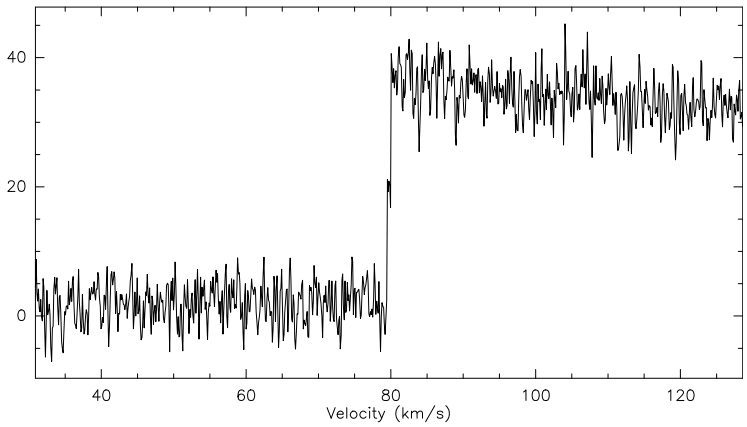

Fig. 3.3: Example plot of a $C^{18}O$ spectrum with platforming in units of [K].

Figure 3.3 shows a typical example of a spectrum which shows platforming, which is an intensity jump in the spectrum. This feature is sometimes produced by the VESPA backend. Fortunately, only certain pixels of the array show this error and it does not occur at all times. We calculated the intensity offsets by taking several baselines on each side of the jump to remove these effects in the spectra. Where this was not possible, we had to flag the affected spectra.

[3]This software is developed and maintained by IRAM: http://www.iram.fr/IRAMFR/GILDAS.

Baseline subtraction (which is the removal of a non-physical offset in the spectra, caused by instrumentational effects) turned out to be complicated in some regions that are crowded with line emission over a large part of the band. A first order baseline fit was usually adequate, but a second order baseline was needed for a small number of pixels and scans. We then corrected for the main beam efficiency via $T_{\rm mb} = (F_{\rm eff}/B_{\rm eff})\,T_{\rm A}^{*}$, where $F_{\rm eff} = 0.94$ is the forward efficiency of the IRAM 30m telescope and $B_{\rm eff} = 0.63$ is the main beam efficiency at 210 GHz (no efficiency measurements have been carried out for the IRAM 30m at 220 GHz so far, but the values should not deviate much from those at 210 GHz).

Finally, the spectra were gridded to two data cubes, one for each line. The pixels are separated by half beam steps, 5.9″ in spatial dimension, and have channel widths of 0.15 km s^{-1}. This step includes the convolution with a Gaussian of beam width. The final cubes have dimensions of 631×937×917 data points[4] (RA–DEC–velocity).

The noise of single spectra varied with the weather and also with the pixel of the HERA-array. Despite our dedicated reduction process, scanning effects are still visible in the resulting maps. They appear as stripes (see upper part of ^{13}CO map in Fig. 3.5) and tiling patterns (see noise difference of diffuse parts of C^{18}O in Fig. 3.6).

3.3 Noise maps

We created noise maps from both the ^{13}CO (2–1) and the C^{18}O (2–1) data cubes. For each spectrum, we determined the rms and created maps from these values. For this purpose, we need to calculate the rms from parts of the spectra that are emission free. We use the velocity range between 120 and 130 km s^{-1}, because it is free of emission for the complete region that we mapped. We assume that the noise level across the complete velocity range is constant. Typical values are found to be around 1 K or even less, while some parts in the south show values of up to 3 K. All values given here are in $T_{\rm mb}$, which are corrected for main beam efficiency. The results can be seen in Fig. 3.4.

We find that the structure of the noise is similar for both lines. The largest differences arise from weather conditions and time of day. This is seen in the squarish pattern, as each square shows single observations that have been carried out in a small time window. Still, there is a striped pattern visible that overlays the whole map. This stems from the nine different pixels that make up the HERA receiver. These pixels have different receiver temperatures, hence the different noise levels. We also note that observations in the northern part of the map are

[4]The readily reduced data cubes can be obtained from: http://www.iram-institute.org/EN/content-page-292-7-158-240-292-0.html

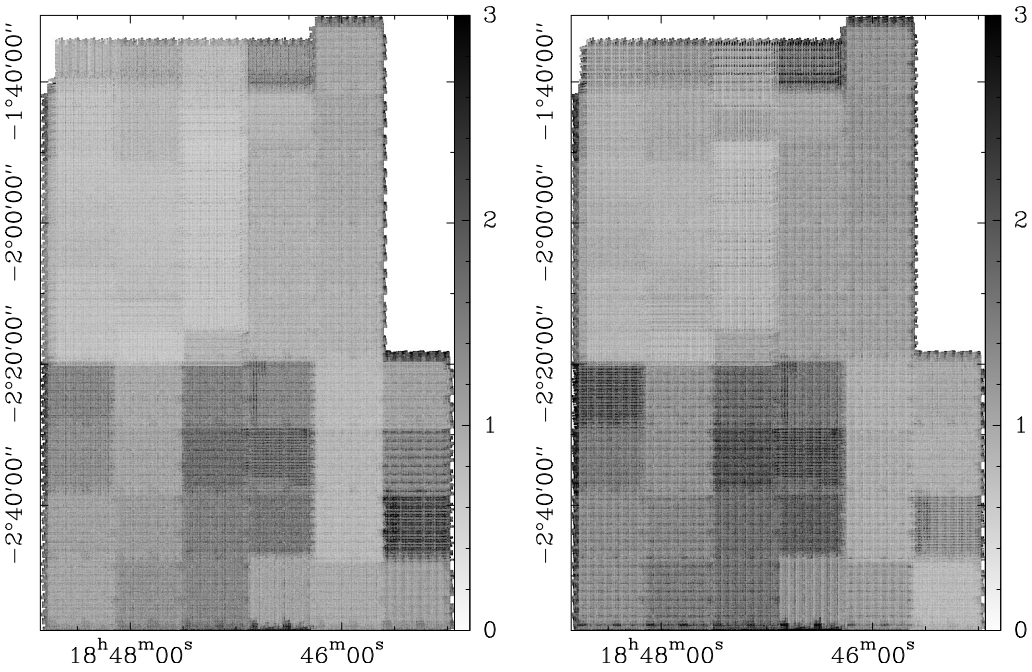

Fig. 3.4: Noise level maps in T_{mb} with scale in [K]. **Left:** *^{13}CO (2–1) map.* **Right:** *C^{18}O (2–1) map.*

usually less noisy than those in the south. This probably results from the different weather in which the observations have been carried out. Last, we find that the C^{18}O (mean rms of 1.3 K, maximum of 6.7 K) data shows a little increase in noise temperature in general compared to the ^{13}CO line (mean rms of 1.1 K, maximum of 3.7 K). The latter has been observed with the HERA1 polarization of the HERA receiver, whereas the first has been observed with HERA2, which has an overall higher receiver temperature.

3.4 Results

Integrated intensity maps of the whole W43 region in both ^{13}CO (2–1) and C^{18}O (2–1) lines are shown in Fig. 3.5 and Fig. 3.6. The maps use the entire velocity range from 30 km s^{-1} to 130 km s^{-1} and show a variety of clouds and filaments. The two main cloud complexes, W43-Main in the upper left part of the maps and W43-South in the lower right part, are clearly visible.

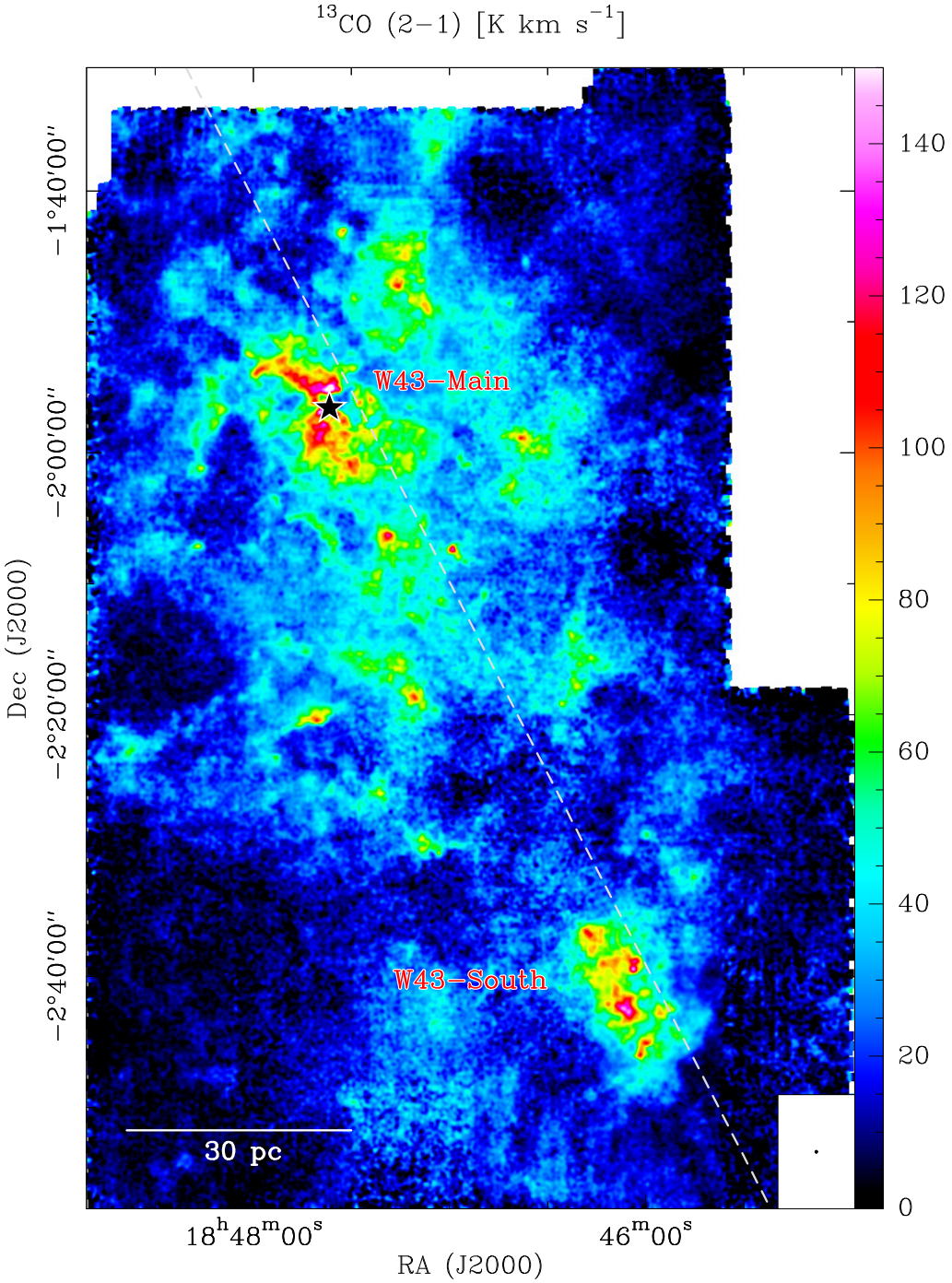

Fig. 3.5: Integrated intensity map of ^{13}CO (2–1), created from the resulting data cube of the complete W43 field in units of [K km s^{-1}]. The complete spectral range of 30 - 130 km s^{-1} has been used to create this map. The dashed line denotes the Galactic plane, while the star in W43-Main marks the OB star cluster. The beam size is indicated in the lower right corner.

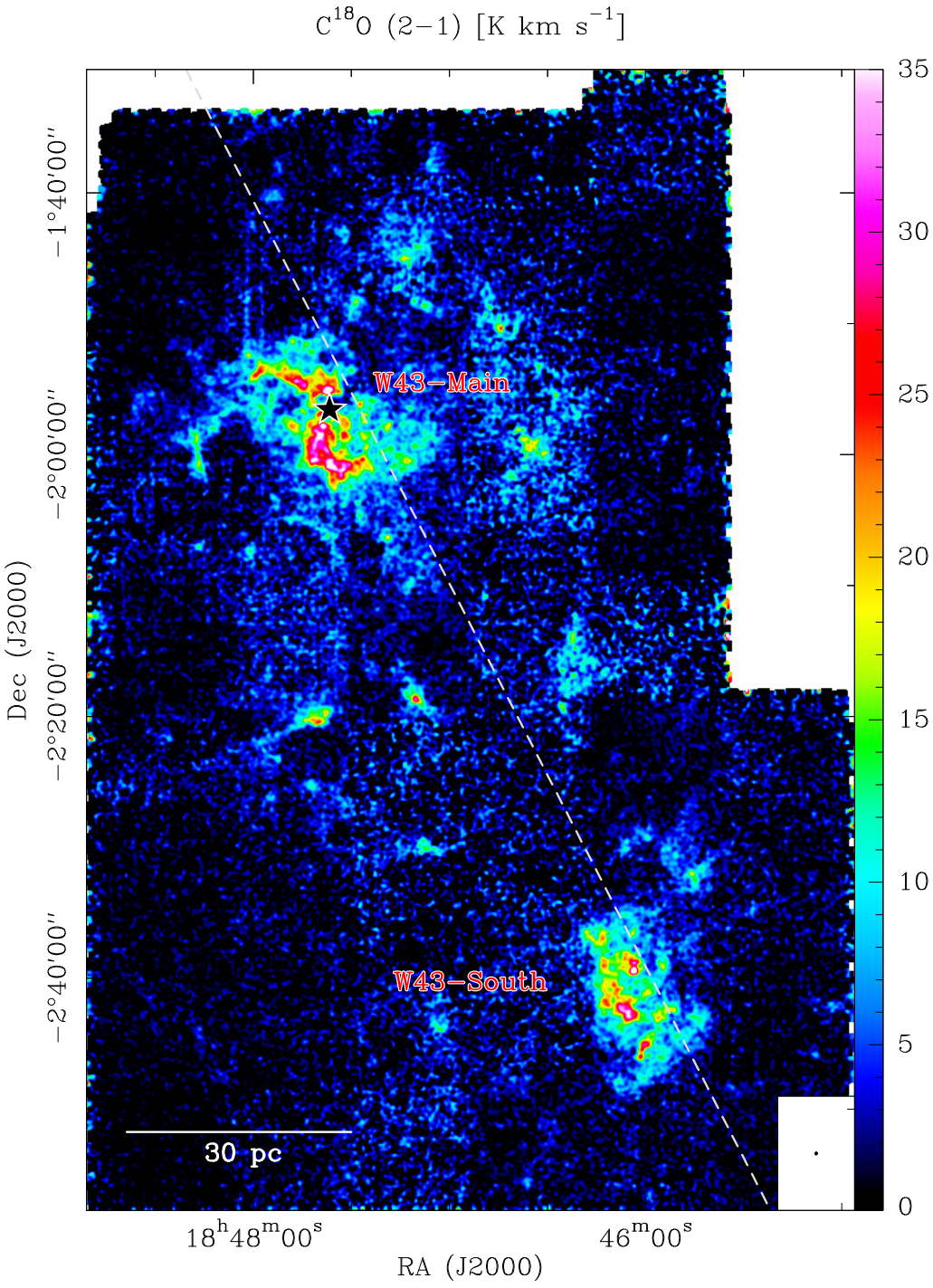

Fig. 3.6: Integrated intensity map of $C^{18}O$ (2–1), created from the resulting data cube of the complete W43 field in units of [K km s^{-1}]. The complete spectral range of 30 - 130 km s^{-1} has been used to create this map. The dashed line denotes the Galactic plane, while the star in W43-Main marks the OB star cluster. The beam size is indicated in the lower right corner.

Chapter 4

Velocity structure of the W43 complex and its position in the Milky Way

In the first step of our analysis we investigate the velocity structure of the CO emission in W43. After displaying some example spectra, we carry out an automated decomposition of the data-cubes into single sources. Then, we determine the distance of of each velocity component and try to pin down the position of W43 in the Galaxy.

4.1 Average spectra

In Fig. 4.1, we show several spectra, taken from the data. The upper plot shows the spectra of ^{13}CO (2–1) and C^{18}O (2–1), averaged over the complete complex; the center and bottom plots show averaged spectra of the W43-Main and W43-South clouds. The spectra of the complete cubes show emission across most parts of the velocity range in ^{13}CO. Only the velocities at $55 - 65$ km s^{-1} and those higher than 120 km s^{-1} do not show any emission. The C^{18}O follows that distribution, although it is not as broad. Thus, we can already distinguish two separated velocity components. One between 35 and 55 km s^{-1}, but most of the emission is concentrated in the velocity range between 65 and 120 km s^{-1}. To give an impression of the complexity of some sources, we plot several spectra of the W43-Main cloud in Fig. 4.2.

4.2 Decomposition into sub-cubes

The multitude of sources found in the W43 region complicates the analysis of the complete data cube. Details get lost when integrating over a range in frequency

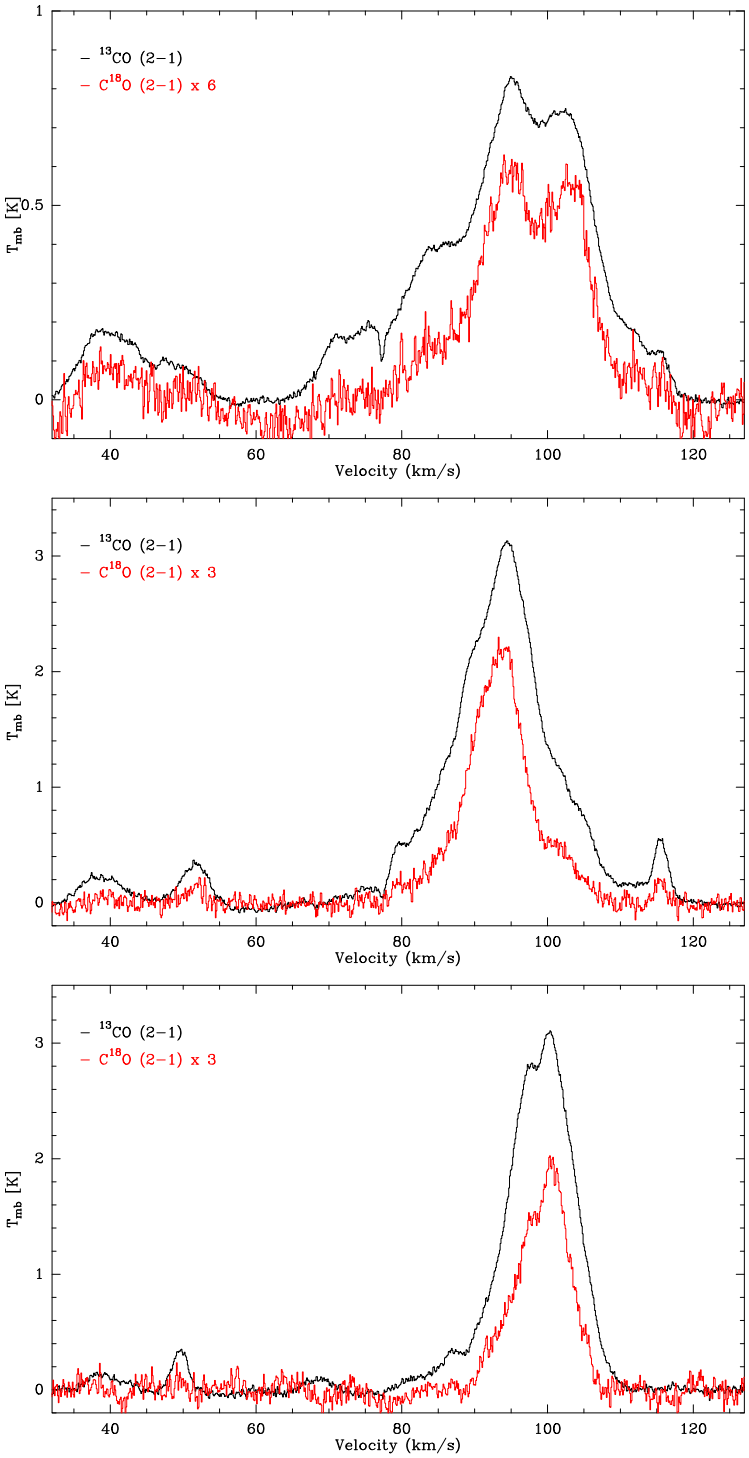

Fig. 4.1: **Top:** *Spectra of ^{13}CO (2–1) and C^{18}O (2–1), averaged over the complete data cubes. The C^{18}O line has been scaled to highlight the features in the line.* **Center:** *Averaged spectra of W43-Main.* **Bottom:** *Averaged spectra of W43-South.*

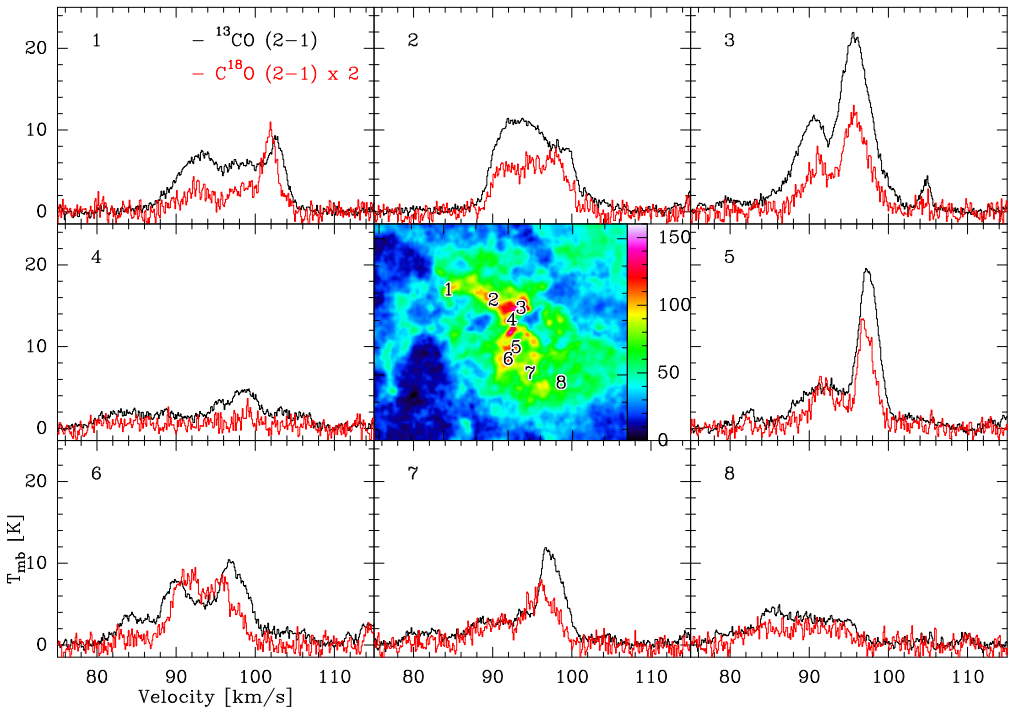

Fig. 4.2: ^{13}CO (2–1) and C^{18}O (2–1) spectra of several points in W43-Main. The central map is a ^{13}CO intensity map integrated over the velocity range of 78 to 110 km s^{-1} in units of [K km s^{-1}].

that is too large. We want to examine each source separately, so we need to decompose the data cube into sub-cubes that only contain one single source, each. This is only done on the ^{13}CO cube, as this is the stronger molecular line. This breakdown is then copied to the C^{18}O cube.

4.2.1 GAUSSCLUMPS decomposition

A first attempt to decompose our large datasets into single clumps is to use the GAUSSCLUMPS algorithm (Stutzki and Guesten 1990). This software is part of the GILDAS package and finds sources of Gaussian shape in three-dimensional datasets. It fits a Gaussian to the emission peak in the dataset and subtracts the fit. This step is iteratively repeated until a certain lower limit of total residual intensity is reached. The fit parameters of all found clumps is given as result, as well as the artificial data-cube, composed of the fitted clumps, and the residual cube, the difference between data and fit.

However, we understand that most clouds in our data are not purely Gaussian shaped, but show a variety of complex shapes that cannot be easily found by GAUSSCLUMPS. It is possible to regain the shape of the emission by fitting a large number of clumps to each cloud. Figure 4.3 shows an example fit of a set of Gaussian clumps of one single cloud (source 23 in our later notation). We

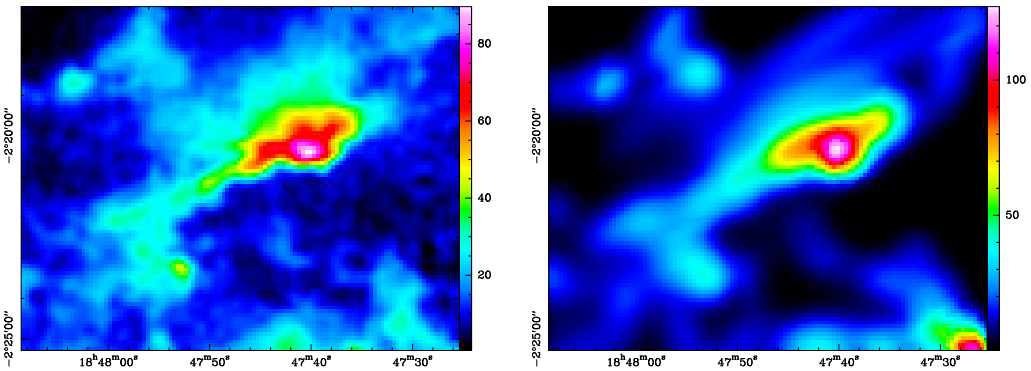

Fig. 4.3: Example of a GAUSSCLUMPS fit of a single cloud (source 23). The left plot shows the ^{13}CO data, taken by the IRAM 30m, while the right plot shows the GAUSSCLUMPS fit. Both maps in [K km s^{-1}].

find that data and fit match quite well, but what we are looking for is a decomposition of the full W43 region, dividing it into single clouds. These clouds should not be further broken down. We therefore neglect this approach and go over to a different method that finds clouds, but preserves their shape.

4.2.2 Duchamp Sourcefinder decomposition

We instead use the Duchamp Sourcefinder software package to automatically find a decomposition which keeps the shape of the found sources. See Whiting (2012) for a detailed description of this algorithm. This software finds connected structures in three-dimensional position-position-velocity data-cubes, by searching for emission that lies above a certain threshold. The value of this threshold is crucial for the success of the process and needs to be carefully adjusted by hand. For the decomposition of the ^{13}CO cube, we use two different cutoffs. The lower cutoff of $5\,\sigma$ per channel is used to identify weaker sources. A higher cutoff of $10\,\sigma$ per channel is needed to distinguish sources in the central part of the complex.

We identify a total of 29 clouds (see Table 4.1), 20 in the W43 complex itself and 9 in the fore-/background (see Sect. 4.4 for details). Source 13 corresponds to W43-Main and source 20 to W43-South. Both show sub-structure, but are considered as single sources in this treatment. The outcome of this method is not trivial, as it is not always clear which parts are still to be considered associated and which ones are separate structures. It still needs some correction by hand in some of the very weak sources and in the strong complexes. A few weak sources that have been identified by eye are manually added to our list (e.g. sources 18 and 28). These are clearly coherent separate structures, but are not identified by the algorithm. On the other hand, a few sources are merged by hand (e.g., source 26) that clearly belong together, but are divided into several sub-sources by the software. Some of these changes are open to interpretation,

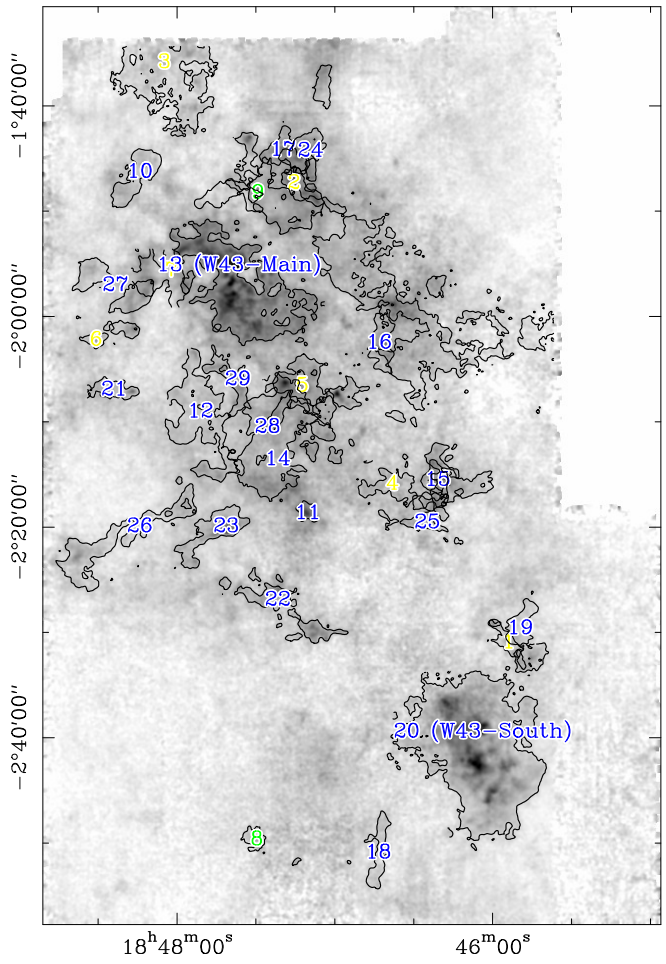

Fig. 4.4: Detection map of the Duchamp Sourcefinder. Detected clouds are overlaid on a gray-scale map of ^{13}CO (2–1). Sources are ordered by their peak velocities. The color-coding relates to the distance of identified clouds: blue for 6 kpc, green for 4.5 kpc, and yellow for the 4 and 12 kpc component.

but they show that some adjustment of the software result is needed. However, the algorithm works well and identifies 25 out of 29 clouds on its own.

The resulting detection map is shown in Fig. 4.4. The numbers shown there are color-coded to show the velocity-component (distance) of each detected cloud (see Sect. 4.4 for details). Sources are sorted by their peak velocities. See Table 4.1 for positions and dimensions of the clouds, Tables 5.1 and 5.2 for derived properties, and Sect. 5.7 for a detailed description of the main complexes, while plots of all clouds can be found in Appendix B. We see a number of different sizes and shapes that range from small spherical clouds to expanded filaments and more complex structures.

	Number	(1) RA peak	(2) DEC peak	(3) Peak ^{13}CO velocity	(4) Velocity extent	(5) ^{13}CO peak	(6) C^{18}O peak	(7) Mean ^{13}CO line width (FWHM)	(8) Assumed distance	(9) Dimensions RA × DEC	(10) Area of ^{13}CO
				[km s^{-1}]	[km s^{-1}]	[K]	[K]	[km s^{-1}]	[kpc]	[pc]	[pc^2] $\times 10^2$
Fore-ground	1	18:45:59.5	-02:29:08.3	35.8	33 – 40	9.0	4.5	1.5	12	12.9 × 13.3	1.6
	2	18:47:15.5	-01:47:17.3	39.9	33 – 45	12.7	4.0	1.6	4	9.7 × 8.3	0.7
	3	18:47:54.5	-01:35:02.5	41.9	33 – 48	14.5	4.0	1.7	4	11.3 × 9.3	1.0
	4	18:46:16.3	-02:15:39.3	45.9	37 – 47	8.5	3.3	1.2	12	47.8 × 22.0	8.7
	5	18:46:59.1	-02:07:22.5	47.8	38 – 51	21.0	5.7	1.4	12	27.9 × 43.3	7.0
	6	18:48:30.7	-02:02:09.8	49.0	46 – 54	8.4	2.7	1.2	3.5	6.7 × 4.4	0.2
	7	18:48:02.0	-01:55:34.3	51.8	48 – 57	8.4	4.0	1.4	3.5	5.7 × 5.6	0.2
	8	18:47:29.8	-02:49:38.1	72.5	69 – 75	12.2	5.8	0.8	4.5	13.1 × 9.2	0.8
	9	18:47:29.5	-01:48:11.9	75.7	69 – 78	10.9	5.4	0.9	4.5	44.9 × 35.4	9.5
W43	10	18:48:10.6	-01:45:37.7	80.9	74 – 85	15.7	4.9	1.6	6	10.3 × 9.9	1.0
	11	18:47:10.2	-02:18:37.7	86.9	84 – 92	18.5	10.0	1.4	6	7.3 × 8.4	0.8
	12	18:47:52.8	-02:03:33.5	91.8	88 – 98	15.5	4.5	2.0	6	11.5 × 22.2	2.3
	13[a]	18:47:36.4	-01:55:06.6	93.8	78 – 108	21.9	9.0	5.2	6	29.0 × 20.9	6.4
	14	18:47:22.6	-02:12:01.8	94.6	91 – 97	8.2	3.3	1.9	6	18.0 × 23.4	3.5
	15	18:46:22.6	-02:14:04.2	94.8	90 – 100	13.6	5.2	2.0	6	18.0 × 10.3	1.2
	16	18:46:43.3	-02:02:28.1	94.8	91 – 97	9.0	3.1	1.0	6	26.4 × 23.9	3.2
	17	18:47:27.1	-01:44:59.1	94.9	89 – 102	12.8	3.7	2.2	6	17.5 × 18.7	2.3
	18	18:46:43.9	-02:53:59.6	96.5	94 – 98	11.2	3.9	1.0	6	4.4 × 14.7	0.7
	19	18:45:50.9	-02:30:31:9	96.7	93 – 102	10.7	4.5	1.1	6	9.9 × 15.4	1.3
	20[b]	18:46:04.0	-02:39:22.2	97.6	89 – 107	27.5	12.8	4.8	6	23.7 × 31.1	6.0
	21	18:48:16.6	-02:07:06.0	103.2	97 – 107	11.8	4.5	1.5	6	8.2 × 3.7	0.4
	22	18:47:08.0	-02:29:32.3	103.9	98 – 108	19.5	9.7	2.2	6	25.0 × 15.4	3.3
	23	18:47:40.1	-02:20:24.3	104.9	100 – 108	20.6	9.0	2.0	6	13.1 × 11.3	1.1
	24	18:47:09.5	-01:44:08.4	105.5	102 – 110	11.5	5.7	1.6	6	11.2 × 26.5	2.9
	25	18:46:26.1	-02:19:11.5	108.1	106 – 117	13.7	6.3	1.0	6	11.2 × 14.8	1.2
	26	18:48:38.1	-02:22:49.1	108.2	104 – 112	11.9	4.8	1.5	6	22.0 × 17.6	2.7
	27	18:48:32.2	-01:55:28.8	111.1	107 – 116	10.4	4.6	1.5	6	14.1 × 10.5	1.4
	28	18:47:22.2	-02:09:25.2	112.5	110 – 116	10.7	4.2	1.0	6	12.0 × 7.7	0.9
	29	18:47:48.6	-02:05:03.7	115.9	110 – 120	15.2	5.8	1.2	6	8.2 × 12.7	1.2

[a] W43-Main
[b] W43-South

Table 4.1: Clouds found by the Duchamp Sourcefinder and their characteristics derived from the CO datasets.

4.2.3 Naming conventions

The resulting data cubes show clouds of different shapes. We define a polygon (at a level of about 20% of the maximum integrated intensity) for each source that contains the ^{13}CO emission and measure its area. It is given in Table 4.1 (10). Thus, we account for shapes that deviate from spheres or rectangles, which is true for most of our clouds. The typical spatial scales lie in the range of 10 to 20 pc (see Table 4.1 (9)). The given values only denote the extent of the clouds in RA and Dec dimension and does not consider their specific shape. We did not specifically deconvolve these values with the beam, as on these scales this would change the values by less than 0.05% and is therefore negligible. Hereafter, structures with a size on the order of 10 pc clouds will be called clouds, while we define clumps as objects on the parsec scale. The whole W43 region is considered a cloud complex.

We will call clouds that have an elongated shape filaments. These filaments are often discussed in the literature in models and observations (see Sect. 2.1.4). Still, there is no overall accepted definition of what exactly a filament is and what its dimensions are. Our filaments have typical lengths on the order of 10 pc and widths of several pc. Filaments identified with *Herschel* observations typically have widths of 0.1 pc (Arzoumanian et al. 2011) and it is

found that structures of our filament size often further break down into smaller structures and should rather be considered a bundle of filaments (Hacar et al. 2013). An analysis on that scale is not possible with the angular resolution of our data, so we will neglect everything below the pc scale. Bear this in mind when we will use the word “filament” in the next chapters.

4.3 PV-Diagram of the region

For a more advanced analysis of the velocity structure, we create a position velocity (pv)-diagram of ^{13}CO (2–1) and C^{18}O (2–1) that are averaged along the Galactic latitude (see Fig. 4.5). This type of two-dimensional diagram plots spatial information on one axis and spectral information on the second axis. The distribution of emission across the velocity range that is seen in the averaged spectra in Fig. 4.1 can also be identified here, but with additional spatial information along the Galactic longitude. We note the similarity of this figure to the plot of ^{13}CO (1–0) displayed in Nguyen Luong et al. (2011). However, we see more details in our plot due to the higher angular resolution of our data.

We further analyze the ^{13}CO position velocity diagram, as shown in Fig. 4.5 (a), to separate our cube into several velocity components. We assume that these different components are also spatially separated.

Two main velocity complexes can be distinguished: one between 35 and 55 km s^{-1}, the other between 65 and 120 km s^{-1}. Both complexes are clearly separated from each other, indicating that they are situated at different positions in the Galaxy. On second sight, it becomes clear that the complex from 65 to 120 km s^{-1} breaks down into a narrow component, spanning the range from 65 to 78 km s^{-1} and a broad component between 78 and 120 km s^{-1}. An analysis of the channel maps of the cube verifies that these structures are indeed separated. The lower component is hardly visible in C^{18}O. See Fig. 4.6 for integrated maps of each velocity component.

On the other hand, it is clearly visible that all three velocity components span the complete spatial dimension along the Galactic longitude. The broadest complex at 78-120 km s^{-1} shows two major components at 29.9° and 30.8° that coincide with W43-South and W43-Main, respectively. The gap between both complexes is bridged by a smaller clump and all three clumps are surrounded by diffuse gas, which forms an envelope around the whole complex. It is thus suggested to consider W43-Main and W43-South as one giant connected molecular cloud complex. This connection becomes more clear in the pv-plot than in the spatial map in Fig. 3.5 (see also Nguyen Luong et al. 2011), although the averaging of values causes blurring, which might merge structures. The ^{13}CO plot of course shows more emission than that of C^{18}O. Especially the more diffuse gas forming the envelope around the two central complexes is only traced in ^{13}CO, because our observations are not sensitive enough to detect ^{13}CO here.

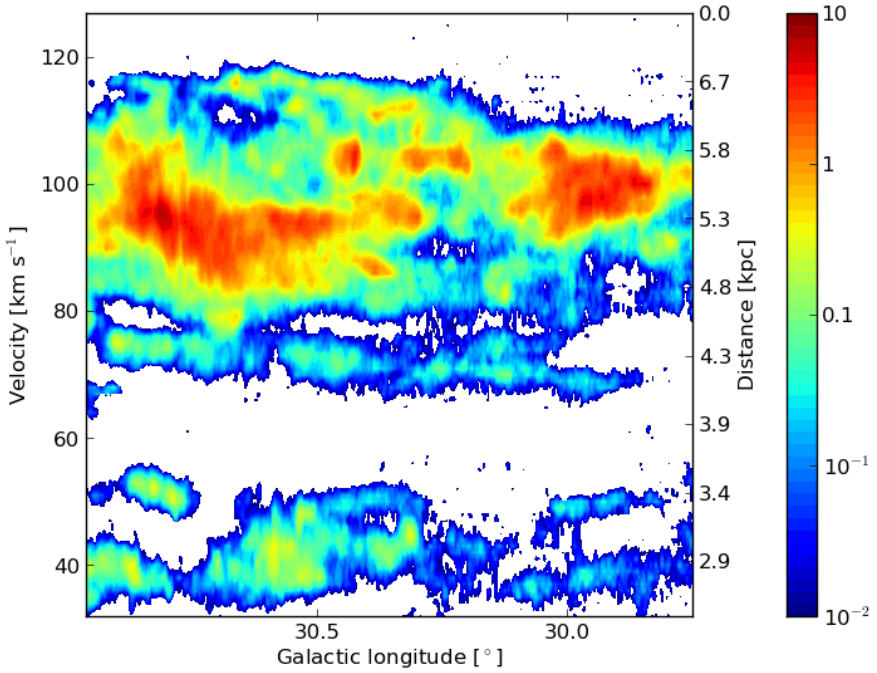

(a) PV-diagram of ^{13}CO (2–1).

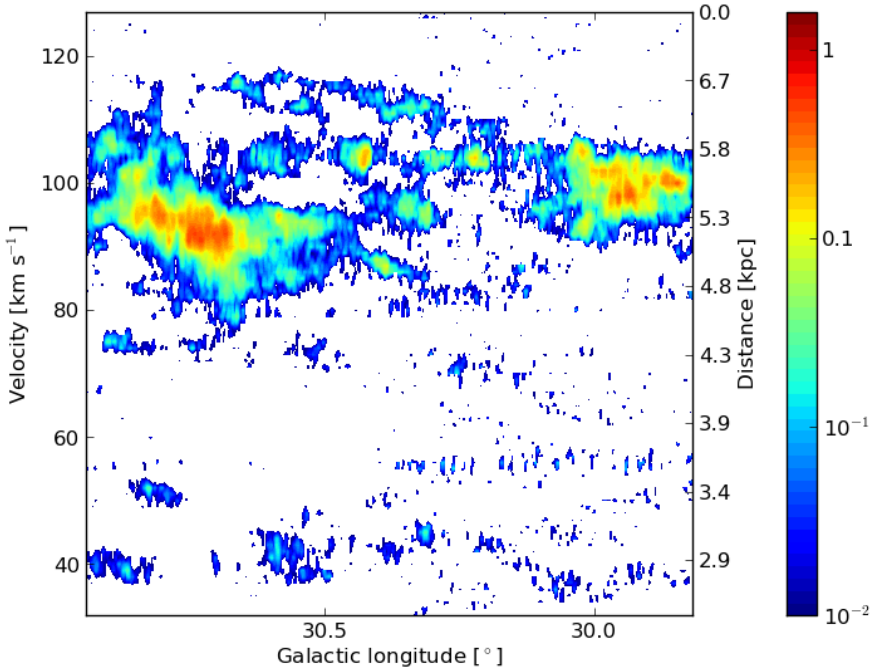

(b) PV-diagram of C^{18}O (2–1).

Fig. 4.5: PV-diagram of both CO lines in [K], averaged along the Galactic latitude, showing several velocity components. The y-axes show the velocity and distance, according to the rotational model seen in Fig. 4.7.

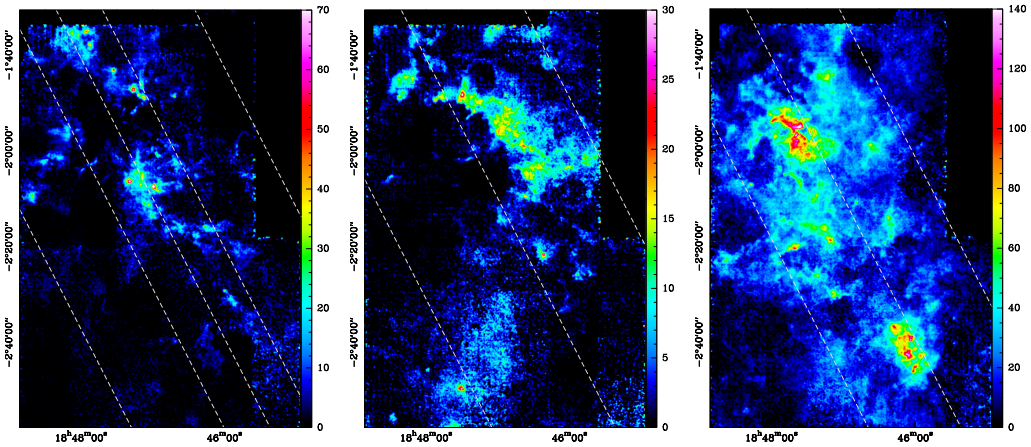

(a) 35 to 55 km s^{-1} component at a distance of 4 and 12 kpc.

(c) 65 to 78 km s^{-1} component at a distance of 4.5 kpc.

(d) 78 to 120 km s^{-1} component at a distance of 5 to 7 kpc.

Fig. 4.6: Integrated ^{13}CO (2–1) maps of the separated velocity complexes in [K km s^{-1}]. The white stripes mark the Galactic plane and the planes 30 pc above and below it. Figure (a) shows sources at two different distances and therefore two different scales, the inner scale for the far distance, the outer one for the near distance.

The lower velocity complex between 35 and 55 km s^{-1} is a bit more fragmented than the other components. One central object at 30.6° spans the whole velocity range, but it splits into two sub-components to the edges of the map. Again, in C^{18}O we only see the most intense clumps. It is hard to tell if we actually see one or two components.

4.4 Determination of the distance of W43

We can analyze our data by using a simple rotational model of the Milky Way. For this model, we assume a rotational curve that increases linearly in the inner 3 kpc of the Galaxy, where the bar is situated. For radii larger than that, we assume a rotation curve that has a value of 254 km s^{-1} at $R_\odot$ and slightly rises with a radius at a rate of 2.3 km s^{-1} kpc^{-1} (see Reid et al. 2009). The Galactocentric radius of a cloud with a certain relative velocity can be calculated using the formula

$$r = R_\odot \sin(l) \frac{V(r)}{V_{\mathrm{LSR}} + V_\odot \sin(l)}, \tag{4.1}$$

as used in Roman-Duval et al. (2009). The parameter $R_\odot$ is the Galactocentric radius of the Sun, which is assumed to be 8.4 kpc (see Reid et al. 2009), l is the Galactic longitude of the source (30°), $V_\odot$ the radial velocity of the Sun

(254 km s^{-1}), and $V(r)$ the radial velocity of the source (241 km s^{-1}). The parameter V_{LSR} is the measured relative velocity between the source and the Sun. With the knowledge of the radius r, we can then compute the relative distance to the source by the equation:

$$d = R_{\odot}\cos(l) \pm \sqrt{r^2 - R_{\odot}^2 \sin^2(l)}. \tag{4.2}$$

Up to the tangent point, two different possible distances exist for each measured velocity: one on the near side and one on the far side of the tangent point. However, this calculation is not entirely accurate, as the assumptions of the geometry of the Galaxy bear large errors. Reid et al. (2009) state that the errors of the kinematic distance can sum up to a factor as high as 2. One main reason for uncertainties are the streaming motions of molecular clouds relative to the motion of the spiral arms (Reid et al. 2009). Figure 4.7 shows the kinematic distance curve for our case at 30° Galactic longitude. This works only for the circular orbits in the spiral arms and not the elliptical orbits in the Galactic bar (see Rodríguez-Fernández and Combes 2008; Rodríguez-Fernández 2011).

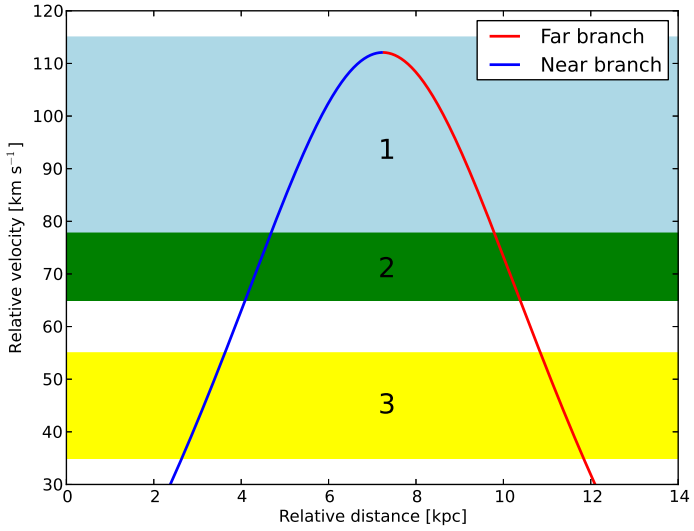

Fig. 4.7: Simple rotational model of the Milky Way, relating the relative velocity and the distance to the Sun for 30° Galactic longitude. The stripes denote the different velocity components found in Fig. 4.5.

To determine the location of each velocity complex, we need to break the kinematic distance ambiguity; that is, we need to decide for each complex if we assume it to be on the near or the far side of the tangent point. Here, we use the distance estimations by Roman-Duval et al. (2009), who utilized H I self absorption from the VLA Galactic Plane Survey (VGPS) project (Stil et al. 2006). It is possible to associate several entries of their extensive catalog with clouds we found in our dataset. Thus, we are able to remove the distance ambiguity and

attribute distances to these clouds. In combination with the detailed model of the Milky Way of Vallée (2008), we are able to fix their position in our Galaxy. We cannot assign a distance to each single cloud in our dataset, as not every single one was analyzed by Roman-Duval et al. We assume the missing sources to have the same distances as sources nearby. This may not be exact in all cases, but the only unclear assignments are two clouds in the 35 to 55 km s^{-1} velocity component (sources 1 and 3). The distance of the W43 complex is unambiguous, as it is well-determined by the calculations found in Roman-Duval et al. (2009).

The complete W43 complex (78 to 120 km s^{-1}) is found to lie on the near side of the tangential point, with distances from 5 to 7.3 kpc, which increase with radial velocity. This places it near the tangential point of the Scutum arm at a Galactocentric radius of $R_{\mathrm{GC}} = 4$ kpc (marker 1 in Fig. 4.8 (a)). For our analysis we use an average distance of 6 kpc for the whole complex, since this is where the mass center is located.

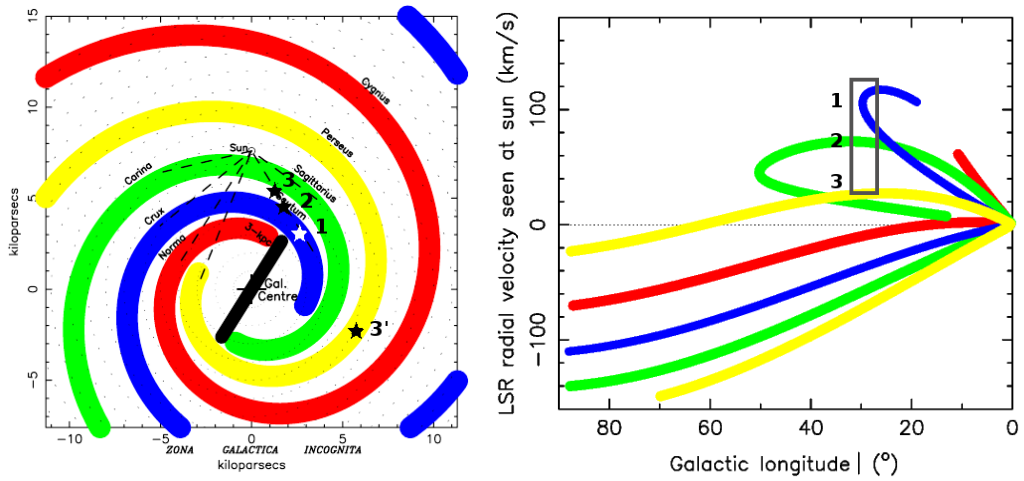

(a) Model of the spiral arm structure of the Milky Way from Vallée (2008). The position of the W43 complex is marked at (1), the fore-/background complexes at (2), (3), and (3′).

(b) PV-diagram of the model from Vallée (2008), showing relative velocities of spiral arms in the first quadrant. The interesting part is around 30° Galactic longitude (gray box), where W43 is located.

Fig. 4.8: Spiral arm structure of the Milky Way, taken from Vallée (2008).

The second velocity component (65 to 78 km s^{-1}) lies in the foreground of the first one, at a distance of 4.5 kpc to the Sun and $R_{\mathrm{GC}} = 4.8$ kpc (marker 2 in Fig. 4.8 (a)). Another indication that these sources are located on the near side of the tangential point is their position above the Galactic plane, as seen in Fig. 4.6 (b). The larger the distance from the Sun, the further above the Galactic plane it would be positioned. This would be difficult to explain, since high-mass star-forming regions are typically located within the plane. It is unclear if this cloud is still situated in the Scutum arm or if it is located between spiral arms. According to the model, it would be placed at the edge of the Scutum arm. In light of the previously discussed uncertainties, it is still possible that this cloud is

part of the spiral arm.

The third component between 35 and 55 km s^{-1} is more complex than the others, since we find sources to be located on both the near and far side of the tangential point. The brightest sources in the center of our map are in the background of W43 in the Perseus arm with a distance of 11 to 12 kpc to the Sun and of $R_{\mathrm{GC}} = 6$ kpc (marker 3 in Fig. 4.8 (a)). However, several other sources in the north and south are found by Roman-Duval et al. to be on the near side, at a distance to the Sun of 3.5 to 4 kpc (marker 3′ in Fig. 4.8 (a)). These sources also have a Galactocentric radius of 6 kpc. Table 4.1 gives an overview of the distance of each source, while Fig. 4.6 shows integrated intensity plots of the individual velocity components.

We can now apply this calculation to our data in Fig. 4.5 (a) by changing the velocity scale into a distance scale. The distance scale is inaccurate for those parts of the lowest component that lie on the far side of the tangent point. Although it is not possible to disentangle near and far clouds in this plot, we still show this scale. These values, taken from the rotation curve, are smaller than the actual distances found when compared to Roman-Duval et al. (2009), since we used the newer rotation curve of Reid et al. (2009). Roman-Duval et al. use the older values from Clemens (1985), which explains the discrepancy. However, this axes still give an idea of the distribution of the clouds. We note that no distance can be assigned for velocities larger than 112 km s^{-1}, hence the zero for the 120 km s^{-1} tick in Fig. 4.5 (a). Subplot (d) shows the related modeled pv-diagram from Vallée (2008). Our dataset is indicated by the gray box.

Figure 4.8 (a) summarizes our determination of the distance in a plot taken from Vallée (2008). The W43 complex (78-120 km s^{-1}, marker 1) lies between 5 and 7 kpc, where the distance increases with velocity, which we found to be located on the near branch. The complex 65 to 78 km s^{-1} (marker 2) is located at the near edge of the Scutum arm, while the 35 to 55 km s^{-1} component is marked by 3 and 3′ on both sides of the tangent point. The far part is located in the Perseus arm at 12 kpc distance and the near part at a distance of 4.5 kpc between the Scutum and the Sagittarius arm.

It may be a bit surprising that no emission from the local part of the Sagittarius arm is seen in our dataset. The reason is that our observed velocity range only goes to 30 km s^{-1}. Possible nearby molecular clouds would have even lower relative velocities of $\sim$20 km s^{-1}, which can be seen in the model in Fig. 4.8 (b). In Nguyen Luong et al. (2011), the ^{13}CO (1–0) spectrum, which is averaged over the W43 complex, shows an additional velocity component at 5 to 15 km s^{-1}, which fits to this spiral arm.

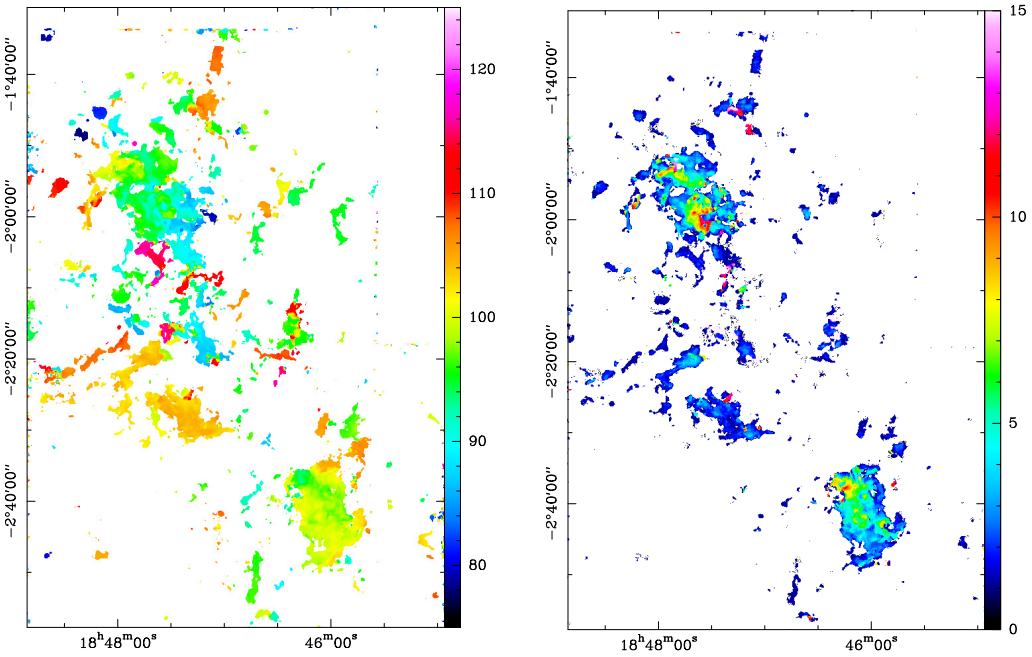

(a) Mean velocity map. **(b)** Line dispersion map.

Fig. 4.9: Moment maps of the W43 complex in [km s^{-1}], derived from the ^{13}CO (2–1) cube. A cutoff of 4 K per channel was used.

4.5 Mean velocity and line width

After separating the different velocity components, we created moment maps of each component. For each spectra of the ^{13}CO data cube, the first and second moment were calculated with the GILDAS `moments` task. The first moment resembles the mean velocity, the intensity-weighted velocity. The second moment is a measure of the velocity dispersion or line width. The maps of the W43 complex are shown in Fig. 4.9, while the plots of the background components can be seen in Fig. 4.10. Care should be taken in interpretation of these maps. As some parts of the maps show complex spectra (see Fig. 4.2 for some examples), the notion of a Gaussian profile is not always a good approximation. In regions where several velocity components are found or in case of self-absorbed lines, the maps may be misleading. This especially concerns the southern ridge of W43-Main, called W43-MM2, as defined in (Nguyen-Luong et al. 2013).

The mean velocity map in Fig. 4.9 (a) traces a variety of coherent structures. Most of these correspond to the sources we identified with the Duchamp software. However, some structures, as mentioned above, overlap and cannot be defined simply from using this velocity map.

The two main clouds, W43-Main and W43-South, are again located in the upper left and lower right part of map, respectively. As in the pv-diagram in Fig. 4.5 (a), we note that the two clouds are slightly shifted in velocity. While

W43-Main lies in the range of 85 to 100 km s^{-1}, W43-South spans velocities from 95 to 105 km s^{-1}. Several smaller sources bridge the gap between the two clouds, especially in the higher velocities. This structure is also seen in the pv-diagram.

In comparison to the pv-diagram, this plot shows the velocity distribution in both spatial dimensions. On the other hand, we lose information of the shape of the lines. Here, we see that the velocity of W43-South is rather homogeneous across the whole cloud. In contrast, W43-Main shows strong velocity gradients from west to east and from south to north, which are already seen in Motte et al. (2003). The velocity changes by at least 30 km s^{-1} on a scale of 25 pc (see Fig. 5.11 in Sect. 5.7.1 for a larger plot of the velocity map of W43-Main). We interpret this as mass, which flows across the cloud, which makes it kinematically much more active than W43-South.

Fig. 4.9 (b) shows a map of the line dispersion of each pixel. Some parts in W43-Main show unrealistically large values of more than 10 km s^{-1}. This is a line-of-sight effect and originates in several velocity components located at the same point on the sky. Therefore, it is more accurate to analyze the line width of each source separately. From these single sources, we determine the mean line width across the polygon defined before, which is given in Table 4.1 (7).

4.6 Moment maps of foreground components

Figure 4.10 shows plots of the mean velocity position and the line width of the two lower velocity components. The maps of the W43 complex itself are shown in Fig. 4.9 and are described in Sect. 4.5.

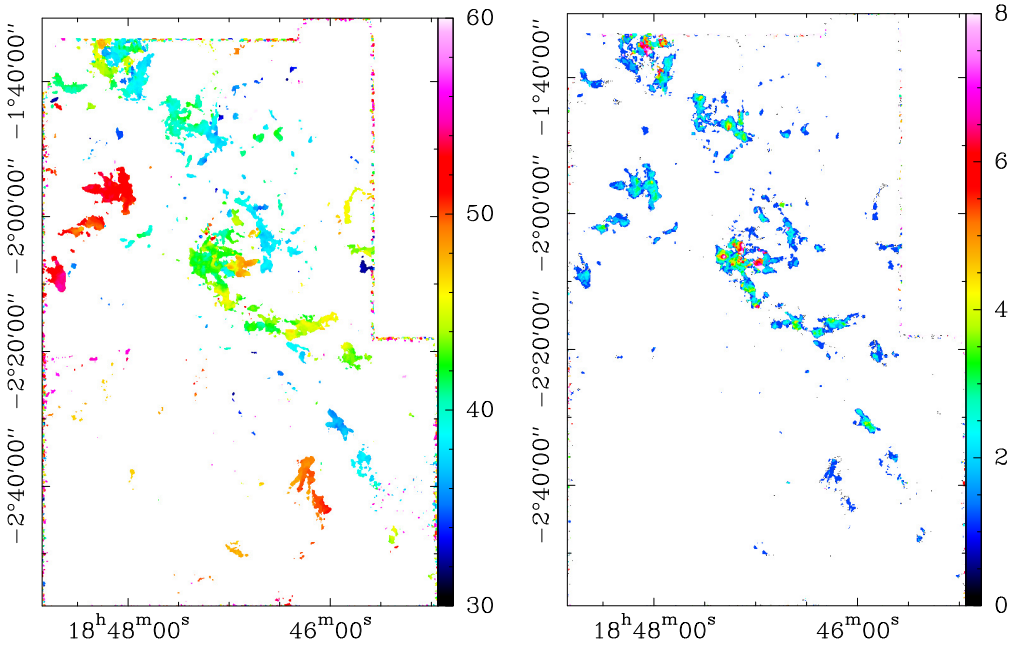

(a) 35 to 55 km s^{-1} component mean velocity.

(b) 35 to 55 km s^{-1} component line width.

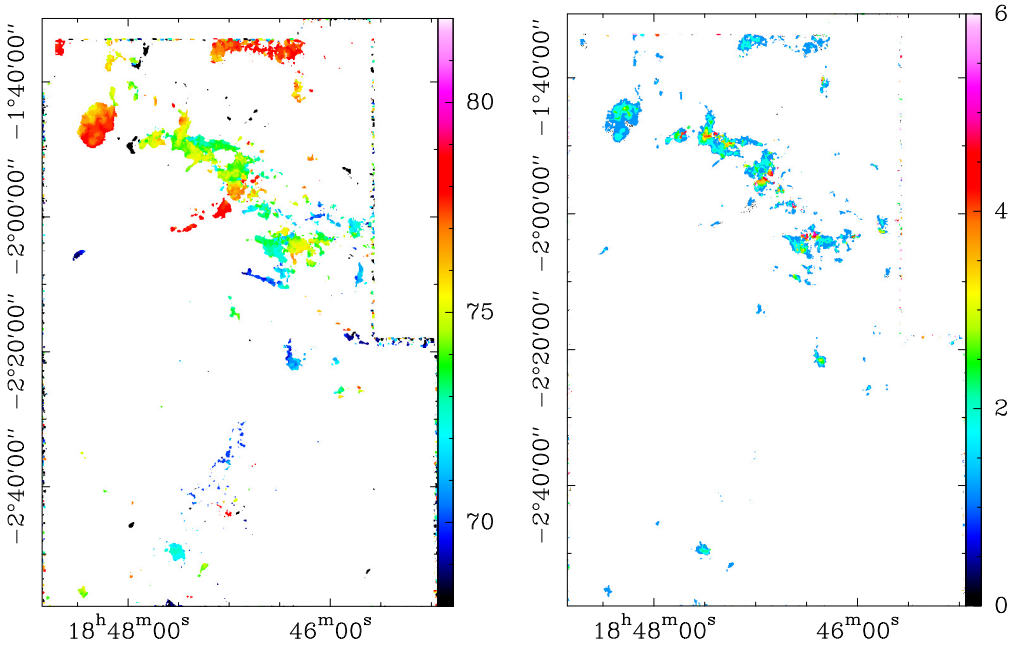

(c) 65 to 78 km s^{-1} component mean velocity.

(d) 65 to 78 km s^{-1} component line width.

Fig. 4.10: Maps of the first (line mean velocity) and second (line width) moment maps of the two fore-/background components in [km s^{-1}].

Chapter 5

Physical properties of molecular clouds in W43

We now continue our investigation of the W43 complex by determining the physical properties of each individual source identified in Sect. 4.2. After this, we compare our findings with the results of other projects. To finish this chapter, we give a description of the two major clouds in the complex, W43-Main and W43-South.

5.1 Derived properties

For each identified source, we conducted a series of calculations to determine its physical properties. We did this on a pixel by pixel basis, using maps integrated over the velocity range that is covered by the specific source. The optical depth of the ^{13}CO gas was calculated from the ratio of the intensities of ^{13}CO (2–1) and C^{18}O (2–1), assuming that C^{18}O is optically thin. (This assumption holds for H_2 column densities up to $\sim 10^{23}$ cm^{-2}, but a clear threshold cannot be given.) Then we computed the excitation temperature of this gas and the H_2 column density, which was then used to estimate the total mass along the line-of-sight. All these calculations are explained in detail below. Example maps for a small filament (source 29) can be seen in Fig. 5.1.

5.1.1 Optical depth

Assuming a constant abundance ratio of ^{12}CO:^{13}CO:C^{18}O, we can estimate the optical depth of the ^{13}CO gas (see e.g. Myers et al. 1983; Ladd et al. 1998). See Table 4.1 for a list of the mean opacities of our identified sources. We compare

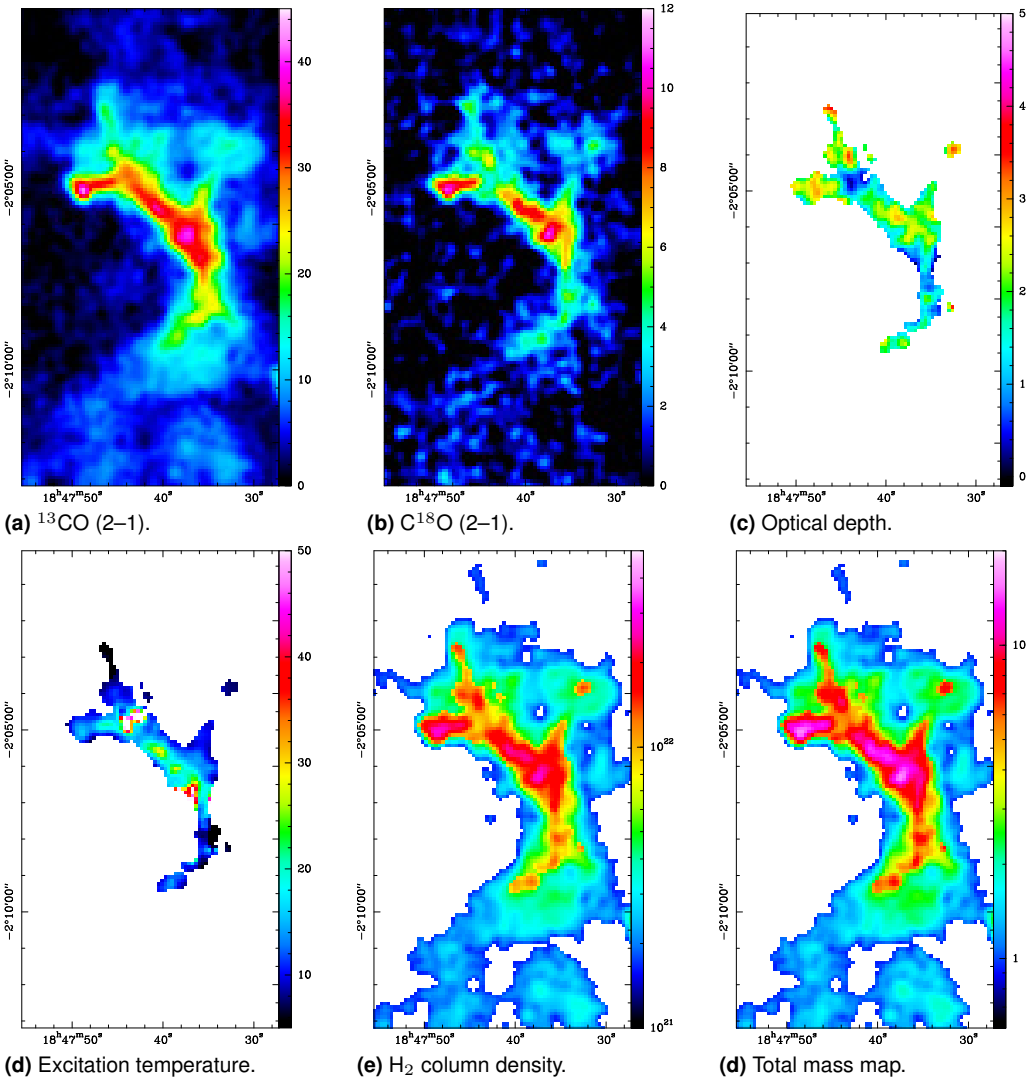

(a) ^{13}CO (2–1). **(b)** C^{18}O (2–1). **(c)** Optical depth.

(d) Excitation temperature. **(e)** H_2 column density. **(d)** Total mass map.

Fig. 5.1: Series of plots showing the different steps of calculations carried out for each source. The example shows source 29, which is located in the center of the W43 complex at a velocity of 115 km s^{-1}. From left to right: **(a)** *^{13}CO (2–1) in [K km s^{-1}],* **(b)** *C^{18}O (2–1) in [K km s^{-1}],* **(c)** *optical depth τ of ^{13}CO (2–1),* **(d)** *excitation temperature in [K],* **(e)** *H_2 column density map in [cm^{-2}] derived from the CO lines as described in Sect 5.1.3, and* **(f)** *mass per pixel map in [$M_\odot$ pixel^{-1}]. The column density has been calculated from an assumed constant excitation temperature.*

the intensities of the ^{13}CO and C^{18}O line emission integrated over the analyzed cloud and solve the equation,

$$\frac{I(^{13}\mathrm{CO})}{I(\mathrm{C}^{18}\mathrm{O})} \approx \frac{1-\exp(-\tau_{13})}{1-\exp(-\tau_{13}/R)}, \tag{5.1}$$

for τ_{13}, where R is the intrinsic ratio of the two mapped CO isotopologues.

The isotopic abundance of C and O in the Milky Way is known to depend on the Galactocentric radius. Often cited values are found in Wilson and Rood (1994). They find the ratio of ^{16}O and ^{18}O to be 272 at 4 kpc radius, 302 at 4.5 kpc, and 390 at 6 kpc, so we take those numbers for the ^{12}CO:C^{18}O ratio. Recent values for the C/^{13}C abundance are given in Milam et al. (2005). Here, we take values derived from CO observations and get a ^{12}CO:^{13}CO ratio of 31 at a Galactocentric radius of 4 kpc for the main component and a ratio of 43 and 52 for the foreground components at a radius of 4.5 and 6 kpc, respectively. In total, we use an intrinsic ratio of ^{12}CO:^{13}CO:C^{18}O of 1:1/31:1/272 for sources in the main complex and ratios of 1:1/43:1/302 and 1:1/52:1/390 respectively for foreground sources.

An example map of τ of ^{13}CO (2–1) is shown in Fig. 5.1 (c). Typical clouds have optical depths of a fraction of 1 in the outer parts and up to 4 at most in the central cores. The extreme case is the W43-main cloud, where the ^{13}CO optical depth goes up to 8. This means that most parts of the clouds are optically thin and we can see through them. Even at most positions where ^{13}CO becomes optically thick, C^{18}O still remains optically thin. Only for the extreme case of the densest part of W43-Main, C^{18}O starts to become optically thick. Naturally, our opacity calculation will deviate from the correct values at those positions. Still, this means that the combination of the two isotopologues reveals most of the information about the medium density CO gas in the W43 complex.

5.1.2 Excitation temperature

Once we know the optical depth, we can determine the excitation temperature of the CO gas.

For this, we use Ladd et al. (1998):

$$T_{\rm mb} = \frac{1}{\eta} \left(J(T_{\rm ex}) - J(T_{\rm BG}) \right) \left(1 - \exp(-\tau) \right). \tag{5.2}$$

With

$$J(T) = \frac{h\nu}{k_{\rm B} \, \exp\left(\frac{h\nu}{k_{\rm B} T} - 1 \right)}, \tag{5.3}$$

we use the line peak intensity $T_{\rm peak}$ for $T_{\rm mb}$. The parameter $T_{\rm BG}$ is the cosmic background radiation of 2.7 K, τ the ^{13}CO optical depth, and η the beam filling factor. This expression can then be solved for $T_{\rm ex}$.

The resulting map is shown in Fig. 5.2, Table 5.1 (4) lists the median temperature of each source. Certain assumptions are made. First, we assumed that $T_{\rm ex}$

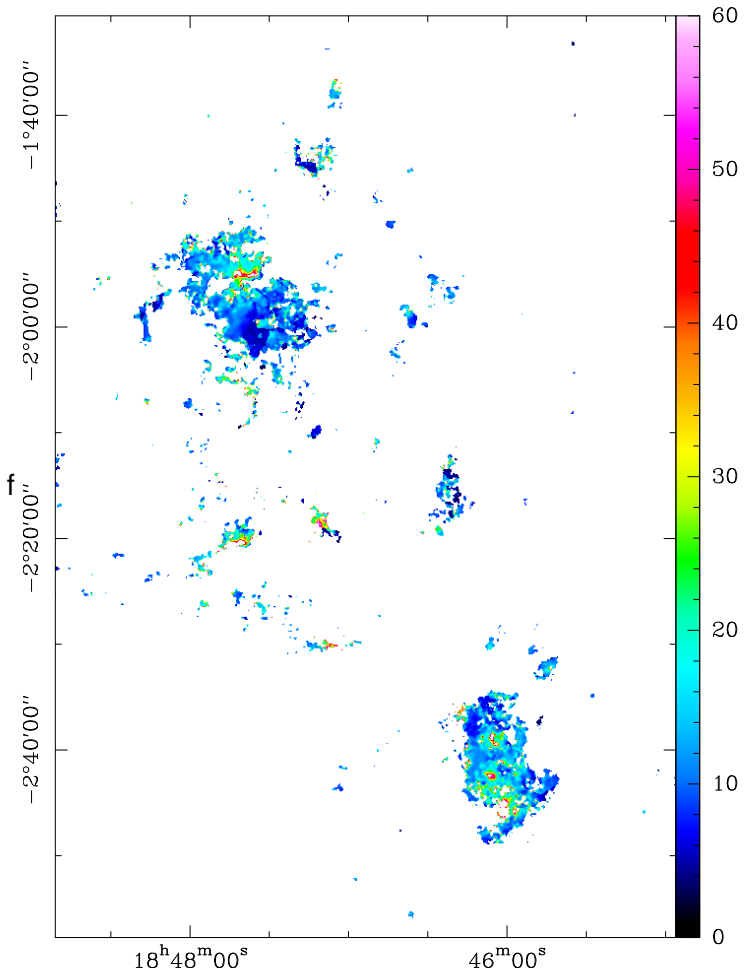

Fig. 5.2: Map of the derived excitation temperature in the W43 complex in units of [K]. This map shows unrealistic low temperatures of ~ 5 K in several regions (cp. Sect. 5.1.2 for a discussion of error sources). The HPBW is identical to those of the CO maps (11″).

is the same for the ^{13}CO and the C^{18}O gas. This method becomes unrealistic when the temperature distribution along the line-of-sight is not uniform anymore. If there was a temperature gradient we would miss the real ratio of the ^{13}CO to C^{18}O line intensities and thus either over- or underestimate the temperature. Thus, the calculated temperature might be incorrect for very large cloud structures that show a complex temperature distribution along the line-of-sight. This problem is partially circumvented by using the spectral information of our observations, but we use intensity maps integrated over at least several km s^{-1} for our calculation of the excitation temperature, which still leaves room for uncertainties. This means we do not confuse different clouds, but we still average the temperature along the line-of-sight over the complete clouds.

The centers of the two main clouds in the W43 region are candidates for an underestimated excitation temperature. In case these regions were internally

	Number	(1) Integrated ^{13}CO intensity	(2) Mean $\tau(^{13}\mathrm{CO})$	(3) Maximum $\tau(^{13}\mathrm{CO})$	(4) Median T_{ex}
		[K km s^{-1} pc^2]$\times 10^3$			[K]
Fore-ground	1	1.3	1.33	3.4	7.0
	2	0.9	0.87	3.5	11.1
	3	1.3	0.88	4.1	9.2
	4	5.9	1.01	3.9	7.1
	5	15.2	0.52	2.2	10.1
	6	0.2	0.81	2.8	7.7
	7	0.3	1.27	4.5	7.7
	8	0.5	1.41	2.6	10.4
	9	5.0	1.22	4.4	7.5
W43	10	1.3	0.97	3.6	8.8
	11	1.2	2.15	5.2	15.0
	12	3.5	1.05	4.4	6.9
	13[a]	30.8	1.70	8.0	10.0
	14	5.8	0.61	3.3	8.3
	15	2.7	1.09	3.0	8.9
	16	3.4	1.50	5.9	7.9
	17	3.9	1.15	4.2	8.2
	18	0.5	1.03	4.2	13.9
	19	1.2	1.37	5.2	8.3
	20[b]	23.2	1.46	5.3	11.3
	21	0.5	1.24	4.8	14.8
	22	4.6	1.11	5.0	11.0
	23	3.2	1.45	3.3	13.2
	24	2.9	1.76	6.5	8.5
	25	1.2	1.80	6.4	9.3
	26	2.3	1.51	6.1	8.5
	27	1.7	1.34	3.7	7.0
	28	0.7	1.28	4.1	9.9
	29	1.5	1.66	5.4	12.6

[a] W43-Main
[b] W43-South

Table 5.1: Opacity and excitation temperature of the W43 clouds and foreground structures as described in Table 4.1.

heated, a decreasing gradient in the excitation temperature would appear from the inside of the cloud to the outside. As ^{13}CO is rather optically thick, only the cooler outside of the cloud would be seen by the observer. In contrast, C^{18}O would be optically thin; thus, the hot center of the cloud would also be observed. Averaging along the line-of-sight, I(C^{18}O) would be increased relative

to $I(^{13}\mathrm{CO})$, which would lead to an overestimated optical depth. This would then lead to an underestimated calculated excitation temperature. External heating, on the other hand, would result in an overestimated excitation temperature. However, we find the first case with regard to low excitation temperatures is more likely in some clouds.

Another effect, which leads to a reduced excitation temperature, is the beam-filling factor η. In our calculations, we assume it to be 1. This corresponds to extended clouds that completely fill the telescope beam. This is not a true representation of molecular clouds, as they are structured on the sub-parsec scale and we would have to use a factor $\eta < 1$. Technically speaking, we calculate the value of $T_{\mathrm{ex}} \times \eta$, which is smaller than T_{ex}.

As the $C^{18}O$ line is much weaker than the ^{13}CO line, we cannot use the ratio of them for those pixels where no $C^{18}O$ is detected, even if ^{13}CO is present. We find typical temperatures to be between 6 and 25 K; in some rare cases it is up to 50 K with a median of 12 K.

Due to the sparsely covered maps (see Fig. 5.2) and the uncertainties described above, we concluded that it was best not to use the excitation temperature maps for the following calculations of the H_2 column density. Instead, we assumed a constant excitation temperature for the complete W43 region. We chose the value to be 12 K, since this was the median temperature found in the W43 complex. Assuming a constant temperature value across the cloud is likely not a true representation of the cloud; in particular, it does not distinguish between star-forming cores and the ambient background. However, such an assumption is a good first approximation to the temperature in the cloud and is more representative of star-forming cores than the aforementioned unrealistically low values.

5.1.3 H_2 column density

We also calculated the column density along the line-of-sight of the ^{13}CO gas from the assumed constant excitation temperature, the ^{13}CO integrated emission, and a correction for the opacity with the formula

$$N(^{13}\mathrm{CO}) = \frac{\tau}{1-\exp(-\tau)}\, f(T_{\mathrm{ex}}) \int T_{\mathrm{mb}}\, \mathrm{d}v, \tag{5.4}$$

where the factor containing τ accounts for the effect that the full gas is not seen for optically thicker clouds and

$$f(T_{\mathrm{ex}}) = \frac{3h}{8\pi^3\mu^2} \frac{Z}{\left(J\left(T_{\mathrm{ex}}\right) - J\left(T_{\mathrm{BG}}\right)\right)\left(1-\exp\left(-\frac{h\nu}{k_{\mathrm{B}}T_{\mathrm{ex}}}\right)\right)} \tag{5.5}$$

with the function

$$Z = \exp\left(\frac{BJ_{\rm u}(J_{\rm u}+1)h}{k_{\rm B}T_{\rm ex}}\right)\frac{k_{\rm B}T_{\rm ex}}{J_{\rm u}Bh}, \tag{5.6}$$

where $B = 5.5099671 \times 10^{10}\,\mathrm{s}^{-1}$ is the rotational constant for ^{13}CO, $\mu = 0.112\,\mathrm{D}$ is its dipole moment, and $J_{\rm u}$ is the upper level of our transition (2 in this case). We correct all those points for the optical depth where we find an opacity larger than 0.5. We assume this is the minimum value we can determine correctly as we might confuse emission with noise for lower opacities.

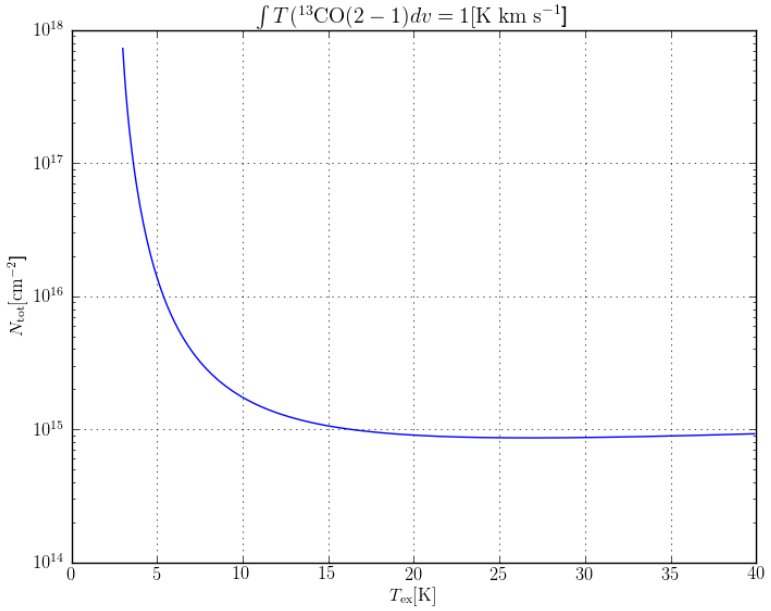

Fig. 5.3: Plot of ^{13}CO column density, depending on the excitation temperature.

In Fig. 5.3, we plot the dependency of the ^{13}CO column density and the excitation temperature. We note that the column density for values of > 15 K is nearly independent of the excitation temperature. On the contrary, it rises steeply for temperatures below 10 K. This is important as we most probably would underestimate the excitation temperature for most clouds as discussed above, if we actually used the calculated $T_{\rm ex}$. We would thus overestimate the column density. Therefore, we can assume that using an excitation temperature of 12 K for our calculation results in a lower limit for the actual column density.

As we want to calculate the H_2 column density, we need to translate $N(^{13}\mathrm{CO})$ into $N(\mathrm{H_2})$. The standard factor of $N(\mathrm{H_2})$:$N(^{12}\mathrm{CO})$ is 10^4 for local molecular clouds, but the ratio varies with sources and also with the Galactocentric radius. Fontani et al. (2012) derive a radius dependent formula for $N(\mathrm{H_2})$:$N(\mathrm{CO})$, using

values of ^{12}C/H and ^{16}O/H from Wilson and Matteucci (1992). This formula gives a ratio of 6550 for a Galactic radius of 4 kpc 7000 at 4.5 kpc and 8500 at 6 kpc. Using our ratios of ^{12}CO:^{13}CO from above, we get $N(\mathrm{H_2}) = 2.0 \times 10^5\, N(^{13}\mathrm{CO})$ for the W43 complex with a radius of 4 kpc and the factors of 3.0×10^5 and 4.4×10^5 for the fore-/background complexes with radii of 4.5 and 6 kpc components, respectively.

All ratios between H_2 and CO isotopologues bear errors, since they depend on the Galactocentric radius and the deviate for different clouds. These errors add up with the uncertainty on the assumed excitation temperature. The final results for column densities and masses must be taken with caution, because there is at least an uncertainty of a factor of 2. Fig. 5.4 shows the calculated H_2 column density map of the full W43 complex. It has been calculated at those points, where the ^{13}CO integrated intensity is higher than 5 K km s^{-1}. Table 5.2 lists mean and maximum column density of each source in our set. The resulting values range from a few times 10^{21} cm^{-2} in the diffuse surrounding gas up to nearly 2×10^{23} cm^{-2} in the center of W43-Main.

The southern ridge of W43-Main, where we calculate high column densities, is the most problematic part of our dataset. The spectra reveal that ^{13}CO is self-absorbed in this part of the cloud. We use the integrated intensity ratio to calculate the opacity at each point, which is strongly overestimated in this case. This leads to both low excitation temperatures and high column densities. The results for this part of the cloud should be used with caution.

5.1.4 Total mass

From the H_2 column density, we then determine the total mass of our sources, given in Table 5.2. To calculate these masses from the H_2 column density it is necessary to consider the relative distance from the Sun to the source. See Sect. 4.4 for the distance determination. We assume the main complex clouds are 6 kpc away, while the foreground clouds have distances of 3.5, 4, 3.5, and 12 kpc. Then, we just have to count the number of H_2 molecules per pixel to receive the mass per pixel in solar masses (see Fig. 5.1 (f)),

$$M_{\mathrm{tot}} = N(\mathrm{H_2})\, \frac{m(\mathrm{H_2})}{M_\odot}\, d^2\, \alpha^2\, \mu. \tag{5.7}$$

Here, d is the distance toward the source, α the angular extent of one pixel on the sky. The value of $\mu = 1.36$ accounts for higher masses of molecules apart from H_2 (compare Schneider et al. 2010).

We find that the total mass of a typical cloud is in the range of a few $\times 10^4$ solar masses. Of course, this is only the mass seen in the mid- to high-density sources. The very extended diffuse molecular gas cannot be seen with ^{13}CO; it

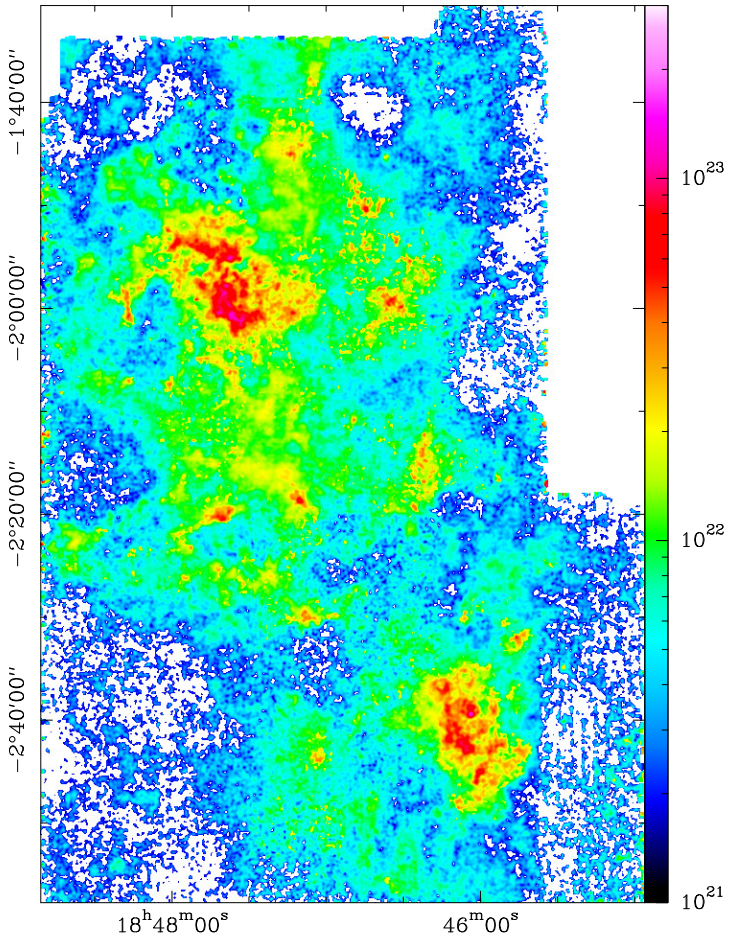

Fig. 5.4: Map of the H_2 column density of the complete W43 complex in [cm^{-2}], derived from the IRAM 30m ^{13}CO and $C^{18}O$ maps. The velocity range between 78 and 120 km s^{-1} was used. The beam size is identical to those of the CO maps (11″).

is generally traced by ^{12}CO lines and accounts for a major fraction of the gas mass (Nguyen Luong et al. 2011).

The total H_2 mass as derived from our ^{13}CO (2–1) and C^{18}O (2–1) observations is found to be

$$M(\mathrm{H_2})_{\mathrm{CO}} = 1.9 \times 10^6\, M_\odot \tag{5.8}$$

for the W43 complex with about 50% within the clouds that we have identified and the rest in the diffuse surrounding gas. Here we have excluded the foreground sources and only considered the W43 complex itself. Nguyen Luong et al. (2011) used similar areas and velocity ranges ($\sim$80$\times$190 pc, 80-120 km s^{-1}) and determined a molecular gas mass in W43 clouds from the Galactic Ring Survey (Jackson et al. 2006) of $4.2 \times 10^6\ M_\odot$. A different estimation of the H_2

column density in W43 was done by Nguyen-Luong et al. (2013) using *Herschel* dust emission maps. Using these maps, we find a value of $2.6 \times 10^6\ M_\odot$. See Sect. 5.5.4 for a discussion of this difference.

We underestimate the real mass where ^{12}CO exists but no ^{13}CO is seen, where C^{18}O might become optically thick, and where our assumption for the excitation temperature is too high. On the other hand, we overestimate the real mass, where our assumption for the excitation temperature is too low. In extreme cases of very hot gas, the gas mass can be overestimated by 40% at most (cp. Fig 5.3), while very cold cores can be underestimated by a factor of nearly 10. Both effects partly cancel out each other, when integrating over the whole region; however, we estimate that the effects, which underestimate the real mass, are stronger. Therefore, the mass we calculated should be seen as a lower limit of the real molecular gas mass in the W43 complex.

5.2 Shear parameter

Investigating the motion of gas streams in the Galaxy is important to explain how large molecular clouds like W43 can be accumulated. While Motte et al. in prep. will investigate streams of ^{12}CO and H I gas in W43 in detail, we only consider here the aspect of radial shear in this field. The shear that is created by the differential rotation of the Galaxy at different Galactocentric radii, can prevent the formation of dense clouds if it is too strong. It is possible to calculate a shear parameter,

$$S_\mathrm{g} = \frac{\alpha_A A \sigma}{\pi G \Sigma}, \tag{5.9}$$

as described in Dib et al. (2012), where Σ and σ are the gas surface density and the velocity dispersion of the cloud, respectively. The factor $\alpha_A = \ln(C)/2$ accounts for the density contrast C between the molecular gas and the surrounding diffuse gas. For an assumed density contrast of 1000, $\alpha_A \approx 3.45$ is found. Finally, the Amplitude of the growth of the density perturbations in the gas is proportional to $1/A$, where the Oort constant,

$$A = -0.5 R \frac{\mathrm{d}\Omega}{\mathrm{d}R} = 0.5 \left(\frac{V}{R} - \frac{\mathrm{d}V}{\mathrm{d}R} \right), \tag{5.10}$$

is given by the angular velocity Ω and the rotation velocity V of the source. For values of S_g higher than 1, the shear is so strong that clouds get ripped apart, while they are able to form for values below 1.

	Number	(1) mean H_2 column density	(2) max H_2 column density	(3) Total mass	(4) Virial mass	(5) Virial parameter
		$[\mathrm{cm}^{-2}] \times 10^{21}$	$[\mathrm{cm}^{-2}] \times 10^{22}$	$[M_\odot] \times 10^3$	$[M_\odot] \times 10^3$	
	1	10.5	3.4	21.5	18.4	3.28
	2	8.7	5.4	13.2	14.1	4.09
	3	10.2	3.8	18.6	19.3	3.97
Fore-	4	7.3	3.2	73.3	27.9	1.46
ground	5	9.2	8.1	202.5	33.9	0.64
	6	7.4	2.0	2.0	8.1	15.62
	7	10.2	5.7	4.8	11.6	9.18
	8	3.7	1.8	2.2	3.7	4.40
	9	4.7	5.1	43.2	16.3	0.98
	10	5.1	2.8	10.5	17.1	2.82
	11	7.1	8.1	11.3	11.5	1.77
	12	5.2	3.4	26.8	39.5	2.56
	13[a]	20.9	12.7	306.3	448.4	2.55
	14	4.6	2.0	38.3	44.5	2.02
	15	5.6	2.8	22.0	28.5	2.25
	16	4.3	2.9	25.0	11.7	0.82
	17	6.2	3.2	30.2	47.6	2.74
	18	3.7	0.9	3.0	5.6	3.28
W43	19	4.2	2.0	9.7	9.0	1.62
	20[b]	14.8	14.9	205.8	369.2	3.12
	21	6.0	4.3	4.1	8.8	3.73
	22	5.5	3.1	33.9	57.1	2.94
	23	8.1	6.9	27.3	27.1	1.73
	24	5.0	3.1	24.5	28.4	2.01
	25	4.6	4.1	6.8	7.3	1.85
	26	4.7	2.9	16.8	24.3	2.53
	27	4.6	2.6	14.0	17.4	2.16
	28	4.1	1.8	4.3	6.3	2.57
	29	5.1	2.8	11.9	10.3	1.51

[a] W43-Main
[b] W43-South

Table 5.2: H_2 column density and mass of the W43 clouds and foreground structures as described in Table 4.1.

The values we use to calculate S_g are the total mass of $1.9 \times 10^6\,M_\odot$, a velocity extent of 40 km s^{-1}, a Galactocentric radius of 4 kpc, which leads to $A = 18$ km kpc^{-1} s^{-1}, according to Dib et al. (2012), and an area of 8×10^3 pc^2. This is the area that is covered by emission and is smaller than the total size of our map. These values yield a shear parameter $S_\mathrm{g} = 0.77$. Accordingly, shear forces are not strong enough to disrupt the W43 cloud. However, we have to keep in mind that we probably underestimate the total gas mass, as described in Sect. 5.1. A higher mass would lead to a lower shear parameter. This calculation is only valid for an axial symmetric potential (i.e. orbits outside the Galactic bar). Shear forces inside the Galactic bar could be stronger due to the different shape of orbits there. As we, however, located W43 at the tip of the bar, the calculation

still holds.

We can also conduct this calculation for the larger gas mass, derived from ^{13}CO (1–0) by Nguyen Luong et al. (2011). They find a gas mass of $4.2 \times 10^6\,M_\odot$ that is spread out over an area of 1.5×10^4 pc^2. These values lead to a shear parameter of $S_\mathrm{g} = 0.66$, which is lower than our value above.

5.3 Virial masses

In Table 4.1 (7) and (10), we have given the mean line width and the area of our sources. This allows us to calculate virial masses, by defining an effective region radius by $R = (A/\pi)^{1/2}$, where A is the area of the cloud. This area cannot be determined exactly, because the extent of a cloud depends on the used molecular line. Here, we use the area of ^{13}CO emission above a certain threshold (20% of the peak intensity).

Virial masses can then be computed, using the relation

$$M_\mathrm{V} = 5\frac{R\,\sigma^2}{G}(M_\odot), \tag{5.11}$$

where σ is the Gaussian velocity dispersion, averaged over the area A, and G is the gravitational constant.

The resulting virial masses are shown in Table 5.2 (4). We notice that most sources in W43 have masses, derived from ^{13}CO, that are smaller than their virial masses. Sources 4 and 5 show much larger molecular than virial masses, which might indicate that their distance was overestimated. This is, because the virial mass is proportional to the distance d of the source, while the mass, derived from the H_2 column density, scales with d^2. The virial parameter $\beta_\mathrm{vir} = M_\mathrm{vir}/M_\mathrm{gas}$ of the W43 clouds, shown in Table 5.2 (5), ranges from 0.82 (source 16) to 3.73 (source 21), with a mean of 2.33.

If the sources would be completely virialized, we would need bigger masses to produce the observed line widths. On the other hand, systematic motion of the gas, apart from turbulence, like infall, outflows, or colliding flows would also broaden the lines. This could be an explanation for the observed large line widths.

Ballesteros-Paredes (2006) stated that usually turbulent molecular clouds are not in actual virial equilibrium, because there is a flux of mass, momentum, and energy between the clouds and their environment. What is normally viewed as virial equilibrium is rather an energy equipartition between self-gravity, kinetic, and magnetic energy. This energy equipartition is found for most clouds due to observational limitations. Clouds out of equilibrium are either not observed due to their short lifetime or not considered clouds at all.

Of course, we also need to consider the shape of our sources. Non-spherical sources have a more complicated gravitational behavior than spheres. Therefore, one has to be extremely careful, using these results. In addition, we neglect here the influence of external pressure and magnetic fields on the virial masses. What we observe agrees with Ballesteros-Paredes (2006) in that most of our detected clouds show a molecular mass on the order of their virial mass, but are usually about a factor of 2 to 3 smaller.

Typically, on the parsec scale, the virial mass and the molecular gas mass are comparable, but on smaller scales (∼0.01 pc) $M_{\rm vir} > M_{\rm gas}$ is found (Sánchez-Monge et al. 2013). Probably, this is due to the fact that at smaller scales the external pressure and magnetic field play a more important role than at larger scales.

5.4 Larson's laws

From the properties of our observations we can also try to verify Larson's laws (Larson 1981), which have been innumerably used in astronomy (some of the newest examples are Kritsuk et al. 2013; Tanaka et al. 2013). Larson's first law relates the velocity dispersion σ of a molecular cloud and the linear size R:

$$\sigma(\mathrm{km\,s^{-1}}) = 1.10 L(\mathrm{pc})^{0.38}. \tag{5.12}$$

The second law relates the velocity dispersion σ and the mass M of the cloud, using the formula

$$\sigma(\mathrm{km\,s^{-1}}) = 0.42 M(M_\odot)^{0.20}. \tag{5.13}$$

Here, we use $L_{\rm eff} = 2(A/\pi)^{1/2}$ (similar to the calculation of the virial masses) as the size of the clouds.

For our set of clouds we create plots that display these relations. Figure 5.5 (a) demonstrates our findings for Larson's first law, while Fig. (b) plots the outcome of Larson's second law. In the first case, we derive a slope of the best linear fit of 0.49, where Larson finds a value of 0.38. This is a significant difference of 30% . For the second law, we find a slope of the linear fit of 0.24, compared to the value in the literature of 0.20, which is 20% lower.

Although both results may be in the same range as the expected values, we also note that the spread of data points, and therefore the error of the results, is quite large. It becomes clear that the results of the linear fit is strongly influenced by the two outlier points in the respective upper right corner of the plots. These points denote W43-Main and W43-South. Without these points no clear correlation could be identified. The large error and the unclear correlation of these findings led to the decision not to further consider this Larson analysis.

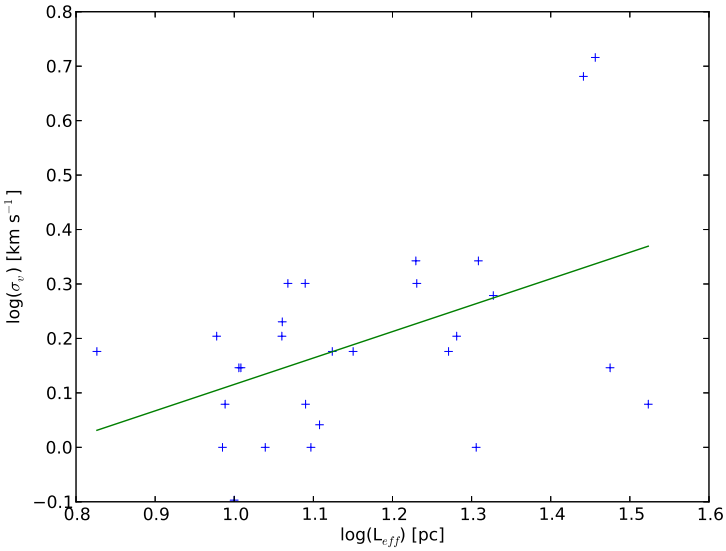

(a) First Larson law.

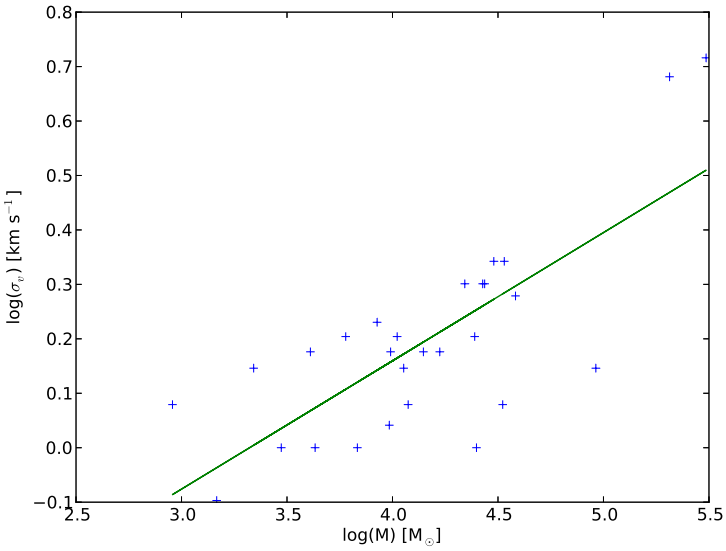

(b) Second Larson law.

Fig. 5.5: Larson's laws plots of the data points (blue crosses) and best linear fits (green line).

5.5 Comparison to other projects

To gather more information about the W43 complex, we compare the IRAM 30m CO data to other existing datasets. We pay special attention to three large-scale surveys in this section: the *Spitzer* GLIMPSE and MIPS Galactic Plane Survey

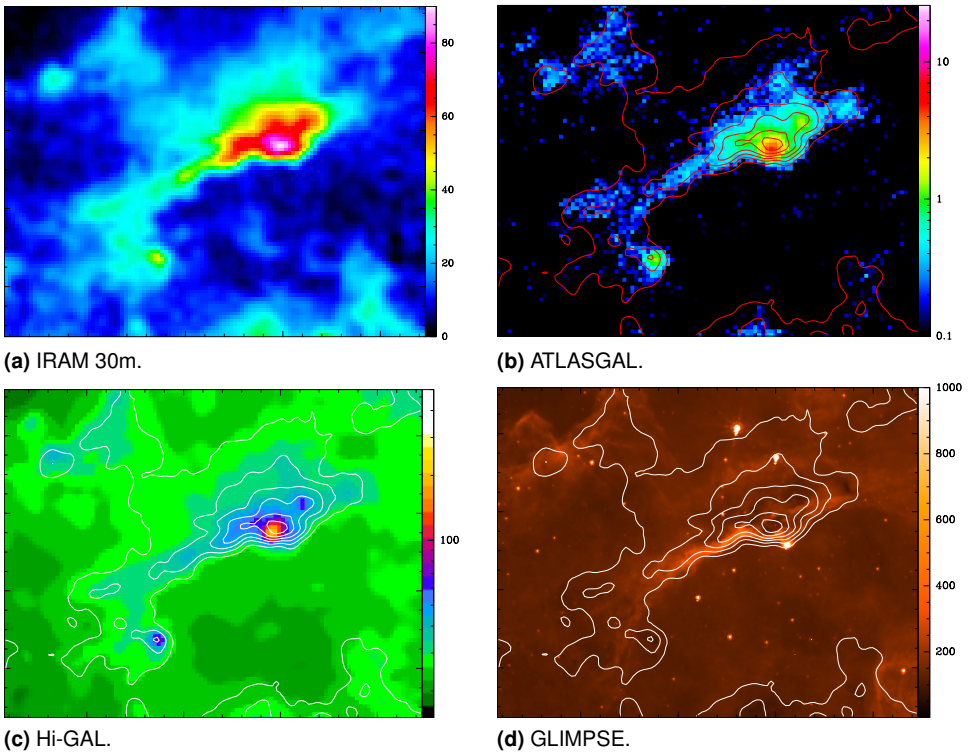

(a) IRAM 30m. **(b)** ATLASGAL.

(c) Hi-GAL. **(d)** GLIMPSE.

Fig. 5.6: Series of plots showing the comparison of different datasets of source 23 (see Table 4.1). From upper left to lower right: **(a)** *IRAM 30m integrated intensity map of* ^{13}*CO (2–1) in [K km s*$^{-1}$*],* **(b)** *IRAM 30m* ^{13}*CO map contours on APEX Telescope Large Area Survey of the Galaxy (ATLASGAL) 870* μ*m map in [Jy beam*$^{-1}$*],* **(c)** *IRAM 30m* ^{13}*CO map contours on Hi-GAL 250 map in [Jy beam*$^{-1}$*], and* **(d)** *IRAM 30m* ^{13}*CO map contours on Galactic Legacy Infrared Mid-Plane Survey Extraordinaire (GLIMPSE) 8* μ*m map in [MJy sr*$^{-1}$*].*

(MIPSGAL) projects, the *Herschel* Hi-GAL survey (with an addition from the *Herschel* imaging survey of OB Young Stellar objects (HOBYS) program), and the Galactic plane program ATLASGAL, observed with the APEX telescope.

All of these datasets consist of total power maps over certain bands. They naturally do not contain spectral information, so line-of-sight confusion is considerable, since the W43 region is a complex accumulation of different sources. It can sometimes be complicated to assign the emission of these maps to single sources. Nevertheless, the additional information is very valuable.

5.5.1 *Spitzer* GLIMPSE and MIPSGAL

The *Spitzer* Space Telescope program GLIMPSE (Benjamin et al. 2003; Churchwell et al. 2009), observed the Galactic plane at several IR wavelengths between 3.6 and 8 μm. It spans the Galactic plane from -65° to 65° Galactic longitude.

	Number	(1) ^{13}CO structure	(2) *Spitzer* structure	(3) Mass ratio Hi-GAL/^{13}CO
Fore-ground	1	Filament	Single core	
	2	Ensemble of cores	Two cores + extended emission	
	3	Ensemble of cores	Single core + extended emission	
	4	Joining filaments	No related emission	
	5	Two cores	Two cores + extended emission	
	6	Complex	Extended emission	
	7	Complex	Single core + extended emission	
	8	Single core	Single core + absorption	
	9	Ensemble of cores	Single core + absorption	
W43	10	Two cores	Two cores + absorption	1.8
	11	Single core	Single core + absorption + extended emission	1.0
	12	Complex	Several cores	1.1
	13[a]	Complex	Bright emission + absorption, Bubble around star cluster	1.2
	14	Ensemble of cores	Absorption	1.3
	15	Complex	One extended core + absorption	1.2
	16	Filament	Absorption	1.5
	17	Complex	Several cores + absorption	1.9
	18	Filament	No related emission	1.1
	19	Complex	Two extended cores + absorption	1.0
	20[b]	Ensemble of cores	Bright extended emission + absorption	0.8
	21	Filament	Single core + extended emission	1.9
	22	Complex	Several cores + absorption + extended emission	1.1
	23	Filament	Single core + absorption + extended emission	0.9
	24	Joining Filaments	Two cores + absorption	1.7
	25	Filament	Two cores + extended emission	1.2
	26	Filament	Single core + extended emission	0.9
	27	Two cores	Single core + extended emission	1.2
	28	Filament	No related emission	1.6
	29	Filament	Several cores	1.0

[a]W43-Main
[b]W43-South

Table 5.3: List of sources, as described in Table 4.1 and a description of their structure.

Here, we concentrated on the 8 μm band. It is dominated by UV-excited PAH emission (Peeters et al. 2004). These PDRs (Hollenbach and Tielens 1997) are heated by young OB stars. By studying this band in comparison to the IRAM 30m CO maps, we can determine which parts of the molecular clouds contain UV-heated dust. This is seen as extended emission in the *Spitzer* maps. We can also identify nearby UV-heating sources, as seen as point sources. Finally, some parts of specific clouds appear in absorption against the background. These IRDCs (see Egan et al. 1998; Simon et al. 2006; Peretto and Fuller 2009) show denser dust clouds that are not heated by UV-radiation. That way we are able to determine which sources heat part of the gas and which parts are shielded from UV radiation. We can also tell if young stellar objects (YSOs) have already formed inside the clumps that we have observed and thus estimate the evolution-

ary stage of the clouds. Nguyen Luong et al. (2011) used this tracer to estimate the SFR (Wu et al. 2005) of the W43 complex.

MIPSGAL (Carey et al. 2009) is a Galactic plane survey using the Multiband Imaging Photometer for *Spitzer* (MIPS) instrument onboard *Spitzer* and has created maps at 24 and 70 μm. Here, we inspect the 24 μm band, which is dominated by the emission of small dust grains. It also detects proto-stellar cores, although these cores are usually too small to be resolved at a distance of 6 kpc or more.

5.5.2 APEX ATLASGAL

The APEX telescope large area survey of the galaxy ATLASGAL project (Schuller et al. 2009) used the LABOCA camera, which is installed at the APEX telescope. It observed the Galactic plane from a Galactic longitude of -60° to 60° at 870 μm. This wavelength traces cold dust and is therefore also a good indicator of dense molecular cloud structures, especially of high-mass star-forming clumps. Schuller et al. also identified hot cores, proto-stars, compact H II regions, and young embedded stars by combining their map with other data. Plots of ^{13}CO (2–1) contours, overlaid on ATLASGAL maps can be found in Appendix B. Our project is a direct follow-up of ATLASGAL, from which the idea was born to observe the W43 region in more detail.

5.5.3 VLA THOR project

A project to observe H I and OH recombination lines with the VLA along large parts of the Galactic plane was initiated by Henrik Beuther (MPIA Heidelberg). Observations for The HI/OH/Recombination line survey of the Milky Way (THOR) project started in 2013. One year before, a pilot study was carried in the W43 field (Bihr et al. 2013) to prove the feasibility of the project's concept. The data of this pilot study is already reduced and its analysis by Henrik Beuther and Simon Bihr (MPIA Heidelberg) is ongoing.

A combined analysis of the THOR and W43 HERO data is planned for the future. We will compare the velocity structure of the CO emission and the H I absorption to find a correlation. We assume that H I forms an envelope around the molecular clouds, similar to the findings in Nguyen Luong et al. (2011) and Motte et al. subm. Figure 5.7 shows example spectra of ^{13}CO (2–1) and H I in W43-Main. It shows a wide H I absorption feature at the position of the ^{13}CO emission line, as expected.

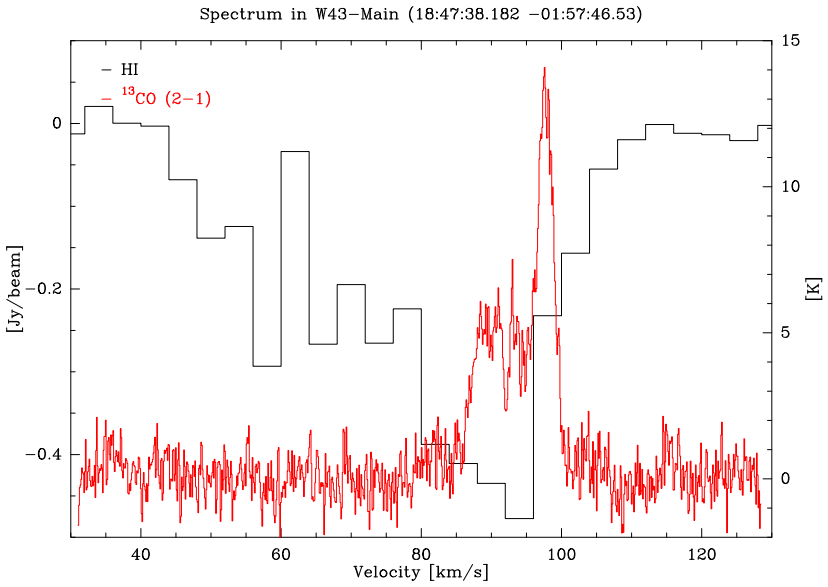

*Fig. 5.7: Spectrum of ^{13}CO (2–1) (right scale) and H*I *absorption (left scale) from the VLA THOR project (Bihr et al. 2013) in W43-Main.*

5.5.4 *Herschel* Hi-GAL

The Hi-GAL project (Molinari et al. 2010) utilizes *Herschel*'s Photodetecting Array Camera and Spectrometer (PACS) and Spectral and Photometric Imaging Receiver (SPIRE) instruments to observe the Galactic plane from a Galactic longitude of -60° to 60° at five wavelengths between 70 and 500 μm. A part of the Hi-GAL maps of the W43 complex are presented in Bally et al. (2010).

Figure 5.6 shows one example of the comparison of the different datasets that we carried out for all identified sources. It shows source 23, sticking to the notation of Table 4.1. See Appendix A for an in depth description of the different sources.

In Table 5.3, we categorize our sources, whether they have a filamentary shape, consist of cores, or show a more complex structure. We also list the structure of the *Spitzer* 8 and 24 μm maps here. Usually, the two wavelengths are similar.

From the Hi-GAL dust emission, it is possible to derive a temperature and a total (gas + dust) H_2 column density map (e.g. Battersby et al. 2011). These calculations were conducted for the W43 region by Nguyen-Luong et al. (2013), following the fitting routine detailed in Hill et al. (2009, 2010) and adapted and applied to *Herschel* data as in Hill et al. (2011, 2012); Molinari et al. (2010); Motte et al. (2010). This approach uses Hi-GAL data for the calculations where possible. As on very bright positions, Hi-GAL data become saturated or enter the nonlinear response regime, HOBYS data was used to fill the missing data points. The idea is to fit a modified black body curve to the different wavelengths

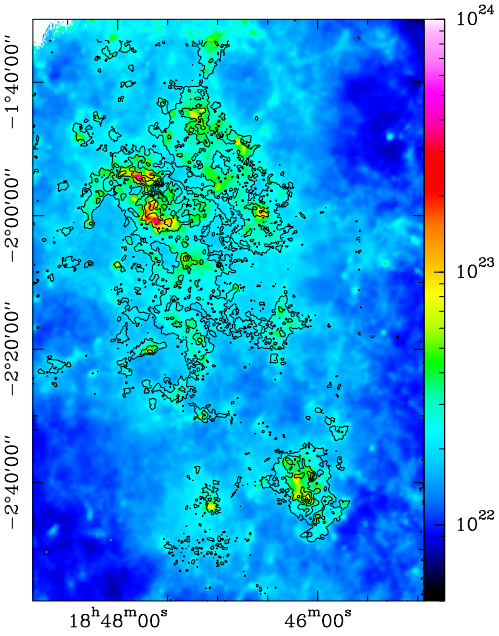

(b) H_2 column density map in $[cm^{-2}]$, derived from three *Herschel* channels (160-350 μm) in color and ^{13}CO (2–1) contours.

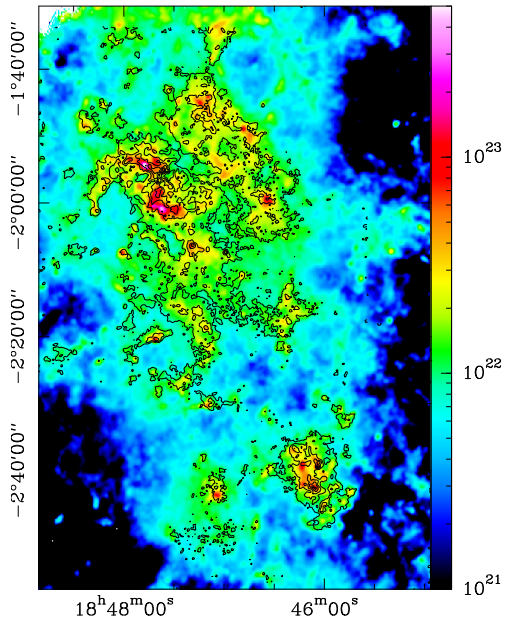

(c) H_2 column density map with removed offset in $[cm^{-2}]$ in color and ^{13}CO (2–1) contours.

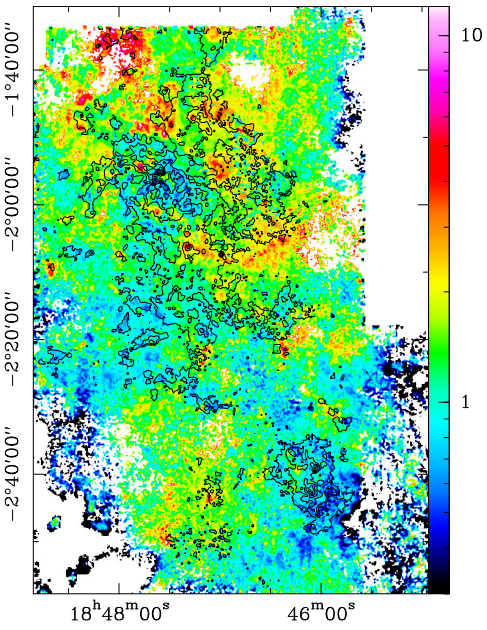

(d) Ratio of the H_2 column density maps in color and ^{13}CO (2–1) contours. The *Herschel* map is divided by the IRAM 30m map.

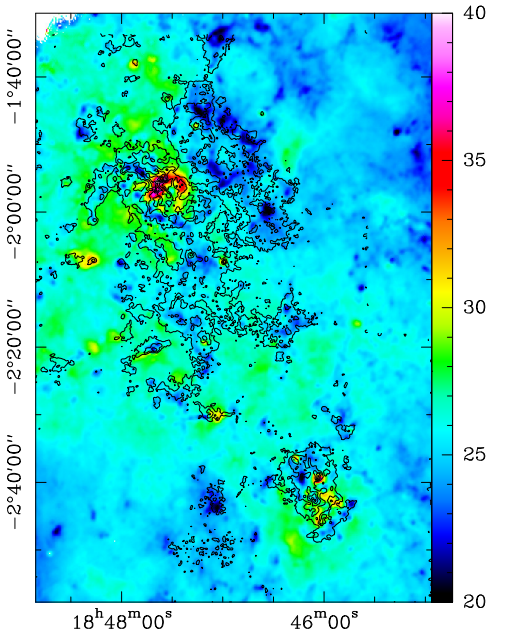

(a) Dust temperature in [K], derived from three *Herschel* channels (160-350 μm) in color and ^{13}CO (2–1) contours.

Fig. 5.8: Maps of H_2 column density and dust temperature, derived from Herschel *HiGAL and HOBYS data (see Nguyen-Luong et al. 2013). The three bands at 160, 250, and 350 μm were used for the calculations.*

(in this case, the 160 to 350 μm channels) for each pixel using a dust opacity law of $\kappa = 0.1 \times (300\,\mu\mathrm{m}/\lambda)^{\beta}$ cm^2 g^{-1} with $\beta = 2$. The final angular resolution of the calculated maps (25″ in this case) results from the resolution of the longest wavelength used. This is the reason that the 500 μm channel has been omitted. *Planck* and IRAS offsets were added before calculating the temperature and H_2 column density.

This approach assumes the temperature distribution along the line-of-sight to be constant. As discussed above in Sect 5.1.2, this is not necessarily the case in reality. Due to temperature gradients along the line-of-sight, the calculated H_2 column density might deviate from the real value. This error is found in the *Herschel* and the CO calculations.

Gas and dust temperatures can deviate in optically thick regions, because the volume densities play a key role here. Only at fairly high densities of more than about 10^5 cm^{-3} does the gas couple to the dust temperature. At lower densities, the dust grains are an excellent coolant, in contrast to the gas. Therefore, the dust usually shows lower temperatures than the gas. This is in contrast to our findings and may indeed indicate that we underestimate the T_{ex} of the gas, as discussed in Sect. 5.1.2. Even in optically thin regions, the kinetic temperature and the values derived from an spectral energy distribution (SED)-fit do not correspond perfectly (see Hill et al. 2010). Figure 5.8 shows the results of these calculations for the W43 region. We show the temperature and H_2 column density maps from the photometry data and overlay ^{13}CO contours to indicate the location of the molecular gas clouds.

The dust temperature derived by Nguyen-Luong et al. (2013) (Fig. 5.8 (d)) lies in the range from 20 to 40 K; the outer parts of the complex show temperatures between 25 and 30 K. The regions where dense molecular clouds are found are colder (about 20 K) than their surroundings; for example the dense ridges in W43-Main are clearly visible. Some places, where the dust is heated by embedded UV-sources, are hotter (up to 40 K), especially for the OB-star cluster in W43 and one core in W43-South catch the eye.

If we compare these results with the excitation temperatures that we calculated above in Sect. 5.1, we note that the temperatures derived from CO are lower ($\sim 7 - 20$ K) than those using *Herschel* images. It is possible that gas and dust are not mixed well and that both could have a different temperature. Another possibility is that the CO gas is sub-thermally excited and that the excitation temperature is lower than its kinetic temperature. The *Herschel* dust temperature map is showing the averaged temperature along the line-of-sight. Thus, lower temperatures of the dense clouds are seen with hotter diffuse gas around it, which leads to higher averaged temperatures. As discussed in Sect. 5.1.2, we most probably underestimate the excitation temperature in our calculations above, due to sub-beam clumpiness. Also, we cannot neglect that the temperatures calculated from *Herschel* bear large errors on their own.

The H_2 column density map derived from *Herschel* data (Fig. 5.8 (a)) nicely

traces the distribution of molecular gas, as indicated by the ^{13}CO (2–1) contours. There is a background level of $\sim 1 - 2 \times 10^{22}$ cm^{-2} that is found outside the complex. The column density rises in the molecular clouds up to a value of $\sim 6 \times 10^{23}$ cm^{-2} in the ridges of W43-Main.

A comparison to the column density values derived from CO (see Sect. 5.1 and the plot in Fig. 5.4) reveal certain differences. In the mid-density regions, calculations of both the medium-sized clouds and most parts of the two large clouds are comparable after subtracting the background level from the *Herschel* maps. These are still systematically higher, but the difference does rarely exceed a factor of 2. The same is true for the extended gas between the denser clouds. The typical values are around a few 10^{21} cm^{-2} for the *Herschel* and CO maps. However, the *Herschel* H_2 column density reaches values of several 10^{23} cm^{-2} in the densest parts of W43-Main with a maximum of $\sim 6 \times 10^{23}$ cm^{-2}, while the CO derived values peak at $\sim 2 \times 10^{23}$ cm^{-2}.

The offset of $\sim 1 \times 10^{22}$ cm^{-2} (which could be a bit higher but we chose the lower limit) that has to be subtracted from the *Herschel* map can partly be explained by diffuse cirrus emission along the line-of-sight, which is not associated with W43. This statistical error of the background brightness has been described for the Hi-GAL project by Martin et al. (2010). Nguyen-Luong et al. find this offset agrees with Battersby et al. (2011). Figure 5.8 (b) plots the H_2 column density map after subtracting this offset.

The total mass that is found for the W43 complex still deviates between both calculations. The exact value depends on the specific region over which we integrate. We find a total mass of W43 from ^{13}CO of $1.9 \times 10^6\ M_\odot$. The *Herschel* map gives $2.6 \times 10^6\ M_\odot$, if we use the total map with an area of 1.5×10^4 pc^2 and consider the diffuse cirrus emission that is included by the *Herschel* data. This is a factor of 1.4 higher than the CO result, although we did not calculate a value for every single pixel for the CO H_2 column density map. The mean H_2 column density in the offset subtracted map is 7.5×10^{21} cm^{-2} (^{13}CO) and 7.4×10^{21} cm^{-2} (*Herschel*), respectively. The difference in total mass can be explained when we consider that the *Herschel* map covers more points (the difference is reduced to a factor of 1.2, when comparing a smaller region which is covered in both maps, although this might be too small and biased toward the larger clouds).

We show a ratio map of the *Herschel* and the IRAM H_2 column densities in Fig. 5.8 (c). We find regions, where the ratio is larger than 1, i.e. the Hi-GAL calculations deliver higher values, and regions with a ratio below 1, where the H_2 column density derived from CO is higher. In the densest central clumps in W43-Main an W43-South the values derived from molecular observations seem to be higher, while in the medium density parts, the dust emission H_2 column density is enhanced. For the diffuse regions no clear picture can be recognized. For a comparison of each Duchamp cloud, see Table 5.3 (3). A comparison of the foreground clouds would be complicated due to line-of-sight effects, so we only give numbers for the W43 sources. Most values lie in the range 1 to 1.5, which

affirms that both calculations deviate by about a factor of 1.4. The difference in the H_2 column density again depends on the examined region.

As stated in Sect. 5.1.4, the mass derived from CO is a lower limit to the real molecular gas mass. As we used the lower limit of the *Herschel* column density offset subtracted in W43, these values are thus an upper limit. Taking this and the errors still included in both calculations into account, the values are nearly consistent.

5.6 Column density probability distribution function

A detailed investigation of the H_2 column density structure of W43 is done by determining a histogram of the H_2 column density, which is normalized to the average column density. These PDFs are a useful tool to scrutinize between the different physical processes that determine the density structure of a molecular cloud, such as turbulence, gravity, feedback, and magnetic fields. Theoretically, it was shown that isothermal turbulence leads to a log-normal PDF (e.g. Federrath et al. 2010), while gravity (Klessen 2000) and non-isothermality (Passot and Vázquez-Semadeni 1998) provoke power-law tails at higher densities. Observationally, power-law tails seen in PDFs that are obtained from column density maps of visual extinction or *Herschel* imaging were attributed to self-gravity for low-mass star-forming regions (e.g. Kainulainen et al. 2009; Schneider et al. 2013) and high-mass star-forming regions (e.g. Hill et al. 2011; Schneider et al. 2012, Russeil et al. in press). Recently, it was shown (Schneider et al. 2012, Tremblin et al. in prep.) that feedback processes, such as the compression of an expanding ionization front, lead to a characteristic 'double-peaked' PDF and a significant broadening.

The determination of PDFs from molecular line data was attempted by Goodman et al. (2009) and Wong et al. (2008), but it turned out to be problematic when these lines become optically thick and thus do not correctly reflect the molecular cloud spatial and density structure. In addition, uncertainties in the abundance can complicate conversion into H_2 column density. On the other hand, molecular lines allow us to significantly reduce line-of-sight confusion, because PDFs can be determined for selected velocity ranges. In addition, using molecules with different critical densities in selected velocity ranges allows us to make dedicated PDFs that focus on a particular subregion like a dense filament.

In this study, we determined the PDFs of W43 in three ways: (i) from a simple conversion of the ^{13}CO (2–1) map into H_2 column density by using a constant conversion factor and one temperature (5 or 10 K); (ii) from the H_2 column density map derived from the ^{13}CO (2–1) emission, which includs a correction for the optical depth that is derived from both CO lines (see Sect. 5.1); and (iii) from the column density map obtained with *Herschel* using SPIRE and PACS photometry. Figure 5.9 shows the resulting distributions. For simplicity, we used the

conversion $N(\mathrm{H_2 + H})/A_\mathrm{V} = 9.4 \times 10^{20} \mathrm{cm}^{-2}$ (Bohlin et al. 1978) for all maps, though the *Herschel* column density map is a mixture of H I and H_2, while the CO derived map is most likely dominated by H_2.

The 'isothermal' PDFs from ^{13}CO without an optical depth correction (in black and red) clearly show that there is a cut-off in the PDF at high column densities where the lines become optically thick (A_v ~20 mag for 10 K and A_v ~70 mag for 5 K). Obviously, there is also a strong temperature dependence that shifts the peak of the PDF to lower column densities with increasing temperature. The assumed gas temperature (see discussion in Sect. 5.1) thus has a strong impact on the resulting PDFs' positions but not their shape (not considering the uncertainty in the conversion factor).

With the more sophisticated approach to create a column density map out of the ^{13}CO emission and to include the information provided by the optically thinner C^{18}O, which is corrected for the optical depth τ, the PDF (in blue) is more reliable. It does not show the cut-off at high column densities, because this effect is compensated by using the optically thin C^{18}O. Only in those regions where even this line becomes optically thick, the method gives lower limits for the column density. Therefore, it drops below the *Herschel* PDF for high column densities, because the molecular lines underestimate the H_2 column densities for very hot gas.

It is remarkable that the PDF derived from ^{13}CO and C^{18}O shows a log-normal distribution for low column densities and a power-law tail for higher densities. This feature is also observed in the *Herschel* PDF. The approach to determine a PDF from the cloud/clump distribution by correcting the opacity using C^{18}O appears to be the right way to get a clearer picture of the distribution of higher column densities. Note that the absolute scaling in column density for both PDFs – from CO or *Herschel* – remains problematic due to the uncertainty in the conversion factor (and temperature) for the CO data, the line-of-sight confusion, and opacity variations for the *Herschel* maps.

We observe that the slope of the *Herschel* power-law tail is steeper than the one obtained from the CO-data and shows a 'double-peak' feature (the low column density component is not strictly log-normally shaped but shows two sub-peaks) as seen in other regions with stellar feedback (Tremblin et al. in prep.). The column density structure of W43 could thus be explained in a scenario where gravity is the dominating process for the high density range, leading to global cloud collapse and individual core collapse; compression by expanding ionization fronts from embedded H II-regions may lead to an increase in column density, and the lower-density extended emission follows a turbulence dominated log-normal distribution. This scenario is consistent with what was proposed for other high-mass star-forming regions, such as Rosette (Schneider et al. 2012), RCW36 and M16 (Tremblin et al. in prep.), and W3 (Rivera-Ingraham 2013).

Though the overall shape of the PDFs is similar, there are significant differ-

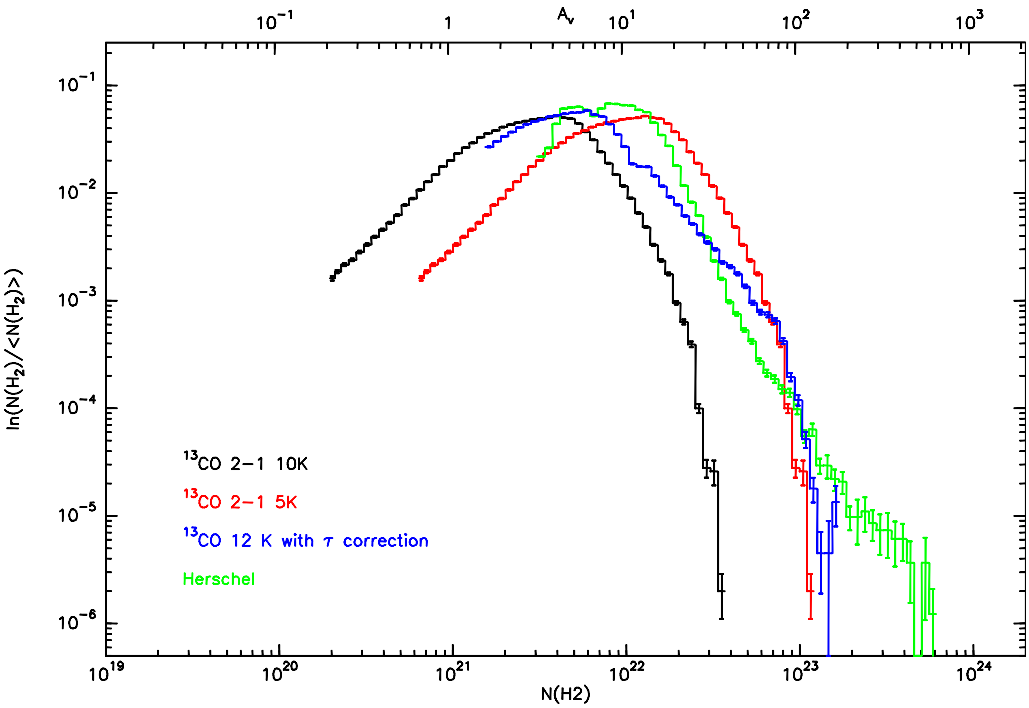

Fig. 5.9: Probability distribution functions of the H_2 column density derived for the whole W43 complex from different data sets and methods. The y-axis is normalized to the mean value of N(H_2). Isothermal CO column densities (5 and 10 K) are plotted in red and black; CO derived values with optical depth correction are in blue, and Herschel *results are in green.*

ences in the slope of the power-law tails. The power-law tail of the *Herschel* PDF is steeper than the CO-PDF. A possible explanation is that the *Herschel* PDF contains atomic hydrogen in addition to molecular hydrogen (which constitutes mainly the CO PDF), which is less 'participating' in the global collapse of the region and individual clump/core collapse. In this case, our method to derive the H_2 column density from ^{13}CO and C^{18}O turns out to be an efficient tool to identify only the collapsing gas that ends up into a proto-star.

5.7 Description of W43-Main and W43-South

Finally, we give a detailed description of the two most important sources in the W43 complex, W43-Main and W43-South. Several other interesting sources are described in Appendix A.

5.7.1 W43-Main, Source 13

Source 13 (see Fig. B.13), or W43-Main, is the largest and most prominent of all sources in the W43 complex. Located in the upper central region of the map with an extent of roughly 30 by 20 pc, it shows a remarkable Z-shape of connected, elongated ridges. The upper part of this cloud extrudes far to the east with a strong emitting filament, where it curves down south in a weaker extension of this filament. This structure is especially clear in ATLASGAL and Hi-GAL dust emission.

There are some details hidden in this cloud that cannot be seen clearly in the complete integrated map. In the velocity range of 80 to 90 km s^{-1}, which are located in the southwest of the source, we see a circular, shell-like structure surrounding an empty bubble (Fig. 5.10 (a)). This bubble is elliptically shaped with dimensions of 10 $\times$ 6 pc, while the molecular shell is about 1.5 pc thick. It is located where a cluster of young OB stars is situated. Possibly, this cavity is formed by the radiation of this cluster. See Motte et al. (2003) for a description of the expansion of clouds at the periphery of this (H II) bubble.

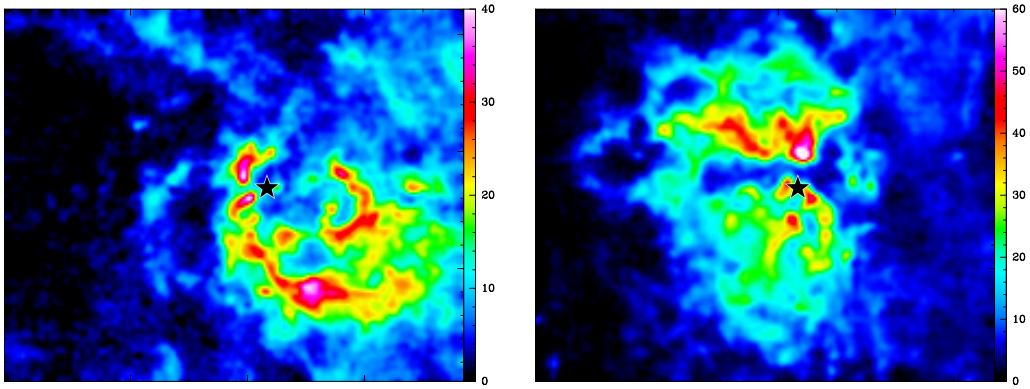

(a) Shell structure. **(b)** Canal structure.

Fig. 5.10: Selected velocity ranges of W43-Main (source 13) in [K km s^{-1}]. The location and size of the figures match those of Fig. 5.11. **(a)** *Shell-like structure in the ^{13}CO map integrated over the channels from 80 to 90 km s^{-1}.* **(b)** *Northern and southern parts of the cloud are separated by an abyss. The black star marks the position of the embedded OB star cluster. The plot is integrated over channels between 94 and 98 km s^{-1}.*

The central Z-shape of this cloud appears to be monolithic on the first sight. However, Fig. 5.10 (b) shows that the northern and southern parts are separated by a gap in the channel maps between 94 and 98 km s^{-1}. Both parts are still connected in channels higher and lower than those velocities. This chasm that we see is narrow in the center of the cloud, where it has a width of 1 to 2 pc, and opens up to both sides. The origin of this structure is the cluster of WR and OB stars situated in the very center that blows the surrounding material out along a plane perpendicular to the line-of-sight. This agrees with the presence of 4 HCO^+ clouds in the range between 81 and 108 km s^{-1} along the line-of-sight of

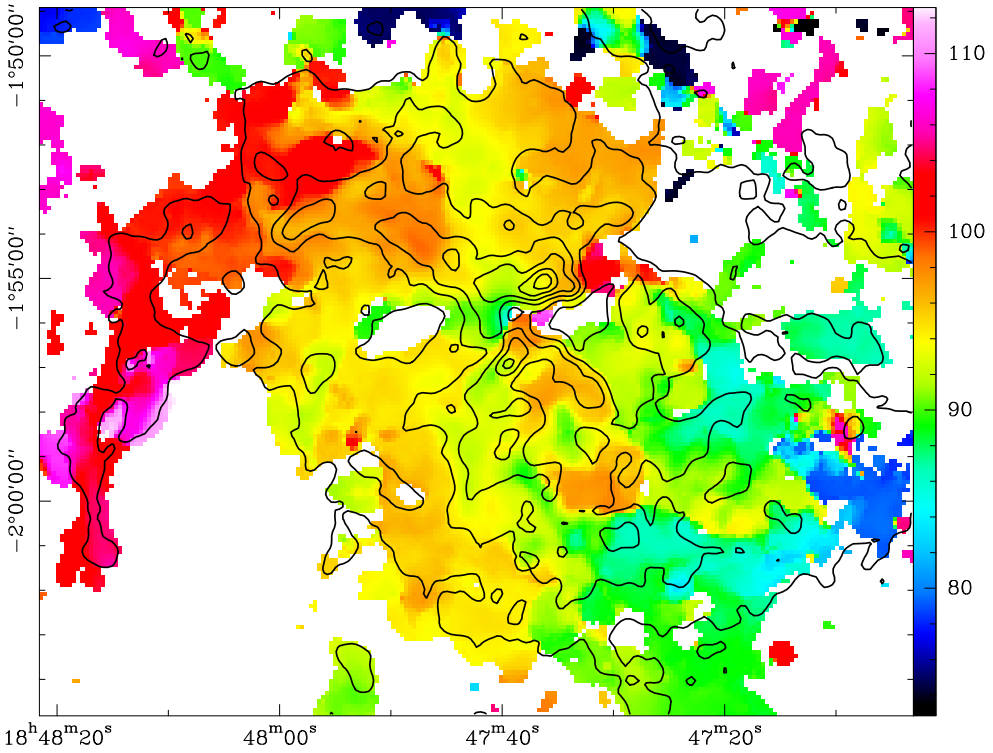

Fig. 5.11: Mean velocity map of W43-Main in [km s^{-1}], derived from the ^{13}CO data cube in colors, contours show ^{13}CO integrated intensities, where levels range from 36 to 162 K km s^{-1} (20 and 90% of peak intensity).

the Wolf-Rayet cluster (Motte et al. 2003).

W43-Main is the most luminous source in our set with integrated ^{13}CO (2–1) emission of up to 170 K km s^{-1} and line peaks of up to 23 K at the peak in the northern filament. Most inner parts of this cloud show integrated intensities of ∼90 to 120 K km s^{-1} and 45 to 60 K km s^{-1} in the outer parts. It is also the most optically thick with an optical depth of ^{13}CO up to 8 in the southern arm, while the bulk of the cloud with 2 to 3 is not exceptionally opaque. It is possible that we overestimated the opacity in the south of this cloud. The spectra show that ^{13}CO is self-absorbed here, while C^{18}O is not. This would lead to an unrealistic ratio of the two isotopologues and an overestimated optical depth.

The cloud shows a velocity gradient across its complete structure (see Fig. 5.11). Beginning at a relative velocity of ~ 80 km s^{-1} at the most southwestern tip (at this position we may see a connection with the foreground components), it winds through the Z-shape and ends in the eastern extension filament at ~ 110 km s^{-1}. The shell-like structure lies at the lower end of the velocity range, between 80 and 90 km s^{-1}. This velocity difference of ~ 30 km s^{-1}, already described in Motte et al. (2003), is huge and the largest discovered in the W43 complex. It could hint at a possible rotation of the cloud. Comparably impressive are the line widths of the central parts of these clouds. We find them to

be up to 15 km s^{-1} especially in the central parts, indicating very turbulent gas or global motions.

In the most luminous parts in the south, we calculate the highest H_2 column densities of about 2×10^{23} cm^{-2}. This is due to the high opacities that have been calculated here. The other central parts of this cloud show H_2 column densities of $5 - 10 \times 10^{22}$ cm^{-2}. Liszt (1995) derived the cloud mass of W43-Main from ^{13}CO (1–0) and find a value of 10^6 M$_\odot$. We find a total mass in this source of $\sim 3 \times 10^5\ M_\odot$ and thus a large fraction of the mass of the complete W43 complex (20%).

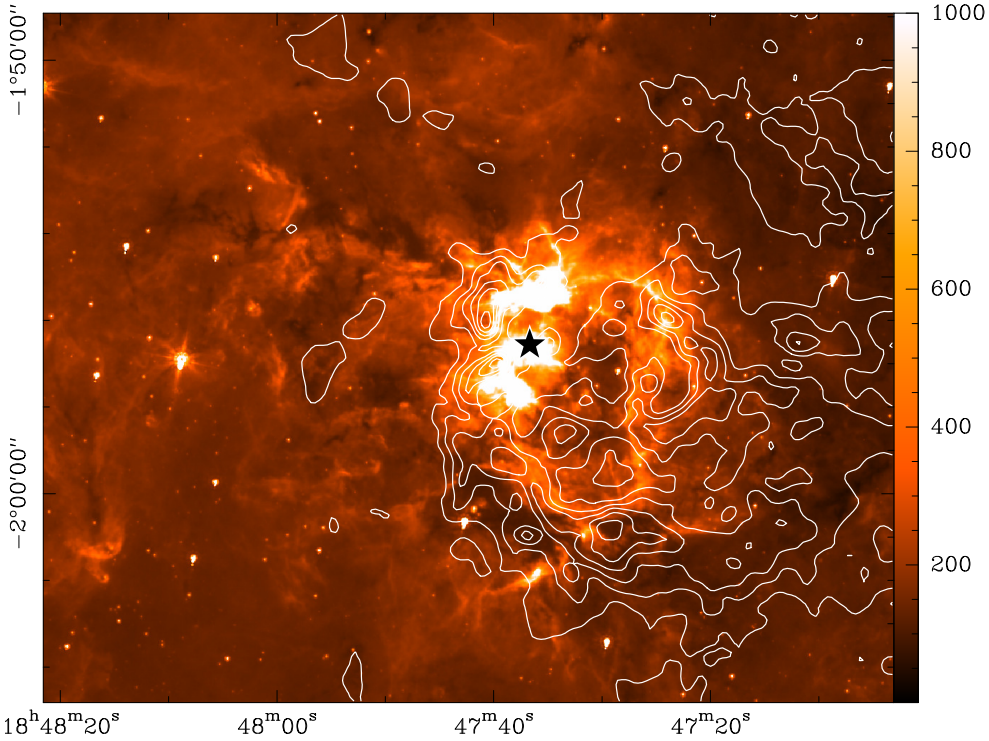

Fig. 5.12: Spitzer GLIMPSE 8 μm map in [MJy sr^{-1}] of the W43-Main cloud with IRAM 30m ^{13}CO (2–1) contours of the shell, seen in Fig. 5.10 (a) (levels ranging from 8 to 37 K km s^{-1}). The black star marks the location of the embedded OB star cluster.

In the GLIMPSE maps at this position we see strong extended IR emission along the walls of a cavity, which are just west of the central Z-shape, formed by a cluster of young OB stars that is located here (see Fig. 5.12). This cluster is probably the first result of the star-formation going on here. The cavity seen in infrared follows clearly the shell-like structure, seen in CO in Fig. 5.10 (a). The CO cavity may be due to the strong radiation of the nearby stars. The northern and southern arm of the Z-shape are seen in absorption in the 8 μm band of GLIMPSE against the infrared background. This indicates dense cold dust and molecular clouds that are shielded from the UV radiation of the stars, which is verified by strong emission of cold dust, as seen in the ATLASGAL and Hi-GAL maps.

5.7.2 W43-South, Source 20

Source 20, also known as W43-South and G029.96–0.02 (see e.g Beltrán et al. 2013), is the second largest source in the W43 complex and dominates the southwestern part of our map. Figure B.20 shows a plot of this source. It has approximately the shape of a tilted ellipse with the dimensions of about 24 $\times$ 31 pc with several smaller clumps scattered across the cloud. These clumps emit strongly in ^{13}CO (2–1) up to 150 K km s^{-1} and are surrounded by less luminous gas, where we see emission between 60 to 90 K km s^{-1} and down to 30 K km s^{-1} in the outer parts of the cloud. Maximum line peaks are 30 K. This source is less optically thick than W43-Main; the opacity is around 2 to 3 for most parts of the cloud and does not exceed 4 in the dense clumps.

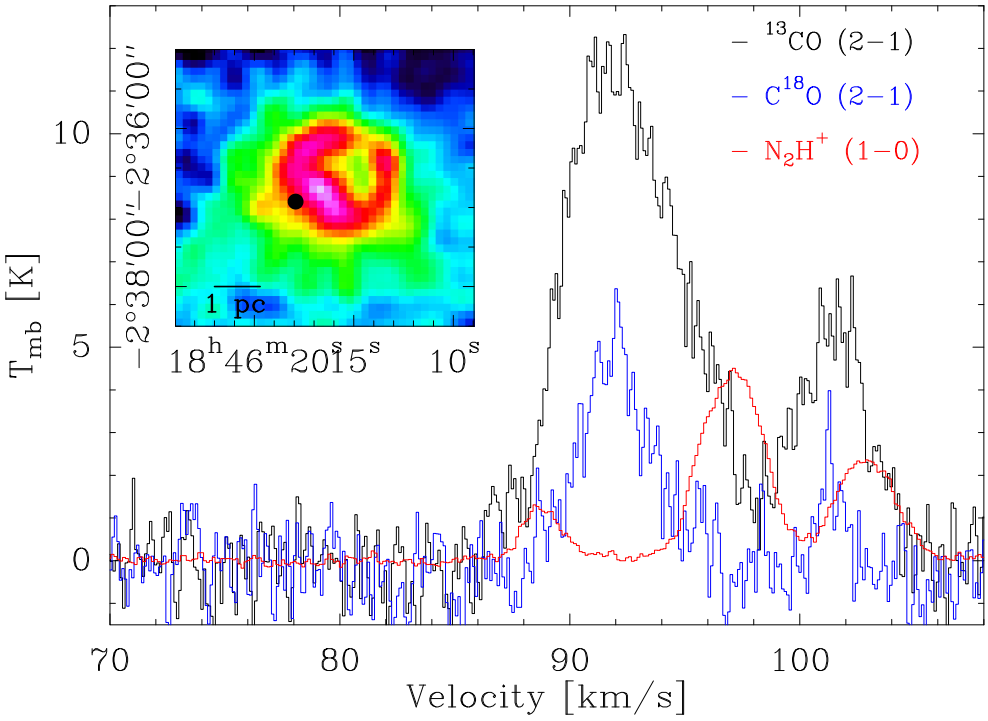

Fig. 5.13: Ring-like structure, as seen in W43-South. Examples of corresponding spectra that show typical infall signatures. The inlay shows the ^{13}CO channel map at 92.7 km s^{-1} in [K]. The black circle marks the position where the spectra were taken and their HPBW.

Studying the details of this source, we see that several of the dense clumps are actually shells of gas. The ringlike structures are clearly recognizable in some channel maps. Figure 5.13 shows the most intriguing example. The spectra across the whole ring show infall signatures as discussed in Walker et al. (1994) in the optically thick ^{13}CO lines. However, C^{18}O, which usually is optically thin shows the same signature as it is still optically thick at this position. In order to confirm this infall (self-absorption) and not two different velocity components, we need to observe more optically thin lines and compare their spectra with the ^{13}CO and C^{18}O spectra. This can be done with the N$_2$H$^+$ (1–0) line, which was

observed with the IRAM 30m during the second part of our project. Although N_2H^+ shows hyperfine structure, we can see that the main set of hyperfine components peaks at the position of the dip in ^{13}CO and $C^{18}O$, confirming these lines are optically thick and trace infall.

This could be interpreted as a bubble of gas, which is heated from the inside by an embedded UV source, although it is not associated with any UCHII region identified by the CORNISH survey (Purcell et al. 2013). The *Spitzer* 8 μm also show a heated ring of dust, which indicates an embedded heating source.

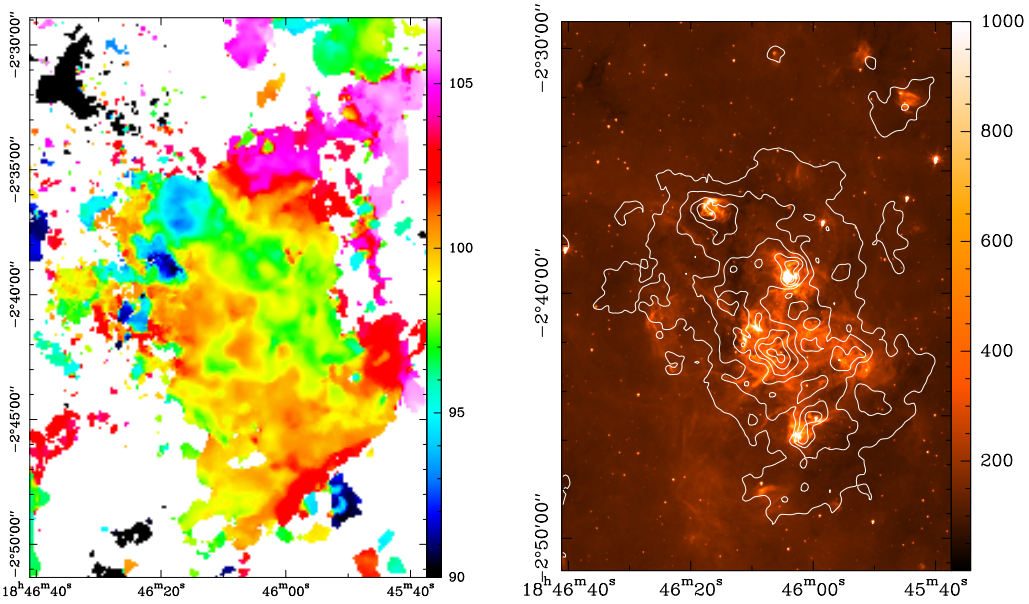

(a) Velocity map. **(b)** GLIMPSE 8 μm map.

Fig. 5.14: Plots of W43-South (source 13). **(a)** *Mean velocity map in [km s^{-1}].* **(b)** *IRAM 30m ^{13}CO (2–1) contours overlaid on GLIMPSE 8 μm map in [MJy sr^{-1}].*

The relative radial velocity of the gas is more or less constant around 100 km s^{-1} across the whole cloud W43-South. Small parts in the east are slower at 95 km s^{-1}, while a tip in the northwest is faster with velocities around 105 km s^{-1} (cf. Fig. 5.14 (a)). However, the velocity gradient is not very pronounced. full width at half maximum (FWHM) line widths show typical values of 5 to 10 km s^{-1} with broad lines that are found mostly in the eastern part of the cloud. The bright clumps do not show distinct broad lines.

The calculated H_2 column density is on the order of a few times of 10^{22} cm^{-2} for most of the cloud, but parts in the northwest and the center peak at about 1.5×10^{23} cm^{-2}. The total mass of this cloud is $\sim 2 \times 10^5\ M_\odot$, and it is thus the second most massive source in the W43 complex.

All bright clumps, except for the one in the central north, are seen in bright emission in the GLIMPSE 8 μm map in Fig. 5.14 (b). They are obviously heated from the inside; no external UV sources can be identified. Apparently, YSOs

have formed in the dense but separated clumps that are seen in CO emission and in dust emission. In the northeast of the cloud, one slab of cold gas is seen in absorption in the GLIMPSE map, separating some of the bright clumps.

Chapter 6

Detailed observations of a filament in W43

In this chapter we pick one of the clouds observed with the IRAM 30m telescope (see description in Chapter 3) and investigate it in more detail. We picked source 28 (see Appendix A.4 for a short description) as it is a clearly defined filament with embedded clumps and a velocity gradient along it. Additional observations with several telescopes have been carried out. All projects explained in this and the next chapter are led by the author of this work, in contrast to the W43 HERO project, which is led by Frédérique Motte and Peter Schilke. This analysis is currently in preparation and is to be submitted soon.

Figure 6.1 shows the integrated intensity map of the W43 complex in ^{13}CO (2–1). See Chapter 3 for a description of the observations and Chapter 4 and 5 for its detailed analysis (see also Carlhoff et al. 2013). This picture also indicates the location of the filament of interest by a black box. The map is integrated over the range of $78-130$ km s^{-1} which only includes the W43 complex itself and omits the fore- and background sources. With the integration over such a large range of velocities, smaller structures that cover a narrow frequency range become almost invisible. A zoom on our source is shown in Fig. 6.2, which is integrated over the spectral range $110-115$ km s^{-1}. Here, the filament becomes clearly visible.

6.1 *Herschel* [C II] observations

Our first additional project was named “Galactic Origins of Star Formation in the W43 Complex” and aimed at observing the [C II] line in our target filament.

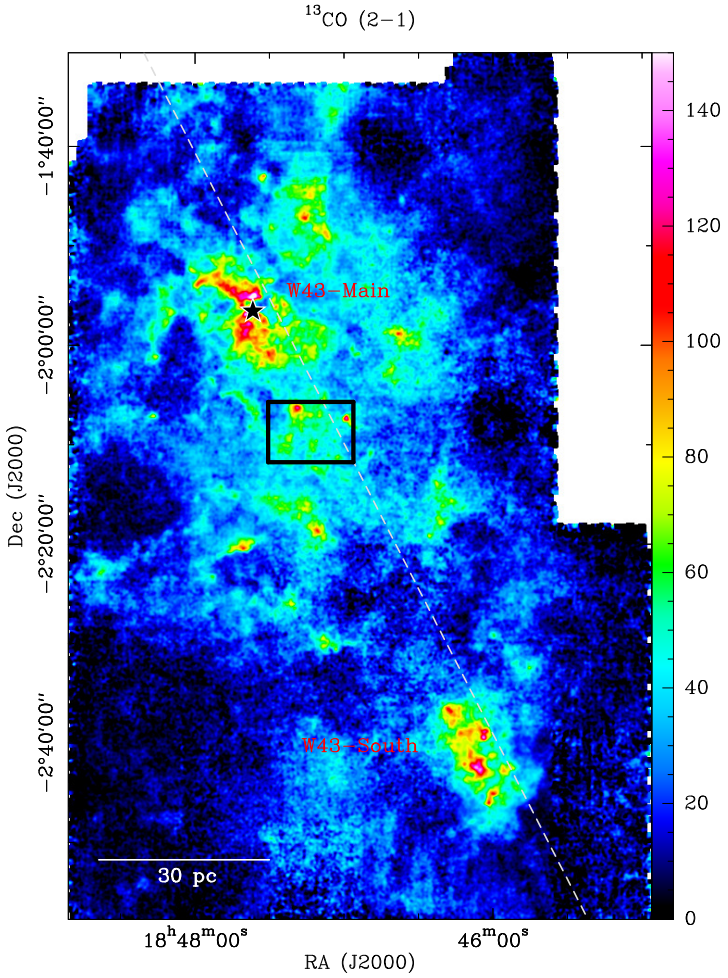

Fig. 6.1: IRAM 30m ^{13}CO (2–1) intensity map of the W43 complex in [K km s^{-1}], integrated over the spectral range of 78 – 130 km s^{-1}. The dashed line denotes the Galactic plane, while the star in W43-Main marks the central OB star cluster. The cloud discussed here is indicated by the black box. Its shape is not visible due to line-of-sight confusion.

6.1.1 The *Herschel* Space Observatory

This dataset was observed with the Heterodyne Instrument for the Far Infrared (HIFI) (de Graauw et al. 2010) receiver on board of the HSO[1] (Pilbratt et al. 2010). See Fig. 6.3 for a picture of *Herschel* in the construction lab.

Herschel was launched in May 2009 and was operated by ESA until March 2013, when it ran out of cooling helium. It carried a 3.5 m silicon carbide main dish which was cooled to 85 K by the 2400 l of helium *Herschel* had on board. Built for observations in the far-infrared and sub-millimeter, *Herschel* covered a spectral range of 55-671 μm.

[1] *Herschel* is an ESA space observatory with science instruments provided by European-led Principal Investigator consortia and with important participation from NASA.

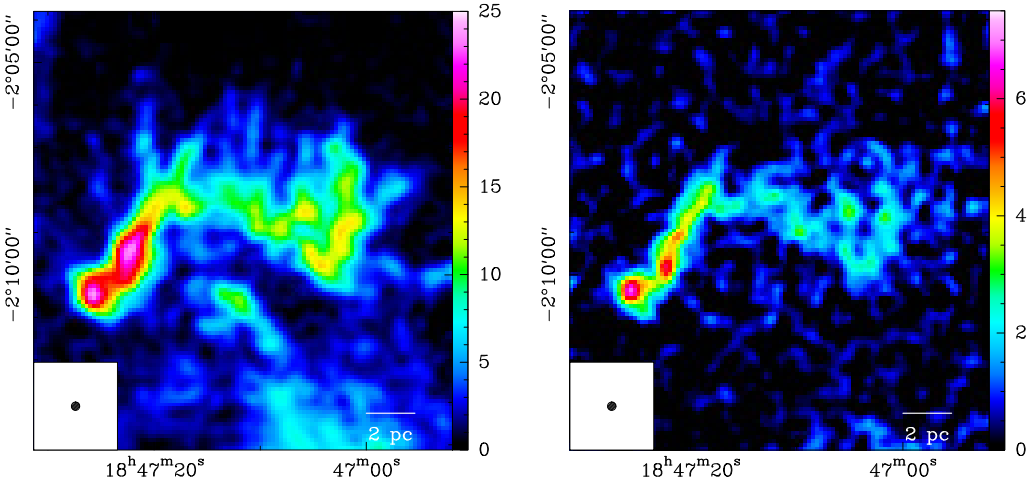

(a) ^{13}CO (2–1). **(b)** C^{18}O (2–1).

Fig. 6.2: IRAM 30m ^{13}CO (2–1) and C^{18}O (2–1) intensity maps of the filament in W43 in [K km s^{-1}], integrated over the spectral range of 110 – 115 km s^{-1}. The beam size of 11.7″ is indicated in the lower left corner, the spatial size in pc in the lower right corner.

The telescope was equipped with three scientific instruments. The PACS (Poglitsch et al. 2010) and SPIRE (Griffin et al. 2010) instruments are two direct detection cameras with medium spectral resolution and are typically used for efficient large scale mapping. The covered spectral range of PACS is 60–210 μm, that of SPIRE is 194–671 μm. One key-project that uses these two cameras is the Hi-GAL project (Molinari et al. 2010), which we shortly describe in Sect. 5.5.4. The third instrument is HIFI (de Graauw et al. 2010), which we used for our project.

6.1.2 The HIFI instrument

HIFI is a single pixel heterodyne receiver with a very high spectral resolution. It covers the spectral range from 480 to 1910 GHz (157–625 μm) with a gap from 1250 to 1410 GHz (212–240 μm). HIFI is a combination of seven single mixers (five SIS and two HEB mixers) each with two mixer sub-assemblies and a diplexer assembly. In our case we used band 7b, one of the HEB mixers.

There are two backends that can be used with HIFI. The first is the High Resolution Autocorrelation Spectrometer (HRS), a pair of auto-correlator spectrometers, which deliver a very high spectral resolution of down to 0.125 MHz but only a limit bandwidth. As we did not need such a high resolution, we used the Wideband Spectrometer (WBS) backend (Schieder et al. 2000), a pair of AOSs. It has a spectral resolution of 1.1 MHz (that leads to a pixel width of 0.54 MHz) and a bandwidth of 4 GHz, which is sufficient for our observations.

Fig. 6.3: Photo of the Herschel *Space Observatory in the lab. Credits: European Space Agency (ESA).*

6.1.3 The [C II] emission line

The emission line used in this project is that in the ground state of ionized carbon. As mentioned in Sect. 2.2.5, this ground state splits up into two states, due to fine structure coupling of electron spins and orbital angular momentum. This transition $^2P_{3/2} \rightarrow {}^2P_{1/2}$ is what we mean, when we just use the term [C II] line.

6.1.4 Telescope setup

We used HIFI's band 7b to observe the ionized carbon line at 1900.5369 GHz in the upper side band. The WBS was used as backend with a spectral resolution of 0.5 MHz which translates to a velocity resolution of 0.08 km s^{-1}, i.e. better than the CO observations. The total bandwidth would cover more than 600 km s^{-1}, far more than needed.

A total of 10 h was granted for the observations which were prepared with the *Herschel* Observation planning tool (HSpot). Two orthogonal, Nyquist-sampled OTF-maps on our filament, shown in Fig. 6.2, were conducted in April 2012 (OBSIDs 1342244581 and 1342244582). The size of the observed section was $8.5' \times 5.5'$ (RA $\times$ Dec). As our source lies in the Galactic plane, no nearby emission-free position could be found which could be used as OFF-position. Therefore, we used an OFF-position (OBSID 1342231452) with emission (at position 18:48:28.87 -2:1614.6 EQ J2000) which was then calibrated against a clean position further outside the Galactic plane (position 18:44:07.70 -01:55:10.9). We could then subtract the emission in the OFF-position. The secondary OFF-position is the same position that was used as OFF for the IRAM project. It can thus not be displayed in the overview map in Fig. 6.1.

6.1.5 Data reduction

The data was then calibrated with the standard pipeline in the *Herschel* Interactive Processing Environment (HIPE)[2] software version 10.0 (Ott 2011). Standing-wave removal and baseline subtraction was applied using the task `FitHifiFringe`. The temperature scale was converted to main-beam temperature $T_{\rm mb}$ to be consistent with the other datasets, using a main-beam efficiency of 0.694. For extended sources like ours, both antenna temperature and main-beam temperature do not exactly represent the real temperature but a lower and upper boundary (see Ossenkopf et al. 2013).

Finally, the spectra were gridded and combined in a data cube, using the GILDAS package[3]. The HPBW of 11.4″ fits well with the already existing IRAM 30m data that has a beam size of 11.7″.

6.1.6 Resulting map

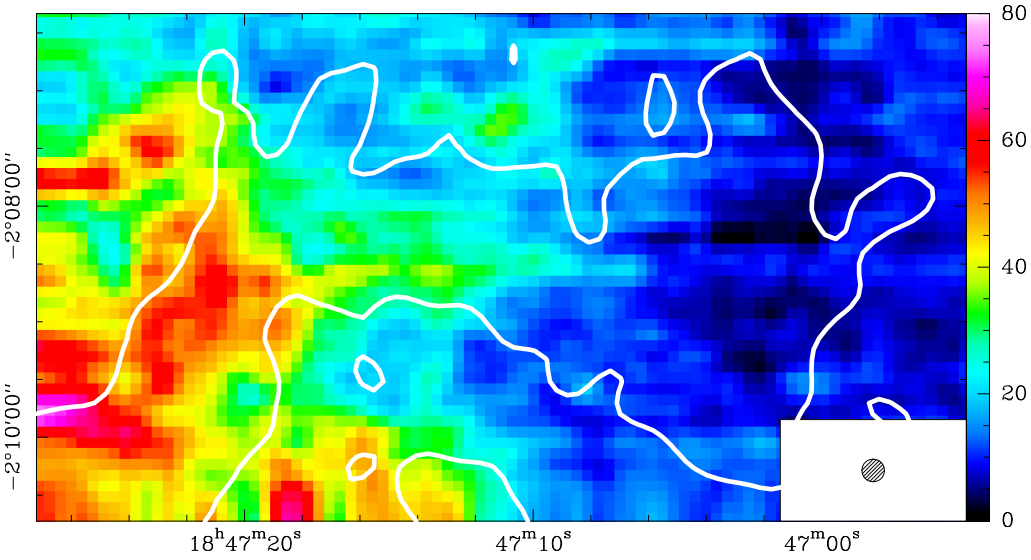

Fig. 6.4: Complete HIFI [C II] intensity map in [K km s^{-1}], integrated over the spectral range of 106 – 122 km s^{-1}. The left branch of the filament is clearly seen in emission, while the right branch does not show any emission. The white contour denotes the position of the filament in ^{13}CO (2–1) emssion.

The complete resulting map of our HIFI observations is plotted in Fig. 6.4. It has been integrated over the velocity range 106 to 122 km s^{-1}, i.e. only the velocity of the filament and has a noise rms level of 2.5 K km s^{-1}. The noise of

[2]This software is provided by ESA and can be downloaded at `http://herschel.esac.esa.int/HIPE_download.shtml`

[3]This software is developed and maintained by IRAM. `http://www.iram.fr/IRAMFR/GILDAS`

the spectra lies between 0.5 and 1 K. The map integrated over the full range is not shown here, as it is not relevant to our studies.

The size and position of the map was chosen to cover the whole filament including the diffuse emission on the right side as seen in Fig. 6.2. Unfortunately it turned out that no emission is seen in the right half of the map, the position of the diffuse filament branch. On the other side of the map emission turned out to be much more extended than the ^{13}CO emission. Therefore, a part of the C^+ emission in the lower left corner of the map is cut off. With hindsight, it would have been better to position the map more to the lower left. Possibly, the map could be completed in the future, using SOFIA.

There is a second source included in our dataset that has been identified from the IRAM 30m data cube. Source 5 (cp. Fig. B.5 in Appendix B) is one of the background sources at 12 kpc distance from the Sun in the Perseus spiral arm (see Sect. 4.4). Its [C II] emission has not been analyzed yet.

The resulting dataset will be discussed in more detail in Sect. 7.1.1.

6.2 APEX CO observations

Fig. 6.5: Photo of the APEX telescope in the Atacama desert in Chile. Credits: ESO.

6.2.1 The APEX telescope

We observed this dataset with APEX[4] (Güsten et al. 2006), a 12 m sub-millimeter telescope located at the Llano de Chajnantor in the Chilean Atacama

[4]APEX is a collaboration between the Max-Planck-Institut für Radioastronomie (MPIfR), the ESO, and the Onsala Space Observatory (OSO).

desert (see Fig, 6.5) at an altitude of 5105 m.

CHAMP$^+$ (Kasemann et al. 2006) is a 7-pixel receiver with two spectral bands which can be operated simultaneously. The lower band runs from 620 to 720 GHz, the higher band from 780 to 950 GHz of which a bandwidth of 4 GHz can be covered during observations. Typical receiver noise temperatures of the lower band array lie at very low 150 K.

6.2.2 Telescope setup

The CO (6–5) line at 691.473076 GHz was observed with the CHAMP$^+$ receiver set to a resolution of $\sim$0.37 MHz, which corresponds to 0.16 km s^{-1}. Several Nyquist-sampled OTF-maps with a size of $2' \times 1.25'$ were taken that covered the whole filament (cf. Fig. 6.2). The HPBW at this frequency is 9.1″ and thus a bit smaller than that of the *Herschel* and IRAM 30m data.

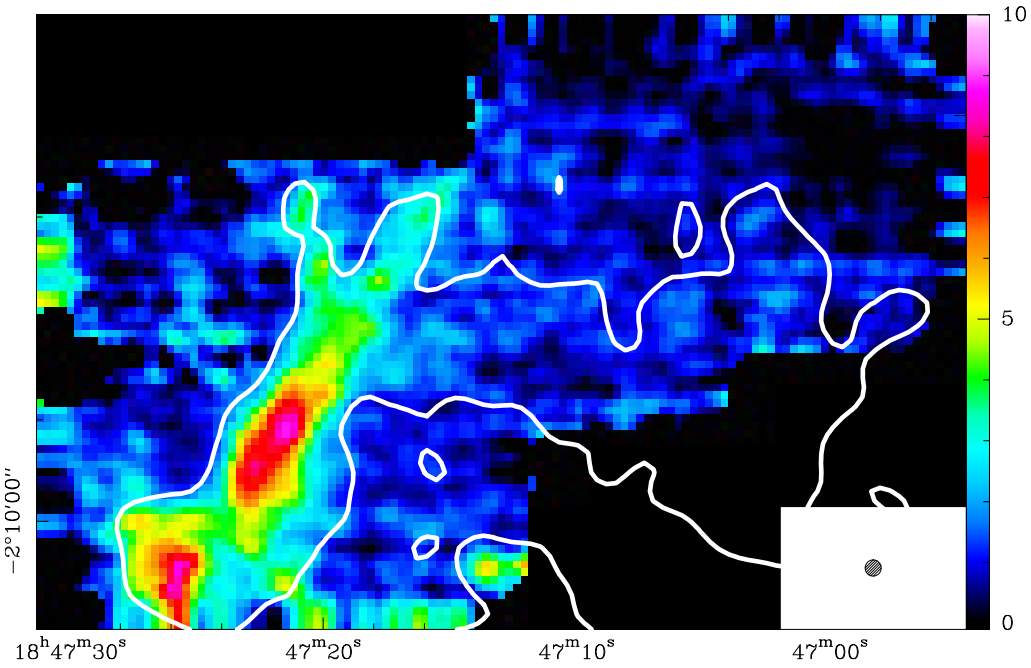

Fig. 6.6: Complete APEX CO (6–5) intensity map in [K km s^{-1}], integrated over the spectral range of 110 – 116 km s^{-1}. The left branch of the filament is clearly seen in emission. The horizontal branch on the right does not show any emission. The position of the filament in ^{13}CO emission is indicated by the white contour line, while the beam size is depicted in the lower right corner.

6.2.3 Data reduction

The resulting calibrated spectra were then reduced with the GILDAS software. After baseline subtraction and gridding we created a data cube that covers the

filament and spans the velocity range from 50 to 130 km s^{-1}.

6.2.4 Resulting map

The final map of our APEX CO (6–5) observations is shown in Fig. 6.6. It was integrated over the velocities 110 – 116 km s^{-1} to cover our filament. There are two other dense clumps included in the data cube that are not related to the filament, so they are not shown here.

We can clearly see that emission is only found in the left part of the map. The maximum integrated intensity is 8.9 K km s^{-1} and the rms level of this map is 0.4 K km s^{-1}. The typical noise of the spectra is at the order of 0.5 K. A more detailed description of the data is given in Sect. 7.1.2.

6.3 CARMA high-density tracers observations

Fig. 6.7: Photo of the CARMA interferometer at Cedar Flat, California. Credits: Jens Kauffmann, Caltech.

6.3.1 The CARMA interferometer

In September 2011 observations of the source were conducted with the CARMA[5] interferometer (Woody et al. 2004), located at Cedar Flat near Owen's Valley in California, USA (see Fig. 6.7) at an altitude of 2200 m. It consists of 23 antennas, six with a diameter of 10.4 m (former Owens Valley Radio Observatory (OVRO) millimeter array), nine with a 6.1 m diameter (former Berkeley

[5]CARMA's development and operations are funded by the National Science Foundation (NSF) and its partner universities (California Institute of Technology, University of California, University of Chicago, University of Illinois and University of Maryland).

Illinois Maryland Association (BIMA) array), and eight 3.5 m antennas (Sunyaev–Zel'dovich Array (SZA)). Originally, the 10 m and 6 m antennas were merged to formed one interferometer, which was separated from the 3.5 m array. The 10/6 m array worked at wavelengths of 1 and 3 mm, the 3.5 m array at wavelengths of 3 mm and 1 cm. From mid-2011 on, it was possible to use all 23 antennas, combined in the so-called CARMA-23 mode, which operates at 3 mm wavelength.

CARMA can be operated in different configurations, certain spatial distributions of the single antennas, that change on a regular basis. Baselines between telescopes, that define points in the uv-plane of the wavefront during observations, vary between 4 m and 2 km. CARMA-23 mode now uses all available antennas, which increases the total amount of baselines to 253. Thus, more points of the uv-plane can be covered at one time, increasing the final quality of the images. The increase of the collecting area from CARMA to CARMA-23 mode lies at only 10% and is therefore not that significant.

6.3.2 Description of the observed lines

We used three different species for this project, HCO^+, HCN, and N_2H^+. All three species are linear molecules that consist of three atoms. As discussed in Sect. 2.2.4, linear molecules have equidistant rotational lines whose frequency depend on the upper total angular momentum J. In this project we only observed the lowest rotational transition (J=1$\rightarrow$0) or abbreviated to (1–0).

In Sect. 2.2.5 we discuss the effect of fine- and hyperfine structure. A fine structure splitting, caused by interaction of the electron angular momentum with the nuclear spin, is observed in the lines of HCN and N_2H^+. The HCN line is split in three levels (Gonzalez-Alfonso and Cernicharo 1993), while the N_2H^+ lines are even split in seven levels (Caselli et al. 1995). These different levels are very close by and can lead to confusion in regions of complex velocity structures, as effects from hyperfine components and velocity components cannot be distinguished anymore.

Luckily, we know the velocity structure of our source from the CO observations and we assume that this structure does not change much from one molecular line to the other. This is also an important issue when creating total integrated emission maps or moment maps, as the velocity limits for these maps have to be defined, carefully. The lines in our filament are quite narrow (1-2 km s^{-1}) and it is therefore possible to create integrated maps and moment maps by only using the most intense component. For HCN this is ($J\,F = 1\,2 \rightarrow 0\,1$) and for N_2H^+ it is the ($J\,F_1\,F = 1\,2\,3 \rightarrow 0\,1\,2$) component, where F and F_1 are the total angular momentum of the outer and central nitrogen nucleus, respectively.

6.3.3 Telescope setup

We observed the left, bright branch of the filament, shown in Fig. 6.2 in CARMA-23 mode. We spent a total of 16 h on this part of the filament, as it was the most promising part. Covering the full source would have taken too long. We used the 3 mm band to receive the lines HCO^+ (1–0) at 89.1885247 GHz, HCN (1–0) at 88.6316022 GHz, and N_2H^+ (1–0) at 93.1733922 GHz.

During our observation run CARMA was positioned in C-configuration, a medium-wide configuration with baselines between 30 and 350 m. The additional 3.5 m array provided short baselines between 4 and 12 m. These short baselines help to improve the data quality on larger scales.

The correlator was set up to observe the three lines simultaneously with a bandwidth of 62 MHz each and a continuum band with a bandwidth of 500 MHz. In CARMA-23 mode this gives a velocity resolution of 1.1 $\mathrm{km\,s^{-1}}$ for the three line windows. Since the primary beam of the 10 m telescopes is $\sim 70''$ at 3 mm, not the whole source could be covered with one pointing. A mosaic consisting of 21 separate pointings, separated by half beam widths, was defined so that the source would be covered in a way that provides uniform noise level across it. The synthesized beam has a size of $6.2'' \times 6.1''$, which is nearly a factor of 2 better than the resolution of our ^{13}CO (2–1) data.

6.3.4 Data reduction

The resulting raw data was then calibrated with the Multichannel Image Reconstruction, Image Analysis and Display (MIRIAD)[6] software package (Sault et al. 1995). We used a standard calibration pipeline, written by John Carpenter at Caltech. After flagging of bad data (bad antennas, shadowed antennas, high elevation data, and individual bad scans) a series of calibration steps was conducted, where the three lines and the continuum were processed separately.

Line calibration estimates phase drifts in the instruments, caused by changes of the baselines. Bandpass calibration is used to ensure uniform telescope response over the complete spectral band. Deviations can be caused by the atmosphere or technical signal delays in the receiver. We used the quasar 3c454.3 for bandpass calibration, as quasars usually show no spectral features and are bright point sources (phase is zero). Therefore, any unusual behavior of the bandpass can be identified with high precision. The next step is the flux calibration, which sets the absolute intensity scale by observing a sources of known intensity, e.g. a planet (in our case Uranus). This is needed, because the flux of quasars can change and has to be calibrated against another source. Finally, gain calibration accounts for variations of amplitude and phase over time. Here

[6] http://www.atnf.csiro.au/computing/software/miriad

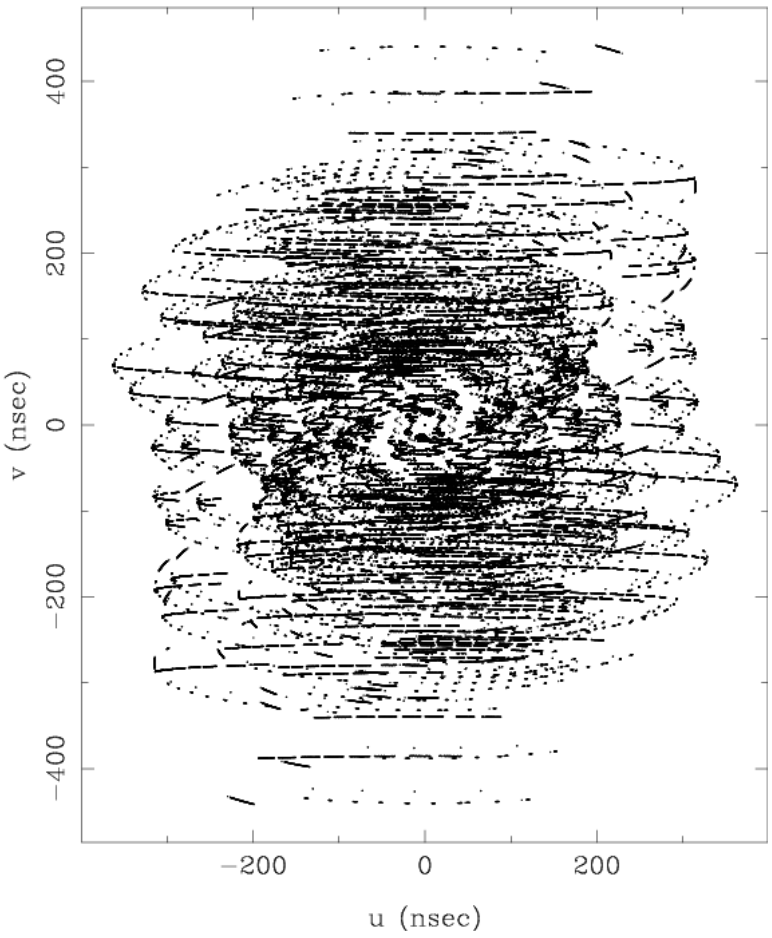

Fig. 6.8: Sample CARMA uv-coverage of one track.

we used again a quasar, 1751+096. For details of the technical part of the calibration, consult the CARMA MIRIAD documentation[7].

These steps create readily calibrated spectra in uv-space, spectra of single pairs of two antennas. These spectra are not yet in an intuitively understandable map form. To create the final map, a conversion from Fourier space to position space is necessary. This process is called "imaging" and was also done with the MIRIAD software. The challenge at this point is that the uv-plane is only partially sampled (a sample plot of the uv-coverage is presented in Fig. 6.8), i.e. we are missing information. Therefore, the transformed position space map is inaccurate to some degree ("dirty map"). A deconvolution process (MIRIAD task `mossdi`) is used to create "clean map" which displays a more realistic intensity distribution. See Sect. 2.2.3 for some of the technical backgrounds of interferometry.

[7] http://bima.astro.umd.edu/miriad/

6.3.5 Resulting maps

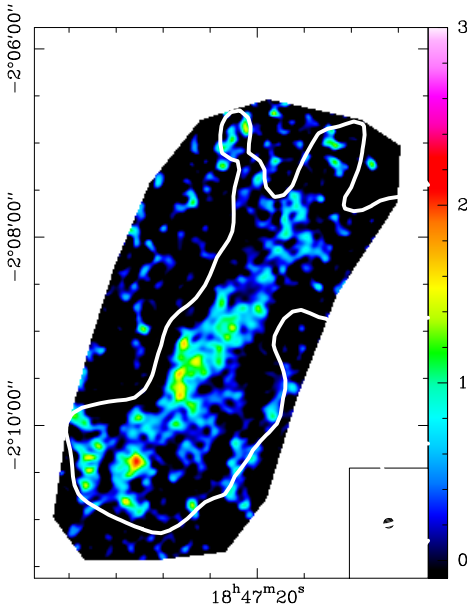

(a) HCN (1–0).

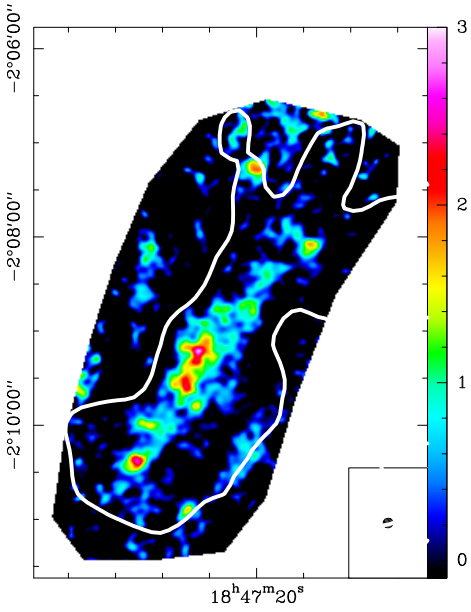

(b) HCO^+ (1–0).

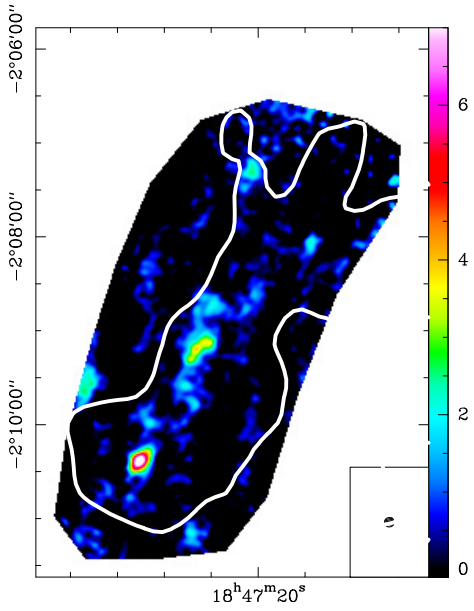

(c) N_2H^+ (1–0).

Fig. 6.9: Integrated intensity maps of the three CARMA high-density tracers in [K km s^{-1}]. The respective beam size is plotted in the lower right corner of the maps. The position of the filament in ^{13}CO is indicated by the white contour line.

The resulting integrated cleaned maps of the CARMA observations can be seen in Fig. 6.9. The maps have been integrated over the velocity range of the filament (110 to 116 km s^{-1}). Only the central region with uniform noise level

is shown here, as the outer parts of the map show strong side-lobe emission, artifacts from the spatial setup of the interferometer which leaves some parts of the UV-plane uncovered. Also, only the inner parts of the maps are covered by several pointings, which results in an increasing noise toward the edge of the maps. The noise rms level of the spectra in these central parts of the maps is $\sim$0.1 K. The analysis of the dataset and its velocity structure is provided in Sect. 7.1.3.

6.3.6 Observations of a second filament

During the CARMA observations we had the chance to observe a second filament in the same three emission lines. The target is source 25 (see description in Appendix A.2 and plots in Fig. B.25 in Appendix B). However, no additional data is available for this cloud. Single strips of C^+ observations across and along the filament were applied for with SOFIA. Unfortunately, the proposal was not successful. Therefore, we did not analyze these datasets, yet, and they are not presented here.

6.4 NANTEN2 [C I] observations

Fig. 6.10: Photo of the NANTEN2 telescope. Credits: Robert Simon.

6.4.1 The NANTEN2 telescope

We used the 4 m NANTEN2[8] telescope (Kawamura et al. 2005) to observe the atomic carbon emission of our source. NANTEN2 is located on Pampa la Bola

[8]NANTEN2 is operated in collaboration between research institutes in Japan (Nagoya and Osaka University), South Korea (Seoul National University), Germany (KOSMA, Universität zu Köln, Argelander-Institut Universität Bonn), Switzerland (ETH Zürich), University of New South Wales (UNSW), and Chile (Universidad de Chile).

in the Atacama desert in Chile, at an altitude of 4900 m. Figure 6.10 shows a photo of the telescope inside its dome.

NANTEN2's Sub-Mm Array Receiver for Two frequencies (SMART) receiver (Graf et al. 2008) is an 8-pixel (2×4 pixel array) heterodyne receiver which operates at two bands, 490 and 810 GHz.

6.4.2 The [C I] emission line

The electronic setup of C I and the fine structure lines of the ground state discussed in Sect. 2.2.5. There are two possible ground state transitions:$^3P_2 \rightarrow {}^3P_1$ and ${}^3P_1 \rightarrow {}^3P_0$ which we will denote (2–1) and (1–0) from here on. In this project we observe the lower of the two transitions.

6.4.3 Telescope setup

We used the lower band to observe [C I] (1–0) at 492.160651 GHz. At this wavelength the telescope beam has a size of 37″. It is therefore more than three times larger than the HPBW of our IRAM 30m observations. We have to remember during our analysis that small scale structures that may be seen in the other maps, cannot be distinguished here. Additionally, the maximum intensities may be smaller compared to a map of higher resolution, due to averaging over a larger area.

The observations were conducted in OTF-mode, where the array covers an area of 340″ × 170″ in steps of 8″. This is the standard sampling, used to ensure Nyquist-sampling for the 810 GHz band. This band was observed, too, but did not yield usable data. The 490 GHz data is thus strongly oversampled. We used two footprints to cover our source, observing them in two orthogonal scanning modes and two orientations of the array to reduce scanning effects in the resulting dataset. The spectral resolution of our data is ∼0.6 km s^{-1} (1 MHz), the bandwidth is 1 GHz. Typical receiver noise channels are between 100 and 200 K in the relevant center of the band.

6.4.4 Data reduction

Data reduction was carried out with CLASS, part of the GILDAS software. The general data quality was quite poor. Many spectra suffered from excessive noise and/or standing waves. About half of the spectra had to be rejected, the rest had to be processed by sine-wave removal. Several known wavelengths were fitted to the data and removed if the resulting baseline had an improved rms.

Additionally, a polynomial baseline of order 9 was subtracted from the spectra to remove large scale perturbations. Only a small section of the spectra is

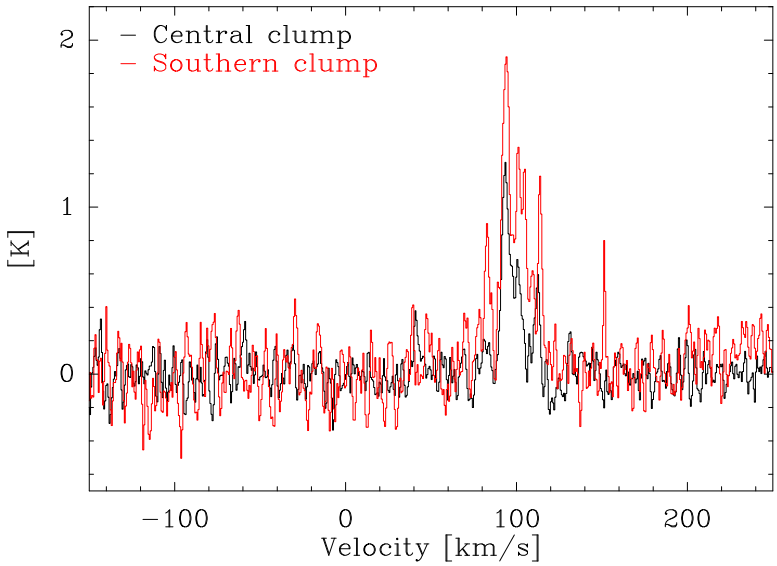

Fig. 6.11: Example spectra of [C I] at the central and southern peak of the ^{13}CO (2–1) emission.

interesting to us anyway, so the baseline has only to be correct in that part. The processed spectra were then combined and gridded to a data cube. In Fig. 6.11 we show the spectrum at the position of the ^{13}CO (2–1) peak over a large velocity range to proof the successful baseline subtraction.

6.4.5 Resulting map

Figure 6.12 shows the final integrated map in [C I] (1–0) with a size of $5.5' \times 5.5'$. It has been integrated over the velocity range 110 to 116 km s^{-1}. In contrast to the [C II] and CO (6–5) data this line shows emission along both branches of the filament as seen in ^{13}CO, although the structure is not the same. The typical noise level of the spectra is on the order of 0.1 K. For the in-depth analysis see Sect. 7.1.4.

As mentioned before, the beam size of [C I] is about three times larger than that of ^{13}CO and [C II]. We thus plot all three maps in Fig. 6.12, where ^{13}CO and [C II] have been regridded and convolved to match the [C I] observation. Thus, the small scale structure of these observations is lost, which becomes especially clear in the [C II] map. We have to assume that sub-beam structure also exists in the [C I] emission, but is averaged out due to the large beam. Still, the general distribution of all three lines can still be recognized, roughly.

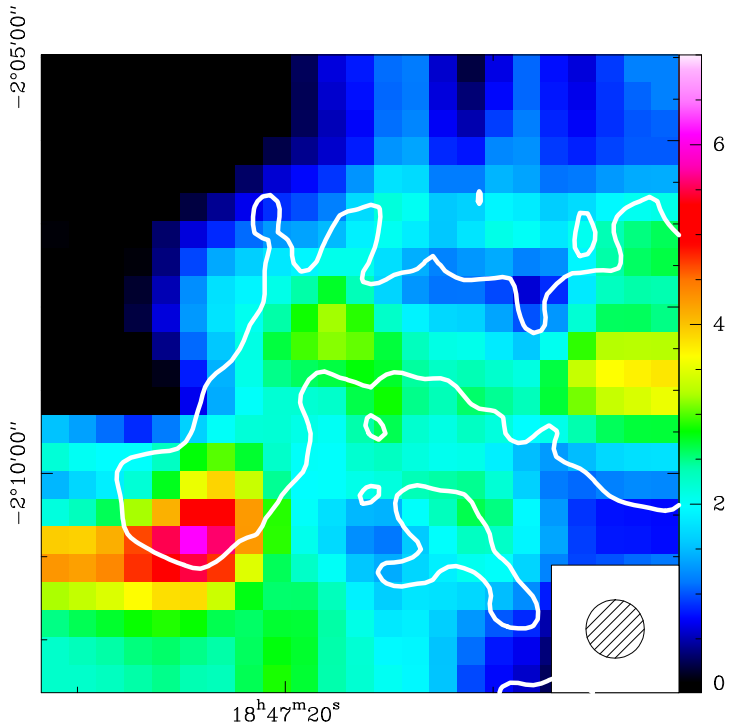

(a) Complete NANTEN2 [C I] (1–0) integrated intensity map.

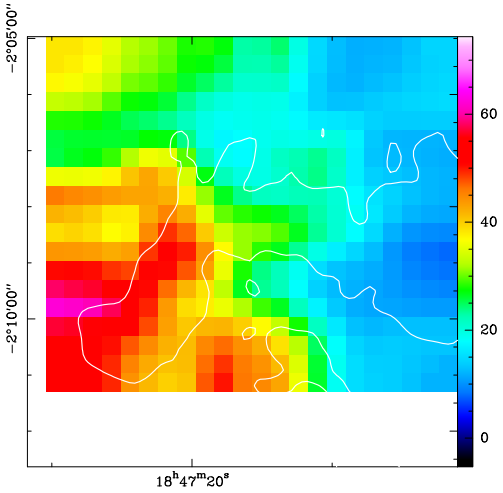

(b) Regridded HIFI [C II] integrated map.

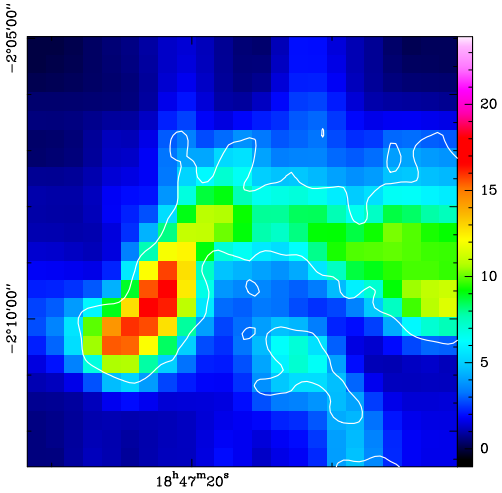

(c) Regridded IRAM ^{13}CO integrated map.

Fig. 6.12: **(a)** *NANTEN2 [C I] (1–0) intensity map, integrated over the spectral range of 110 − 116 km s^{-1}. The southern and northern clump of the left branch are visible. The position of the filament in ^{13}CO emission is indicated by the white contour line.* **(b)** *IRAM 30m ^{13}CO (2–1) and* **(c)** *HIFI [C II] maps, regridded to the NANTEN2 [C I] map and convolved with a 37″ beam. All maps in units of [K km s^{-1}].*

6.5 SMA CO observations

In addittion, we applied for observations of the ^{13}CO and C^{18}O (2–1) lines with the Submillimeter Array (SMA). This project was intended to improve the IRAM 30m data by increasing the spatial resolution of the maps. The proposal was accepted and the observations were conducted in June 2011. Unfortunately, the data was not of good quality and our calibration attempts failed. We will not go into detail here about the calibration steps that were tried.

6.6 Overview

(1) Telescope	(2) Line	(3) Frequency	(4) HPBW	(5) Channel width	(6) $\Delta T_{\rm rms}$
		[GHz]	[″]	[km s^{-1}]	[K]
IRAM 30m	^{13}CO (2–1)	220.4	11.7	0.16	1.0
	C^{18}O (2–1)	219.6	11.7	0.16	1.2
Herschel	C$^+$	1900.5	11.4	0.08	0.8
APEX	CO (6–5)	691.5	9.1	0.16	0.5
CARMA	HCN (1–0)	88.6	6.2×6.1	1.1	0.1
	HCO$^+$ (1–0)	89.2	6.2×6.1	1.1	0.1
	N_2H^+ (1–0)	93.2	6.2×6.1	1.1	0.1
NANTEN2	C I (1–0)	492.2	37.1	0.6	0.1

Table 6.1: Some technical details of the observations of the W43 filament.

An overview of some technical details of all observations are given in Table 6.1. It points out that IRAM 30m, *Herschel*, and APEX observations are comparable in HPBW and in velocity resolution. CARMA data is of high spatial resolution but has wide velocity channels and NANTEN2 observations are of less resolution, both spectrally and spatially.

Chapter 7

Analysis of a filament in W43

We will now give a detailed description of the single datasets and the properties of the different phases of the filament (see again Fig. 6.1 for its position in the W43 complex). We will then combine the information extracted from these datasets by comparing them with each other. Thus, we will be able to give a complete overview of the filament.

In the following we will first discuss the different observations in comparison to the ^{13}CO (2–1) reference data. See again Appendix A.4 for a description of the IRAM 30m data and the derived properties. Plots of all relevant characteristics of this cloud can be found in Fig. B.28 in Appendix B. Most overlay plots in this chapter will show contours of the IRAM 30m ^{13}CO (2–1) integrated emission map overlaid on the respective color map.

7.1 Spatial and spectral analysis

7.1.1 *Herschel* data

As shown in Fig. 6.4 only the left branch of the filament displays any [C II] emission. The right part is mostly emission free, so we will concentrate on the left part in the following discussion. Plots will also only show the relevant part of the cloud.

Figure 7.1 (a) shows the integrated *Herschel* [C II] map with contours of ^{13}CO (2–1). Note, that the ^{13}CO map was created by integrating over the range of 110 to 116 km s^{-1} which is the complete velocity extent of the filament in this line. In contrast, the [C II] emission is spread out much wider in velocity (this will also be discussed later). The map was integrated over the range of 106 to 122 km s^{-1}.

Some parts of this emission do not seem to be directly related to the ^{13}CO emission. We therefore split the cube in two velocity components, the first from

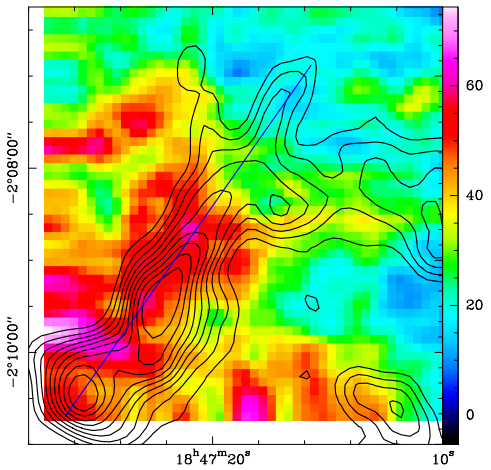

(a) HIFI [C II] map in [K km s^{-1}], IRAM ^{13}CO contours overlaid. The blue line indicates the pv-cut in Fig. (b).

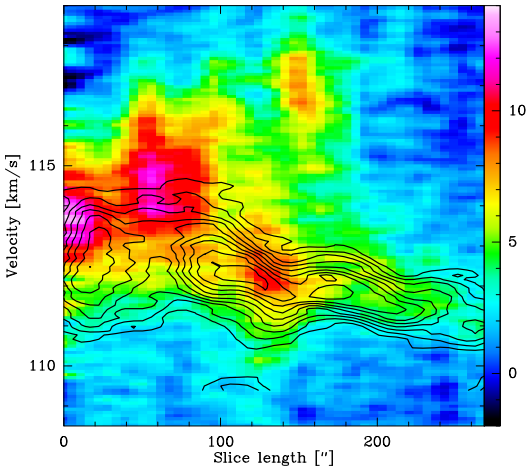

(b) pv-diagram of [C II] in [K] in color and IRAM ^{13}CO contours along the cut displayed in Fig. (a).

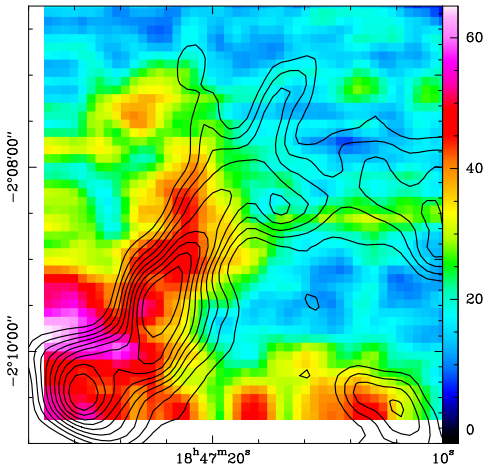

(c) HIFI [C II] map of velocity range 109 – 117 km s^{-1} in [K km s^{-1}].

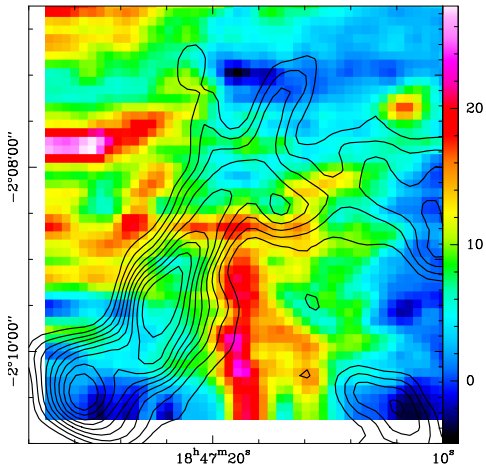

(d) HIFI [C II] map of velocity range 117 – 122 km s^{-1} in [K km s^{-1}].

Fig. 7.1: Herschel *HIFI map of [C II] of the left branch of the filament. The right branch does not show any emission in [C II]. Contours show IRAM 30m ^{13}CO (2–1) emission, as seen in Fig. 6.2. The left side of the pv-diagram corresponds to the lower left corner of the pp-map, while the right side corresponds to the upper right corner. The lower plots display two different velocity sub-components.*

109 to 117 km s^{-1} and the second from 117 to 122 km s^{-1}. These are shown in Fig. 7.1 (c) and Fig. 7.1 (d). This division is not exact, as some [C II] spectra are wider than the first component. Still, it is interesting how different the distribution of emission of the two components is. The more spread out emission is found at higher velocities.

We understand that the ionized carbon emission is generally more spread out than that of CO in the lower left parts of the map where the two bright CO clumps are found. The width of the filament across the central CO peak (i.e. the

width of the emission that is stronger than the half maximum value along the cut), is twice as broad in C^+ emission (3.1 pc) than in CO emission (1.7 pc).

Toward the upper tip of the filament, the point where the two branches of the CO emission meet, we see a decay of the [C II] intensity, which is much steeper than that seen in CO. The integrated [C II] emission of the central part of the filament, where CO is most intense, ranges from 50 to a maximum of 70 K km s^{-1}, while the rim of the emission shows intensities of about 30 K km s^{-1}. The peak intensity of the spectra ranges from 2 to 4 K in the outskirts of the filament and rises up to a maximum of 11 K in the southern central clump. Unfortunately, as described above, the map does not show the complete emission on the lower left corner. Here we cannot state how extended the emission would be.

Interestingly, not only the spatial but also the velocity extent of the ionized carbon is much broader than the carbon monoxide emission. Figure 7.1 (b) is a good demonstration of this. We see a position-velocity diagram along the filament. The position of the cut is indicated by the blue line in Fig. 7.1 (a). It becomes clear that the lower boundary of the pv-diagram, which corresponds to the blue shifted wings of the spectra, is similar in both emission lines. In contrast, the upper part of the diagram, the red shifted wings of the spectra, strongly deviates. C^+ reaches much higher velocities than ^{13}CO, especially on the left side of the diagram, which corresponds to the lower left part of the filament. Here, the [C II]line is between 4 and 5 km s^{-1} wide, while the CO line only reaches a width of 1.5 to 2 km s^{-1}. Both line widths converge toward the upper left part of the filament, seen on the right side of the pv-diagram, where both lines show a width of 1 to 1.5 km s^{-1}.

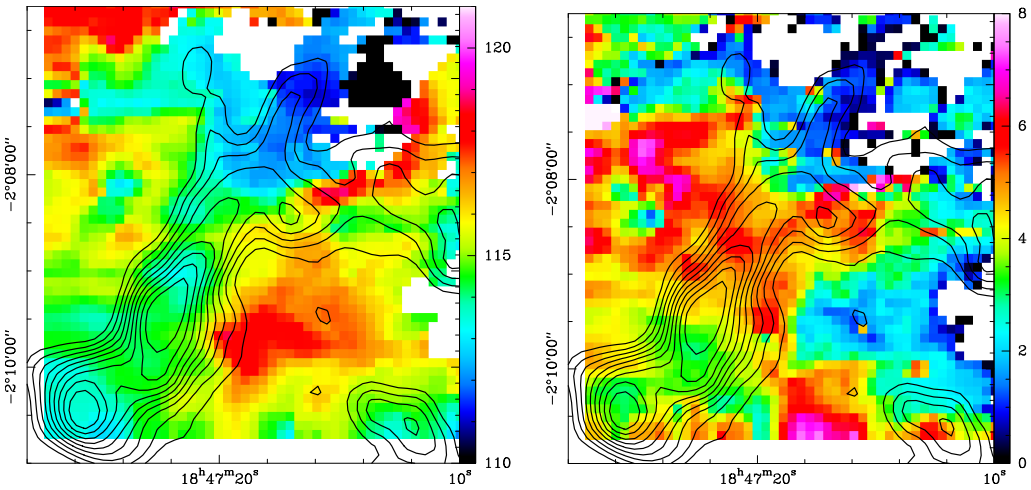

(a) HIFI [C II] mean velocity map. **(b)** HIFI [C II] line width map.

Fig. 7.2: Herschel *HIFI [C II] mean velocity and FWHM line width maps in [km s^{-1}]. Contours show IRAM 30m ^{13}CO (2–1) emission.*

This discovery is in agreement with Fig. 7.2, which shows maps of the first and second moment of the [C II] cube, the mean velocity in Fig. (a) and the

FWHM line width in Fig. (b). Moment maps of ^{13}CO can again be found for comparison in Fig. B.28 inf Appendix B.

The velocity structure of the cloud shows certain differences between the ionized and the molecular gas. Mean velocities of both lines are comparable in the upper left tip of the filament, with values of ~ 110 km s^{-1}, consistent with the findings in the pv-diagram in Fig. 7.1 (b). From there on, mean velocities of both lines rise along the filament, although the velocity gradient of C$^+$ is the steeper one. It rises to 115 km s^{-1} at the position of the central ^{13}CO halfway through the filament, from where it drops again to 113 km s^{-1} in the southern end of the filament. The velocity gradient from the upper left tip to central clump has a value of 1.6 km s^{-1} pc^{-1}. In contrast, the CO peak position rises throughout the complete filament. It rises from 110 km s^{-1} to 114 km s^{-1} in the southern clump of the cloud. The CO velocity gradient has a value of 0.5 km s^{-1} pc^{-1}.

Another interesting feature of the C$^+$ velocity structure is the difference between the positions of the filament and the gas surrounding it. There is a distinct offset between the central backbone of the filament and the outer parts of 2 to 3 km s^{-1}. There is no such offset seen in the [C II] line width, which is mostly uniform across the filament, although it changes along it. Therefore we really see a shift of the line between the inside and the outside of the filament.

As a conclusion from the description of the C$^+$ data in comparison with the ^{13}CO (2–1) data, we can interpret the basic setup of the filament as a dense, narrow molecular backbone surrounded by an envelope of ionized gas. This notion would be in agreement with theory that describes the transition from regions of atomic to molecular hydrogen, which is usually traced by [C II] emission (e.g. Velusamy et al. 2010). This would explain the broader distribution and larger line widths of the [C II] line. We will discuss the origin of this emission later in Sect. 7.2.3.

7.1.2 APEX data

The APEX CO (6–5) data is a good complement to the IRAM 30m observation as ^{13}CO (2–1) traces the cold molecular gas. In contrast, CO (6–5) is an indicator for hot molecular gas. Usually ^{12}CO is much more (the difference can be up to 50%) extended than ^{13}CO. But here we compare the higher ^{12}CO transition and find that both datasets show emission of similar extent.

Figure 7.3 (a) shows the CO (6–5) emission map, integrated over the range of 110 to 116 km s^{-1}, overlaid by ^{13}CO (2–1). Both lines correlate well in the left branch of the filament, which is seen here. In general, the APEX data is slightly less extended than the IRAM 30m observation. However, no emission is seen in the right part of the filament. Integrated intensities of CO (6–5) have typical values of 4 to 6 K km s^{-1}, in the mid-intense parts of the filament and 9 K km s^{-1} in the central clump. This is much weaker than the ^{13}CO (2–1) integrated emission with 15 and 25 K km s^{-1}, respectively.

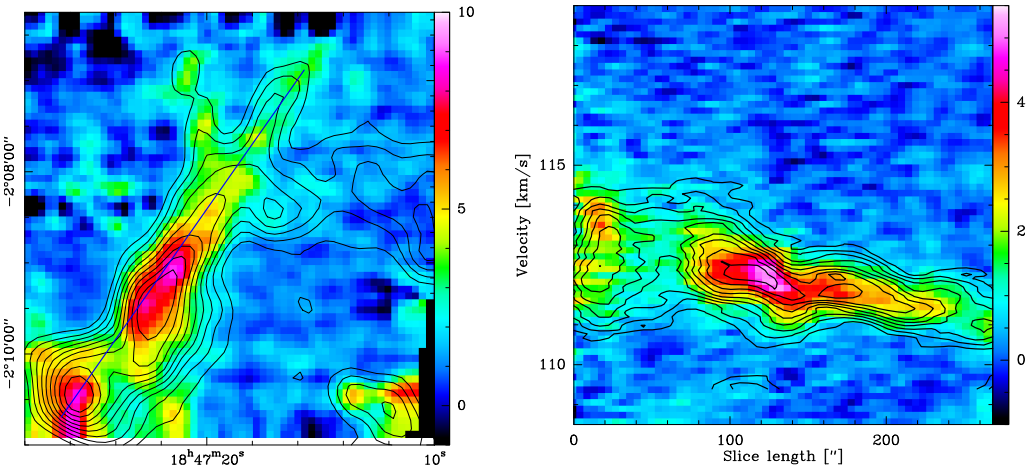

(a) APEX CO (6–5) map in [K km s^{-1}], IRAM ^{13}CO contours overlaid. The blue line indicates the pv-cut in Fig. (b).

(b) pv-diagram of CO (6–5) in [K] in color and IRAM ^{13}CO contours along the cut displayed in Fig. (a).

Fig. 7.3: APEX map of CO (6–5) of the left branch of the filament integrated over the range 110 to 116 km s^{-1}. The right branch does not show any emission in CO (6–5). Contours show IRAM 30m ^{13}CO (2–1) emission, seen in Fig. 6.2.

The pv-diagram, shown in Fig. 7.3 (b), correlates well with the IRAM 30m data. Again, emission is less broad in velocity dimension similar to the spatial dimension. The velocity structure however matches well, which is also seen in the mean velocity map in Fig. 7.4 (a). The distribution of the CO (6–5) peak position is nearly identical to the one of ^{13}CO (2–1), seen in Fig. B.28 (c) in Appendix B. Both lines show the same velocity gradient from 111 km s^{-1} in the uppermost part of the filament which rises to 114 km s^{-1} in the lower part of it.

As stated, when discussing the pv-diagram, the FWHM line width of the APEX CO data is systematically smaller than that of ^{13}CO. While CO ranges from 0.5 to 1.5 km s^{-1} across the filament, ^{13}CO line widths range from 1 to 2 km s^{-1}. This narrower line width and the overall lower intensity of CO (6–5) explain the difference in integrated intensity. The mean peak intensity across the whole filament shows a value of 3.2 K in CO and of 7.0 K in ^{13}CO.

The CO (6–5) observation gives a good overview of the hotter molecular gas. It is no surprise that the distribution matches well that of ^{13}CO (2–1), but the information on the temperature is still valuable. Both datasets complement each other. We will give a detailed estimation of the temperature of the gas from these lines in Sect. 7.2.1.

7.1.3 CARMA data

With the CARMA interferometer we observed three different lines, HCN (1–0), HCO^+ (1–0), and N_2H^+ (1–0), in this filament. These lines trace dense gas

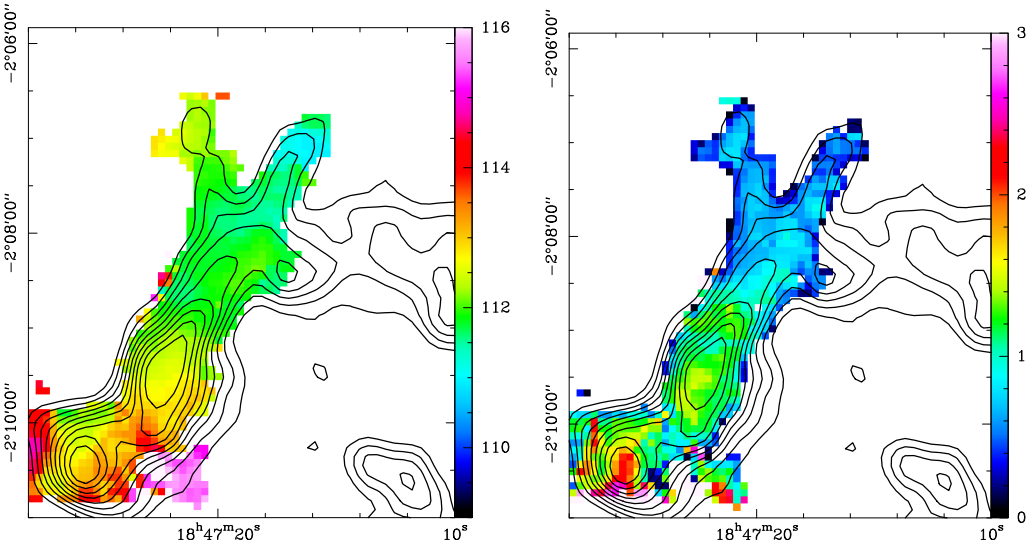

(a) APEX CO (6–5) mean velocity map. **(b)** APEX CO (6–5) line width map.

Fig. 7.4: APEX CO (6–5) mean velocity and FWHM line width maps in [km s^{-1}]. Contours show IRAM 30m ^{13}CO (2–1) emission.

which is usually found in the center of molecular clouds. Due to time constraints, we only observed the left branch of the filament. Concerning the fact that C^+ and CO (6–5) show no emission in the other part of the filament, which is also more diffuse in ^{13}CO, it is likely that no detection of the three high-density tracers would have been made here. But of course we cannot be sure about this.

All three lines are quite weak. More observation time would have been required for a clearer detection. Still, the data is good enough to get an idea of the conditions inside the dense molecular cloud. Figure 6.9 shows integrated intensity maps of all three lines, but the structure of the emission becomes clearer in Fig. 7.5 which shows contour plots of the three lines overlaid on the IRAM 30m ^{13}CO emission map.

We have to remark that the HCN and N_2H^+ lines show a hyperfine structure. We have to consider this when creating maps by integrating over a certain velocity range. All following integrated intensity and moment maps have only been created by using the main hyperfine component.

The contour plots show that all line's emission is much narrower than the IRAM 30m ^{13}CO emission, especially the one of N_2H^+. The typical width of the emission, higher than half maximum, is 0.7 pc (HCN and HCO^+) and 0.5 pc (N_2H^+). Remember, that the width of the ^{13}CO emission is 1.7 pc, that of C^+ 3.1 pc. However, the more extended emission is partially filtered out by the interferometer. The integrated emission is mostly centered around the two clumps in the center and the south of the filament. Both HCO^+ and N_2H^+ also show a little core in the northern part of the filament.

Integrated emission in the clumps of HCN ranges from 1 to 2 K km s^{-1},

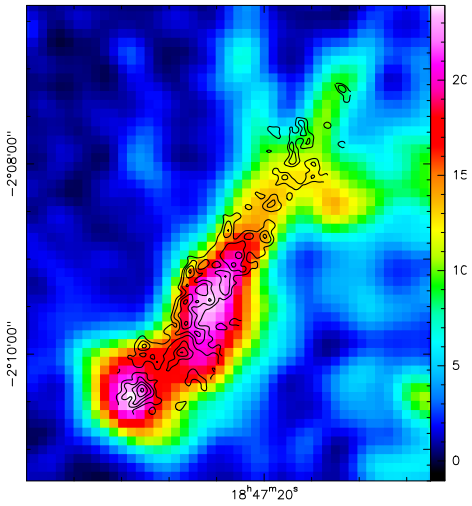

(a) HCN (1–0).

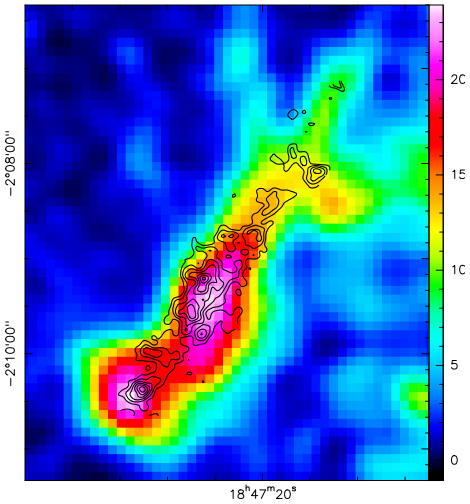

(b) HCO^+ (1–0).

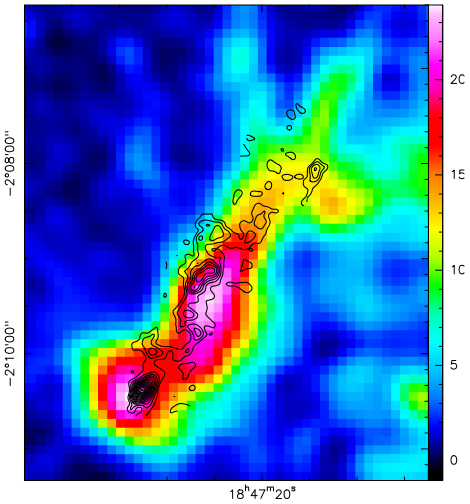

(c) N_2H^+ (1–0).

Fig. 7.5: Contour maps of the three CARMA high-density tracers, overlaid on IRAM 30m ^{13}CO (2–1) emission color map in [K km s^{-1}].

where the southern clump is the most intense part. Maximum peak intensities are 0.6 K. In contrast, the integrated emission of HCO^+ peaks at 2.5 K km s^{-1} in both clumps and peak intensities of up to 1.2 K in the center. The most exceptional emission is found in the N_2H^+ line. The central clump has emission of 3.5 K km s^{-1} and line peaks of up to 0.9 K. The southern clump has a maximum integrated emission of 8.9 K km s^{-1} with a line peak intensity of 2 K.

The velocity structure of the high-density tracers is seen in Fig. 7.6. Due to the low signal-to-noise ratio the maps are rather sparsely covered, this becomes especially evident in the N_2H^+ map. Still, we can see a clear structure of the mean velocity. HCN and HCO^+ show a clear velocity gradient along the filament where the mean velocity changes from 111 km s^{-1} to 114 km s^{-1}. This is exactly

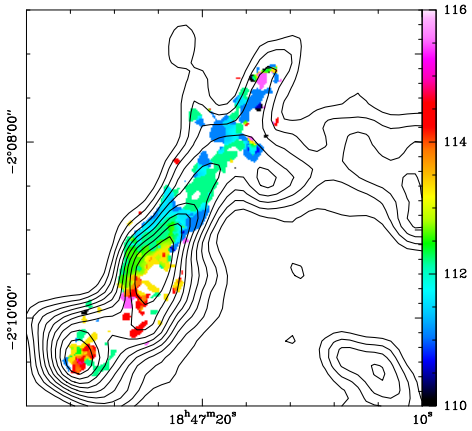

(a) HCN (1–0).

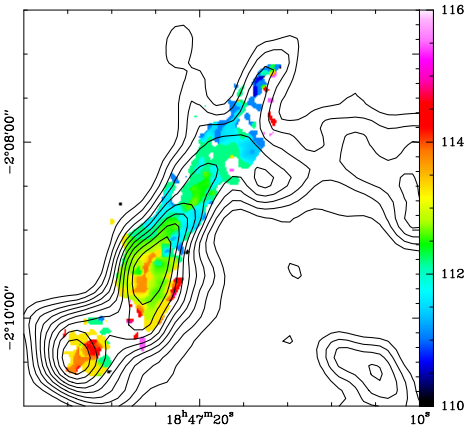

(b) HCO^+ (1–0).

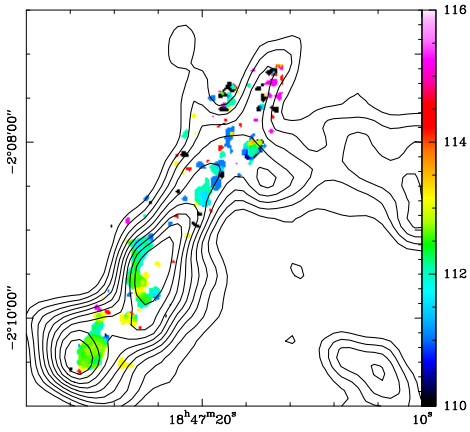

(c) N_2H^+ (1–0).

Fig. 7.6: Plots of the three CARMA high-density tracer velocity maps in [km s^{-1}], overlaid by IRAM 30m ^{13}CO (2–1) contours.

consistent with the gradient seen in ^{13}CO (2–1) (cf. Fig. B.28 (c) in Appendix B). N_2H^+ also shows a velocity gradient along the filament but it is slightly smaller. The velocity rises from 111 km s^{-1} to 113 km s^{-1}.

Plots of the FWHM line width are shown in Fig. 7.7. Again, only the main hyperfine component of HCN and N_2H^+ was used for these maps. All three lines have typical widths of 1.2 km s^{-1} throughout the filament with maxima of about 2 km s^{-1} in the intense CO clumps. The southern clump of N_2H^+ shows the highest values of about 2.5 km s^{-1}. These broad lines also explain large integrated intensities on this position. It would be possible to fit the hyperfine structure of the emission and thus get a more precise result of the velocity structure. We will probably do this during our future analysis of this data.

These datasets are a nice addition to the existing CO data. They trace a different phase of the molecular cloud and provide insight into the structure of the dense backbone of the filament. We will provide an estimation of the density

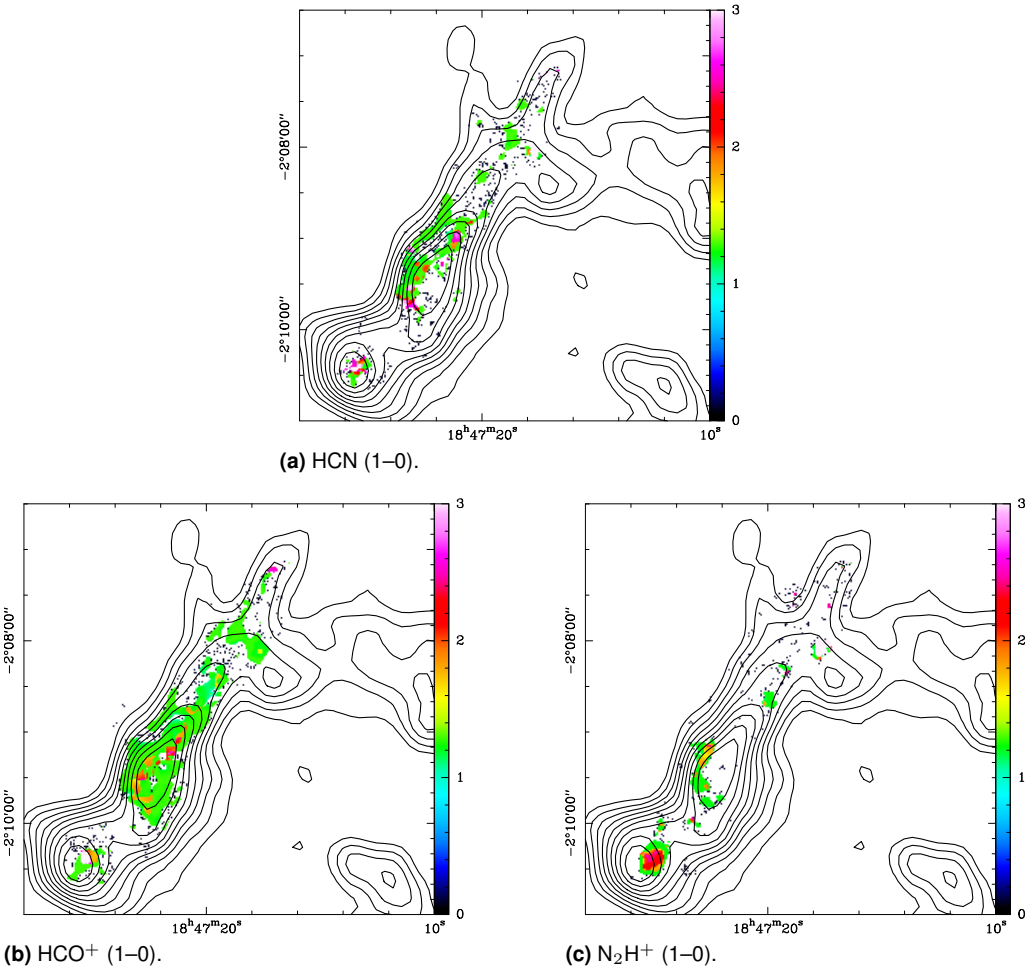

(a) HCN (1–0).

(b) HCO^+ (1–0).

(c) N_2H^+ (1–0).

Fig. 7.7: Plots of the three CARMA high-density tracer FWHM line width maps in [km s^{-1}], overlaid by IRAM 30m ^{13}CO (2–1) contours.

of the filament from these lines in Sect. 7.2.1.

7.1.4 NANTEN2 data

Our last dataset contains emission of the lower atomic carbon transition, observed with the SMART receiver of the NANTEN2 telescope. Figure 7.8 (a) provides a plot of the integrated intensity map of [C I] with an overlay of IRAM 30m ^{13}CO (2–1) contours. We have to remember that the HPBW of the [C I] (37″) is larger than those of the other datasets. Values range from 2 to 6 K km s^{-1} with the maximum in the southern clump. Line peak intensities vary from 1 to 2 K. In contrast to the [C II] and CO (6–5) maps, we find emission across the whole filament, including the right branch. This is interesting, as this branch is the more diffuse one in ^{13}CO (2–1).

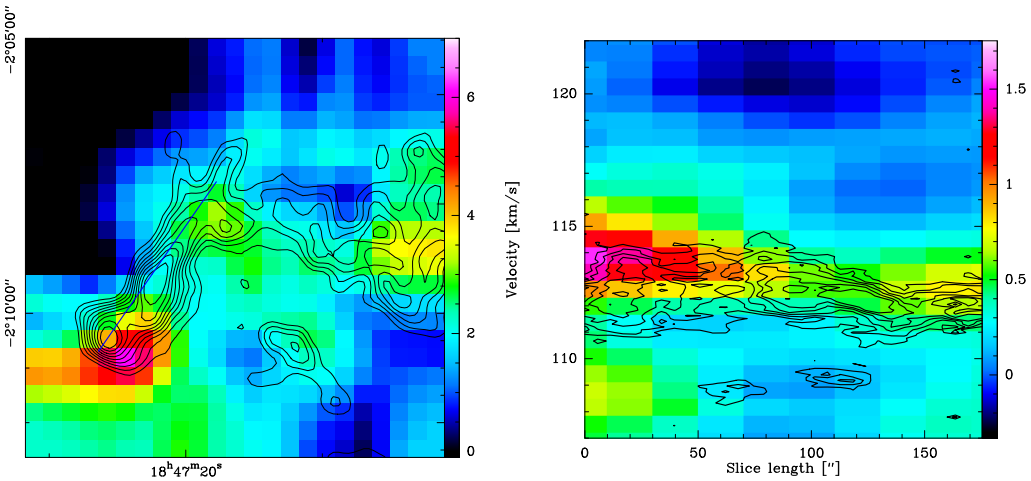

(a) NANTEN2 [C I] (1–0) map in [K km s^{-1}], IRAM ^{13}CO contours overlaid. The blue line indicates the pv-cut in Fig. (b).

(b) pv-diagram of [C I] (1–0) in [K] in color and IRAM ^{13}CO contours along the cut displayed in Fig. (a).

Fig. 7.8: NANTEN2 map of [C I] (1–0) of the left branch of the filament integrated over the range 110 to 116 km s^{-1}. The right branch does not show any emission in CO (6–5). Contours show IRAM 30m ^{13}CO (2–1) emission, seen in Fig. 6.2.

The map shows three clumps along the filament. The most luminous one is found in the south of the left branch of the filament, which is slightly shifted to the southwest from the ^{13}CO peak. The second most intense clump is located in the westernmost part of the right filament branch. No clump is seen on that position in ^{13}CO. The third clump, which is less intense, is found at the junction point of the two filament parts. It is remarkable that no intensity peak is found at the position of the central ^{13}CO clump in the left filament part. This clump has been a prominent peak in all other observed lines.

The position-velocity diagram in Fig. 7.8 (b) shows the comparison with the ^{13}CO (2–1) pv-diagram. It is again indicated in plot (a) by the blue line. The left edge of the diagram corresponds to the lower left part of the filament. We note a similarity in the shape of both lines. There is a minor difference of the line width at the position of the central clump, where CO is broader than [C I]. Apart from the width, there is a general shift in velocity of both lines. [C I] is red-shifted by about 1 km s^{-1} relative to ^{13}CO.

The velocity shift of [C I] compared to ^{13}CO is also seen in the mean velocity map in Fig. 7.9 (a). The general structure is similar to that of ^{13}CO. There is a velocity gradient from the junction point of the two filament parts to the southern tip of the left filament and a less pronounced one from the junction to the tip on the right side of the filament. Again, we see that mean velocities are shifted relative to ^{13}CO. The left gradient starts at 112.5 km s^{-1} in the north and reaches 114 km s^{-1} in the south.

Line widths of 1 to 3 km s^{-1} are found in the [C I] data (cf. Fig. 7.9 (b)). The maximum is found in the lower left clump. These values are constantly larger

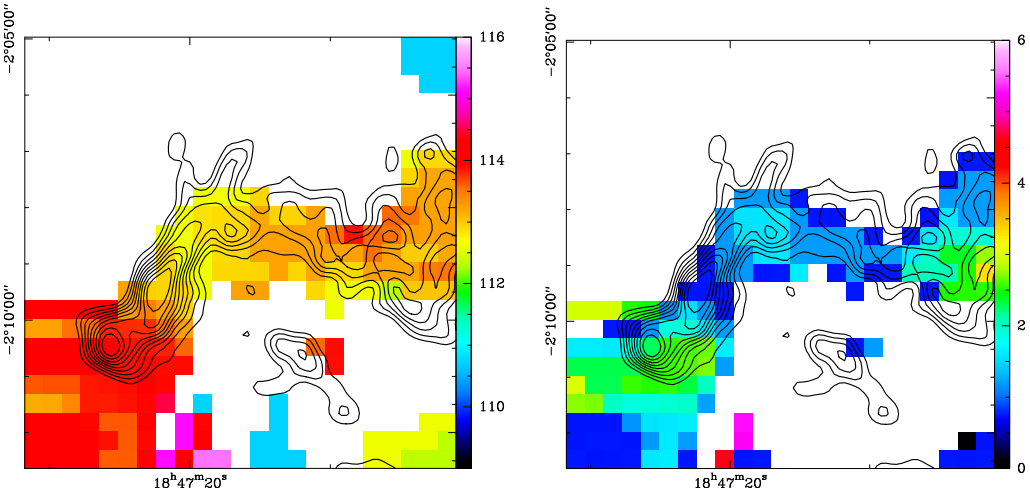

(a) NANTEN2 [C I] (1–0) mean velocity map. **(b)** NANTEN2 [C I] (1–0) line width map.

Fig. 7.9: NANTEN2 [C I] (1–0) mean velocity and FWHM line width maps in [km s^{-1}]. Contours show IRAM 30m ^{13}CO (2–1) emission.

than those of ^{13}CO (2–1), where we find a maximum of 2 km s^{-1}.

Now, we have a complete dataset of this filament. We combined information on its different phases, beginning at the dense central spine (traced by the CARMA observations), through the medium density cold and hot molecular gas (^{13}CO and C^{18}O IRAM 30m and APEX CO observations), to the transition phase between atomic and molecular gas (*Herschel* [C II] and NANTEN2 [C I] observations). In the next step we will begin to analyze the filament's properties.

7.1.5 Filament shape and size

We can now study the length and size of the filament. This analysis was carried out in the Bachelor thesis of Klatt (2013). It is possible to measure the length of the filament by fitting several lines of equal length along it. Figure 7.10 shows this measurement by white lines. We define the end points of the length measurement where the integrated emission has dropped to 20% ($\sim$5 K km s^{-1}) of the maximum of the map. We find a length for this source of 14.7 pc, the length of the left branch is 6.0 pc. The ratio between the total length and the connection between both ends (red line in Fig. 7.10) is a measure for the curvature of the filament and has a value of 1.25. The higher this number, the more the shape of a filament deviates from a straight line.

In comparison, we can also measure the width of the emission along the filament. For this, we define cuts along the length of the filament (seen in black in Fig. 7.10) at equidistant positions. They are located either at the center or the ends of each length segment and are orthogonal to these. When two length segments join at an angle, the width cut will be drawn along half of this angle.

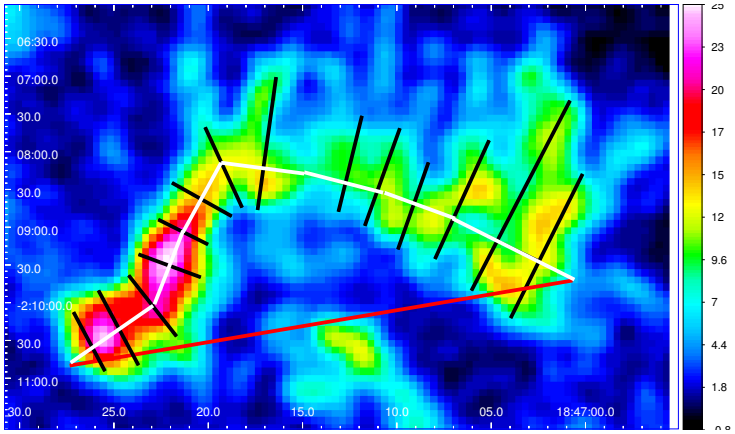

Fig. 7.10: Size analysis of the filament, as carried out by Klatt (2013). IRAM 30m integrated map in [K km s^{-1}]. White lines denote the length of the filament, black lines the width, and the red line the connection between both ends of the filament.

The length of each cut is defined by the extension of the emission along the cut, higher than half of the peak emission along this cut. We find an average width of 2.4 pc, which leads to a ratio of length to width of 6.1. The width ranges from 1.3 to 4.9 pc.

Klatt (2013) studied the shape of 13 filaments in the W43 complex and found an average length to width ratio of 6.7. So this source is about 10% below the average ratio. It has 83% the length of the average filament (17.8 pc) and 86% of the average width (2.8 pc).

Filaments are often discussed in the literature but there is no general definition of this term. As mentioned in Sect. 4.2.3, we use our own definition, where a filament is an elongated cloud with a mostly uniform width along it. The typical size of a filament in our dataset is on the order of 10 pc. Filaments can be found on several scales in the literature, but are often much smaller and narrower than our sources. Arzoumanian et al. (2011), for example, find an average filament width of 0.1 pc in Hi-GAL maps, while (Hacar et al. 2013) find a typical filament lenght of 0.5 pc in the L1495/B213 molecular cloud in Taurus. This underlines the fractal structure of molecular filaments. An analysis of our filaments on smaller scales would be interesting but due to the large distance this is not possible with our dataset. Observations with high angular resolution with interferometers (e.g. ALMA) could be interesting future follow-up projects.

7.1.6 Example spectra

In Fig. 7.11 we present spectra of several species at two important positions. These points are the ^{13}CO (2–1) integrated emission peaks in the central and southern clump in the left branch of our filament, which will be used to conduct

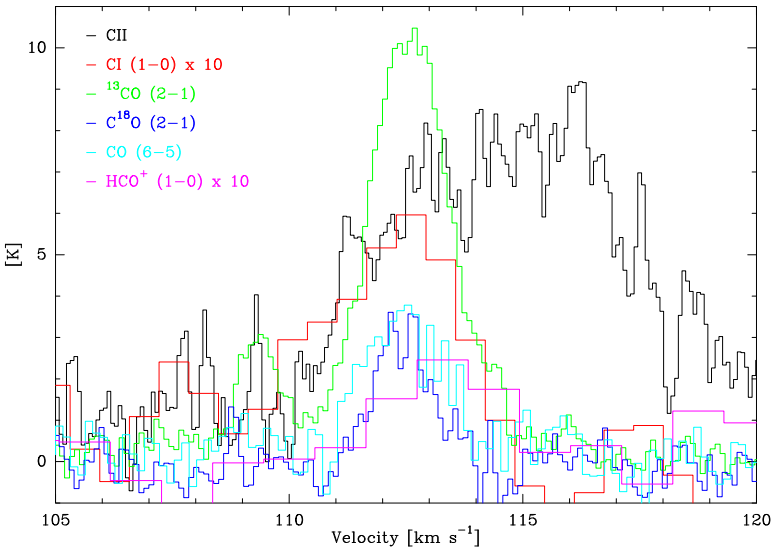

(a) Spectra at central clump peak.

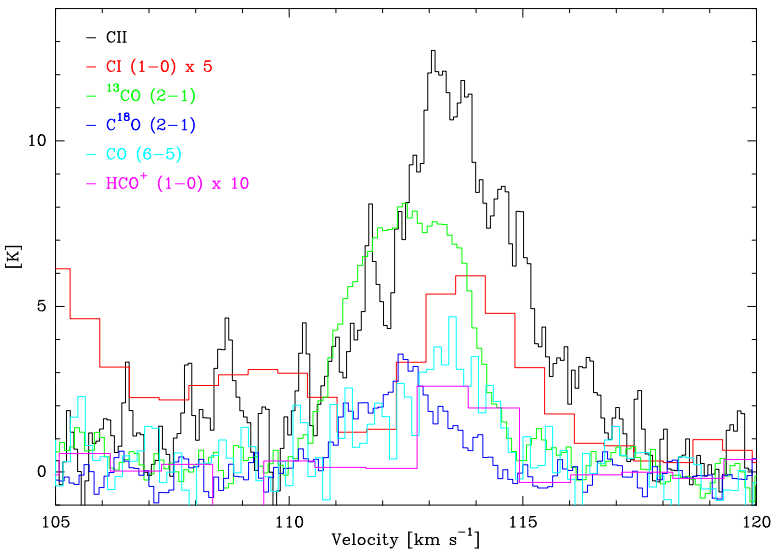

(b) Spectra at southern clump peak.

Fig. 7.11: Spectra at two important positions as indicated in Fig. 7.12 (a).

our in-depth analysis in Sect. 7.2. Their exact positions are indicated by black stars in Fig. 7.12 (a).

We first note that as expected the ^{13}CO and C^{18}O (2–1) show the same symmetric shape. Interestingly, the CO (6–5) deviates somehow. The width of the line is broader in the central clump and the line in the southern clump is shifted to higher velocities and shows a skewness, a larger blue-shifted wing. The [C II] line is red-shifted and broader than the CO lines in both positions, although these effects are more extreme at the central position. We see much more structure in this line than in the CO lines. The [C I] line does not correlate

with CO or with [C II]. In the central clump it correlates rather well with the ^{13}CO line, although with a stronger blue wing and deviates strongly from [C II]. In the southern clump [C I] correlates better with [C II] and is shifted to higher velocities from the ^{13}CO line.

7.2 Properties of the filament

7.2.1 Temperature and density

Now that we have a collection of several line observations of our target, we want to determine its properties. First, we want to estimate the temperature and density of the filament. We pick two different locations, at which we carry out the following calculations. Both are, of course, located in the left branch of the filament, as only there we have detected emission in all lines. The first point is the ^{13}CO (2–1) peak position in the central clump, the second one the ^{13}CO (2–1) peak position of the clump in the lower-left part of the filament (see Fig. 7.12 (a)).

Naive density estimation

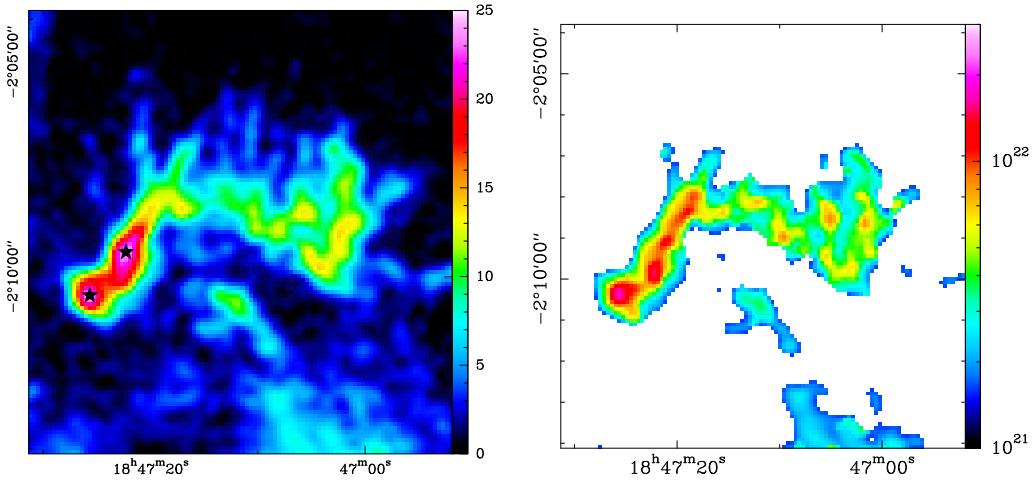

(a) ^{13}CO (2–1) integrated map in [K km s^{-1}], indicating modeled positions.

(b) $N(H_2)$ column density map in [cm^{-2}].

Fig. 7.12: Indicator of positions used in calculations and H_2 column density map.

We can give a naive estimation of the density in the two mentioned positions by considering the H_2 column density at those positions. These values are 8.3×10^{21} cm^{-2} at the center position and 1.7×10^{22} cm^{-2} at the southern position. If we now assume the filament to be approximately cylindrical, i.e. its extent along the line-of-sight is comparable to that in the plane on the sky, we can calculate the mean density at the two positions. We first measure the width of the filament

across the two positions, where we define the width as the extent of emission larger than 20% of the peak emission. This yields a filament width of 2.7 pc at both positions.

Dividing the H_2 column density by this length gives an average volume density of 1.0×10^3 cm^{-3} at the center position and 2.0×10^3 cm^{-3} at the southern position. Of course, this is just a vague approximation and should not be taken as an exact value. We also have to take into account that we just estimated the average density along the cloud. This can only be a lower limit to the density in its center. Also, the calculation of the H_2 column density comes with its own uncertainties, as discussed in Sect. 5.1.3.

The RADEX algorithm

Some years ago, van der Tak et al. (2007) published the RADEX[1] algorithm that would compute intensities of molecular emission lines from molecular clouds. They used a non-local thermal equilibrium (LTE) radiative transfer code and included collisional processes. This program assumes an isothermal homogeneous medium without large-scale velocity field.

To calculate the intensity of a cloud of gas as seen by the observer one has to solve the radiative transfer equation (see also Eq. 2.9 in Chapter 2):

$$I_\nu(\tau_\nu) = I_\nu(0)\mathrm{e}^{-\tau_\nu} + \int_0^{\tau_\nu} \mathrm{e}^{-(\tau_\nu - \tau')} S_\nu \mathrm{d}\tau', \tag{7.1}$$

where $I_\nu(\tau_\nu)$ is the detected intensity at frequency ν, $I_\nu(0)$ is the background radiation behind the source, S_ν the source function of the emitting cloud itself, and τ_ν the optical depth of the cloud. The source function and the optical depth depend on the level populations of the gas, which is determined by its excitation temperature. This is given by the local radiation field at the position of the gas, which again has to be calculated by using the radiative transfer. So this is a complicated problem to solve.

In fact, this would not be possible to solve, if the small scale structure of the gas was of interest for us. But fortunately, we are only interested in the large scale average properties of the gas. For this average treatment it is possible to consider the probability that a photon escapes a certain cell of gas where it was created. This is called the escape probability β and depends only on the optical depth and the global geometry of the cloud. We will now consider a uniform sphere of gas, which is probably the closest approximation of the clumps in our

[1] The software can be obtained from http://home.strw.leidenuniv.nl/~moldata/radex.html

filament. Then, the escape probability is given by (see again van der Tak et al. 2007):

$$\beta_{\rm sphere} = \frac{1.5}{\tau}\left[1 - \frac{2}{\tau^2} + \left(\frac{2}{\tau} + \frac{2}{\tau^2}\right)\mathrm{e}^{-\tau}\right]. \tag{7.2}$$

The local radiation field in the gas is then given by

$$I_\nu \propto S_\nu(1-\beta) \tag{7.3}$$

and ignores any background radiation. The optical depth can be computed from the column density and the velocity dispersion of the gas which the user has to provide and the line populations.

Now, the program starts by assuming an optically thin gas and a local radiation field that is completely given by the background radiation. This radiation is then used to guess a first line population and with that calculates a first guess for the actual optical depth. This is used to estimate a first guess for the local radiation field. From there on, the software iteratively calculates optical depth and radiation field until it found a consistent description of the gas. This is separately done for each line.

As input for the software we have to give the specific line and transition and several other values. The width of the line has to be given, the kinetic temperature of the cloud, the number density of H_2, and the column density of the observed molecule. As background radiation we chose the typical cosmic background of 2.73 K. After the calculation, the software will give the excitation temperature of the line, its optical depth, and the observed intensity as output.

RADEX results

The RADEX software produces line intensities from the density and temperature of the gas. As we know the intensities and are interested in the other values, it would be best for us to reverse the calculation, which is, unfortunately, not possible. Therefore, we create a program, written in python, that runs the RADEX algorithm several times for different sets of input parameters and creates a grid of line intensities. We then find the combination of input values that produces an intensity closest to our observations.

The three-dimensional parameter space consists of kinetic temperature, volume density and column density of the gas. The line width can be directly taken from our observations. For this modeling we use four different lines: CO (6–5), ^{13}CO (2–1), C^{18}O (2–1), and ^{13}CO (3–2), where the last line is taken from James

Clerk Maxwell Telescope (JCMT) observations of the W43-Main region, carried out by R. Plume[2] and T. Moore[3].

We create a data-cube for each line, where a single point contains the intensity given by RADEX and its coordinates are determined by the values of the three input variables. We can then define a χ^2 function which is the squared difference between model calculation and observed intensity, summed for all lines:

$$\chi^2 = \frac{1}{n-3} \sum_i \left(\frac{I_{\mathrm{m,i}} - I_{\mathrm{o,i}}}{\sigma_i} \right)^2 , \tag{7.4}$$

with the number of lines n, the modeled intensity $I_{\mathrm{m,i}}$, the observed intensity $I_{\mathrm{o,i}}$, and the measurement error σ_i of each line i. Thus, we get another data-cube which contains these χ^2 values. The position of the minimum in this χ^2-cube gives the input values that produce the most realistic output intensities.

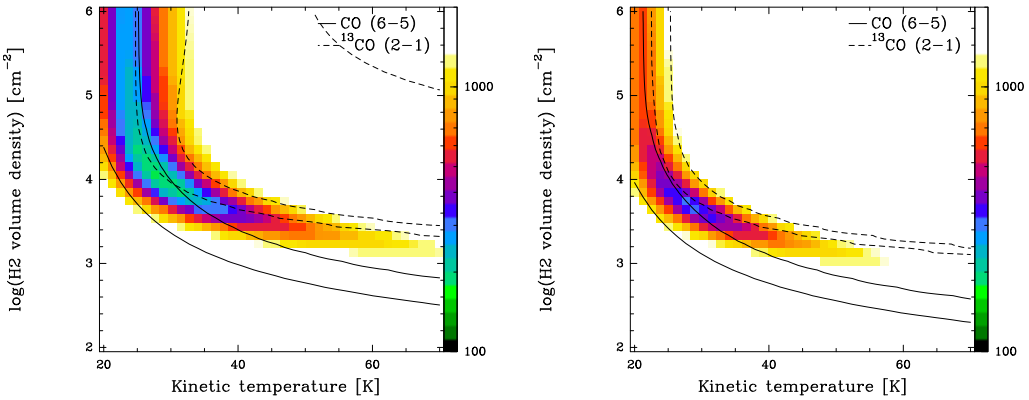

(a) Central clump. Channel map of $N(\mathrm{CO}) = 1.4 \times 10^{18}\,\mathrm{cm}^{-2}$, including the minimum total χ^2.

(b) Southern clump. Channel map of $N(\mathrm{CO}) = 2.4 \times 10^{18}\,\mathrm{cm}^{-2}$, including the minimum total χ^2.

Fig. 7.13: χ^2-maps resulting from the RADEX algorithm. Colors show the total χ^2 of all lines, the straight line contours show the area where the χ^2 of CO (6–5) is smaller than 50, the dashed line shows the area χ^2 <50 of ^{13}CO (2–1).

As input parameters we choose kinetic temperatures between 20 and 70 K, volume densities between 10^2 and 10^6 cm^{-3}, and column densities between 10^{15} and $10^{18.5}$ cm^{-2}. The column densities have to be scaled by the relative abundances of the different lines, so that the position of the final data-cubes will be aligned and the lines are comparable. A column density of 10^{15} cm^{-2} will denote the column density of CO, but a ^{13}CO value of $10^{15}/31$ cm^{-2}, and a C^{18}O column density value of $10^{15}/272$ cm^{-2}. For the assumptions of the relative abundances in W43, see Sect. 5.1.1. We also assume that the emission does not completely fill the beam, but that there is some sub-beam structure. The

[2]Institute for Space Imaging Science Radio Astronomy, University of Calgary, Canada
[3]Astrophysics Research Institute, Liverpool John Moores University, UK

Clump	$T_{\rm peak}$ [K]	$T_{\rm kin}$ [K]	$\log(n)$ $\log(\mathrm{cm}^{-3})$	$\log(N(\mathrm{CO}))$ $\log(\mathrm{cm}^{-2})$
Central	4.3	25 – 35	3.8 – 4.4	18.0 – 18.5
Southern	2.8	25 – 35	3.5 – 4.0	18.0 – 18.5

Table 7.1: Range of RADEX input parameters that best fit our observations for a given peak temperature of the CO (6–5) line.

beam-filling factor η is assumed to be 0.6 and the observed intensities have to be divided by this factor to be comparable to the model.

The resulting data-cubes have dimensions of 40×40×30 (temperature-density-column density) values. The larger the cubes, the finer the parameter space is covered and the more exact is the best fit value, but it also increases the computing time needed. Plots of those channel maps of the total χ^2-cubes that contain the minimum value are shown in Fig. 7.13.

These plots show color maps of the total χ^2 value of all lines added up, with the kinetic temperature along the x-axis and the volume density along the y-axis. The third axis contains the column density of CO. Remember that the input of the column density of the ^{13}CO lines has been scaled to fit the CO column density. We can now identify a certain range for all three parameters that give the best fit to our observed values. These values are given in Table 7.1.

We now have to decide if these values seem reasonable. We can compare the derived kinetic temperature with the excitation temperature that we computed in Sect. 5.1.2. There we found temperatures between 8 and 20 K, with all uncertainties as discussed in the mentioned section. $T_{\rm ex}$ at the central clump position is 18.6 K, while the excitation temperature at the southern clump position is found to be 11.5 K. As discussed, this value does not include the beam filling factor η and we assumed a filling factor of 0.6 for the RADEX calculations. Considering this factor leads to a $T_{\rm ex}$ of 31.0 and 19.2 K for the central and southern position, respectively. The first value lies in the range deduced with RADEX, the second one is a bit lower.

Of course, the kinetic and the excitation temperature are only equal, if we assume LTE. It is absolutely possible, that the molecular gas at the southern position is sub-thermally excited. Also, the first calculation only takes the ^{13}CO and C^{18}O (2–1) observations into account, while the RADEX calculation also considers the CO (6–5) data. Naturally, this higher line needs a higher temperature of the gas to become excited often enough to create a considerable amount of emission. Therefore, the RADEX algorithm probably creates the more comprehensive output.

The density range which the RADEX algorithm finds is between 3 and 10 times higher than our naive estimation in Sect. 7.2.1. As mentioned there, it is only the mean density along the line-of-sight if the filament and both, the uncer-

tainties of the H_2 column density computation (cp. Sect. 5.1.3) and the assumption about the geometry of the filament enter this value. We can assume that the filament is roughly cylindrical and shows a radial density distribution, rising toward the center (e.g. Arzoumanian et al. 2011). The higher density parts are optically thicker and contribute more to the molecular emission than the thinner envelope. Thus, the RADEX result mostly give the density of the inner part of the filament and at least the lower limit should be consistent with our naive density estimation.

Finally, we can compare the results for the column density. In Sect. 5.1.3, we derived the total column density of the molecular hydrogen, which constitutes nearly all of the molecular gas, but it was derived from the ^{13}CO column density, assuming a constant factor for the ^{13}CO abundance in the cloud. RADEX gives the CO column density, so we have to convert it to H_2 column density first. This abundance factor, that related ^{13}CO and H_2 was 2×10^5, that, relating CO and H_2 is 6550.

We find the RADEX result for the H_2 column density ranging between 6.6×10^{21} cm^{-2} and 2.1×10^{22} cm^{-2} for both analyzed positions. The values derived only from the IRAM 30m data are 8.3×10^{21} cm^{-2} and 1.7×10^{22} cm^{-2} in the central and southern position, respectively. These values lie in the range found by the RADEX simulations.

Thus, all values, for the kinetic temperature, the volume density, and the column density derived from the RADEX simulation are consistent with those values that we derived from the IRAM 30m before. This provides a good constraint for the physical conditions in our filament.

CARMA data density estimation

As HCN, HCO^+ and N_2H^+ have an electric dipole moment larger than that of CO, these molecules need much more energy to become rotationally excited. Therefore, a higher gas density can be assumed, when emission from these molecules is detected (e.g. Christopher et al. 2005). Often the so-called critical density $n_c(jk) = A_{jk}/\gamma_{jk}$ is used to describe the molecular gas density, necessary to create reasonable line intensities of the transition from state j to k. A_{jk} is the corresponding Einstein A coefficient and γ_{jk} the collisional deexcitation rate of level j per molecule.

Evans (1999) lists n_c for several lines but also notes that even a lower density can be sufficient to create intensities that can be observed by a sensitive enough telescope. Thus, in addition, Evans gives a n_{eff} which gives a line intensity of 1 K. For HCN (1–0) n_c is 2.6×10^6 cm^{-3}, while n_{eff} is 2.9×10^4 cm^{-3}. The HCO^+ (1–0) line has a critical density of 1.7×10^5 cm^{-3} and an n_{eff} of 2.4×10^3 cm^{-3}. All densities are given for an assumed kinetic gas temperature of 10 K. As we find typical peak temperatures of 1 K in our CARMA observations, this n_{eff} of HCN should be a lower limit for the gas density.

Detection of N_2H^+ implies a density of at least a few 10^4 cm^{-3} (Daniel et al. 2006) and stronger emissions can even detect densities of up to several 10^6 cm^{-3} (Johnstone et al. 2010). Thus, we should assume a few 10^4 cm^{-3} for those parts of the filament, where we detect emission with CARMA, which is the central backbone of 0.5 to 0.8 pc width of the left branch. The broader area, traced by the IRAM 30m observations will probably have lower densities as no line can be detected with CARMA there. These values are consistent with the upper limits derived from the RADEX models.

In a future extension of this analysis it would be possible to estimate the opacity of N_2H^+ from its hyperfine components. We could thus calculate column densities of this molecule and, assuming a certain abundance and geometry of the filament, we could finally find a value for the H_2 volume density. This value could then be compared to the previous findings.

7.2.2 UV-field

C^+ emission is often discussed in the framework of PDRs, sometimes they are even considered the only source of this emission (e.g. Israel and Maloney 2011). We will now try to analyze the UV-field that surrounds our filament. There are several ways of doing so. Our approach is to treat the filament as a PDR, where it would be embedded in a UV-field which could explain the [C I] and [C II] emission. Using a PDR model, we can estimate the necessary UV-field strength. Finally, we can use emission maps of typical UV-field tracers to check, whether this values can be verified and the assumption of a PDR still holds.

C^+ in PDRs

A PDR (Hollenbach and Tielens 1997) is created, when strong UV-fields shine into molecular clouds and dissociate the molecules. The source of the field can be nearby OB stars or the interstellar radiation field, if it becomes strong enough. From the direction of the UV source into the molecular cloud different phases that arrange in layers can be identified. A plot of how these layers arrange is given in Fig. 7.14.

In the outermost phase molecules are completely dissociated or even ionized. Atomic hydrogen and oxygen can be found here and also ionized carbon. Gas temperatures are high, up to 10^3 K. Further into the cloud, the gas will be partially shielded from the radiation field and hydrogen can already occur in molecular form. However, carbon is still found in ionized or atomic form. Only in the innermost part of the clouds carbon is found in molecules, mostly in CO, but also in other combinations.

This stratification of carbon in C^+, C, and CO is often observed (e.g. Röllig et al. 2011; Pérez-Beaupuits et al. 2012). In general, the [C II] and [C I] emission

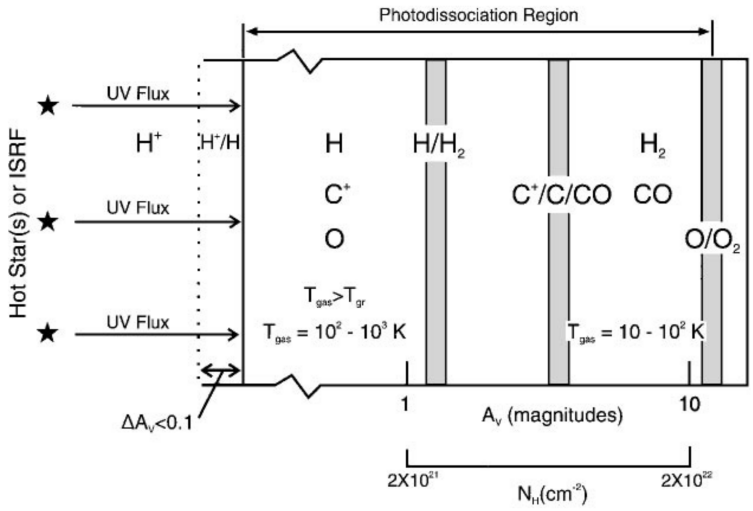

Fig. 7.14: Schematic of a PDR, taken from Hollenbach and Tielens (1997), showing the different layers in the cloud created by UV-radiation.

is found to be more spread out than the CO emission. This characteristic feature is often simulated (See Bisbas et al. 2012, for a comparison of this feature using several codes.), since this steady state setup is relatively easy to model and the physics are quite well understood.

The KOSMA-τ model

There are several algorithms that calculate the abundances in PDRs, e.g. Cloudy (Ferland et al. 2013) or the Meudon code (Le Petit et al. 2006). Here, we will use the KOSMA-τ model (Störzer et al. 1996; Röllig et al. 2006) that is run in the Mathematica software.

This model comes in two different versions. The simple one assumes a single spherical cloud with a certain mass m and density n, which is embedded in a given isotropic UV-field χ. It also takes the metallicity Z into account. These four values have to be provided as input to the program which then solves equations of heating and cooling, the chemical equilibrium and radiative transfer. Final outputs are the intensities of all calculated emission lines. So far, the following species are included in the output of the model: C^+, C, O, CO, ^{13}CO, $^{13}C^+$, ^{13}C, HCO^+, $H^{13}CO^+$, H_3O^+, and CH^+. However, the chemical network that is solved by the algorithm includes 32 different species.

The more advanced version of the software does not only consider one spherical clump but an ensemble of many different spheres that fill the beam. The size and mass of these clouds are defined by a power-law distribution, where only the upper and lower bound of the distribution is given as input to the program. The embedding UV-field and the metallicity of the gas

Line	Central position	Southern position
^{13}CO (2–1)	23.69	23.93
C^{18}O (2–1)	3.90	6.63
^{13}CO (3–2)	8.77	11.20
CO (6–5)	7.04	7.22
[C II]	44.16	47.78
[C I] (1–0)	1.96	3.87
HCO$^+$ (1–0)	1.09	0.79

Table 7.2: KOSMA-τ input values in K km s^{-1}.

is fixed for the whole ensemble. This is the model we use here with the `clumpyIntensityKelvin` task.

As with the RADEX algorithm, the input values are what we are actually interested in, while the output values, the observed intensities, are what we already have. So again a grid of modeled intensities covering a certain range of input parameters is created. As these calculations need a lot of computing time, we use a previously existing dataset, created by Markus Röllig. In contrast to our RADEX program, the KOSMA-τ not only provides solutions for the given parameter grid points but can interpolate and even extrapolate between those points. Of course, solutions that are extrapolated are less reliable than those that lie inside the model grid. We show the list of input values in Table 7.2.

KOSMA-τ results

We used the same two positions as before (see Fig. 7.12) so that our findings will be comparable. In contrast to the RADEX analysis, we use not only CO data, but also the ionized and atomic carbon line and the HCO$^+$ (1–0) line (we use the integrated [C II] emission from the lower component, shown in Fig. 7.1 (c)). All these lines can be modeled by the KOSMA-τ model.

Again, in contrast to our approach before, we neglect the beam filling factor in this step. It is possible that this filling factor varies between CO, [C I], and [C II] observations. Even our resulting maps of CO and [C II] show a different amount of structure, (cf. Fig. 6.2 and Fig. 6.4 in Chapter 6) and we do not know the sub-beam structure. Therefore, we refrain from guessing these values.

Similar to our procedure with the RADEX model in Eq. 7.4, we define a χ^2 function that sums up the squared differences between modeled and observed intensities. We then find a list of input parameters which minimizes this χ^2 function with the `NMinimize` task. Figure 7.15 shows the values found at both positions. It also plots the intensities that we observed, compared to those values that the model finds for the best fitting set of parameters.

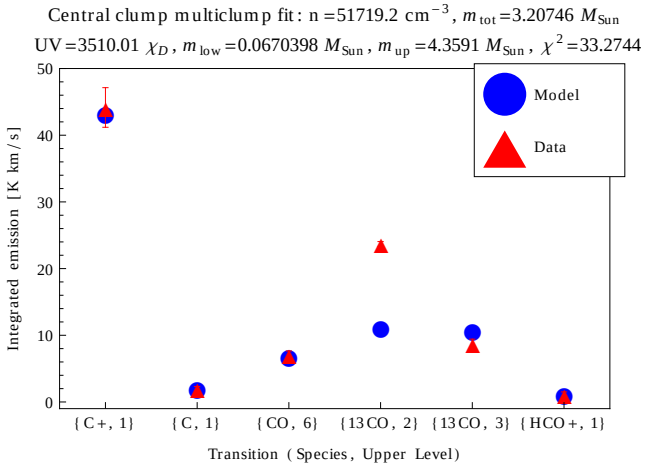

(a) Central clump.

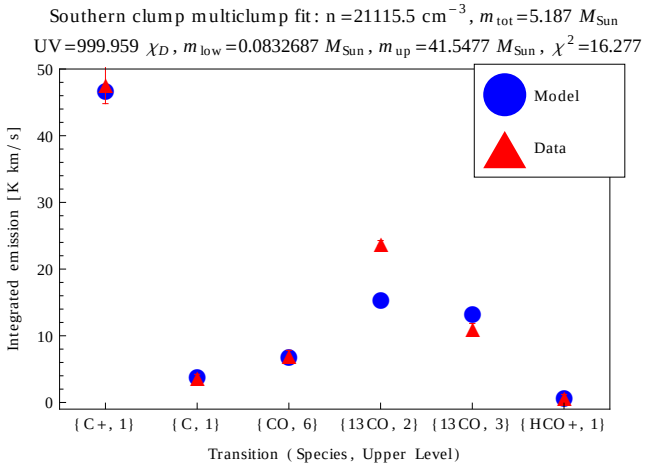

(b) Southern clump.

Fig. 7.15: KOSMA-τ results for the two positions in our filament.

First, we note that most modeled line emission fit the observed values quite well. Only the ^{13}CO (2–1) line deviates strongly in the model. Interestingly, the [C II] line is simulated very well.

According to the model, a volume density of 5.2×10^4 cm^{-3} (central clump) and 2.1×10^4 cm^{-3} (southern clump) would be necessary to explain the observed emission by a PDR. This is about a factor of 2 higher than the upper bound of the RADEX result for the density (2.5×10^4 cm^{-3} and 1.0×10^4 cm^{-3}, respectively), which in turn was about a factor 10 higher than the rough density estimation from the H_2 column density. On the other hand, the CARMA observations indicate a density of a few times 10^4 cm^{-3} in the central region of the filament. This high density is not traced by the CO lines that have been used for the RADEX estimation. Thus, the result of the KOSMA-τ model could be seen as an upper limit for the volume density of the gas.

On the contrary, the total mass of the clump ensemble in the beam is found to be 3.2 $M_\odot$ in the central position and 5.2 $M_\odot$ in the southern position, which is somewhat low. We can compare these values with our mass calculation, conducted in Sect. 5.1.4. Derived from the H_2 column density, we find a mass-per-pixel value of 4.8 $M_\odot$ (1.5 times higher than model) for the central position and 9.5 $M_\odot$ (1.8 times higher) for the southern position. Still, this is on the right order of magnitude.

The results for the upper and lower bound of the mass distribution are somewhat problematic. First, the values for the lower limits lie outside of the range that is defined by the KOSMA-τ model. The grid is defined for lower mass limits between 0.001 and 0.01 $M_\odot$. Thus, the found solution lies outside the grid of input parameters and has to be extrapolated. The results are therefore less reliable. The reason is probably the large distance of our target cloud. Due to the distance, more mass can be contained inside the beam.

Second, we get a large value for the upper mass limit in the southern clump. This value is larger than the total mass in the beam, which is unusual. It could be interpreted that the largest clump in the simulated clump ensemble is larger than the beam and only a fraction of its mass can be seen. It is unclear how this effects the reliability of the found results.

Concerning the UV-field, needed for proper line emissions, we find very large simulated values of 3.5×10^3 and 1.0×10^3 χ_D for the central and southern clump, respectively. These values are given in units of the mean interstellar radiation field as described by Draine (1978). The [C II] emission in the model directly depends on the UV-field. Reducing the field strength input yields much lower emission of ionized carbon. We also have to remember that we did not used the full [C II] integrated emission, as we removed the velocity component between 117 and 122 km s^{-1}, which is likely unrelated to the filament. The results discussed here, should therefore be seen as a lower limit. We can thus state, that a high UV-field is essential to explain our observations in the picture of a static PDR.

Comparison with UV-field tracers

A high radiation field is also found in other observations of PDRs. For example, Röllig et al. (2011) find a UV-field of $3{-}6 \times 10^3$ χ_D for the PDR in NGC 3603, which is only a few pc away from a massive OB-star cluster. Marconi et al. (1998) find a UV-field of $1{-}3 \times 10^4$ χ_D in the Orion bar, induced by the Trapezium stars at a distance of 0.25 pc.

To decide whether such a high UV-field is realistic in our case, we have to inspect typical UV tracers. The most likely source would be the OB cluster in W43-Main. However, it is located at a distance of more than 20 pc from our filament and completely surrounded by the dense molecular ridges in W43-Main

(see Fig. 5.10 in Sect. 5.7.1). This should nearly completely absorb the stars' radiation.

It turns out that the combination of dust emission and Hα is a good indicator for the presence of UV-fields. Carey et al. (2009) state that a dust SED, composed of big grains, small grains, and PAHs, changes under the influence of different radiation fields. Carey et al. present the relative intensities of the 8 μm, 24 μm, and 70 μm bands for different UV-fields[4]. The ratio 24:8μm is typically below 1 for low UV fields between 1 and 100 $\chi_{\rm D}$, while it is above 1 for a radiation on the order of several 10^3 to 10^4 $\chi_{\rm D}$.

Carey et al. (2009) explain that strong UV-fields especially heat large dust grains. At low temperatures, i.e. low UV-fields, their peak emission lies at high wavelengths, beyond 70 μm. This peak moves to 70 μm at around 100 $\chi_{\rm D}$. Only for high UV-fields around 10^4 $\chi_{\rm D}$ this peak is shifted to the 24 μm band. Thus, our KOSMA-τ findings imply that in our case the dust emission should have its maximum at 24 μm and fall off for higher wavelenghts and also for 8 μm.

Maps of Hα directly detect H II regions that are created by strong UV radiation illuminating molecular clouds. The source of these fields are mostly nearby hot stars that are embedded in molecular clouds, where the can trigger further star formation (see Sect. 2.1.1). Here, we use a map of the SuperCOSMOS Hα Survey (SHS) (Parker et al. 2005), observed with the UK Schmidt Telescope (UKST), to trace this UV radiation in our filament.

Figure 7.16 shows plots of the *Spitzer* GLIMPSE 8 μm map, the MIPSGAL 24 μm map, *Herschel* Hi-GAL maps of three bands (70, 250, and 500 μm), and the SHS map. The position of the ^{13}CO filament is indicated by contours. We have increased the map size to be able to also recognize nearby sources. On the left of the map we see the ^{13}CO contours of the source 29 (see Fig. 4.4 in Sect. 4.2), in the south we find some diffuse extended ^{13}CO emission which is not directly related to any of our identified sources.

We note that no extended 8 and 24 μm emission is found close to the filament in Fig. 7.16 (a) and (b). Both maps show a very similar structure. There are several spots of emission in the vicinity of the filament and also in those parts which belong to cloud 29. We also find several point sources in this area but only one inside the filament, in the right branch. There are two bright sources directly north of our target, one bright point source in the north of the junction point between left and right branch of our cloud and a more extended one above the right part. Both sources are clearly related to dense clumps in source 5, which is one of the background sources, several kpc away from the W43 complex. They do not have any influence on the cloud that we are interested in here.

[4]Carey et al. (2009) use the interstellar radiation field (ISRF) defined by Mathis et al. (1983), in contrast to the field introduced by Draine (1978), which is used by the KOSMA-τ model. The Draine-Field is a factor of $\sim$1.4 higher than the Mathis-Field, thus, the order of magnitude of both fields is comparable.

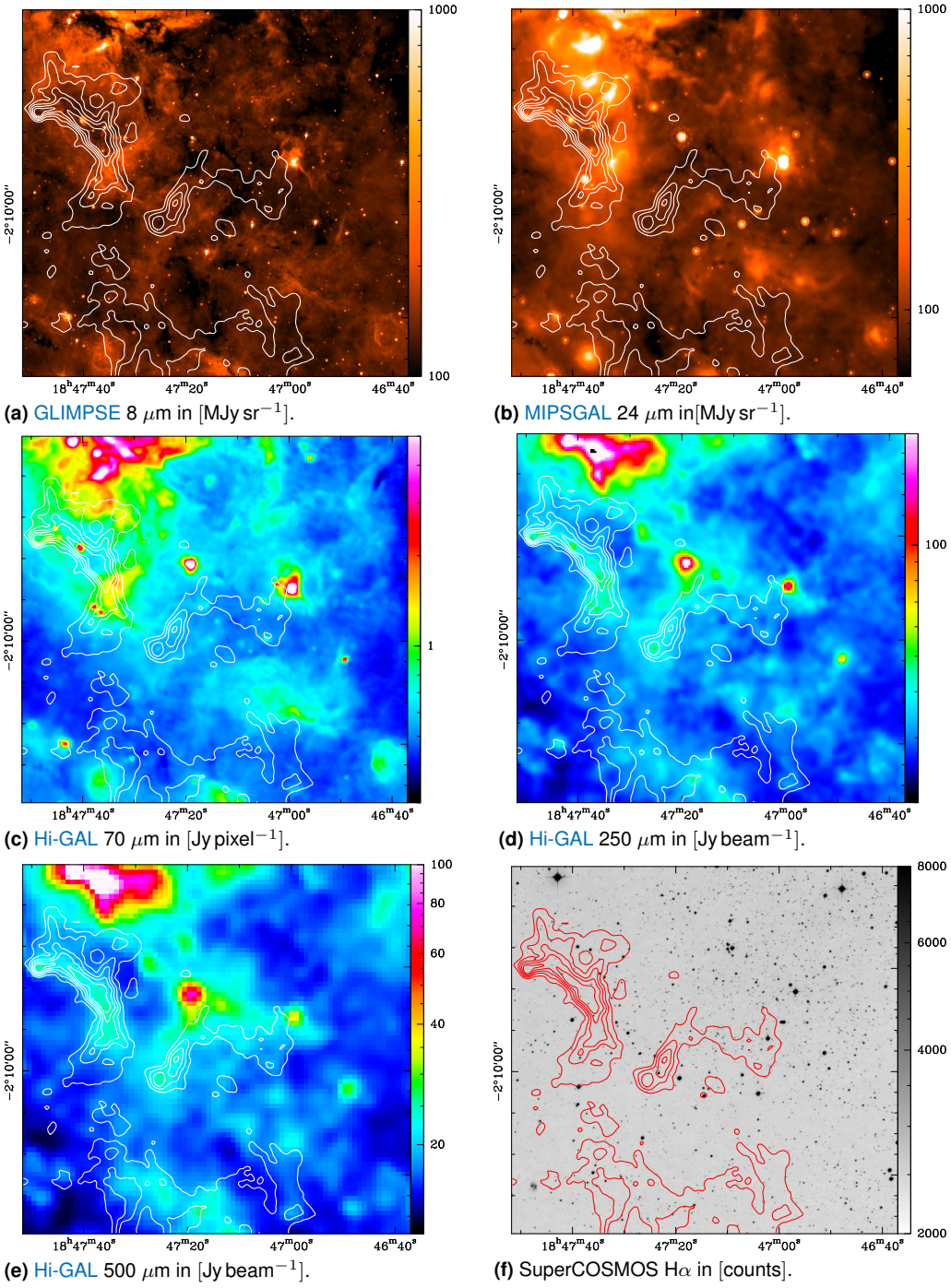

(a) GLIMPSE 8 μm in [MJy sr^{-1}].
(b) MIPSGAL 24 μm in[MJy sr^{-1}].
(c) Hi-GAL 70 μm in [Jy pixel^{-1}].
(d) Hi-GAL 250 μm in [Jy beam^{-1}].
(e) Hi-GAL 500 μm in [Jy beam^{-1}].
(f) SuperCOSMOS Hα in [counts].

Fig. 7.16: Overlay of ^{13}CO (2–1) contours on PAH, dust and UV emission maps.

The area covered by our filament shows the typical background brightness, probably even a bit fainter than most parts of the map. However, it is not faint enough to be considered an absorption feature. There are several dark absorbed

patches and lines seen in the map, some of them could be considered IRDCs. Still, none are obviously related to our cloud. It seems that the 8 and 24 μm *Spitzer* emission is totally unaffected by this source.

It would be possible that the source is not visible in the 8 and 24 μm maps due to its distance. Its emission could be lost in background or foreground sources, but in contrast, several other sources in W43 at the same distance clearly show extended emission. Examples are sources 22 and 23, although these are larger and much more massive than our cloud (cp. Tables 4.1 and 5.2 in Chapter 5). A clear extended emitting clump can also be seen in the south of source 25, which is directly comparable to our filament in size and mass. This means that it is unlikely that the non-detection of 24 μm is a distance effect. It is more likely that this is due to a lack of UV-heated dust and thus a lack of UV-radiation in the filament.

The ratio of 8 to 24 μm is $\sim$1.3 in the central clump (130:103 MJ sr^{-1}) and the southern clump (126:99 MJ sr^{-1}). The MIPSGAL 70 μm maps are not yet publicly available, only unreduced data can be downloaded from the *Spitzer* data archive. Therefore, we do not plot this map, as the data shows stripes and offsets. However, we can state that no extended emission is seen in our filament and the background emission level es between 1000 and 2000 MJ sr^{-1}, way larger than 8 and 24 μm. Clearly, our filament is not in a regime of high UV radiation ($\sim$10^4 $\chi_{\rm D}$), as the peak emission is not found at 24 μm.

Figure 7.16 (c) to (e) show of Hi-GAL maps of the 70, 250, and 500 μm bands, respectively. We find the dust emission increasing from 70 to 250 μm and decreasing again at 500 μm. We find that the dust emission peaks beyond 70 μm and therefore a UV-field of less than $\sim$100 $\chi_{\rm D}$ has to be assumed, which is way below the values we obtained from the KOSMA-τ model.

Figure 7.16 (e) plots the SHS Hα map which displays an ensemble of point sources. We do not find any strong extended emission, as this survey shows, for example, in the Galactic center region (Parker et al. 2005). Although there are several point sources scattered across the map, most are not related to any of the IRAM 30m or *Spitzer* emission. The bright slightly extended 24 μm source at the upper right part of the filament is found to contain a UV point source. It is probably an H II region heated by a bright embedded star. However, we identified this source before as being located in a different spiral arm, far away from the W43 complex. The other point sources inside the filament are not traced by 24 μm emission and are probably unrelated stars.

We conclude that apparently no strong UV-heated clouds are found in this single filament. Neither the *Spitzer* dust emission, nor the SHS Hα maps show any hint for a strong radiation field in this source. At the moment, we can only give a roughly estimated upper limit for the UV-field of <100 $\chi_{\rm D}$, but we plan to improve this by the time this analysis will be published. However, we can be confident that these observations are not compatible with the field strength derived with the KOSMA-τ model.

7.2.3 Origin of C^+ in the filament

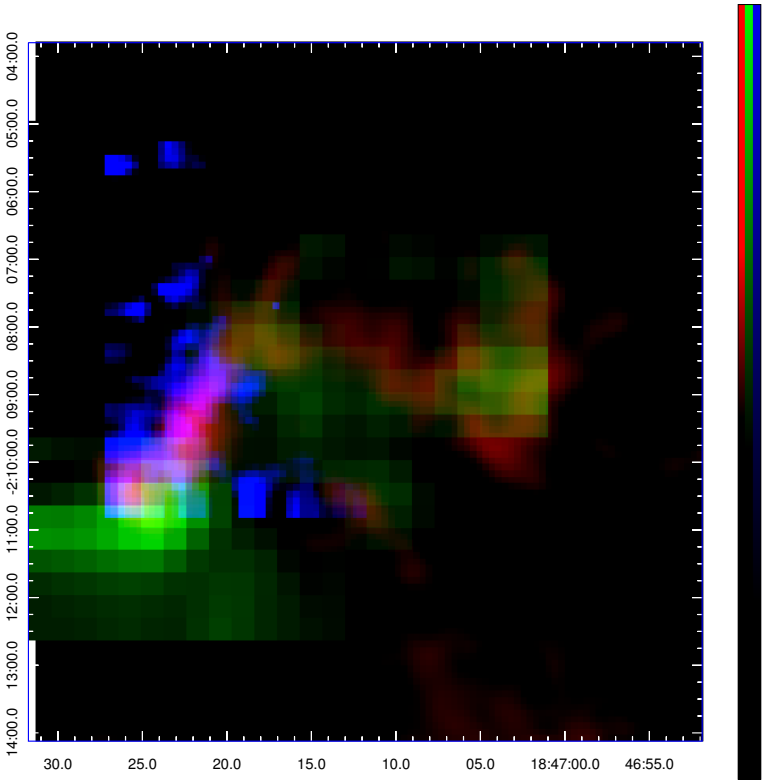

Fig. 7.17: RGB-plot of different carbon emission lines. The blue channel shows [C II], the green channel [C I] and the red channel ^{13}CO (2–1). The different spatial distributions of the three lines become apparent.

We have analyzed a single filament (source 28) in detail in this chapter. As C^+ emission is most often discussed in the framework of static PDRs, where UV radiation photo-dissociates the formerly molecular carbon, we have treated this source accordingly. We tried to simulate our observations with the KOSMA-τ model in Sect. 7.2.2 and found constraints for the UV-field embedding the source and the average density of its gas. Varying the radiation field strength shows a strong dependence of the [C II] line. In Sect. 7.2.2 we analyzed the UV-tracer maps of 24 μm and Hα. Both should show emission in the presence of the strong fields that are necessary to create our observed C^+ emission. However, we do not find any indication for strong radiation. A PDR therefore cannot be the only explanation for our observations.

Another evidence that contradicts the assumption of a PDR is shown in Fig. 7.17. A typical PDR creates a stratification of the [C II], [C I], and CO emission. This is not seen in the RGB-plot of these three lines. The ionized carbon is shifted toward the upper left direction from the ^{13}CO emission. In contrast, atomic carbon is shifted toward the south, which does not point to a typical PDR.

We thus conclude that considering our filament a PDR is misleading. We cannot (completely) explain the observed C^+ emission by assuming a steady-state PDR. Thus, at least part of the [C II] emission has to have a different origin.

The other possibility is that the C^+ emission traces the transition zone between atomic and molecular CO gas. In the initial atomic gas, the WNM, carbon cannot exist in molecular form, but is dissociated. As this gas is very diffuse (see our discussion of the phases of the ISM in Sect. 2.1.2), we cannot detect this C^+ with our current approach. When this initial gas converts to molecular gas, there exists a phase of diffuse molecular gas that has already formed H_2 but it is not dense enough to have already formed CO. This phase is found in observations from gamma-ray observations (Grenier et al. 2005; Abdo et al. 2010) and infrared continuum (Goldsmith et al. 2010). Wolfire et al. (2010) find in their simulations that this phase can take up to 30% of the molecular mass of typical clouds and that this fraction is not sensitive to an existing UV field for fixed column densities.

This phase is traced by [C II], as stated by Pineda et al. (2013); Velusamy et al. (2010) and Langer et al. (2010) that observed several single positions along the Galactic plane with HIFI in their Galactic Observations of Terahertz C^+ (GOT C+) program. Our dataset could be a direct detection of this phase. As stated before, it is still quite warm and of low mass. We would thus witness the dynamic formation process of a young filament from the initial atomic gas.

This picture could also explain the wide distribution of the [C II] emission and the broad line widths in Fig. 7.1 compared to ^{13}CO emission. The broader distribution of C^+ could indicate that the molecular gas as traced by ^{13}CO is still surrounded by an envelope of dark molecular gas that has already formed from the surrounding gas, but ^{13}CO could only form in the dense central parts so far. The higher velocity component, seen in Fig. 7.1 (d) reveals several narrow, elongated regions of emission, perpendicular to the main filament. These can be interpreted as gas streams, collapsing onto the filament, funneling matter into it from the surrounding gas.

The broad line width of C^+ could be interpreted as the warmer and diffuser dark gas that shows stronger turbulences than the already dense and cold CO gas. We also noted before, that the [C II] line is red-shifted in comparison to the ^{13}CO emission. This could indicate that the dark warm gas collapses onto the denser molecular gas from the observers point of view. Also, the difference in line peak velocity, which is demonstrated in Fig. 7.2 in Sect. 7.1.1, could be evidence that C^+ surrounds the CO gas like a shell.

Chapter 8

Summary and Conclusion

We described the process of star formation in Sect. 2.1 and pointed out the relevance of molecular clouds which form from atomic gas. Then, we discussed the formation of these clouds, mentioned the theory of colliding flows, which role filaments play, and showed that a variety of models exist, which try to explain molecular cloud formation. We concluded that many open questions still exist and that it is unclear, which models best describe reality.

8.1 Summary

In order to investigate GMCs and their origin, the W43 HERO project was initiated. This project observed large scale maps of ^{13}CO (2–1) and C^{18}O (2–1) with the IRAM 30m telescope in the star-forming region W43. These lines are ideal to trace the spread out molecular gas of medium density; a high spectral resolution provides the information needed to study the velocity structure of this gas. It was later completed by further observations of a single filament.

We chose the W43 region as target for our project, as it is an ideal place to study the evolution of molecular clouds. It is one of the most massive star-forming regions in our Galaxy and is located at a position of strong gas interactions in the Galactic plane, where matter is swept up (see Sect. 2.1.6). We now summarize the findings of our project that characterize this region.

8.1.1 Analysis of the large scale structure of the W43 complex

We observed maps with a size of $\sim$1.4$\times$1.0 degrees with the IRAM 30m telescope in both lines, which cover the complete W43 molecular cloud complex. Plots of the resulting integrated maps are shown in Fig. 3.5 and Fig. 3.6 in Sect. 3.4.

We found maps, crowded by complex emission. Beside the two main cloud complexes W43-Main and W43-South, a variety of clouds, clumps, and filaments could be recognized. To be able to systematically analyze the dataset, we used the Duchamp Sourcefinder software to identify and separate single sources in the data cubes. We found a total of 29 clouds and characterized position, velocity, and size of each one. These results are given in Table 4.1.

We created a pv diagram from our dataset in Sect. 4.3 and could identify several velocity components. The diagram also revealed the connection between W43-Main and W43-South, which confirmed that both clouds together establish W43, as previously found by Nguyen Luong et al. (2011).

Based on the spectral information of our data and a model of the spiral structure of the Galaxy, we applied distances to the different velocity components of our dataset (see Sect. 4.4). We could disentangle the W43 complex itself from several fore- and background clouds. The W43 complex was found to reside near the tangential point of the Scutum arm, at a distance of about 6 kpc from the Sun. As expected, this places W43 near the tip of the elongated Galactic bar.

We then used the observed intensities of both lines to estimate the optical depth τ of the ^{13}CO line in Sect. 5.1.1. Typical opacities were found to range from a fraction of 1 to about 4 in the typical clouds and filaments. The maximum was found in the southern ridge of W43-Main, where the opacity reaches a value of 8.

The excitation temperature $T_{\rm ex}$ of the gas could be computed (cf. Sect. 5.1.2), using the optical depth. We found typical temperatures of about 10 K in most parts of the clouds, but up to 30 K in several sources. The densest part of our dataset, the northern ridge in W43-Main, even has an excitation temperature of $\sim$60 K. The median value is 12 K.

Finally, we determined the total column density of the molecular gas in Sect. 5.1.3. Typically, these are in the range of a few 10^{21} cm^{-2} to several 10^{22} cm^{-2} in the medium density gas. The highest values were again found in W43-Main, where they peak at 2×10^{23} cm^{-2}. This also allowed us to find the mass of each cloud. A typical source has a mass of several $10^4\ M_\odot$. The total mass of the mid-density molecular gas, as traced by ^{13}CO and C^{18}O, was thus found to be $1.9 \times 10^6\ M_\odot$. Plots of these results of each single identified source can be found in Appendix B.

Next, we calculated the shear parameter of the W43 complex. It determines whether the shear forces, induced by the differential rotation of the Galaxy, is able to disrupt a cloud of a certain size and mass. We concluded that W43 is massive enough to withstand these shear forces.

We also compared our findings with results from *Herschel* dust emission observations. In Sect. 5.5.4 we plotted excitation temperature and H_2 column density maps, as described in Nguyen-Luong et al. (2013). Although we find certain differences, these can be explained by the details of both calculations.

The total mass that was derived from the IRAM 30m observations is a factor of 1.4 lower than that taken from Hi-GAL maps. This discrepancy can mostly be explained by the coverage of our map. In contrast to the *Herschel* maps, we did not calculate a column density value for each single pixel, but used an intensity cut-off. We could thus conclude that our derivation of H_2 column density and mass of the W43 complex is consistent with those derived from *Herschel* maps.

Finally, we created column density PDFs from the IRAM and Hi-GAL observations in Sect. 5.6. The plot in Fig. 5.9 revealed that both PDFs show a log-normal distribution at lower masses and a power-law tail at higher masses. This is usually considered a sign of onsetting star-formation activity in the clouds. We appreciate that we were able to trace denser gas with the applied optical depth correction. Still, the IRAM function breaks off at lower masses and the power-law tail is less steep than the *Herschel* PDF. However, we found that creating PDFs from molecular emission lines can be an effective tool to study the conditions in molecular gas.

8.1.2 Analysis of a single filament in W43

In the next step, we initiated a series of smaller scale observations of a single filament, in order to study it in greater detail. We wanted to further estimate the physical conditions of this filament and, if possible, analyze its formation process. We conducted observations of C^+ with the *Herschel* HIFI instrument, of CO (6–5) with APEX, [C I] with NANTEN2, and HCN, HCO^+, and N_2H^+ with CARMA. The details of these observations are described in Chapter 6.

This filament has a length of 13.2 pc and an average width of 2.4 pc. From the two CO isotopologues we found an average opacity of 1.3, a median excitation temperature of 9.9 K, and a mean H_2 column density of 4.1×10^{21} cm^{-2}. The total mass of this source was determined to be $4.3 \times 10^3\ M_\odot$.

We used the combination of data to estimate the density and the temperature of the molecular gas. We picked two positions, the ^{13}CO intensity peak in the central clump and the intensity peak in the southern clump of the filament, to which we then applied the next calculations. First, in Sect. 7.2.1, we made a rough estimation of the density at those points, by assuming a cylindrical geometry of the filament, and then computing the average density along the line of sight from the H_2 column density. We found values of 1.0×10^3 cm^{-3} at the center position and 2.0×10^3 cm^{-3} at the southern position.

Next, we used the RADEX algorithm, which models line intensities for several CO species from input values for temperature, density, and column density of the assumed model cloud (cf. Sect. 7.2.1). We could thus create a grid of input parameters and find the set of parameters that would lead to those simulated results which would best fit our observations. These best fit values are given in Table 7.1, we find kinetic temperatures between 25 and 35 K, densities around

10^4 cm^{-3}, and H_2 column densities of $\sim 10^{22}$ cm^{-2}. All values are consistent with our previous findings, at least if we take the uncertainties into account that we discussed during the description of the calculations.

In Sect. 7.2.1 we then used the CARMA observation to assume a lower limit for the density of the central parts of the filament. Here, we found values of a few 10^4 cm^{-3} from taking the critical density of these lines into account.

Finally, in Sect. 7.2.2, we analyzed the C^+ emission in our filament. If we assume that the ionized carbon is created by a PDR, a certain UV-field would be necessary to explain the observed emission. We used the KOSMA-τ software to obtain the UV-field, gas density, and total mass contained in the beam, that would be needed to create the observed line strengths. The results are shown in Fig. 7.15. The obtained radiation field strength was surprisingly high and we therefore checked, whether this would be realistic.

Inspecting typical UV-tracer observations at these positions, we did not find any signs for a strong UV-field. The assumption of [C II] emission in the context of a PDR is therefore unsustainable and a different origin has to be found.

8.2 Conclusion

Our project W43 HERO led to a complete description of the mid-density molecular gas in the W43 region. The distribution of ^{13}CO and C^{18}O emission is now well documented. We gave a thorough description of found sources and their properties.

With an analysis of the velocity information in our dataset and a comparison with a dynamic model of the Galactic spiral structure we could clearly fix the position of W43 in our Galaxy (Sect. 4.4). It is located near the tangential point of the Scutum arm near the tip of the elongated bar. We could distinguish the complex from foreground and background clouds.

Temperature, H_2 column density, and mass of the molecular gas were determined and give a characterization of the physical conditions in the clouds (cf. Tables 5.1 and 5.2). The total mass of the molecular clouds in the W43 complex was found to be $1.9 \times 10^6\ M_\odot$ and is thus one of the most massive molecular cloud complexes in the Milky Way, (cf. also the comparison of several GMCs in Nguyen Luong et al. 2011). We calculated the shear parameter and concluded that W43 is massive enough to withstand the disrupting forces of differential rotation in the Galaxy. These findings are compatible with the results taken from *Herschel* dust maps, which emphasizes that our method yields realistic values, although the detailed distribution differs slightly.

The PDF that we derived in Fig. 5.9 in Sect. 5.6 shows clear signs of collapsing clouds in W43 and thus active star formation. The dust and the molecular emission line PDF show certain differences, which would have to be studied in

other sources to ensure that these are structural. It is possible that the molecular line PDF rather traces the collapsing gas in the clouds. Therefore, it could be an interesting diagnostics tool for further studies of star-forming regions.

In the next step we analyzed a single filament in greater detail. Source 28 was found to be a filament of clearly defined shape and smaller than average size and mass. We concentrated on the analysis of one of its two branches as we only detected emission of all lines in this part. The source shows a clear velocity gradient along this branch of which varies between 3 and 4 km s^{-1} in different lines. This gradient is evidence of the differential movement of the gas. However, there are different possible explanations for this. The filament could either expand or collapse along its length or this could be expression of the dynamical movement of this source.

We then conducted a series of estimations of temperature and volume density at two distinct positions in the filament. We found a typical kinetic temperature between 25 and 35 K. The typical density of the CO gas is on the order of 10^4 cm^{-3} and the central narrow backbone, which is traced by our CARMA observations, has densities of at least a few times 10^4 cm^{-3}. We can therefore identify this source as a small, medium dense cloud which is still quite warm and has probably not accreted much mass, yet.

Finally, we studied the [C II] emission that we observed with HIFI. In most cases, emission of C^+ is discussed in the context of PDRs (e.g. Röllig et al. 2011; Israel and Maloney 2011; Pineda et al. 2010), which would require an ionizing UV-field. However, in Sect. 7.2.2 we found an unrealistically high UV-field, necessary to explain the C^+ emission in our case. In Sect. 7.2.3 we then concluded that a PDR can be ruled out as the only origin of [C II] in our analyzed filament. Most of the emission has to have a different cause.

Probably, the [C II] emission traces the transition zone between the initial warm atomic gas and the cold molecular gas. It denotes this zone, where H_2 has already formed but CO could not form yet. The data would therefore depict the dynamic formation of the filament. From the distribution of C^+ and the broad line widths we conclude that we observe matter currently collapsing onto the filament.

Is it now possible to make a statement about the exact formation process of this filament or even the whole W43 complex? Probably not. None of our observations contradict the notion of colliding flows, but they could also be compatible with other formation processes. Also, the information of one single filament does not imply information about the large scale condition, although it may be tempting. Therefore, we cannot distinguish between different formation processes at the moment.

8.3 Outlook

Although this thesis tried to draw a picture of the W43 region as complete as possible from the existing data, there are still several open questions and pending tasks. First of all, the filament observations and their analysis in Chapter 7 still await publication. We will write an article, containing this analysis but also go into more detail at specific points. In addition to the KOSMA-τ software we will use other PDR algorithms to verify our results concerning the calculated UV-field. There, we also aim at giving a more exact upper limit of the UV-field, derived from the UV-field tracers. For this purpose, it would be interesting to propose a radio continuum observation of the filament with the VLA. It could search for embedded H II regions that could account for the UV-field, but which are not visible in 24 μm emission.

Also, we plan to propose a re-observation of the filament in C I with the APEX telescope. The NANTEN2 observations are quite coarse compared to all other observation, with a HPBW of nearly 40″. Also, the SMART receiver was rather unstable during our observation time. A new observation would probably improve the data quality significantly.

Some interesting studies of filament structures have been conducted lately. Arzoumanian et al. (2011) find a typical filament width of 0.1 pc in *Herschel* dust maps, while Hacar et al. (2013) analyze a filamentary cloud, about the size of our typical filamentary sources, and find that it breaks down into a bundle of smaller filaments of sub-parsec length. Due to the distance of W43, these kind of studies are not possible with our data. The resolved spatial scale is ~ 0.3 pc, which is too large for a detailed breakdown of our clouds. We suspect, that each of our identified sources features a sub-structure, which is not available to us, yet. Therefore, we plan to propose the observation of a single filament (source 26 would be a good candidate, as it already shows several sub-filaments) with ALMA during the next observation cycle. With this interferometer we could achieve much higher spatial resolution, a factor of 10 increase would easily be feasible, and even higher resolution would be possible. Thus, the sub-parsec scale would become accessible to us.

We know, that magnetic fields play an important role in the formation of filaments. Observations of the polarization of dust emission could be a way to give an idea of the strength and direction of magnetic fields in our filament. However, these polarization observations are often complicated to perform and concluding from *Herschel* dust maps in this region, separating information of a single filament from the superimposed sources would be extremely difficult.

Another desirable project would be to observe C^+ emission on larger scales in W43 to check if our findings could also be reproduced in other parts of the complex. A complete map of the region could provide a complete picture of the formation of this GMC and probably answer the question of the detailed formation process. However, the only facility to observe [C II] at the moment is

SOFIA and observing a square degree map of [C II] with the needed noise level would take on the order of thousands of hours to observe. This complete map will therefore stay a great dream for a long time.

Anyway, there is also still information in the existing datasets that could be extracted. Although we gave a first decomposition of the CO data cubes in this work and Klatt (2013) did a similar manual search for sources, a systematic search for filaments in three dimensions has not been realized, yet. The Discrete Persistent Structures Extractor (DisPerSE) algorithm was created to find filaments in cosmological simulations (Sousbie 2011; Sousbie et al. 2011), but it can also be used in molecular line emission cubes. First tests on the W43 data have already be done, but a thorough study has still to be conducted. The aim is to compile a complete list of all filaments found in W43, their exact position, shape, and scale. In the best case, the software could be used to automate a statistical analysis of the filaments properties.

In addition, the velocity field of the complex has not been completely described, so far. It is still unclear whether it is possible to discover the imprint of the initial Galactic gas streams in the region's velocity structure. Motte el al. in prep. claim to find evidence of converging gas streams in the velocity distribution of large scale (on the order of 100 pc) gas streams of H I and CO. Can this signature also be found in our dataset, which covers a smaller region, but has a higher spectral and spatial resolution? Could this be used to verify the creation of the whole W43 region by converging flows?

The most important open questions are presumable the following:

- Can the theory of colliding flows be verified by observations of W43?
- What additional observations would be needed?
- Can different models be distinguished by comparison with observations?

Thus, our final conclusion from this thesis is that we learned much about the W43 complex. We gave a full characterization of the molecular clouds in the region and gained first insights into its formation process by analyzing a single filament. We find that a PDR is an unlikely explanation for our observations and that the [C II] emission most likely originates from the dynamic formation process of the filament. Although our findings are compatible with colliding flows, we cannot verify this with certainty. But our work provides the fundament for further investigations to verify the theory of colliding flows or distinguish between different classes of models.

References

Abdo, A. A., M. Ackermann, et al. (2010). In: ApJ 710, pp. 133–149 (cit. on p. 133).

Anderson, L. D. and T. M. Bania (2009). In: ApJ 690, pp. 706–719 (cit. on p. 19).

André, P., A. Men'shchikov, et al. (2010). In: A&A 518, L102, p. L102 (cit. on pp. 2, 7, 9, 15).

Arzoumanian, D., P. André, et al. (2011). In: A&A 529, L6, p. L6 (cit. on pp. 15, 46, 116, 123, 140).

Audit, E. and P. Hennebelle (2005). In: A&A 433, pp. 1–13 (cit. on pp. 12, 13, 16).

Ballesteros-Paredes, J. (2006). In: MNRAS 372, pp. 443–449 (cit. on pp. 68, 69).

Bally, J., L. D. Anderson, et al. (2010). In: A&A 518, pp. L90+ (cit. on p. 74).

Banerjee, R. and R. E. Pudritz (2007). In: ApJ 660, pp. 479–488 (cit. on p. 10).

Banerjee, R., E. Vázquez-Semadeni, et al. (2009). In: MNRAS 398, pp. 1082–1092 (cit. on pp. 2, 13, 16).

Battersby, C., J. Bally, et al. (2011). In: A&A 535, A128, A128 (cit. on pp. 74, 77).

Beltrán, M. T., L. Olmi, et al. (2013). In: A&A 552, A123, A123 (cit. on p. 84).

Benjamin, R. A., E. Churchwell, et al. (2003). In: PASP 115, pp. 953–964 (cit. on p. 71).

Benson, P. J. and P. C. Myers (1989). In: ApJS 71, pp. 89–108 (cit. on p. 7).

Beuther, H., E. B. Churchwell, et al. (2007). In: *Protostars and Planets V*, pp. 165–180 (cit. on p. 9).

Bihr, S., H. Beuther, et al. (2013). In: *Protostars and Planets VI, Heidelberg, July 15-20, 2013. Poster #1S050*, p. 50 (cit. on pp. 73, 74).

Binney, J. (1982). In: MNRAS 201, pp. 1–14 (cit. on p. 18).

Bisbas, T. G., T. A. Bell, et al. (2012). In: MNRAS 427, pp. 2100–2118 (cit. on p. 125).

Blum, R. D., A. Damineli, and P. S. Conti (1999). In: AJ 117, pp. 1392–1401 (cit. on p. 19).

Bodenheimer, P. (1978). In: ApJ 224, pp. 488–496 (cit. on p. 9).

Bohlin, R. C. (1975). In: ApJ 200, pp. 402–414 (cit. on p. 12).

Bohlin, R. C., B. D. Savage, and J. F. Drake (1978). In: ApJ 224, pp. 132–142 (cit. on p. 79).

Bondi, H. (1952). In: MNRAS 112, p. 195 (cit. on p. 9).

Bonnell, I. A., M. R. Bate, and S. G. Vine (2003). In: MNRAS 343, pp. 413–418 (cit. on p. 10).
Burke, J. R. and D. J. Hollenbach (1983). In: ApJ 265, pp. 223–234 (cit. on p. 13).
Burkert, A. and L. Hartmann (2013). In: ApJ 773, 48, p. 48 (cit. on p. 8).
Carey, S. J., A. Noriega-Crespo, et al. (2009). In: PASP 121, pp. 76–97 (cit. on pp. 73, 129).
Carlhoff, P., Q. Nguyen Luong, et al. (2013). In: A&A 560, A24, A24 (cit. on pp. 4, 31, 87).
Caselli, P., P. C. Myers, and P. Thaddeus (1995). In: ApJ 455, p. L77 (cit. on pp. 28, 95).
Casuso, E. and J. E. Beckman (2010). In: AJ 139, pp. 1406–1412 (cit. on p. 12).
Chabrier, G. (2003). In: ApJ 586, pp. L133–L136 (cit. on p. 7).
Charnley, S. B. and S. B. Rodgers (2009). In: *Bioastronomy 2007: Molecules, Microbes and Extraterrestrial Life*. Ed. by K. J. Meech, J. V. Keane, et al. Vol. 420. Astronomical Society of the Pacific Conference Series, p. 29 (cit. on p. 12).
Chen, W., N. Gehrels, et al. (1996). In: A&AS 120, p. C315 (cit. on p. 17).
Christopher, M. H., N. Z. Scoville, et al. (2005). In: ApJ 622, pp. 346–365 (cit. on p. 123).
Churchwell, E., B. L. Babler, et al. (2009). In: PASP 121, pp. 213–230 (cit. on pp. 18, 71).
Clemens, D. P. (1985). In: ApJ 295, pp. 422–428 (cit. on pp. 18, 52).
Connors, T. W., D. Kawata, and B. K. Gibson (2006). In: MNRAS 371, pp. 108–120 (cit. on p. 18).
Crutcher, R. M., N. Hakobian, and T. H. Troland (2009). In: ApJ 692, pp. 844–855 (cit. on p. 9).
Dame, T. M., D. Hartmann, and P. Thaddeus (2001). In: ApJ 547, pp. 792–813 (cit. on pp. 19, 26).
Daniel, F., J. Cernicharo, and M.-L. Dubernet (2006). In: ApJ 648, pp. 461–471 (cit. on p. 124).
de Graauw, T., F. P. Helmich, et al. (2010). In: A&A 518, L6, p. L6 (cit. on pp. 88, 89).
Dib, S., G. Helou, et al. (2012). In: ApJ 758, 125, p. 125 (cit. on pp. 66, 67).
Draine, B. T. (1978). In: ApJS 36, pp. 595–619 (cit. on pp. 128, 129).
— (2011). Princeton University Press, (cit. on pp. 9, 11, 24, 27).
Dutrey, A., G. Duvert, et al. (1991). In: A&A 247, pp. L9–L12 (cit. on p. 15).
Dwek, E., R. G. Arendt, et al. (1997). In: ApJ 475, p. 565 (cit. on p. 13).
Dwek, E. and J. M. Scalo (1980). In: ApJ 239, pp. 193–211 (cit. on p. 12).
Eden, D. J., T. J. T. Moore, et al. (2013). In: MNRAS 431, pp. 1587–1595 (cit. on p. 18).
Edwards, S., T. Ray, and R. Mundt (1993). In: *Protostars and Planets III*. Ed. by E. H. Levy and J. I. Lunine, pp. 567–602 (cit. on p. 9).
Egan, M. P., R. F. Shipman, et al. (1998). In: ApJ 494, p. L199 (cit. on p. 72).
Evans II, N. J. (1999). In: ARA&A 37, pp. 311–362 (cit. on pp. 10, 26, 123).

Evans II, N. J., M. M. Dunham, et al. (2009). In: ApJS 181, 321, pp. 321–350 (cit. on p. 8).
Federrath, C., J. Roman-Duval, et al. (2010). In: A&A 512, A81+ (cit. on p. 78).
Ferland, G. J., R. L. Porter, et al. (2013). In: Rev. Mexicana Astron. Astrofis. 49, pp. 137–163 (cit. on p. 125).
Ferrarotti, A. S. and H.-P. Gail (2006). In: A&A 447, pp. 553–576 (cit. on p. 12).
Ferrière, K. M. (2001). In: *Reviews of Modern Physics* 73, pp. 1031–1066 (cit. on p. 11).
Fiege, J. D. and R. E. Pudritz (2000). In: MNRAS 311, pp. 105–119 (cit. on p. 16).
Field, G. B., D. W. Goldsmith, and H. J. Habing (1969). In: ApJ 155, p. L149 (cit. on p. 11).
Fontani, F., A. Giannetti, et al. (2012). In: MNRAS 423, pp. 2342–2358 (cit. on p. 63).
Frisch, P. C. and J. D. Slavin (2003). In: ApJ 594, pp. 844–858 (cit. on p. 12).
Galametz, M., R. C. Kennicutt, et al. (2012). In: MNRAS 425, pp. 763–787 (cit. on p. 12).
Gent, F. A., A. Shukurov, et al. (2013). In: MNRAS 432, pp. 1396–1423 (cit. on p. 12).
Genzel, R., C. Pichon, et al. (2000). In: MNRAS 317, pp. 348–374 (cit. on p. 18).
Ghez, A. M., S. Salim, et al. (2008). In: ApJ 689, pp. 1044–1062 (cit. on p. 18).
Glover, S. C. O. and M.-M. Mac Low (2007). In: ApJ 659, pp. 1317–1337 (cit. on p. 16).
Goldbaum, N. J., M. R. Krumholz, et al. (2011). In: ApJ 738, 101, p. 101 (cit. on p. 13).
Goldsmith, Paul (1996). In: *in Chemistry, Physics, and Observations of Molecules in Space: Proceedings of the 1996 INAOE Summer School on Millimeter-Wave Astronomy* (cit. on p. 21).
Goldsmith, P. F., T. Velusamy, et al. (2010). In: ApJ 715, pp. 1370–1382 (cit. on p. 133).
Gómez, G. C., B. Pichardo, and M. A. Martos (2013). In: MNRAS 430, pp. 3010–3016 (cit. on p. 18).
Gonzalez-Alfonso, E. and J. Cernicharo (1993). In: A&A 279, pp. 506–520 (cit. on p. 95).
Goodman, A. A., J. E. Pineda, and S. L. Schnee (2009). In: ApJ 692, pp. 91–103 (cit. on p. 78).
Graf, U. U., C. E. Honingh, et al. (2008). In: *Ninteenth International Symposium on Space Terahertz Technology*. Ed. by W. Wild, p. 488 (cit. on p. 100).
Grenier, I. A., J.-M. Casandjian, and R. Terrier (2005). In: *Science* 307, pp. 1292–1295 (cit. on p. 133).
Griffin, M. J., A. Abergel, et al. (2010). In: A&A 518, L3, p. L3 (cit. on p. 89).
Güsten, R., L. Å. Nyman, et al. (2006). In: A&A 454, pp. L13–L16 (cit. on p. 92).
Hacar, A., M. Tafalla, et al. (2013). In: A&A 554, A55, A55 (cit. on pp. 15, 47, 116, 140).

Hänsel, A. and W. Neumann (1995). Spektrum Akademischer Verlag, Heidelberg (cit. on p. 24).
Hayashi, C., S. Narita, and S. M. Miyama (1982). In: *Progress of Theoretical Physics* 68, pp. 1949–1966 (cit. on p. 9).
Heitsch, F., A. Burkert, et al. (2005). In: ApJ 633, pp. L113–L116 (cit. on p. 12).
Heitsch, F., L. W. Hartmann, and A. Burkert (2008). In: ApJ 683, pp. 786–795 (cit. on p. 13).
Heitsch, F., A. D. Slyz, et al. (2006). In: ApJ 648, pp. 1052–1065 (cit. on p. 16).
Hennebelle, P., R. Banerjee, et al. (2008). In: A&A 486, pp. L43–L46 (cit. on pp. 13, 16).
Hennebelle, P. and G. Chabrier (2008). In: ApJ 684, pp. 395–410 (cit. on p. 16).
Herbig, G. H. (1962). In: *Advances in Astronomy and Astrophysics* 1, pp. 47–103 (cit. on p. 5).
Hernández, J., N. Calvet, et al. (2007). In: ApJ 671, pp. 1784–1799 (cit. on p. 9).
Hertz, H. (1887). In: *Annalen der Physik* 267, pp. 421–448 (cit. on p. 1).
Hill, T., P. André, et al. (2012). In: A&A 548, L6, p. L6 (cit. on p. 74).
Hill, T., S. N. Longmore, et al. (2010). In: MNRAS 402, pp. 2682–2702 (cit. on pp. 74, 76).
Hill, T., F. Motte, et al. (2011). In: A&A 533, A94, A94 (cit. on pp. 74, 78).
Hill, T., C. Pinte, et al. (2009). In: MNRAS 392, pp. 768–782 (cit. on p. 74).
Hoare, M. G., S. E. Kurtz, et al. (2007). In: *Protostars and Planets V*, pp. 181–196 (cit. on p. 10).
Hollenbach, D. J. and A. G. G. M. Tielens (1997). In: ARA&A 35, pp. 179–216 (cit. on pp. 72, 124, 125).
Hollenbach, D. and E. E. Salpeter (1971). In: ApJ 163, p. 155 (cit. on p. 12).
Hoyle, F. and R. A. Lyttleton (1939). In: *Proceedings of the Cambridge Philosophical Society* 35, p. 405 (cit. on p. 9).
Inoue, Y. and T. Totani (2009). In: ApJ 702, 523, pp. 523–536 (cit. on p. 16).
Israel, F. P. and P. R. Maloney (2011). In: A&A 531, A19, A19 (cit. on pp. 124, 139).
Jackson, J. M., J. M. Rathborne, et al. (2006). In: ApJS 163, pp. 145–159 (cit. on pp. 19, 65).
Jansky, K. G. (1933). In: *Popular Astronomy* 41, p. 548 (cit. on p. 1).
Johnstone, D., E. Rosolowsky, et al. (2010). In: ApJ 711, pp. 655–670 (cit. on p. 124).
Kainulainen, J., H. Beuther, et al. (2009). In: A&A 508, pp. L35–L38 (cit. on pp. 14, 78).
Kasemann, C., R. Güsten, et al. (2006). In: *Society of Photo-Optical Instrumentation Engineers (SPIE) Conference Series*. Vol. 6275. Society of Photo-Optical Instrumentation Engineers (SPIE) Conference Series (cit. on p. 93).
Kawamura, A., N. Mizuno, et al. (2005). In: *IAU Symposium*. Vol. 235. IAU Symposium, 275P (cit. on p. 99).
Kennicutt Jr., R. C. (1998). In: ApJ 498, p. 541 (cit. on p. 8).
Kim, S.-H., P. G. Martin, and P. D. Hendry (1994). In: ApJ 422, pp. 164–175 (cit. on p. 13).

Klatt, P. (2013). Bachelorthesis (cit. on pp. 115, 116, 141).
Klessen, R. S. (2000). In: ApJ 535, pp. 869–886 (cit. on pp. 14, 78).
Klessen, R. S. and A. Burkert (2001). In: ApJ 549, pp. 386–401 (cit. on p. 9).
Klessen, R. S. and P. Hennebelle (2010). In: A&A 520, A17, A17 (cit. on p. 13).
Könyves, V., P. André, et al. (2010). In: A&A 518, L106, p. L106 (cit. on pp. 7, 8).
Koyama, H. and S.-i. Inutsuka (2002). In: ApJ 564, pp. L97–L100 (cit. on p. 12).
Kritsuk, A. G., C. T. Lee, and M. L. Norman (2013). In: MNRAS (cit. on p. 69).
Kroupa, P. (2001). In: MNRAS 322, pp. 231–246 (cit. on p. 7).
Kuiper, R., H. Klahr, et al. (2010). In: ApJ 722, pp. 1556–1576 (cit. on p. 10).
Kurtz, S. (2005). In: *Massive Star Birth: A Crossroads of Astrophysics*. Ed. by R. Cesaroni, M. Felli, et al. Vol. 227. IAU Symposium, pp. 111–119 (cit. on p. 10).
Lada, C. J., J. F. Alves, and M. Lombardi (2007). In: *Protostars and Planets V*, pp. 3–15 (cit. on p. 7).
Ladd, E. F., G. A. Fuller, and J. R. Deane (1998). In: ApJ 495, p. 871 (cit. on pp. 57, 59).
Langer, W. D., T. Velusamy, et al. (2010). In: A&A 521, pp. L17+ (cit. on p. 133).
Larson, R. B. (1981). In: MNRAS 194, pp. 809–826 (cit. on p. 69).
— (2003). In: *Reports on Progress in Physics* 66, pp. 1651–1697 (cit. on p. 9).
Lebouteiller, V., J. Bernard-Salas, et al. (2011). In: ApJ 728, 45, p. 45 (cit. on p. 12).
Leger, A. and J. L. Puget (1984). In: A&A 137, pp. L5–L8 (cit. on p. 12).
Le Petit, F., C. Nehmé, et al. (2006). In: ApJS 164, pp. 506–529 (cit. on p. 125).
Lester, D. F., H. L. Dinerstein, et al. (1985). In: ApJ 296, pp. 565–575 (cit. on p. 19).
Levine, E. S., L. Blitz, and C. Heiles (2006). In: *Science* 312, pp. 1773–1777 (cit. on p. 18).
Li, D. and P. F. Goldsmith (2003). In: ApJ 585, pp. 823–839 (cit. on p. 13).
Lin, C. C. and F. H. Shu (1964). In: ApJ 140, p. 646 (cit. on p. 18).
Liszt, H. S. (1995). In: AJ 109, pp. 1204–1210 (cit. on p. 83).
Low, C. and D. Lynden-Bell (1976). In: MNRAS 176, pp. 367–390 (cit. on p. 9).
Lynden-Bell, D. and A. J. Kalnajs (1972). In: MNRAS 157, p. 1 (cit. on p. 18).
Lynden-Bell, D. and J. E. Pringle (1974). In: MNRAS 168, pp. 603–637 (cit. on p. 9).
Marconi, A., L. Testi, et al. (1998). In: A&A 330, pp. 696–710 (cit. on p. 128).
Martin, P. G., M.-A. Miville-Deschênes, et al. (2010). In: A&A 518, L105, p. L105 (cit. on p. 77).
Mathis, J. S., P. G. Mezger, and N. Panagia (1983). In: A&A 128, pp. 212–229 (cit. on p. 129).
Mathis, J. S., W. Rumpl, and K. H. Nordsieck (1977). In: ApJ 217, pp. 425–433 (cit. on p. 12).
Matzner, C. D. and C. F. McKee (2000). In: ApJ 545, pp. 364–378 (cit. on p. 8).
Maxwell, J. C. (1873). Clarendon Press, Oxford, Macmillan and Co., London (cit. on p. 1).

McKee, C. F. and E. C. Ostriker (2007). In: ARA&A 45, pp. 565–687 (cit. on pp. 2, 5, 11).
McKee, C. F. and J. P. Ostriker (1977). In: ApJ 218, pp. 148–169 (cit. on p. 12).
Mezger, P. G. and L. F. Smith (1977). In: *Star Formation*. Ed. by T. de Jong and A. Maeder. Vol. 75. IAU Symposium, pp. 133–163 (cit. on p. 6).
Milam, S. N., C. Savage, et al. (2005). In: ApJ 634, pp. 1126–1132 (cit. on p. 59).
Molinari, S., B. Swinyard, et al. (2010). In: A&A 518, pp. L100+ (cit. on pp. 7, 9, 15, 74, 89).
Moore, T. J. T., J. S. Urquhart, et al. (2012). In: MNRAS 426, pp. 701–707 (cit. on p. 18).
Motte, F., P. Schilke, and D. C. Lis (2003). In: ApJ 582, pp. 277–291 (cit. on pp. 19, 54, 81, 82).
Motte, F., A. Zavagno, et al. (2010). In: A&A 518, L77, p. L77 (cit. on p. 74).
Myers, P. C. (2009). In: ApJ 700, pp. 1609–1625 (cit. on p. 16).
Myers, P. C., T. M. Dame, et al. (1986). In: ApJ 301, pp. 398–422 (cit. on p. 8).
Myers, P. C., R. A. Linke, and P. J. Benson (1983). In: ApJ 264, pp. 517–537 (cit. on p. 57).
Nakamura, F. and Z.-Y. Li (2008). In: ApJ 687, pp. 354–375 (cit. on p. 16).
Nakano, T. (1983). In: PASJ 35, pp. 87–90 (cit. on p. 9).
Nguyen Luong, Q., F. Motte, et al. (2011). In: A&A 529, A41+ (cit. on pp. 2, 19, 47, 52, 65, 68, 73, 136, 138).
Nguyen-Luong, Q., F. Motte, et al. (2013). In: ApJ 775, 88, p. 88 (cit. on pp. 53, 66, 74–77, 136).
Nishiyama, S., T. Nagata, et al. (2005). In: ApJ 621, pp. L105–L108 (cit. on p. 18).
Onishi, T., A. Mizuno, et al. (2002). In: ApJ 575, pp. 950–973 (cit. on p. 7).
Ossenkopf, V., M. Krips, and J. Stutzki (2008a). In: A&A 485, pp. 719–727 (cit. on p. 14).
— (2008b). In: A&A 485, pp. 917–929 (cit. on p. 14).
Ossenkopf, V., M. Röllig, et al. (2013). In: A&A 550, A57, A57 (cit. on p. 91).
Ostriker, J. (1964). In: ApJ 140, p. 1529 (cit. on p. 16).
Ott, S. (2011). In: *Astronomical Data Analysis Software and Systems XX*. Ed. by I. N. Evans, A. Accomazzi, et al. Vol. 442. Astronomical Society of the Pacific Conference Series, p. 347 (cit. on p. 91).
Padoan, P., M. Juvela, et al. (2001). In: ApJ 553, pp. 227–234 (cit. on p. 16).
Palmeirim, P., P. André, et al. (2013). In: A&A 550, A38, A38 (cit. on p. 7).
Pandian, J. D., E. Momjian, and P. F. Goldsmith (2008). In: A&A 486, pp. 191–208 (cit. on p. 19).
Parker, Q. A., S. Phillipps, et al. (2005). In: MNRAS 362, pp. 689–710 (cit. on pp. 129, 131).
Parkin, T. J., C. D. Wilson, et al. (2012). In: MNRAS 422, pp. 2291–2301 (cit. on p. 12).
Passot, T. and E. Vázquez-Semadeni (1998). In: Phys. Rev. E 58, pp. 4501–4510 (cit. on p. 78).

Peeters, E., H. W. W. Spoon, and A. G. G. M. Tielens (2004). In: ApJ 613, pp. 986–1003 (cit. on p. 72).
Peretto, N. and G. A. Fuller (2009). In: A&A 505, pp. 405–415 (cit. on p. 72).
Pérez-Beaupuits, J. P., H. Wiesemeyer, et al. (2012). In: A&A 542, L13, p. L13 (cit. on p. 124).
Pichardo, B., M. Martos, and E. Moreno (2004). In: ApJ 609, pp. 144–165 (cit. on p. 18).
Pilbratt, G. L., J. R. Riedinger, et al. (2010). In: A&A 518, L1, p. L1 (cit. on p. 88).
Pineda, J. L., W. D. Langer, et al. (2013). In: A&A 554, A103, A103 (cit. on p. 133).
Pineda, J. L., T. Velusamy, et al. (2010). In: A&A 521, L19, p. L19 (cit. on p. 139).
Planck Collaboration, P. A. R. Ade, et al. (2011). In: A&A 536, A19, A19 (cit. on p. 12).
Poglitsch, A., C. Waelkens, et al. (2010). In: A&A 518, L2, p. L2 (cit. on p. 89).
Popping, G., R. S. Somerville, and S. C. Trager (2013). In: *ArXiv e-prints* (cit. on p. 11).
Pratap, P., S. T. Megeath, and E. A. Bergin (1999). In: ApJ 517, pp. 799–818 (cit. on p. 19).
Purcell, C. R., M. G. Hoare, et al. (2013). In: ApJS 205, 1, p. 1 (cit. on p. 85).
Reid, M. J., K. M. Menten, et al. (2009). In: ApJ 700, pp. 137–148 (cit. on pp. 18, 49, 50, 52).
Rivera-Ingraham, A. et al. (2013). In: in prep. (Cit. on p. 79).
Rix, H.-W. and J. Bovy (2013). In: A&A Rev. 21, p. 61 (cit. on p. 18).
Rodríguez-Fernández, N. J. (2011). In: *Memorie della Societa Astronomica Italiana Supplementi* 18, p. 195 (cit. on pp. 18, 50).
Rodríguez-Fernández, N. J. and F. Combes (2008). In: A&A 489, pp. 115–133 (cit. on pp. 18, 50).
Röllig, M., C. Kramer, et al. (2011). In: A&A 525, A8, A8 (cit. on pp. 124, 128, 139).
Röllig, M., V. Ossenkopf, et al. (2006). In: A&A 451, pp. 917–924 (cit. on p. 125).
Roman-Duval, J., J. M. Jackson, et al. (2009). In: ApJ 699, pp. 1153–1170 (cit. on pp. 49–52).
Rosolowsky, E. (2005). In: PASP 117, pp. 1403–1410 (cit. on p. 7).
Rowles, J. and D. Froebrich (2011). In: MNRAS 416, pp. 294–301 (cit. on p. 14).
Rubin, V. C., W. K. J. Ford, and N. . Thonnard (1980). In: ApJ 238, pp. 471–487 (cit. on p. 19).
Russeil, D., M. Pestalozzi, et al. (2011). In: A&A 526, A151, A151 (cit. on p. 19).
Rybicki, G. B. and A. P. Lightman (1979) (cit. on p. 28).
Salpeter, E. E. (1955). In: ApJ 121, p. 161 (cit. on p. 7).
— (1976). In: ApJ 206, pp. 673–678 (cit. on p. 12).
Sánchez-Monge, Á., A. Palau, et al. (2013). In: MNRAS 432, pp. 3288–3319 (cit. on p. 69).
Sanders, R. H., P. J. Teuben, and G. D. van Albada (1983). In: *Internal Kinematics and Dynamics of Galaxies*. Ed. by E. Athanassoula. Vol. 100. IAU Symposium, p. 221 (cit. on p. 18).

Sault, R. J., P. J. Teuben, and M. C. H. Wright (1995). In: *Astronomical Data Analysis Software and Systems IV*. Ed. by R. A. Shaw, H. E. Payne, and J. J. E. Hayes. Vol. 77. Astronomical Society of the Pacific Conference Series, p. 433 (cit. on p. 96).
Schieder, R. T., O. Siebertz, et al. (2000). In: *Society of Photo-Optical Instrumentation Engineers (SPIE) Conference Series*. Ed. by J. B. Breckinridge and P. Jakobsen. Vol. 4013. Society of Photo-Optical Instrumentation Engineers (SPIE) Conference Series, pp. 313–324 (cit. on p. 89).
Schilke, P., C. M. Walmsley, et al. (1997). In: A&A 321, pp. 293–304 (cit. on p. 13).
Schneider, N., P. André, et al. (2013). In: ApJ 766, L17, p. L17 (cit. on p. 78).
Schneider, N., T. Csengeri, et al. (2010). In: A&A 520, A49+ (cit. on pp. 15, 64).
Schneider, N., T. Csengeri, et al. (2012). In: A&A 540, L11, p. L11 (cit. on pp. 7, 14, 78, 79).
Schuller, F., K. M. Menten, et al. (2009). In: A&A 504, pp. 415–427 (cit. on p. 73).
Schuster, K.-F., C. Boucher, et al. (2004). In: A&A 423, pp. 1171–1177 (cit. on p. 33).
Seab, C. G. (1987). In: *Interstellar Processes*. Ed. by D. J. Hollenbach and H. A. Thronson Jr. Vol. 134. Astrophysics and Space Science Library, pp. 491–512 (cit. on p. 12).
Shull, J. M. and S. Beckwith (1982). In: ARA&A 20, pp. 163–190 (cit. on p. 12).
Silant'ev, N. A., E. E. Lekht, et al. (2006). In: A&A 453, pp. 989–1002 (cit. on p. 29).
Simon, R., J. M. Jackson, et al. (2006). In: ApJ 639, pp. 227–236 (cit. on p. 72).
Sirono, S.-i. (2013). In: ApJ 765, 50, p. 50 (cit. on p. 12).
Sousbie, T. (2011). In: MNRAS 414, pp. 350–383 (cit. on p. 141).
Sousbie, T., C. Pichon, and H. Kawahara (2011). In: MNRAS 414, pp. 384–403 (cit. on p. 141).
Stahler, S. W., F. H. Shu, and R. E. Taam (1980). In: ApJ 241, pp. 637–654 (cit. on p. 9).
Stark, A. A. and Y. Lee (2006). In: ApJ 641, pp. L113–L116 (cit. on p. 7).
Stil, J. M., A. R. Taylor, et al. (2006). In: AJ 132, pp. 1158–1176 (cit. on pp. 19, 50).
Störzer, H., J. Stutzki, and A. Sternberg (1996). In: A&A 310, pp. 592–602 (cit. on p. 125).
Stutzki, J., F. Bensch, et al. (1998). In: A&A 336, pp. 697–720 (cit. on pp. 2, 7, 14).
Stutzki, J. and R. Guesten (1990). In: ApJ 356, pp. 513–533 (cit. on pp. 7, 43).
Tanaka, T., F. Nakamura, et al. (2013). In: ApJ 778, 34, p. 34 (cit. on p. 69).
Toomre, A. (1982). In: ApJ 259, pp. 535–543 (cit. on p. 9).
Vallée, J. P. (1995). In: ApJ 454, p. 119 (cit. on p. 17).
— (2002). In: ApJ 566, pp. 261–266 (cit. on p. 17).
— (2005). In: AJ 130, pp. 569–575 (cit. on p. 17).
— (2008). In: AJ 135, pp. 1301–1310 (cit. on pp. 17, 51, 52).

van der Tak, F. F. S., J. H. Black, et al. (2007). In: A&A 468, pp. 627–635 (cit. on pp. 119, 120).
Van Loo, S., I. Ashmore, et al. (2013). In: MNRAS 428, pp. 381–388 (cit. on p. 12).
Vázquez-Semadeni, E., R. Banerjee, et al. (2011). In: MNRAS 414, pp. 2511–2527 (cit. on p. 16).
Vázquez-Semadeni, E., G. C. Gómez, et al. (2007). In: ApJ 657, pp. 870–883 (cit. on pp. 13, 14).
Velusamy, T., W. D. Langer, et al. (2010). In: A&A 521, pp. L18+ (cit. on pp. 108, 133).
Vorobyov, E. I. (2011). In: ApJ 729, 146, p. 146 (cit. on p. 9).
Voshchinnikov, N. V. and T. Henning (2010). In: A&A 517, A45, A45 (cit. on p. 12).
Walker, C. K., G. Narayanan, and A. P. Boss (1994). In: ApJ 431, pp. 767–782 (cit. on p. 84).
Watson, W. D. (1972). In: ApJ 176, p. 103 (cit. on p. 13).
Westerhout, G. (1958). In: Bull. Astron. Inst. Netherlands 14, p. 215 (cit. on p. 19).
Whiting, M. T. (2012). In: MNRAS 421, pp. 3242–3256 (cit. on p. 44).
Williams, J. P., L. Blitz, and C. F. McKee (2000). In: *Protostars and Planets IV*, p. 97 (cit. on p. 6).
Williams, J. P., L. Blitz, and A. A. Stark (1995). In: ApJ 451, p. 252 (cit. on p. 13).
Williams, J. P. and C. F. McKee (1997). In: ApJ 476, p. 166 (cit. on p. 7).
Wilson, T. L. and F. Matteucci (1992). In: A&A Rev. 4, pp. 1–33 (cit. on p. 64).
Wilson, T. L., K. Rohlfs, and S. Hüttemeister (2009). 5th edition. Springer-Verlag Berlin (cit. on pp. 21, 28).
Wilson, T. L. and R. Rood (1994). In: ARA&A 32, pp. 191–226 (cit. on pp. 26, 59).
Wolfire, M. G. and J. P. Cassinelli (1987). In: ApJ 319, pp. 850–867 (cit. on p. 10).
Wolfire, M. G., D. Hollenbach, and C. F. McKee (2010). In: ApJ 716, pp. 1191–1207 (cit. on p. 133).
Wolfire, M. G., D. Hollenbach, et al. (1995). In: ApJ 443, pp. 152–168 (cit. on p. 11).
Wong, T., E. F. Ladd, et al. (2008). In: MNRAS 386, pp. 1069–1084 (cit. on p. 78).
Woody, D. P., A. J. Beasley, et al. (2004). In: *Society of Photo-Optical Instrumentation Engineers (SPIE) Conference Series*. Ed. by C. M. Bradford, P. A. R. Ade, et al. Vol. 5498. Society of Photo-Optical Instrumentation Engineers (SPIE) Conference Series, pp. 30–41 (cit. on p. 94).
Woolf, N. J. and E. P. Ney (1969). In: ApJ 155, p. L181 (cit. on p. 12).
Wu, H., C. Cao, et al. (2005). In: ApJ 632, pp. L79–L82 (cit. on p. 73).
Xilouris, E. M., F. S. Tabatabaei, et al. (2012). In: A&A 543, A74, A74 (cit. on p. 13).
Zinnecker, H., M. McCaughrean, and J. Rayner (1997). In: *Herbig-Haro Flows and the Birth of Stars*. Ed. by B. Reipurth and C. Bertout. Vol. 182. IAU Symposium, 198P (cit. on p. 10).

Appendix A

Description of important sources

In the following, we want to give a description of several important and interesting sources of the W43 complex ($d = 6$ kpc) found in our datasets. Information on these sources are listed in Table 4.1, while their location is indicated in Fig. 4.4. The corresponding maps can be found in Fig. B. We discuss the shape, topology, and intensity of the maps and fundamental properties like velocity gradients, FWHM line widths, temperature, and column density. We also mention conclusions from the comparison to different datasets. Sources are ordered by their peak velocities.

A.1 Source 23

Source 23 (plots can be seen in Fig. 5.6 and also Fig. B.23) consists of one central elliptical clump with one elongated thin extension, protruding from the southeast, that ends in a hook-like tip and is curved to the south. The central clump is elliptically shaped, with a length of the major axes of 5 and 3 parsec and is bound sharply at the southern edge, while it is much more diffuse and more extended in the north. The extension has a length of 7.5 pc. We find the maximum integrated intensity of the ^{13}CO (2–1) line to be about 90 K km s^{-1} at the peak of the clump, while the filamentary extension lies around 30 to 45 K km s^{-1}. The line peak intensity rises from 12 K in the filament to 24 K in the clump. The opacity has typical values of 1 to 2.5 with higher values in the central clump.

We see a gradient in the radial velocity of the cloud from the filament to the center of the source of ~ 3 km s^{-1}, which can be interpreted as a flow of gas along the outrigger onto the clump. The line width (FWHM) changes between 4.5 km s^{-1} in the inner clump and 2 to 2.5 km s^{-1} in the outer parts of the cloud.

The H_2 column density that we calculated rises from $\sim 5 \times 10^{21}$ cm^{-2} in the edges of the cloud to $\sim 7 \times 10^{22}$ cm^{-2} in the center. The total mass is calculated to be $2.7 \times 10^4\ M_\odot$ and thus resembles a typical total mass of our set of sources.

The CO emission that we measure in our maps is nearly exactly matched by the dust emission maps of ATLASGAL and Hi-GAL (see Fig. 5.6 (b) and (c) respectively). Both show the strong peak in the central clump and the weaker filament in the southeast, including that of the curved tip. The GLIMPSE map shows very interesting features (see Fig. 5.6 (d)). There is one strong UV point source less than 1 pc off to the south of the CO clump.

A.2 Source 25

This filament, as seen in Fig. B.25, resides in the central western part of the W43 complex, which is half-way between W43-Main and W43-South. It is shaped like an inverted L with two branches and connected by an orthogonal angle. The vertical branch has a length of 14 pc; the horizontal one is 10 pc long. The typical width of both branches is between 2 and 3 pc. One strong clump is seen in the southern part with an integrated line intensity of the ^{13}CO (2–1) line of 40 K km s^{-1}, while the rest of the filament backbone only reaches 18 to 22 K km s^{-1}. Line peak intensities range from a few K in the outer parts of the filament up to 15 K in the strong southern clump.

Investigating the line mean velocity map, we find that the two branches of this source are actually separated. The horizontal branch has a constant radial velocity of 108 km s^{-1} across, while the vertical branch shows a gradient from 110 km s^{-1} in the north to 115 km s^{-1} in the south. Line widths range between 1 and 2 km s^{-1} in the whole source. The H_2 column density varies between 2×10^{21} cm^{-2} in the outer parts and 4×10^{22} cm^{-2} around the southern core. The total mass is $\sim 6.8 \times 10^3\ M_\odot$.

Comparing this source to the complementary projects is complicated, because the source 17 is located at the same place and overlaps this source. Most emission that is seen in the northern part of the source is presumably part of source 17. Only the embedded core in the south is clearly seen in dust emission and as a compact *Spitzer* source.

A.3 Source 26

Located in the easternmost central part of the W43 complex lies this filamentary shaped source, whose plot is found in Fig. B.26. It stretches over a range of 26 pc from southeast to northwest. The filament consists of three sub-sections that contain several clumps and has a typical width of 5 pc. The integrated emission map of the ^{13}CO (2–1) line shows values of up to 35 K km s^{-1} in the clumps,

which is surrounded by weaker gas. The strongest clump lies in the southeastern end of the filament, while the highest line peak intensities are found in the northwest with up to 13 K.

The velocity structure of this filament is nearly symmetrical, starting around 106 km s^{-1} in the middle of the filament and increasing toward its tips up to 110 km s^{-1} in the west and 112 km s^{-1} in the east. The width of the lines has nearly homogeneous values around 2 km s^{-1} in the center and western part of the filament but shows broad lines with a width of more than 5 km s^{-1} in the eastern clump.

This filament shows a typical distribution of its H_2 column density. Several denser clumps are embedded along the filament. Column densities vary from a few 10^{21} cm^{-2} in the outer parts of the filament up to a maximum of 3×10^{22} cm^{-2} in one clump. The total mass of this source is $1.7 \times 10^4\ M_\odot$.

The CO emission of this source matches nicely with the dust emission of ATLASGAL and Hi-GAL. However, the eastern part of the filament is stronger in the 850 μm map than the shorter wavelengths of Hi-GAL and vice versa in the western part. Only the clump in the west of this filament can be seen in the 8 μm *Spitzer* data, the east is not traced. There is one extended source seen in emission in the center part of this source, but this is probably unrelated.

A.4 Source 28

Source 28 (see Fig. B.28) is located in the southwest of W43-Main in the central region of the complex. It is not visible in the total integrated maps of the region, as it is confused with sources of a different relative velocity. It becomes visible by investigating the channel maps between 110 and 115 km s^{-1} radial velocity. The source has dimensions of 12 pc in the east-west direction and 8 pc in the north-south direction. Its shape is that of a two-armed filament, whose two parts join at an angle of $\sim 135^\circ$ where the eastern arm runs from southeast to northwest and the western arm from east to west. We see two stronger clumps in the eastern filament: one in the center of it and one in the southeastern tip. This is a relatively weak source with an integrated ^{13}CO (2–1) emission of only 25 K km s^{-1} at the peak in the center of the eastern filament, where the maximum line peak is around 13 K. The integrated intensity goes down to 8 K km s^{-1} in the outskirts of the filament. Yet, it is a valuable source, due to its pronounced filamentary structure and the embedded clumps.

We carried out several additional observations of this filament, as described in Chapter 6. The analysis of these observations is given in Chapter 7.

The eastern arm is especially interesting. It has a length of 6 pc and a typical width of 1.5 pc. We note two embedded clumps embedded in it and a velocity gradient along the filament, which starts at 110 km s^{-1} in the north and increases

to 114 km s^{-1} in the southeastern part of this arm. The typical line width varies between 1 and 2 km s^{-1}, increasing toward the inside of the cloud and reaching the maximum width at the clumps.

As this source is rather weak, we also find H_2 column densities to be only around 2×10^{22} cm^{-2} at the maximum around the embedded clumps. The total derived mass of the molecular gas is $\sim 4300\ M_\odot$, which makes it one of the less massive sources identified.

Surprisingly, this source is one of the few that is not traced at all in the GLIMPSE 8 μm map. It appears that there are no nearby UV sources that could heat the gas. The two nearest sources were identified to be related to background sources in another Galactic spiral arm. Also, the gas and the related dust is obviously too faint to appear in absorption. This is also verified by the ATLASGAL an Hi-GAL maps, which show only weak dust emission in the filament.

A.5 Source 29

This source is found in the very center of our region maps, directly south of the W43-Main cloud. Its shape resembles a crescent moon, opened toward the southeast, where it is sharply bound. The outside is more diffuse and shows several outflows away from the center. See Fig. B.29 for a plot of the ^{13}CO emission. The extent of the source is 12 pc from northeast to southwest, and the filament has a typical width of 2 to 3 pc. Two stronger clumps with an integrated ^{13}CO intensity of 40 K km s^{-1} are seen in the center and the northeastern tip. The strong backbone of this source has still an integrated intensity of ~ 20 K km s^{-1}, where line peak intensity goes up to 18 K.

The central western part of the source moves with a relative radial velocity of 112 km s^{-1} and increases to 118 km s^{-1} toward both ends of the crescent. The lines show widths of 2 to 3 km s^{-1} in the central region, decreasing to 1 km s^{-1} in the outer parts. H_2 column densities only reach a few 10^{22} cm^{-2} across the inner parts of the structure. We find a total mass of $1.2 \times 10^4\ M_\odot$.

In the dust emission maps of ATLASGAL and Hi-GAL, only the strong backbone of this source can be seen. The weaker outliers are not traced. The *Spitzer* 8 μm map shows several bright compact sources in the center, and some extended emission in the south is most probably related to this source. However, the northern tip that shows strong CO emission is not traced by *Spitzer* at all.

Appendix B

Plots of all sources

In this chapter we show several plots of all sources extracted from the IRAM 30m observations, described in Chapter 3. See Sect. 4.2 for details of the decomposition process, where we identify 29 clouds, contained in the ^{13}CO and C^{18}O data cubes. Physical properties of these sources are displayed in Table 4.1 on page 46, while several derived properties can be found in Table 5.1 on page 61 and Table 5.2 on page 67.

The structure of the plots will be the following, for all sources:

- (a) ^{13}CO (2–1) map in [K km s^{-1}]
- (b) C^{18}O (2–1) map in [K km s^{-1}]
- (c) ^{13}CO peak velocity map in [km s^{-1}]
- (d) ^{13}CO line width map in [km s^{-1}]
- (e) ^{13}CO optical depth map
- (f) CO excitation temperature map in [K]
- (g) H_2 column density map in [cm^{-2}]
- (h) GLIMPSE 8 μm map in [MJy sr^{-1}]
- (i) MIPSGAL 24 μm map in [MJy sr^{-1}]
- (j) Hi-GAL 160 μm map in [Jy pixel^{-1}]
- (k) Hi-GAL 350 μm map in [Jy beam^{-1}]
- (l) ATLASGAL map in [Jy beam^{-1}]

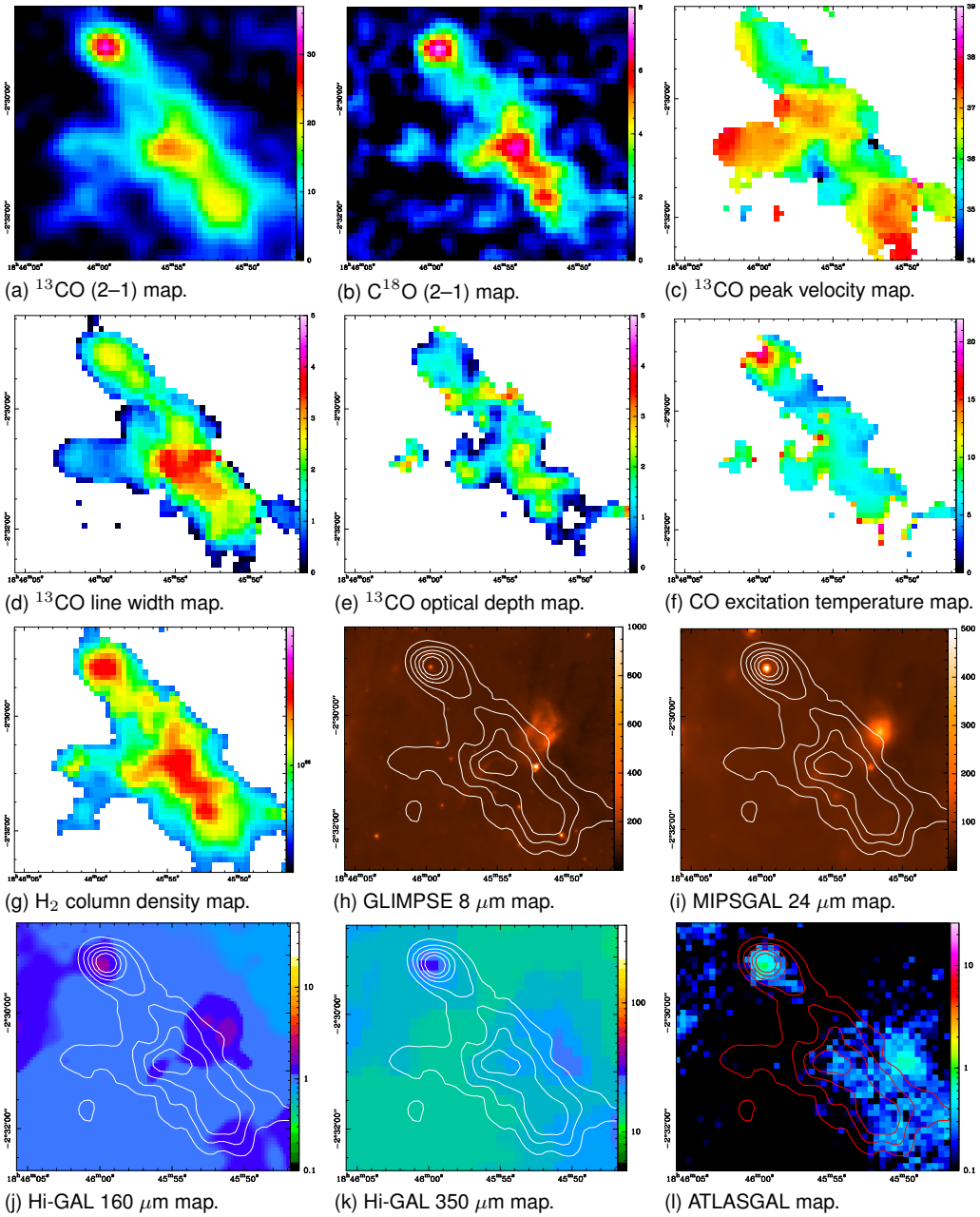

(a) ^{13}CO (2–1) map.
(b) C^{18}O (2–1) map.
(c) ^{13}CO peak velocity map.
(d) ^{13}CO line width map.
(e) ^{13}CO optical depth map.
(f) CO excitation temperature map.
(g) H_2 column density map.
(h) GLIMPSE 8 μm map.
(i) MIPSGAL 24 μm map.
(j) Hi-GAL 160 μm map.
(k) Hi-GAL 350 μm map.
(l) ATLASGAL map.

Fig. B.1: Several maps showing data and derived properties of source 1.

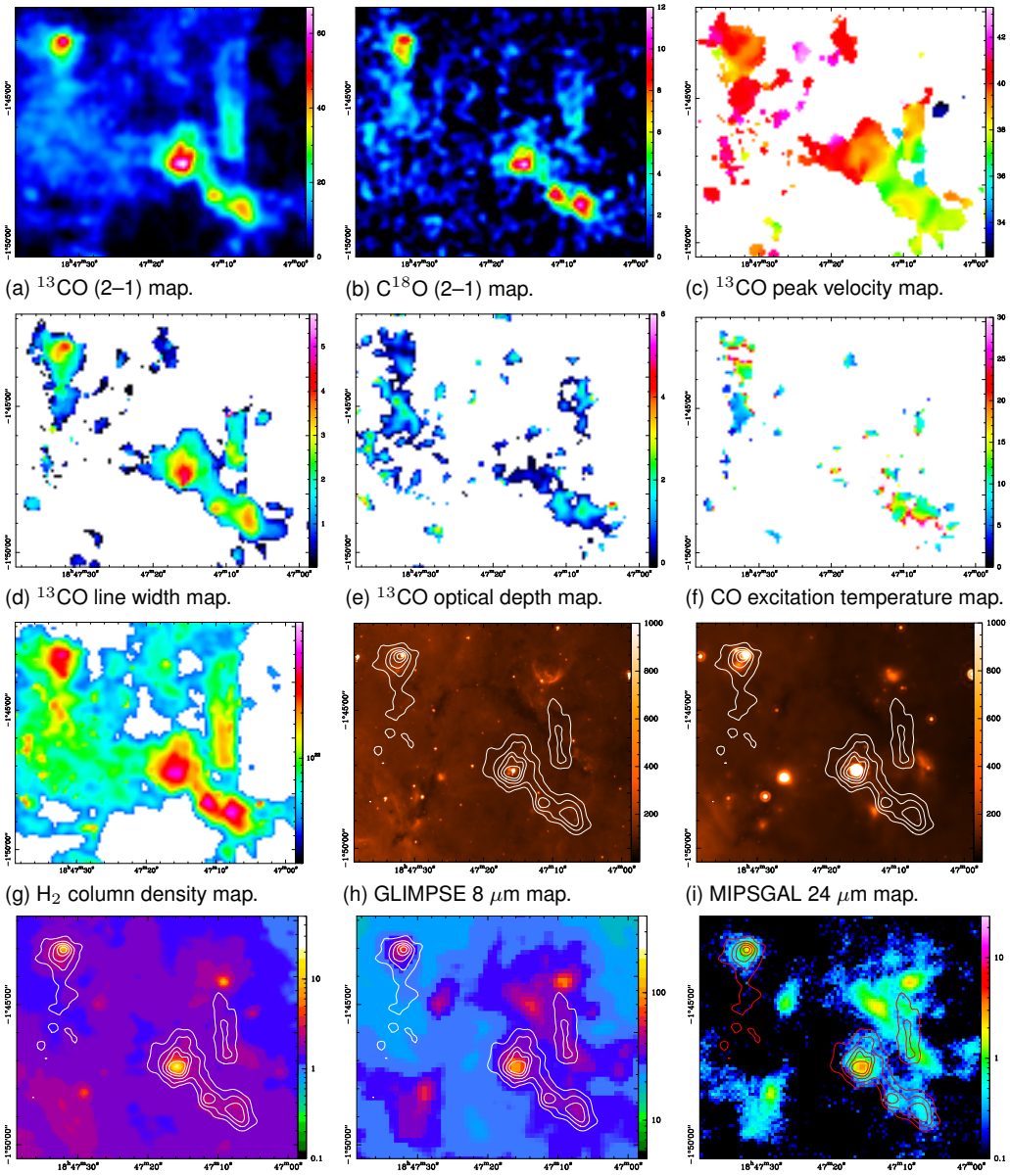

(a) ^{13}CO (2–1) map. (b) C^{18}O (2–1) map. (c) ^{13}CO peak velocity map.

(d) ^{13}CO line width map. (e) ^{13}CO optical depth map. (f) CO excitation temperature map.

(g) H_2 column density map. (h) GLIMPSE 8 μm map. (i) MIPSGAL 24 μm map.

(j) Hi-GAL 160 μm map. (k) Hi-GAL 350 μm map. (l) ATLASGAL map.

Fig. B.2: Several maps showing data and derived properties of source 2.

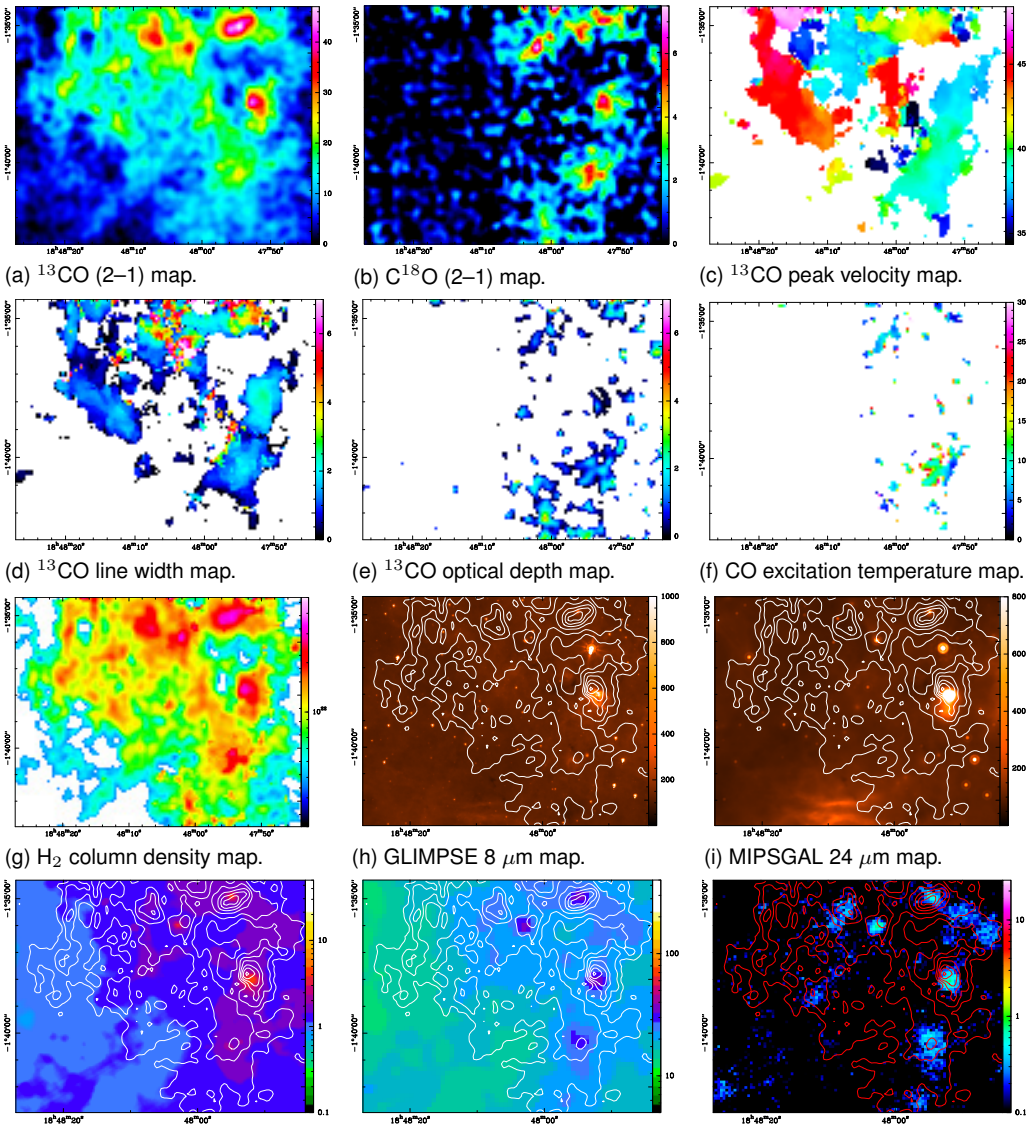

(a) ^{13}CO (2–1) map.
(b) C^{18}O (2–1) map.
(c) ^{13}CO peak velocity map.
(d) ^{13}CO line width map.
(e) ^{13}CO optical depth map.
(f) CO excitation temperature map.
(g) H_2 column density map.
(h) GLIMPSE 8 μm map.
(i) MIPSGAL 24 μm map.
(j) Hi-GAL 160 μm map.
(k) Hi-GAL 350 μm map.
(l) ATLASGAL map.

Fig. B.3: Several maps showing data and derived properties of source 3.

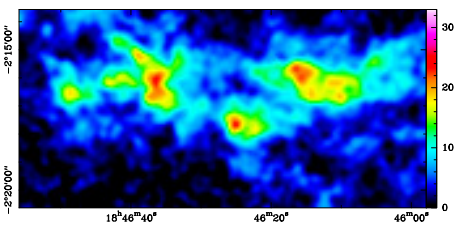

(a) ^{13}CO (2–1) map.

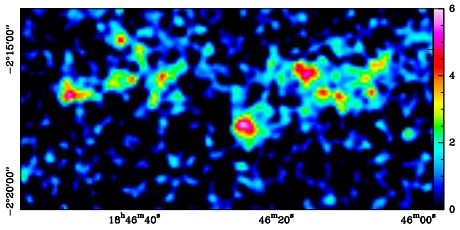

(b) C^{18}O (2–1) map.

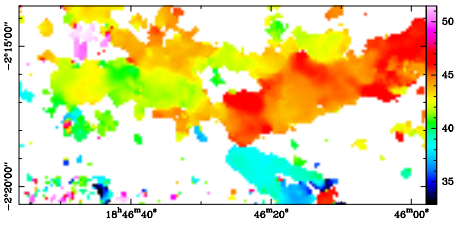

(c) ^{13}CO peak velocity map.

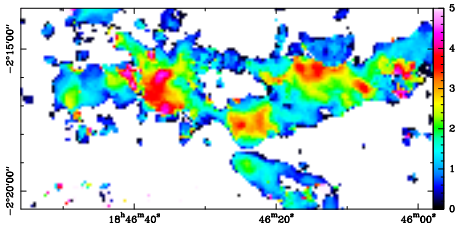

(d) ^{13}CO line width map.

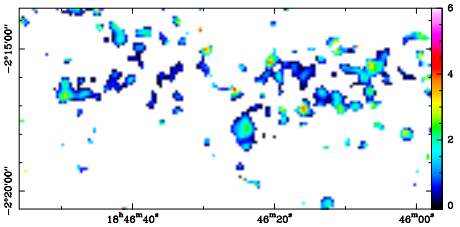

(e) ^{13}CO optical depth map.

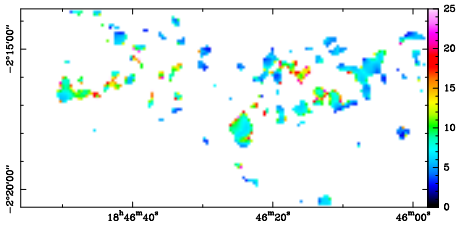

(f) CO excitation temperature map.

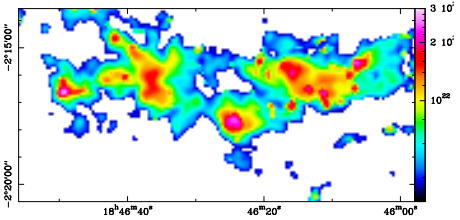

(g) H_2 column density map.

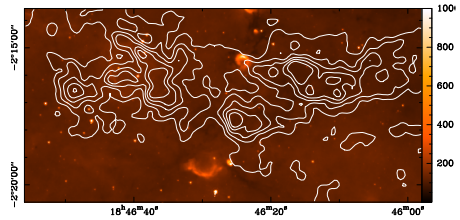

(h) GLIMPSE 8 μm map.

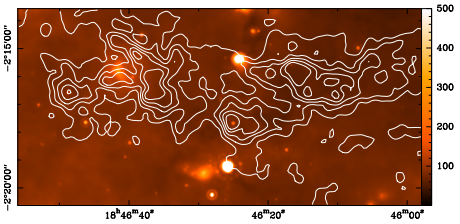

(i) MIPSGAL 24 μm map.

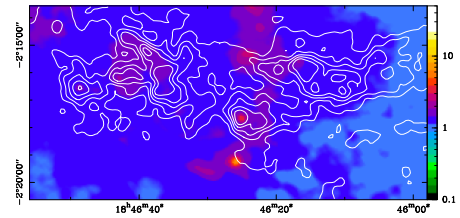

(j) Hi-GAL 160 μm map.

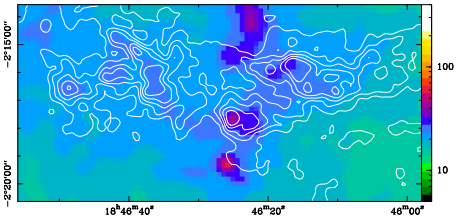

(k) Hi-GAL 350 μm map.

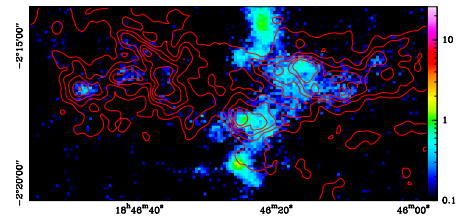

(l) ATLASGAL map.

Fig. B.4: Several maps showing data and derived properties of source 4.

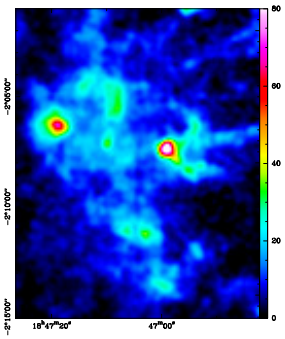

(a) ^{13}CO (2–1) map.

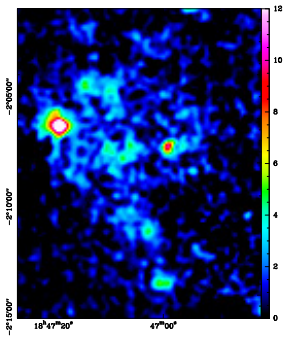

(b) C^{18}O (2–1) map.

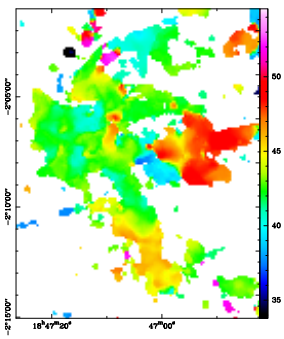

(c) ^{13}CO peak velocity map.

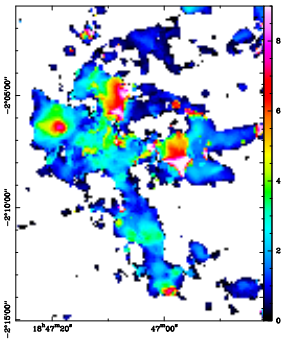

(d) ^{13}CO line width map.

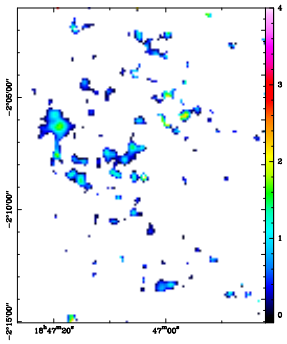

(e) ^{13}CO optical depth map.

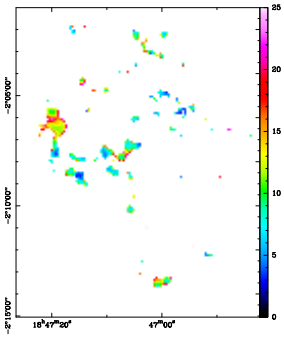

(f) CO excitation temperature map.

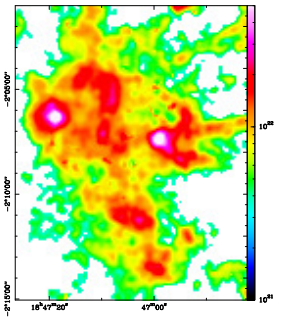

(g) H_2 column density map.

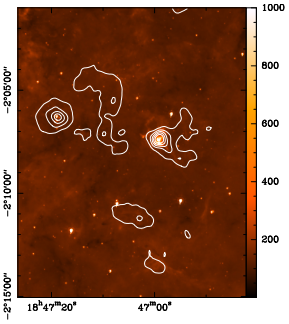

(h) GLIMPSE 8 μm map.

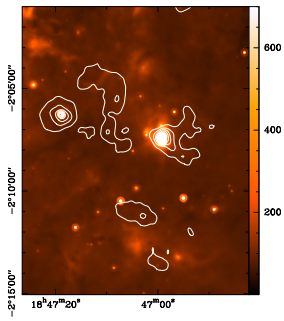

(i) MIPSGAL 24 μm map.

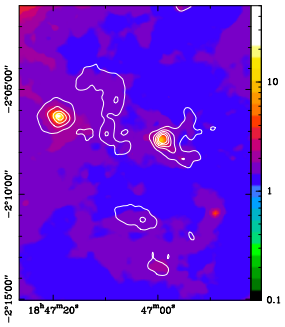

(j) Hi-GAL 160 μm map.

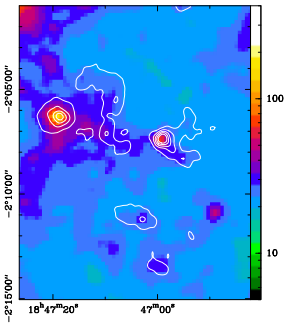

(k) Hi-GAL 350 μm map.

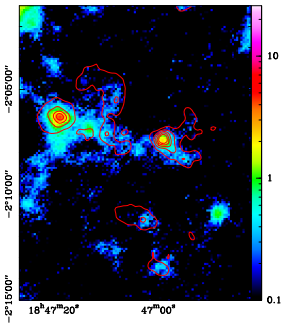

(l) ATLASGAL map.

Fig. B.5: Several maps showing data and derived properties of source 5.

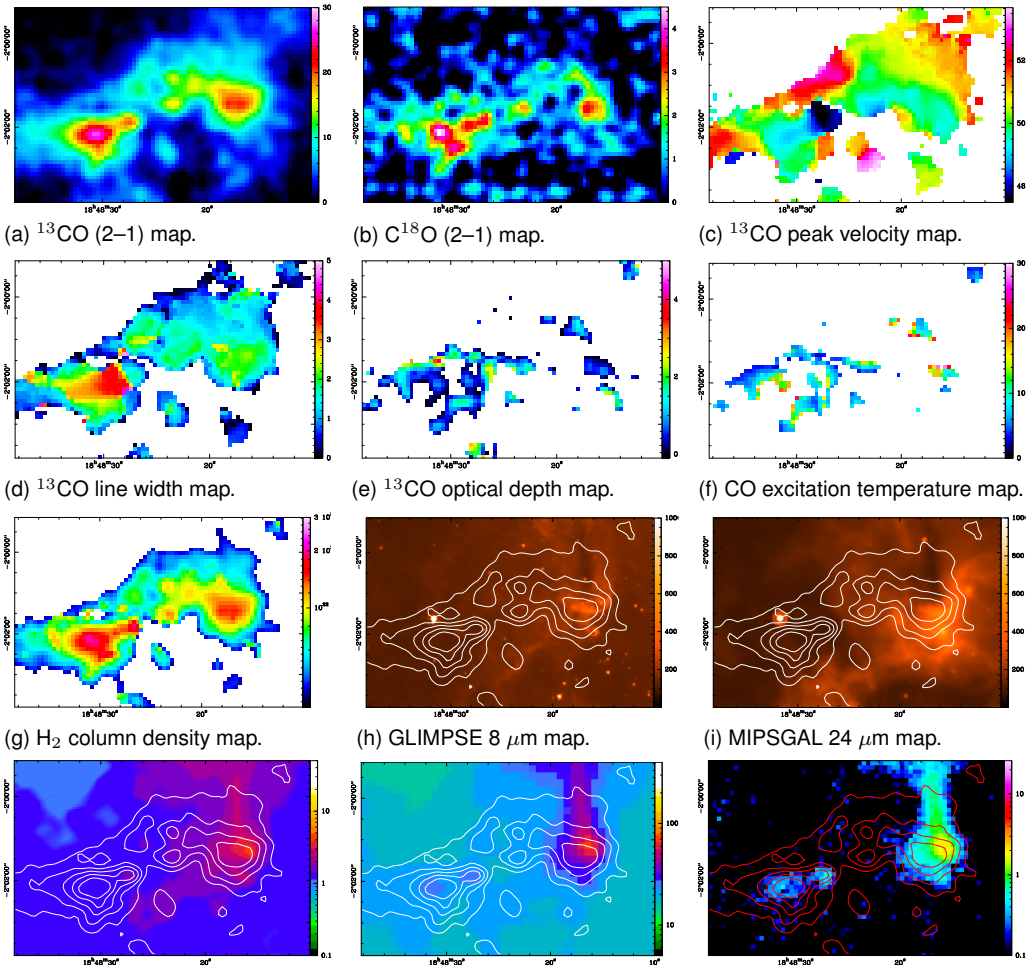

(a) ^{13}CO (2–1) map. (b) C^{18}O (2–1) map. (c) ^{13}CO peak velocity map.

(d) ^{13}CO line width map. (e) ^{13}CO optical depth map. (f) CO excitation temperature map.

(g) H_2 column density map. (h) GLIMPSE 8 μm map. (i) MIPSGAL 24 μm map.

(j) Hi-GAL 160 μm map. (k) Hi-GAL 350 μm map. (l) ATLASGAL map.

Fig. B.6: Several maps showing data and derived properties of source 6.

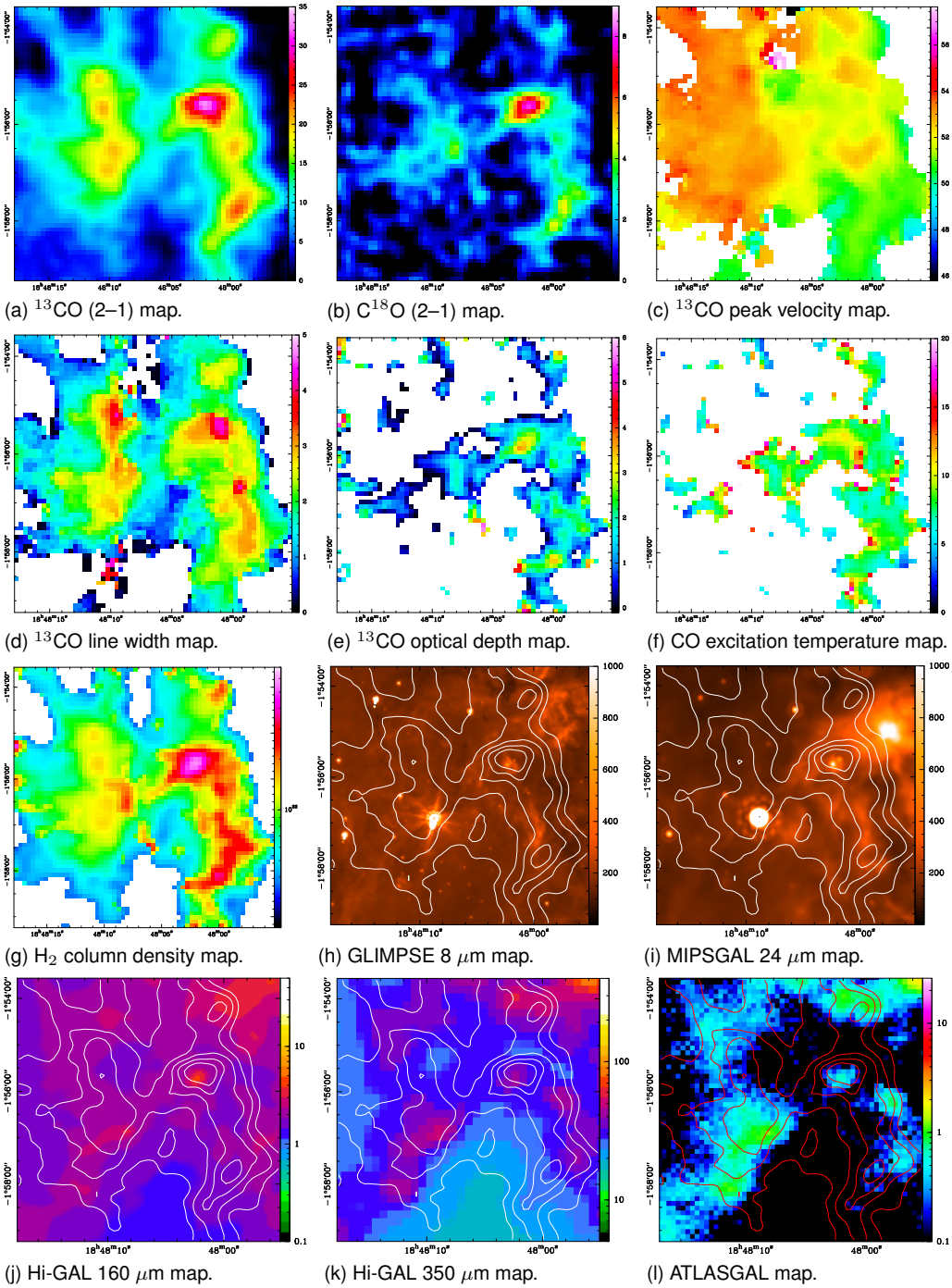

(a) ^{13}CO (2–1) map. (b) C^{18}O (2–1) map. (c) ^{13}CO peak velocity map.

(d) ^{13}CO line width map. (e) ^{13}CO optical depth map. (f) CO excitation temperature map.

(g) H_2 column density map. (h) GLIMPSE 8 μm map. (i) MIPSGAL 24 μm map.

(j) Hi-GAL 160 μm map. (k) Hi-GAL 350 μm map. (l) ATLASGAL map.

Fig. B.7: Several maps showing data and derived properties of source 7.

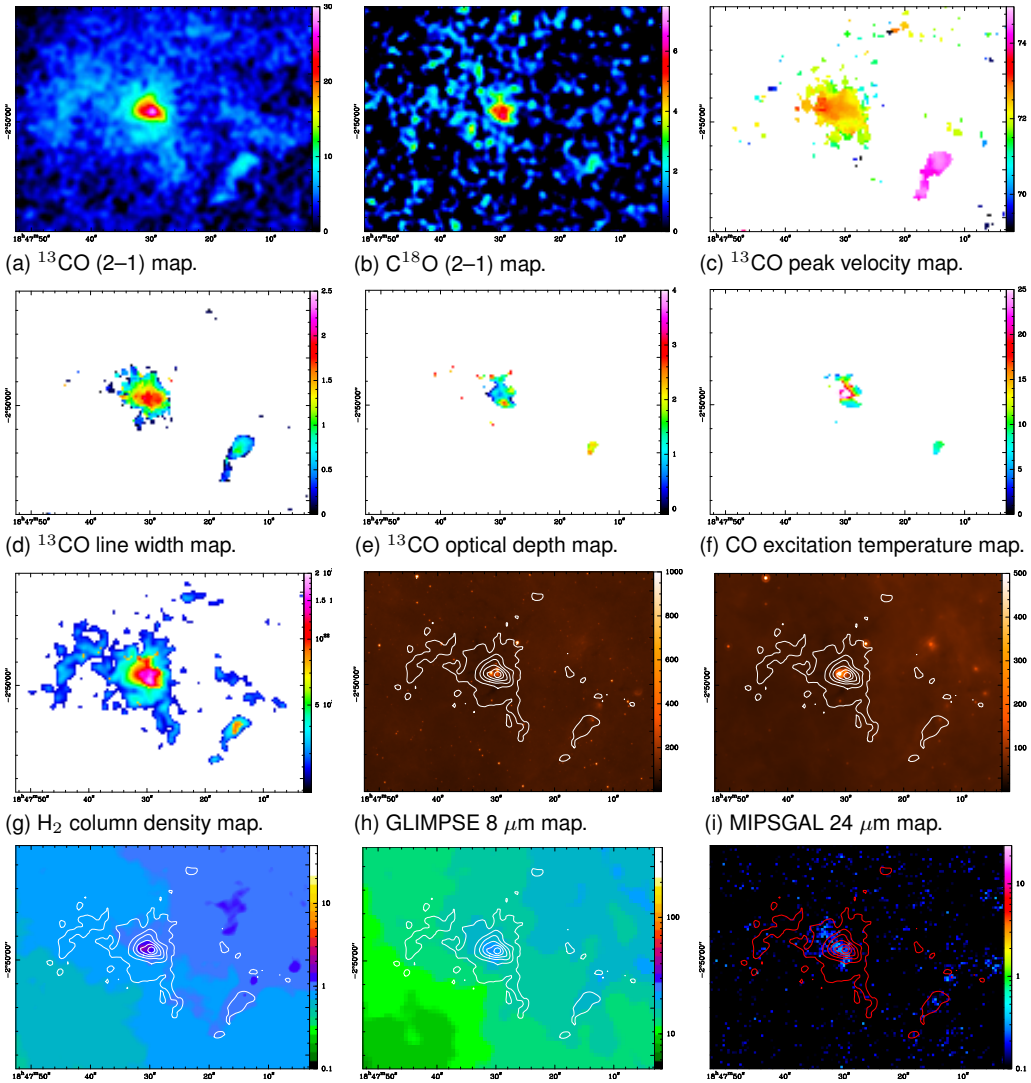

(a) ^{13}CO (2–1) map. (b) C^{18}O (2–1) map. (c) ^{13}CO peak velocity map.

(d) ^{13}CO line width map. (e) ^{13}CO optical depth map. (f) CO excitation temperature map.

(g) H_2 column density map. (h) GLIMPSE 8 μm map. (i) MIPSGAL 24 μm map.

(j) Hi-GAL 160 μm map. (k) Hi-GAL 350 μm map. (l) ATLASGAL map.

Fig. B.8: Several maps showing data and derived properties of source 8.

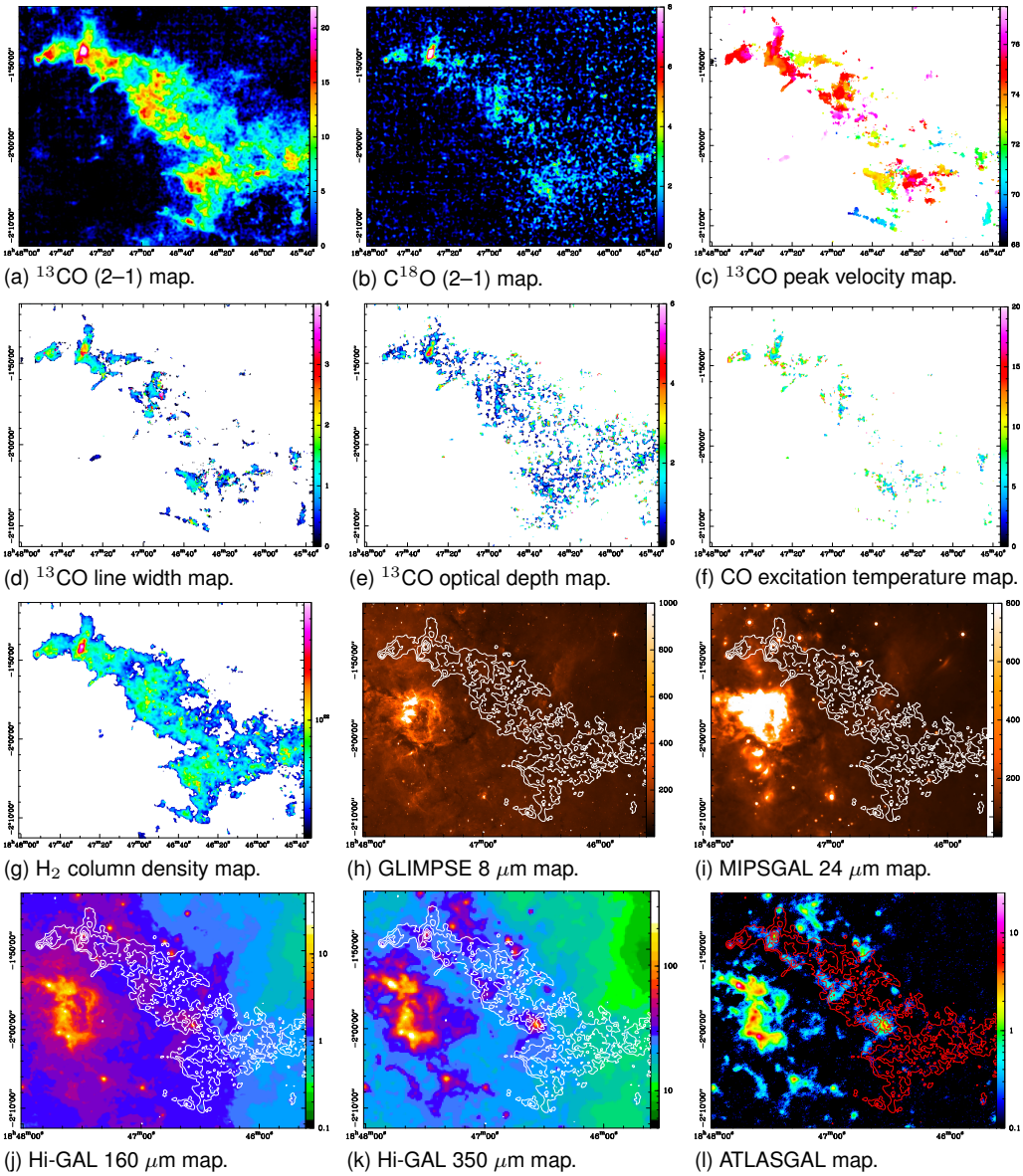

(a) ^{13}CO (2–1) map.
(b) C^{18}O (2–1) map.
(c) ^{13}CO peak velocity map.
(d) ^{13}CO line width map.
(e) ^{13}CO optical depth map.
(f) CO excitation temperature map.
(g) H_2 column density map.
(h) GLIMPSE 8 μm map.
(i) MIPSGAL 24 μm map.
(j) Hi-GAL 160 μm map.
(k) Hi-GAL 350 μm map.
(l) ATLASGAL map.

Fig. B.9: Several maps showing data and derived properties of source 9.

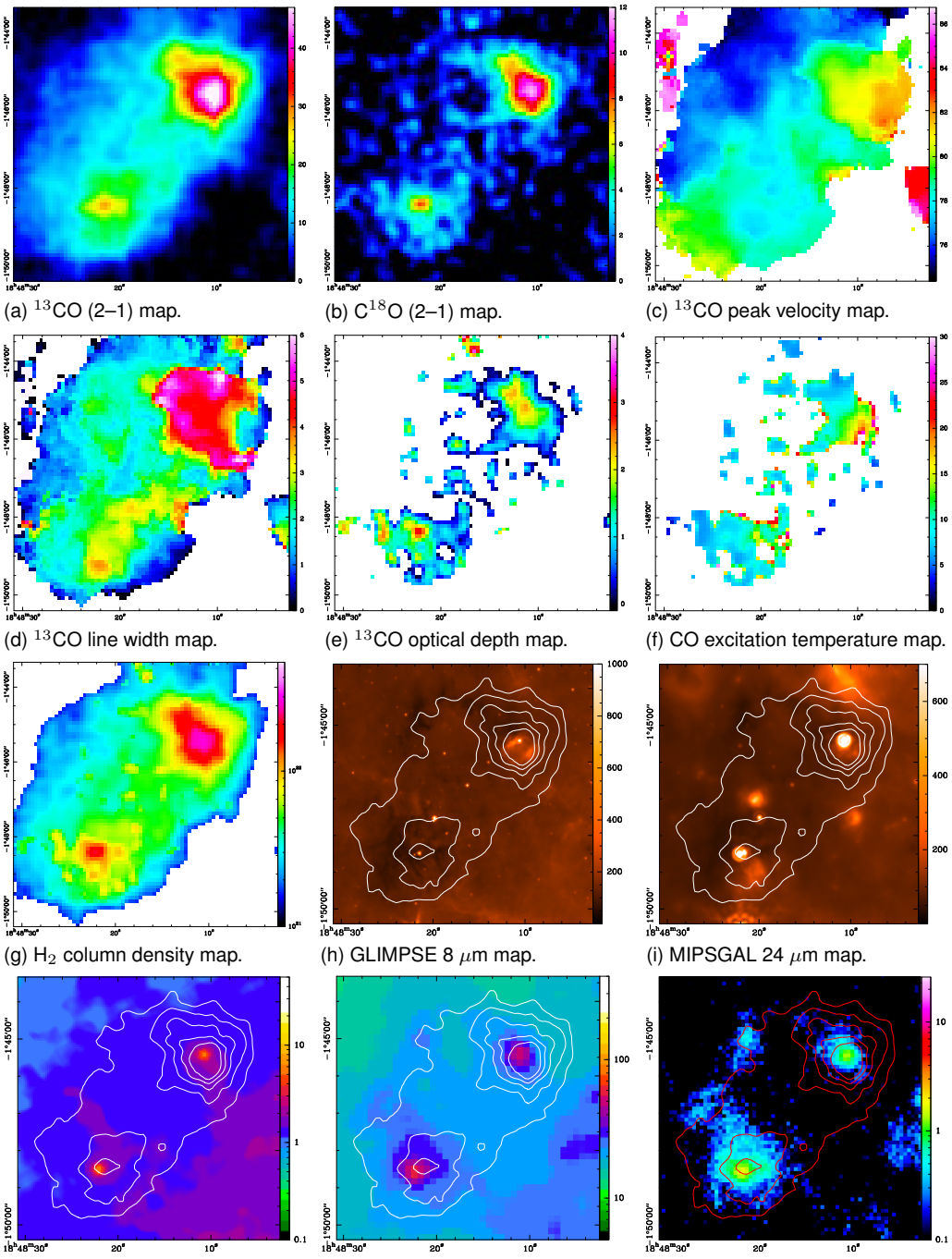

(a) ^{13}CO (2–1) map.
(b) C^{18}O (2–1) map.
(c) ^{13}CO peak velocity map.
(d) ^{13}CO line width map.
(e) ^{13}CO optical depth map.
(f) CO excitation temperature map.
(g) H_2 column density map.
(h) GLIMPSE 8 μm map.
(i) MIPSGAL 24 μm map.
(j) Hi-GAL 160 μm map.
(k) Hi-GAL 350 μm map.
(l) ATLASGAL map.

Fig. B.10: Several maps showing data and derived properties of source 10.

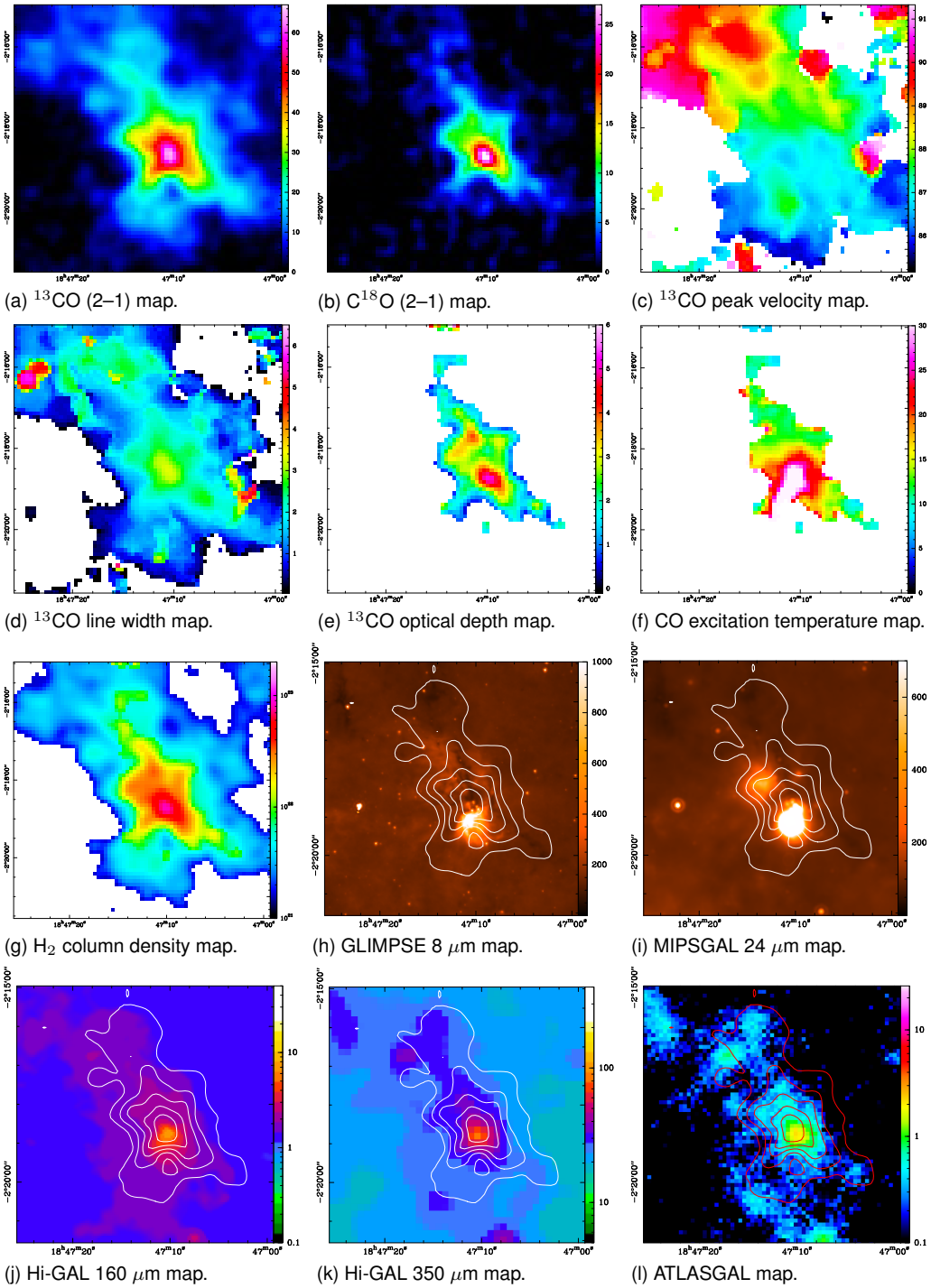

(a) ^{13}CO (2–1) map. (b) C^{18}O (2–1) map. (c) ^{13}CO peak velocity map.

(d) ^{13}CO line width map. (e) ^{13}CO optical depth map. (f) CO excitation temperature map.

(g) H_2 column density map. (h) GLIMPSE 8 μm map. (i) MIPSGAL 24 μm map.

(j) Hi-GAL 160 μm map. (k) Hi-GAL 350 μm map. (l) ATLASGAL map.

Fig. B.11: Several maps showing data and derived properties of source 11.

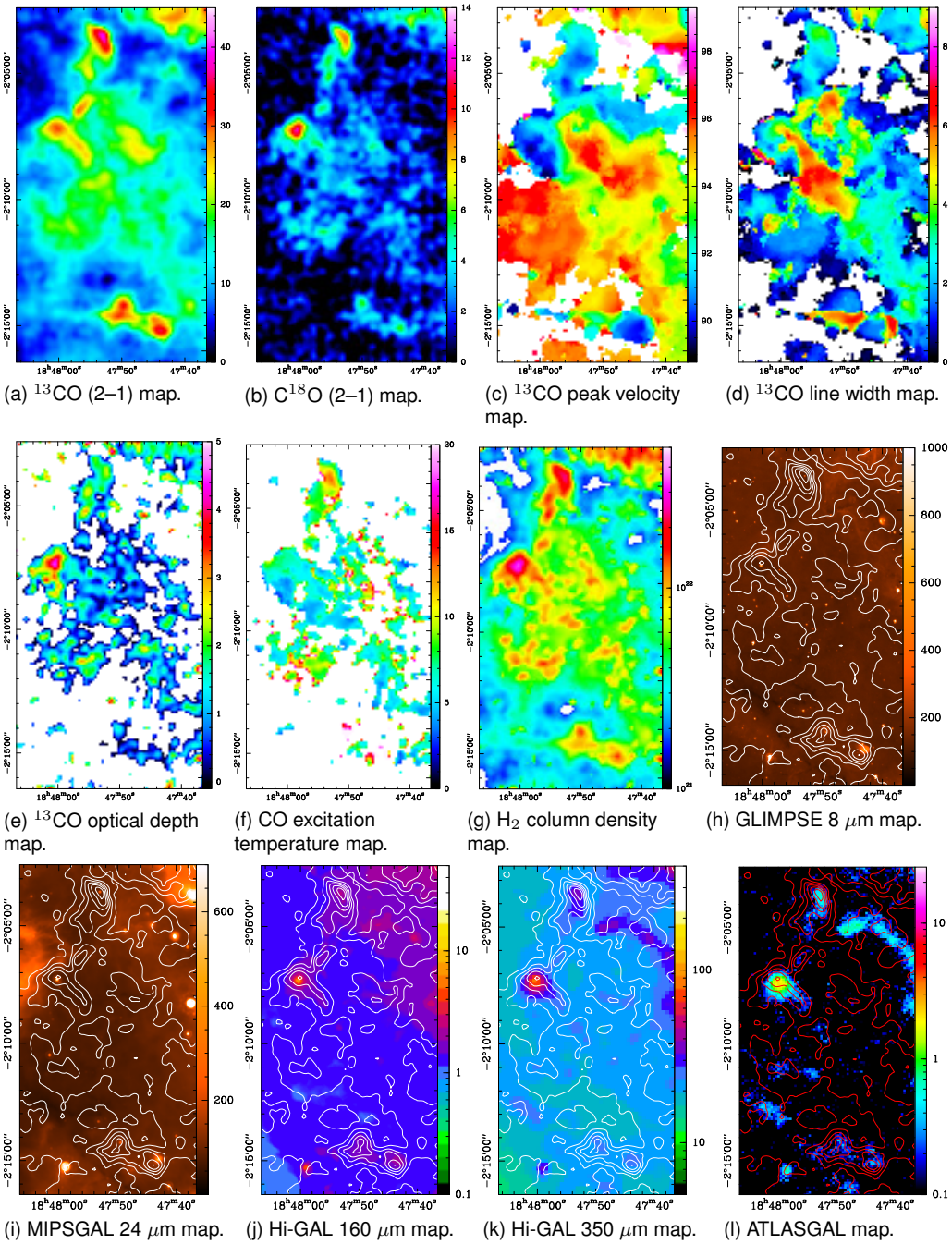

(a) ^{13}CO (2–1) map. (b) C^{18}O (2–1) map. (c) ^{13}CO peak velocity map. (d) ^{13}CO line width map.

(e) ^{13}CO optical depth map. (f) CO excitation temperature map. (g) H_2 column density map. (h) GLIMPSE 8 μm map.

(i) MIPSGAL 24 μm map. (j) Hi-GAL 160 μm map. (k) Hi-GAL 350 μm map. (l) ATLASGAL map.

Fig. B.12: Several maps showing data and derived properties of source 12.

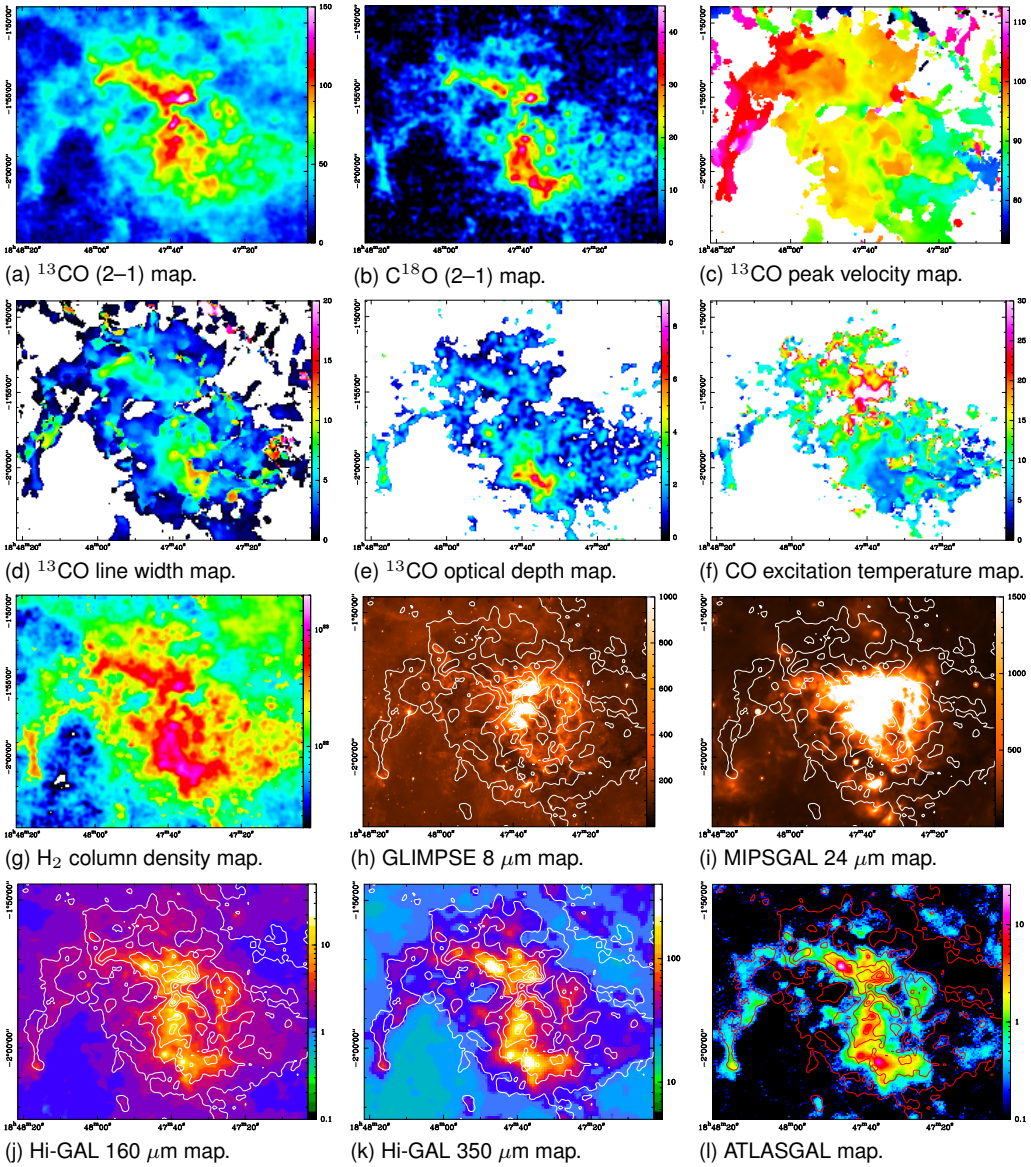

(a) ^{13}CO (2–1) map.
(b) C^{18}O (2–1) map.
(c) ^{13}CO peak velocity map.
(d) ^{13}CO line width map.
(e) ^{13}CO optical depth map.
(f) CO excitation temperature map.
(g) H_2 column density map.
(h) GLIMPSE 8 μm map.
(i) MIPSGAL 24 μm map.
(j) Hi-GAL 160 μm map.
(k) Hi-GAL 350 μm map.
(l) ATLASGAL map.

Fig. B.13: Several maps showing data and derived properties of source 13.

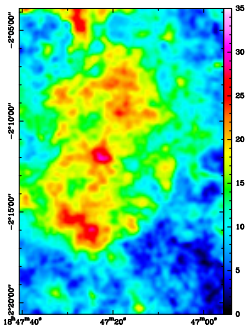

(a) ^{13}CO (2–1) map.

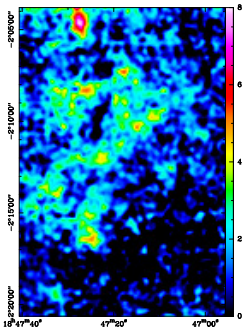

(b) C^{18}O (2–1) map.

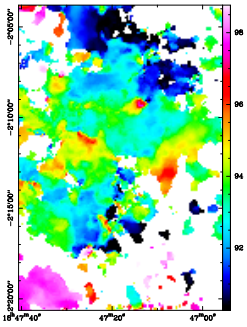

(c) ^{13}CO peak velocity map.

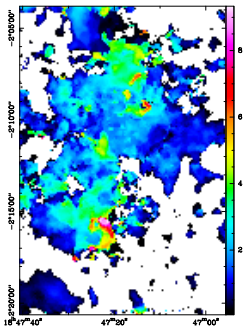

(d) ^{13}CO line width map.

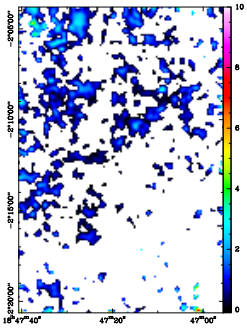

(e) ^{13}CO optical depth map.

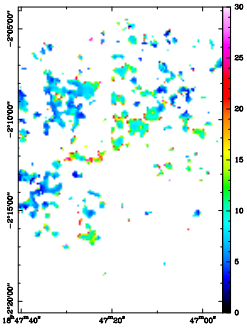

(f) CO excitation temperature map.

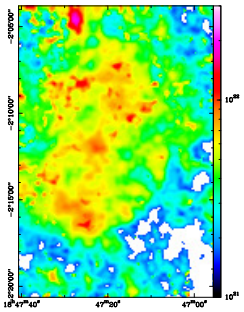

(g) H_2 column density map.

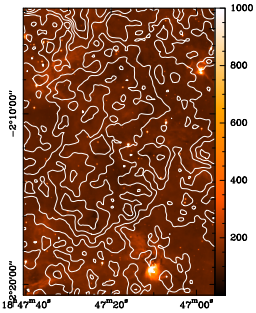

(h) GLIMPSE 8 μm map.

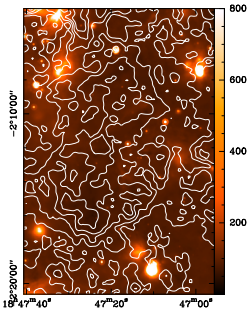

(i) MIPSGAL 24 μm map.

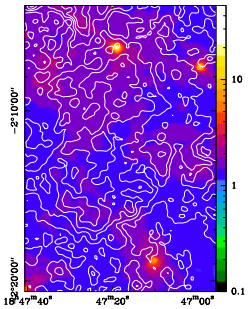

(j) Hi-GAL 160 μm map.

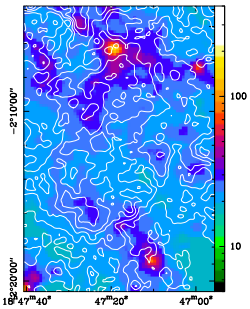

(k) Hi-GAL 350 μm map.

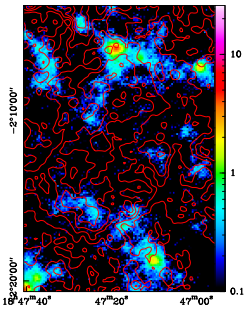

(l) ATLASGAL map.

Fig. B.14: Several maps showing data and derived properties of source 14.

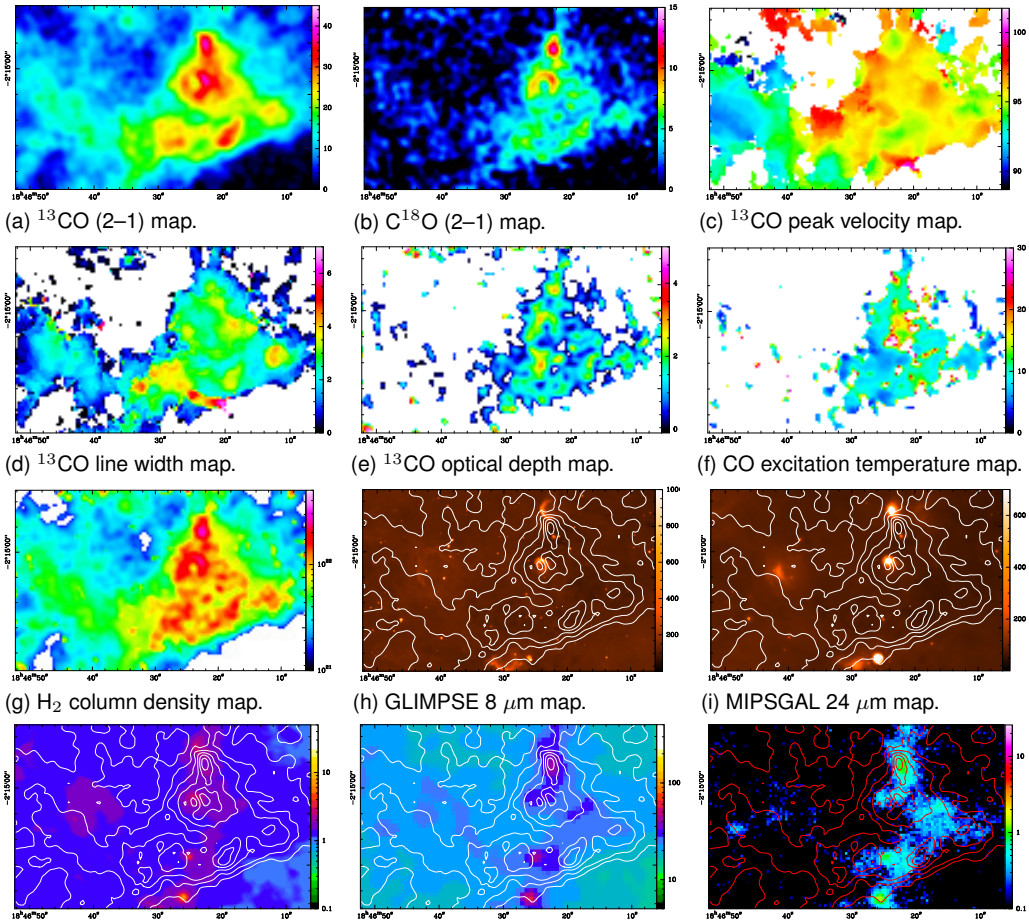

(a) ^{13}CO (2–1) map.
(b) C^{18}O (2–1) map.
(c) ^{13}CO peak velocity map.
(d) ^{13}CO line width map.
(e) ^{13}CO optical depth map.
(f) CO excitation temperature map.
(g) H_2 column density map.
(h) GLIMPSE 8 μm map.
(i) MIPSGAL 24 μm map.
(j) Hi-GAL 160 μm map.
(k) Hi-GAL 350 μm map.
(l) ATLASGAL map.

Fig. B.15: Several maps showing data and derived properties of source 15.

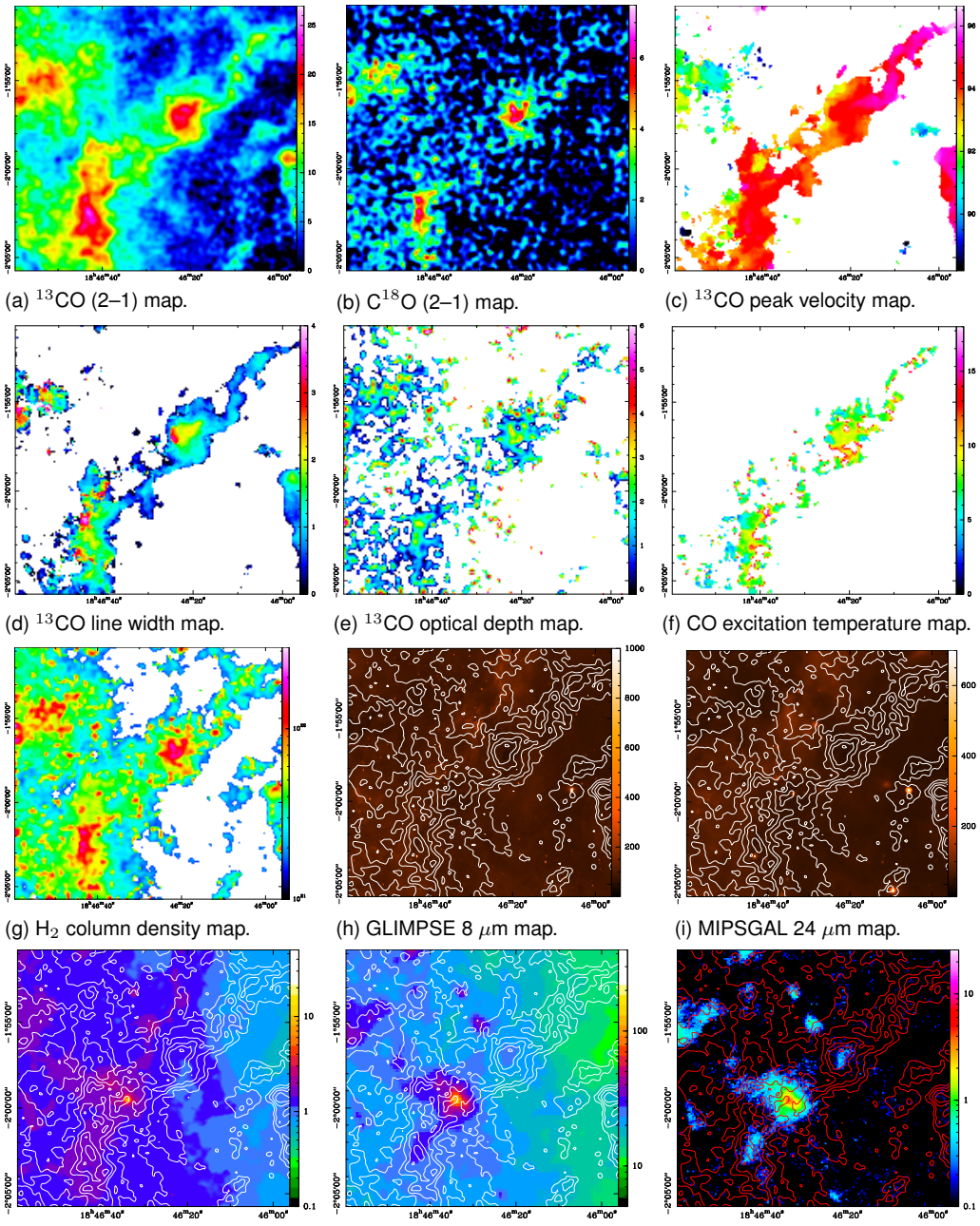

(a) ^{13}CO (2–1) map.
(b) C^{18}O (2–1) map.
(c) ^{13}CO peak velocity map.
(d) ^{13}CO line width map.
(e) ^{13}CO optical depth map.
(f) CO excitation temperature map.
(g) H_2 column density map.
(h) GLIMPSE 8 μm map.
(i) MIPSGAL 24 μm map.
(j) Hi-GAL 160 μm map.
(k) Hi-GAL 350 μm map.
(l) ATLASGAL map.

Fig. B.16: Several maps showing data and derived properties of source 16.

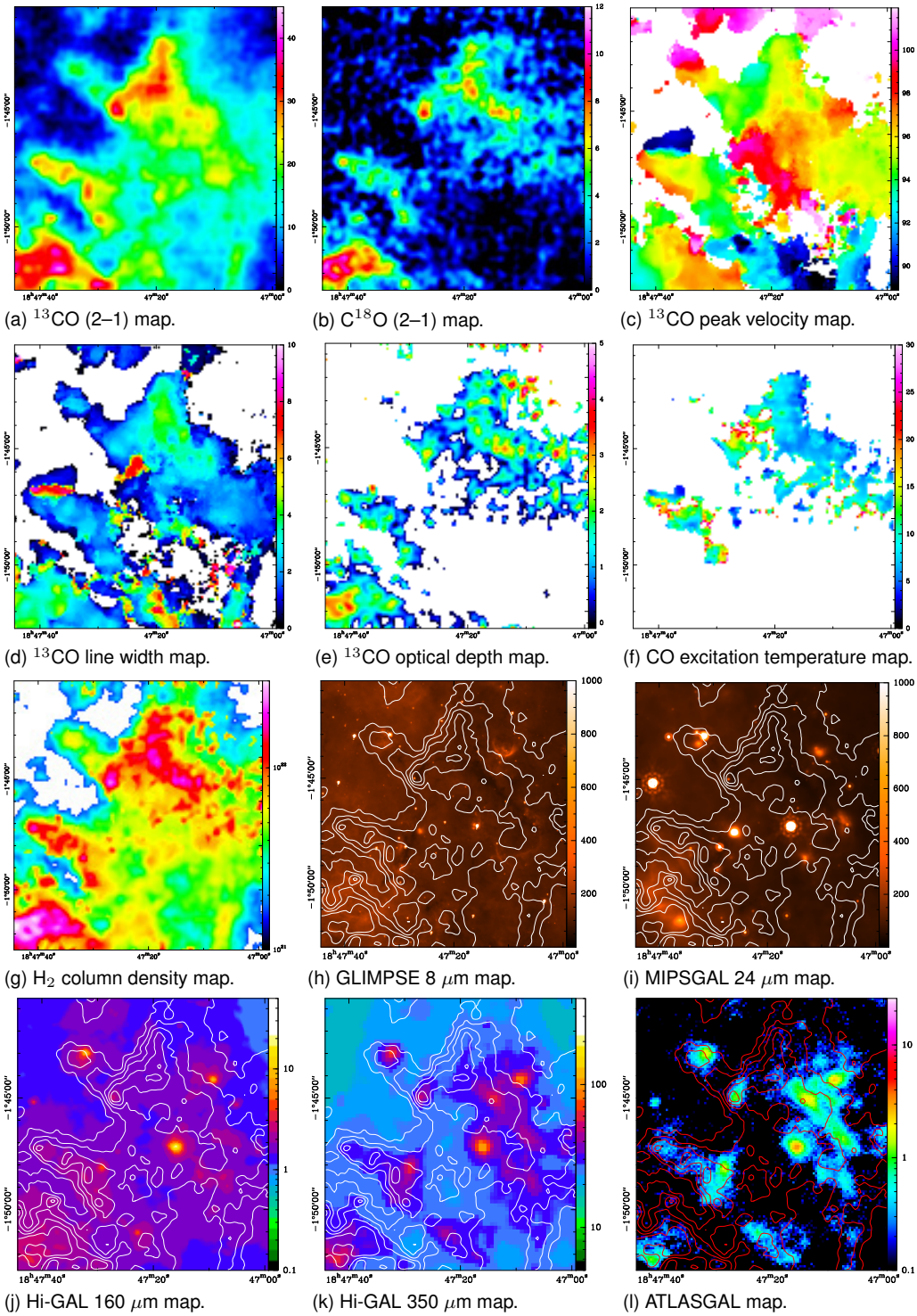

(a) ^{13}CO (2–1) map. (b) C^{18}O (2–1) map. (c) ^{13}CO peak velocity map.

(d) ^{13}CO line width map. (e) ^{13}CO optical depth map. (f) CO excitation temperature map.

(g) H_2 column density map. (h) GLIMPSE 8 μm map. (i) MIPSGAL 24 μm map.

(j) Hi-GAL 160 μm map. (k) Hi-GAL 350 μm map. (l) ATLASGAL map.

Fig. B.17: Several maps showing data and derived properties of source 17.

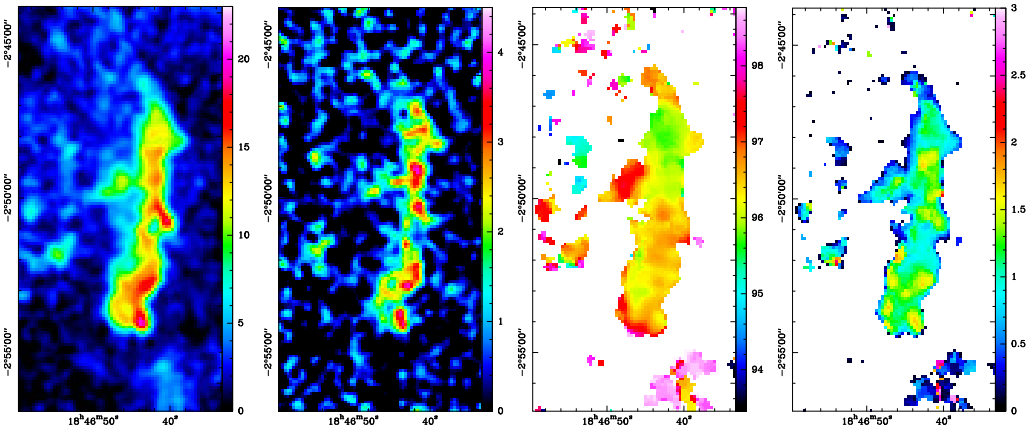

(a) ^{13}CO (2–1) map. (b) C^{18}O (2–1) map. (c) ^{13}CO peak velocity map. (d) ^{13}CO line width map.

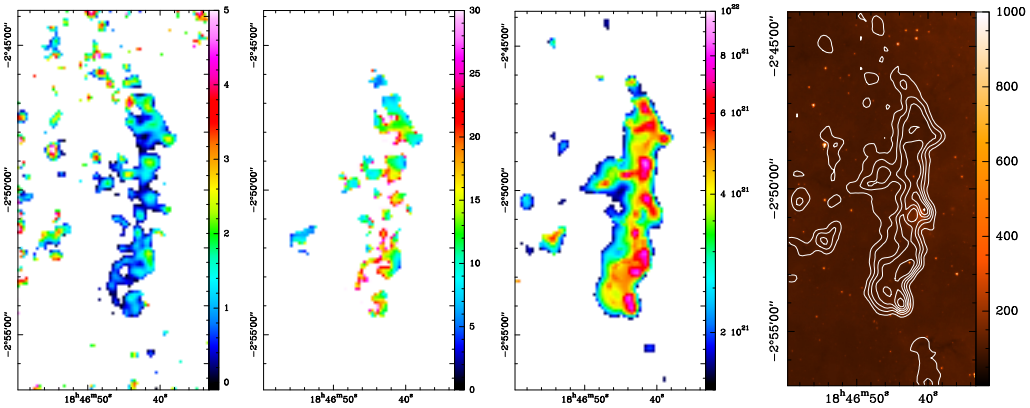

(e) ^{13}CO optical depth map. (f) CO excitation temperature map. (g) H_2 column density map. (h) GLIMPSE 8 μm map.

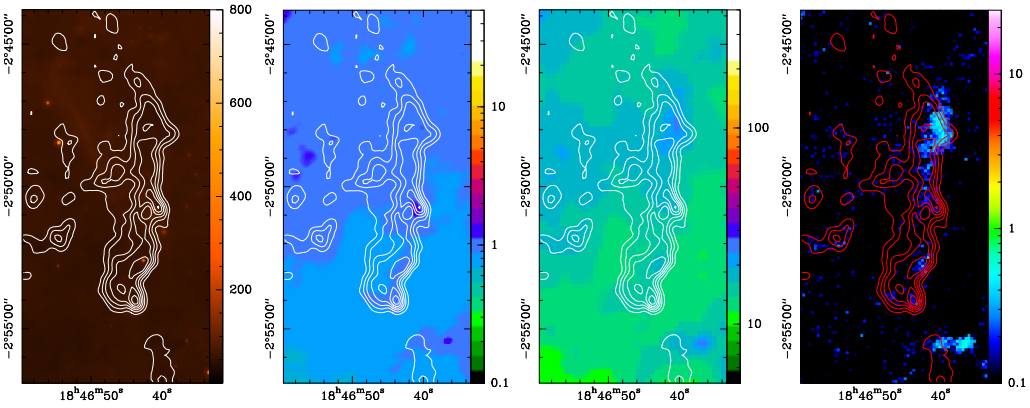

(i) MIPSGAL 24 μm map. (j) Hi-GAL 160 μm map. (k) Hi-GAL 350 μm map. (l) ATLASGAL map.

Fig. B.18: Several maps showing data and derived properties of source 18.

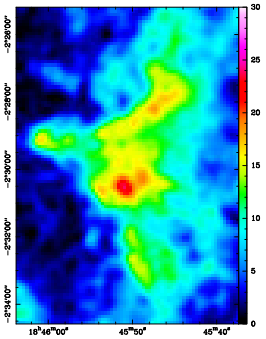

(a) ^{13}CO (2–1) map.

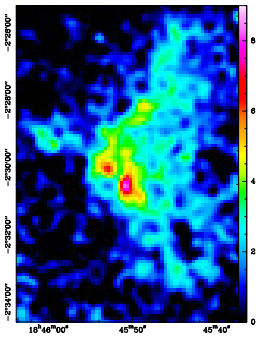

(b) C^{18}O (2–1) map.

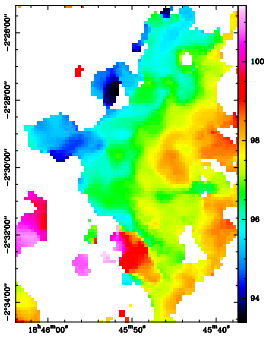

(c) ^{13}CO peak velocity map.

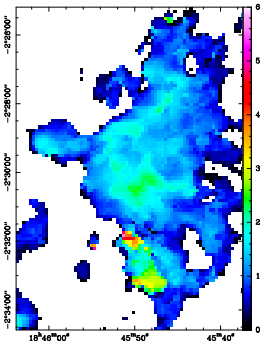

(d) ^{13}CO line width map.

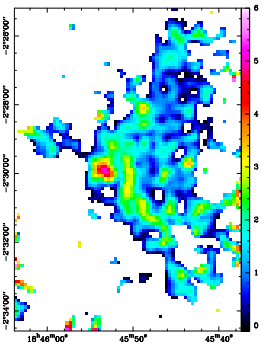

(e) ^{13}CO optical depth map.

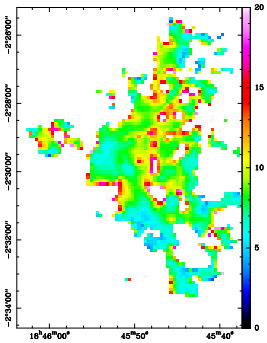

(f) CO excitation temperature map.

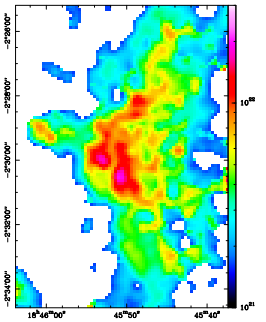

(g) H_2 column density map.

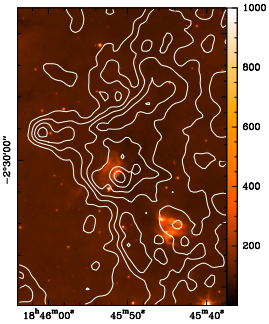

(h) GLIMPSE 8 μm map.

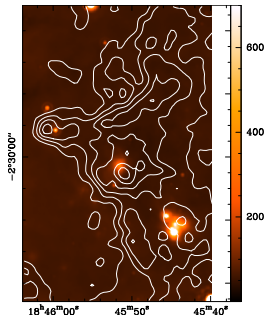

(i) MIPSGAL 24 μm map.

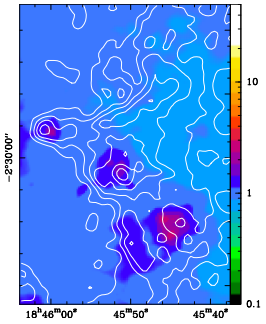

(j) Hi-GAL 160 μm map.

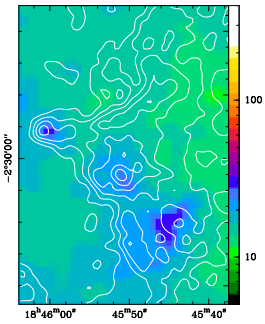

(k) Hi-GAL 350 μm map.

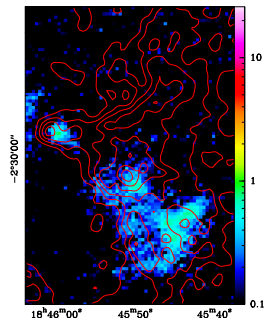

(l) ATLASGAL map.

Fig. B.19: Several maps showing data and derived properties of source 19.

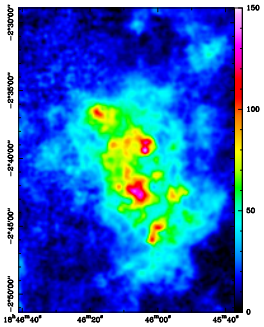

(a) ^{13}CO (2–1) map.

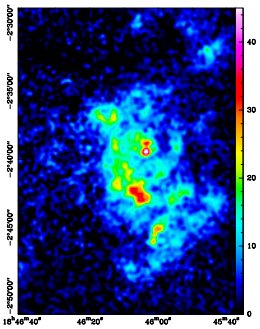

(b) C^{18}O (2–1) map.

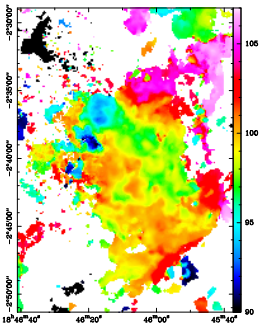

(c) ^{13}CO peak velocity map.

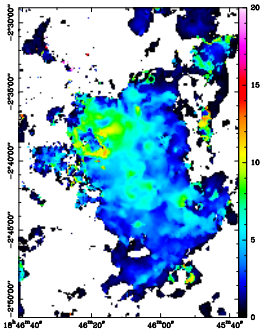

(d) ^{13}CO line width map.

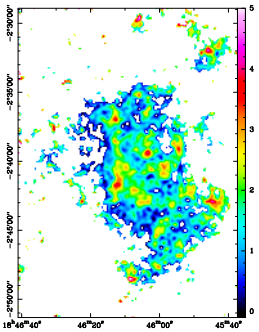

(e) ^{13}CO optical depth map.

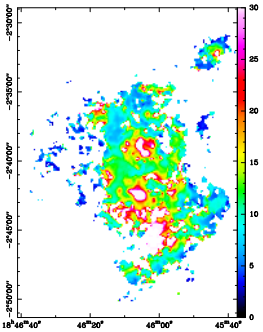

(f) CO excitation temperature map.

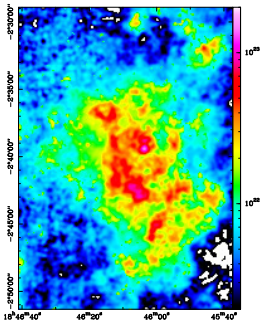

(g) H_2 column density map.

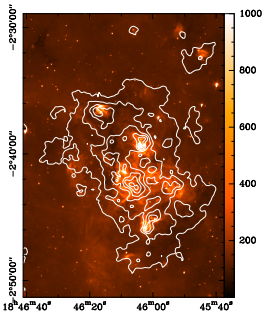

(h) GLIMPSE 8 μm map.

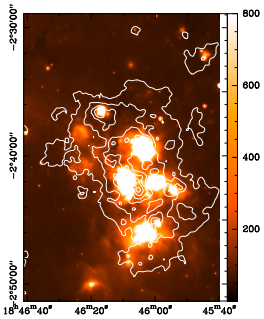

(i) MIPSGAL 24 μm map.

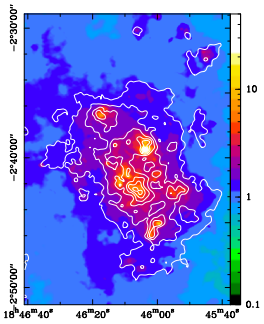

(j) Hi-GAL 160 μm map.

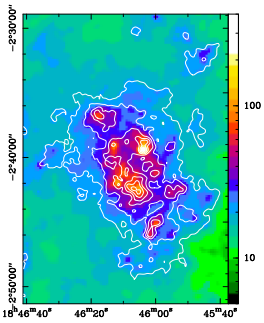

(k) Hi-GAL 350 μm map.

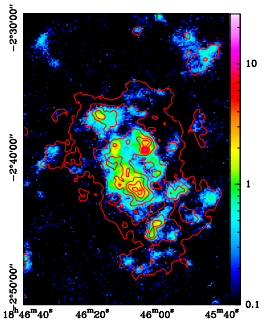

(l) ATLASGAL map.

Fig. B.20: Several maps showing data and derived properties of source 20.

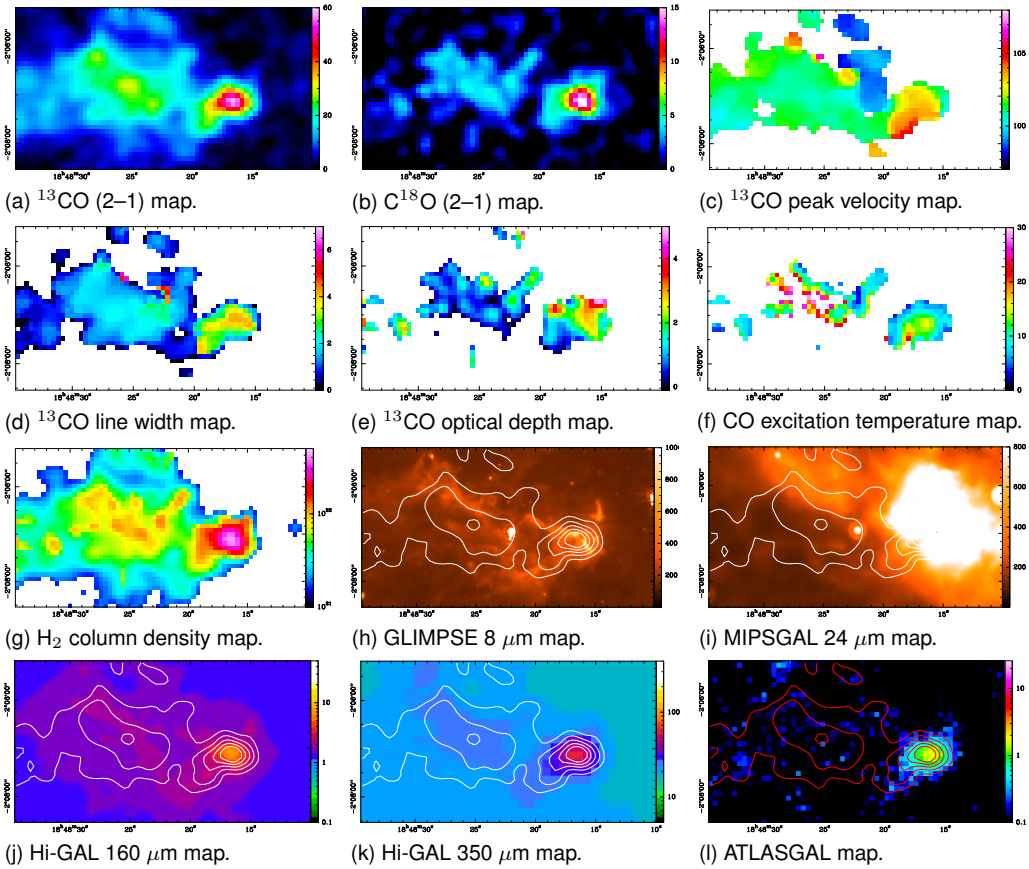

(a) ^{13}CO (2–1) map.
(b) C^{18}O (2–1) map.
(c) ^{13}CO peak velocity map.
(d) ^{13}CO line width map.
(e) ^{13}CO optical depth map.
(f) CO excitation temperature map.
(g) H_2 column density map.
(h) GLIMPSE 8 μm map.
(i) MIPSGAL 24 μm map.
(j) Hi-GAL 160 μm map.
(k) Hi-GAL 350 μm map.
(l) ATLASGAL map.

Fig. B.21: Several maps showing data and derived properties of source 21.

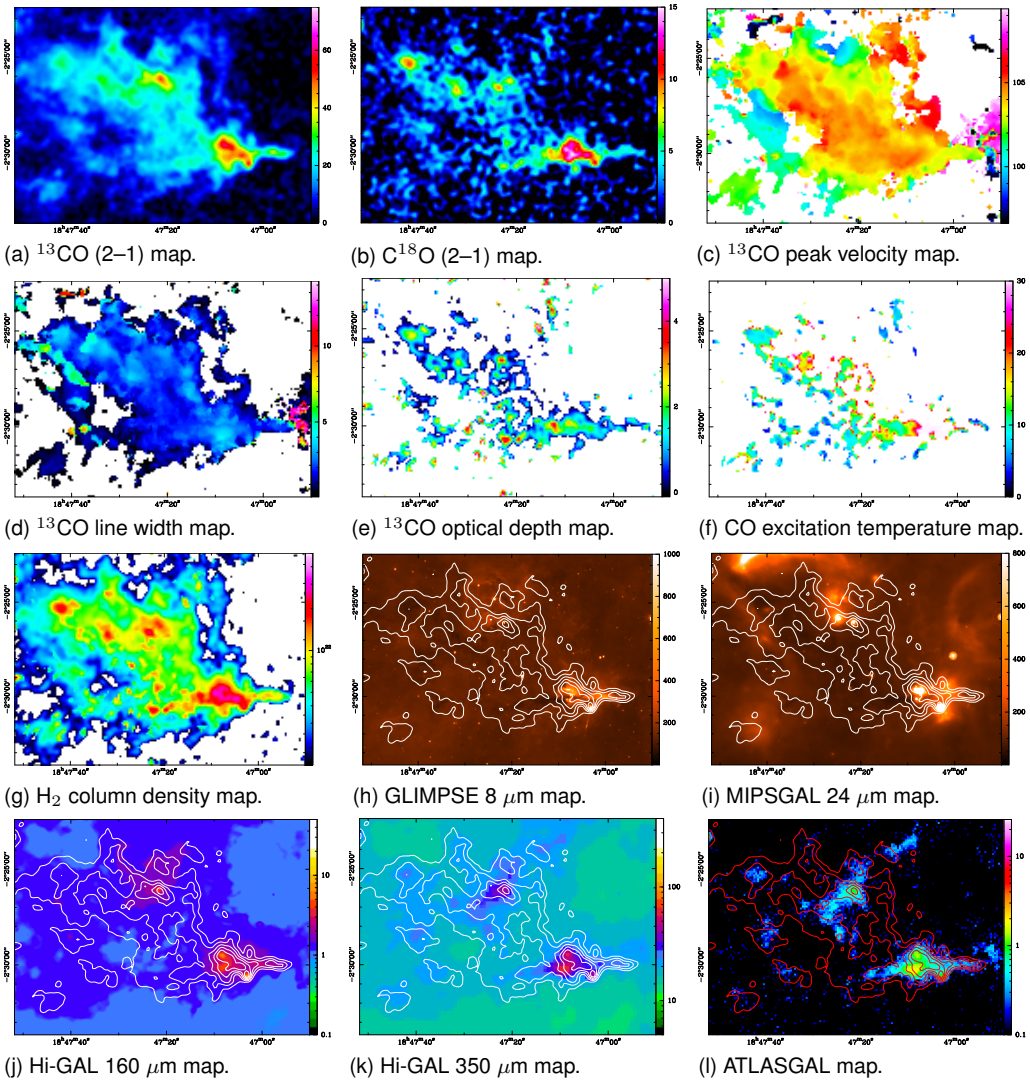

(a) ^{13}CO (2–1) map. (b) C^{18}O (2–1) map. (c) ^{13}CO peak velocity map.

(d) ^{13}CO line width map. (e) ^{13}CO optical depth map. (f) CO excitation temperature map.

(g) H_2 column density map. (h) GLIMPSE 8 μm map. (i) MIPSGAL 24 μm map.

(j) Hi-GAL 160 μm map. (k) Hi-GAL 350 μm map. (l) ATLASGAL map.

Fig. B.22: Several maps showing data and derived properties of source 22.

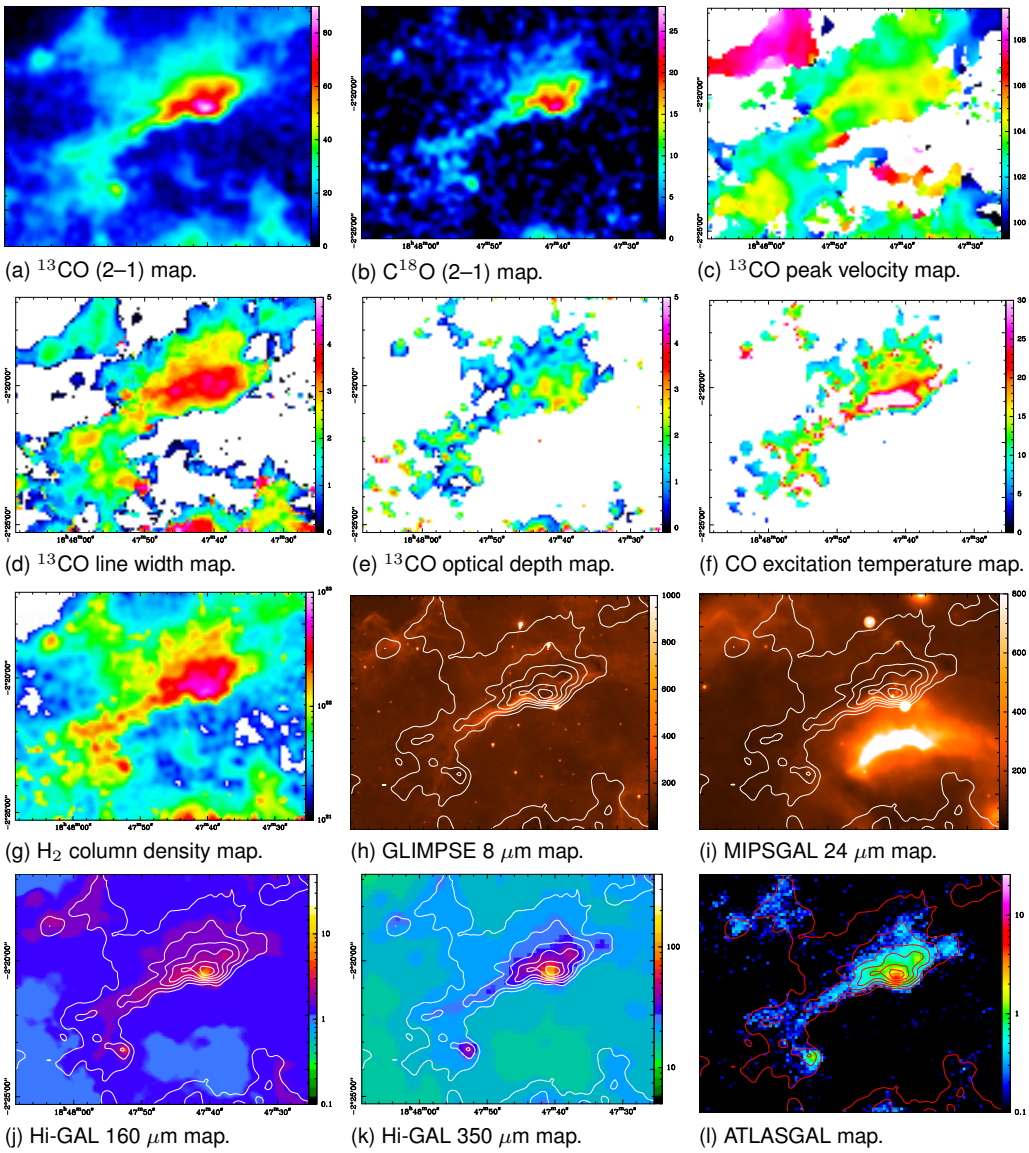

(a) ^{13}CO (2–1) map.
(b) C^{18}O (2–1) map.
(c) ^{13}CO peak velocity map.
(d) ^{13}CO line width map.
(e) ^{13}CO optical depth map.
(f) CO excitation temperature map.
(g) H_2 column density map.
(h) GLIMPSE 8 μm map.
(i) MIPSGAL 24 μm map.
(j) Hi-GAL 160 μm map.
(k) Hi-GAL 350 μm map.
(l) ATLASGAL map.

Fig. B.23: Several maps showing data and derived properties of source 23.

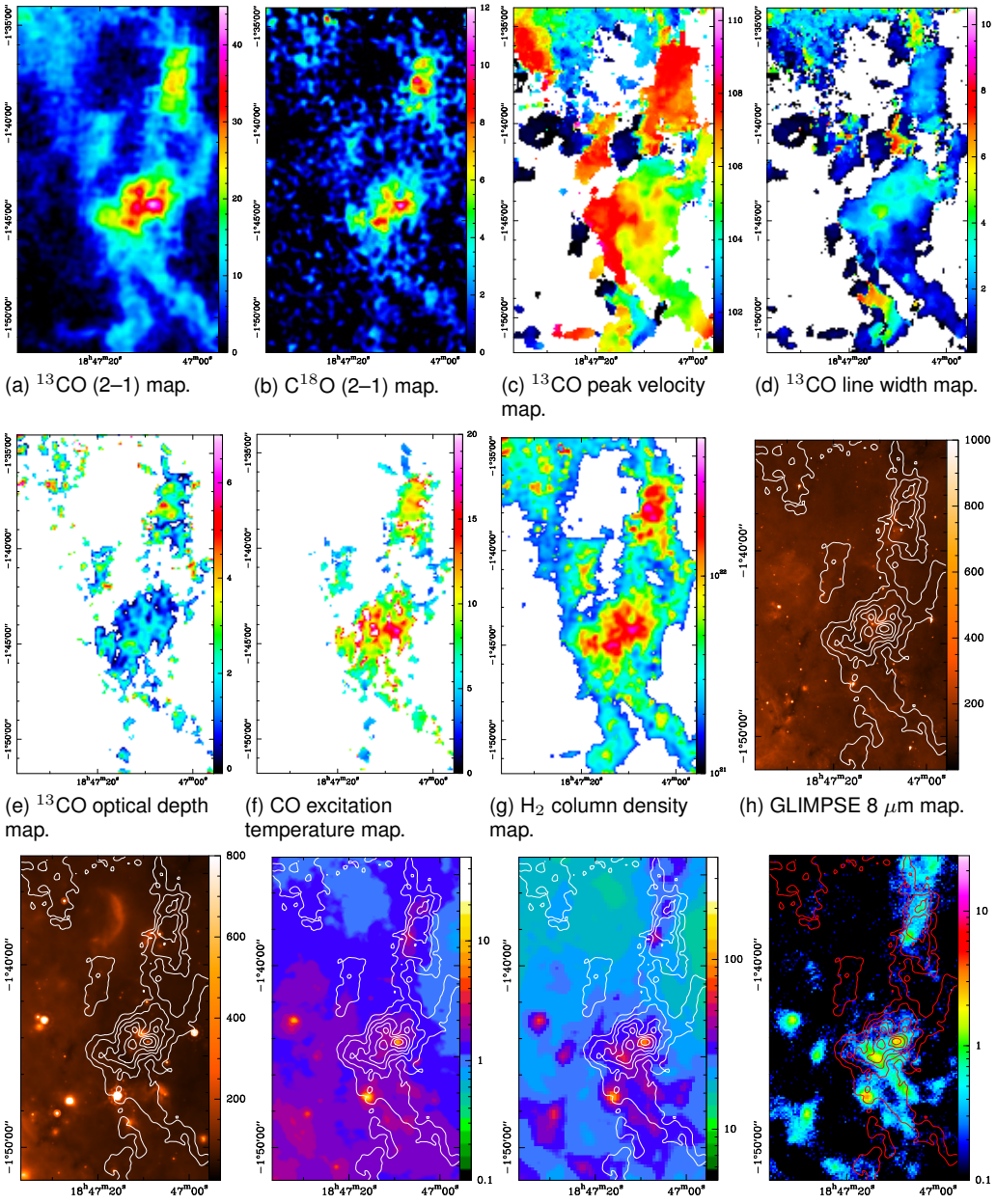

(a) ^{13}CO (2–1) map. (b) C^{18}O (2–1) map. (c) ^{13}CO peak velocity map. (d) ^{13}CO line width map.

(e) ^{13}CO optical depth map. (f) CO excitation temperature map. (g) H_2 column density map. (h) GLIMPSE 8 μm map.

(i) MIPSGAL 24 μm map. (j) Hi-GAL 160 μm map. (k) Hi-GAL 350 μm map. (l) ATLASGAL map.

Fig. B.24: Several maps showing data and derived properties of source 24.

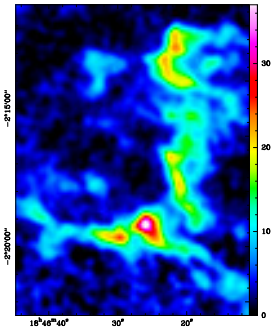

(a) ^{13}CO (2–1) map.

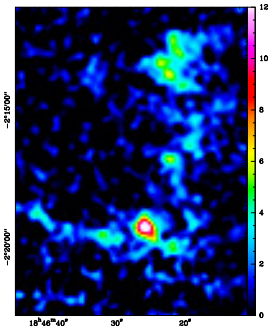

(b) C^{18}O (2–1) map.

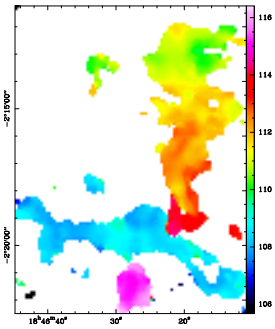

(c) ^{13}CO peak velocity map.

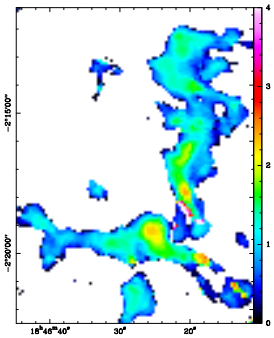

(d) ^{13}CO line width map.

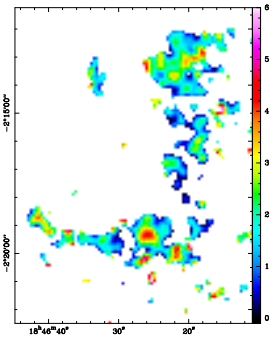

(e) ^{13}CO optical depth map.

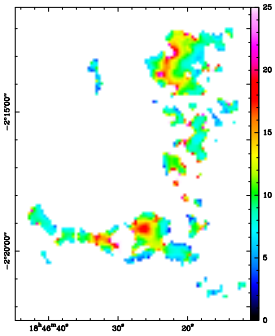

(f) CO excitation temperature map.

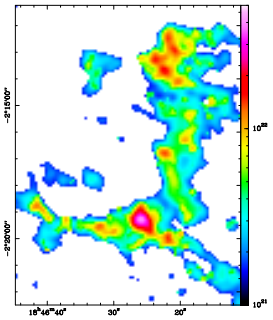

(g) H_2 column density map.

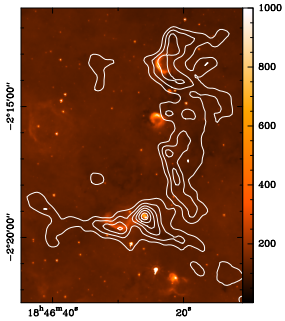

(h) GLIMPSE 8 μm map.

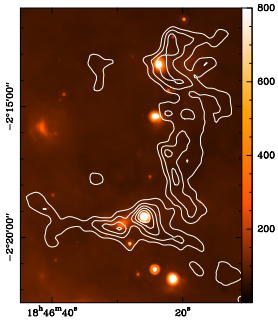

(i) MIPSGAL 24 μm map.

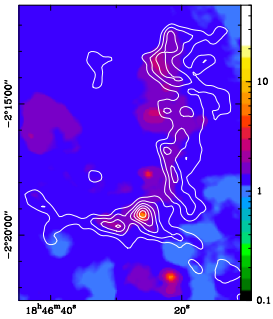

(j) Hi-GAL 160 μm map.

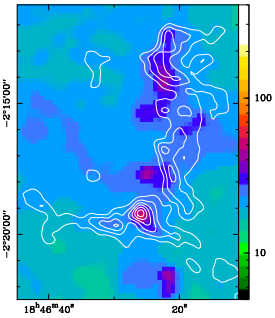

(k) Hi-GAL 350 μm map.

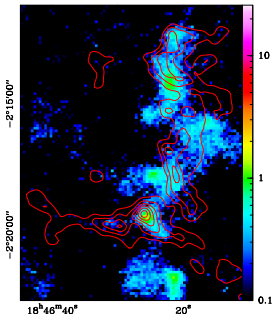

(l) ATLASGAL map.

Fig. B.25: Several maps showing data and derived properties of source 25.

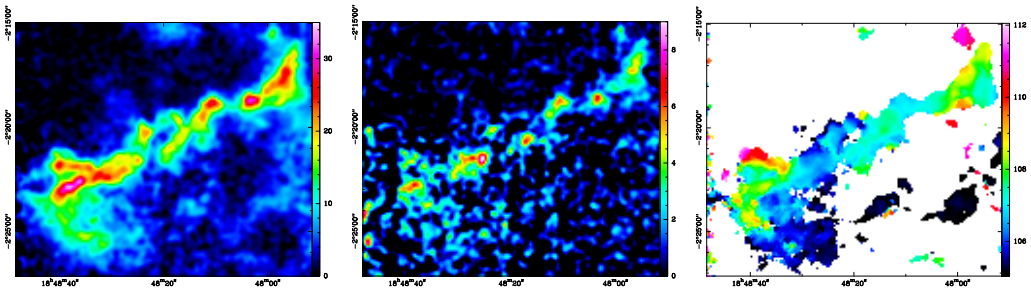

(a) ^{13}CO (2–1) map. (b) C^{18}O (2–1) map. (c) ^{13}CO peak velocity map.

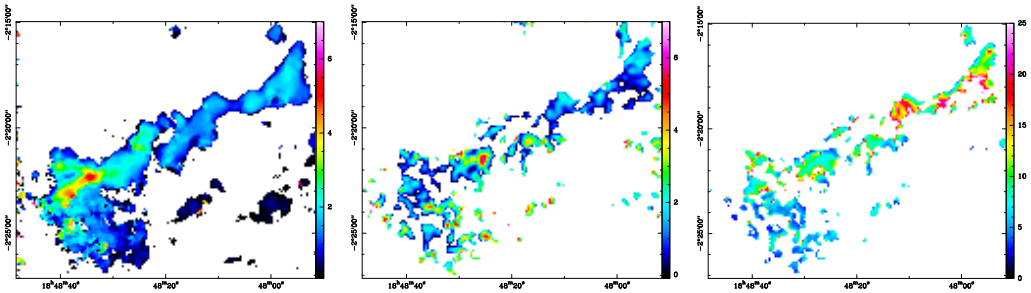

(d) ^{13}CO line width map. (e) ^{13}CO optical depth map. (f) CO excitation temperature map.

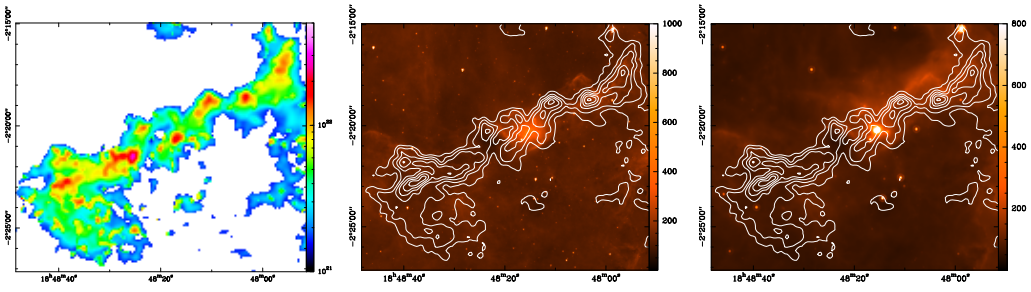

(g) H_2 column density map. (h) GLIMPSE 8 μm map. (i) MIPSGAL 24 μm map.

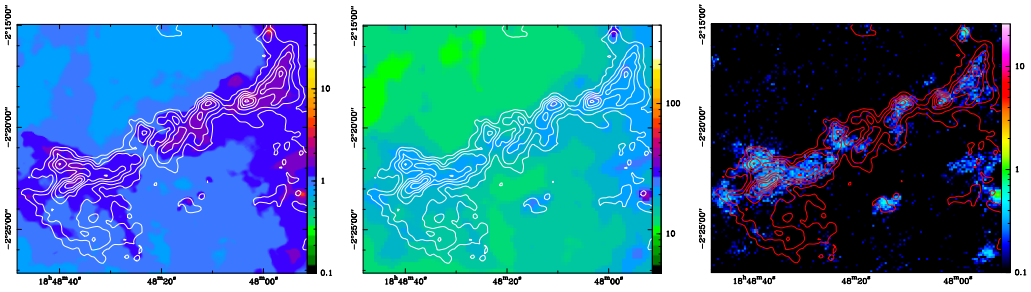

(j) Hi-GAL 160 μm map. (k) Hi-GAL 350 μm map. (l) ATLASGAL map.

Fig. B.26: Several maps showing data and derived properties of source 26.

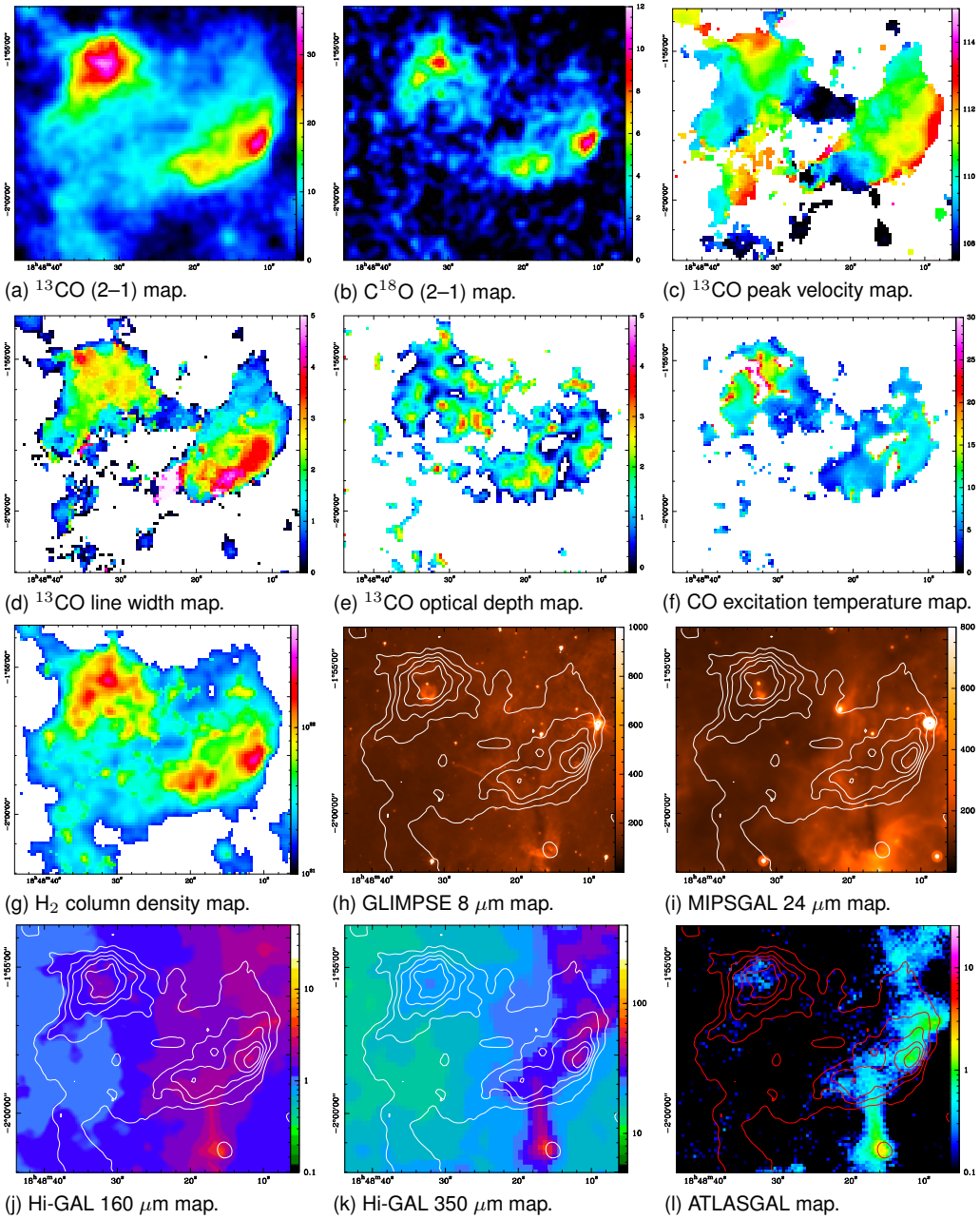

(a) ^{13}CO (2–1) map.
(b) C^{18}O (2–1) map.
(c) ^{13}CO peak velocity map.
(d) ^{13}CO line width map.
(e) ^{13}CO optical depth map.
(f) CO excitation temperature map.
(g) H_2 column density map.
(h) GLIMPSE 8 μm map.
(i) MIPSGAL 24 μm map.
(j) Hi-GAL 160 μm map.
(k) Hi-GAL 350 μm map.
(l) ATLASGAL map.

Fig. B.27: Several maps showing data and derived properties of source 27.

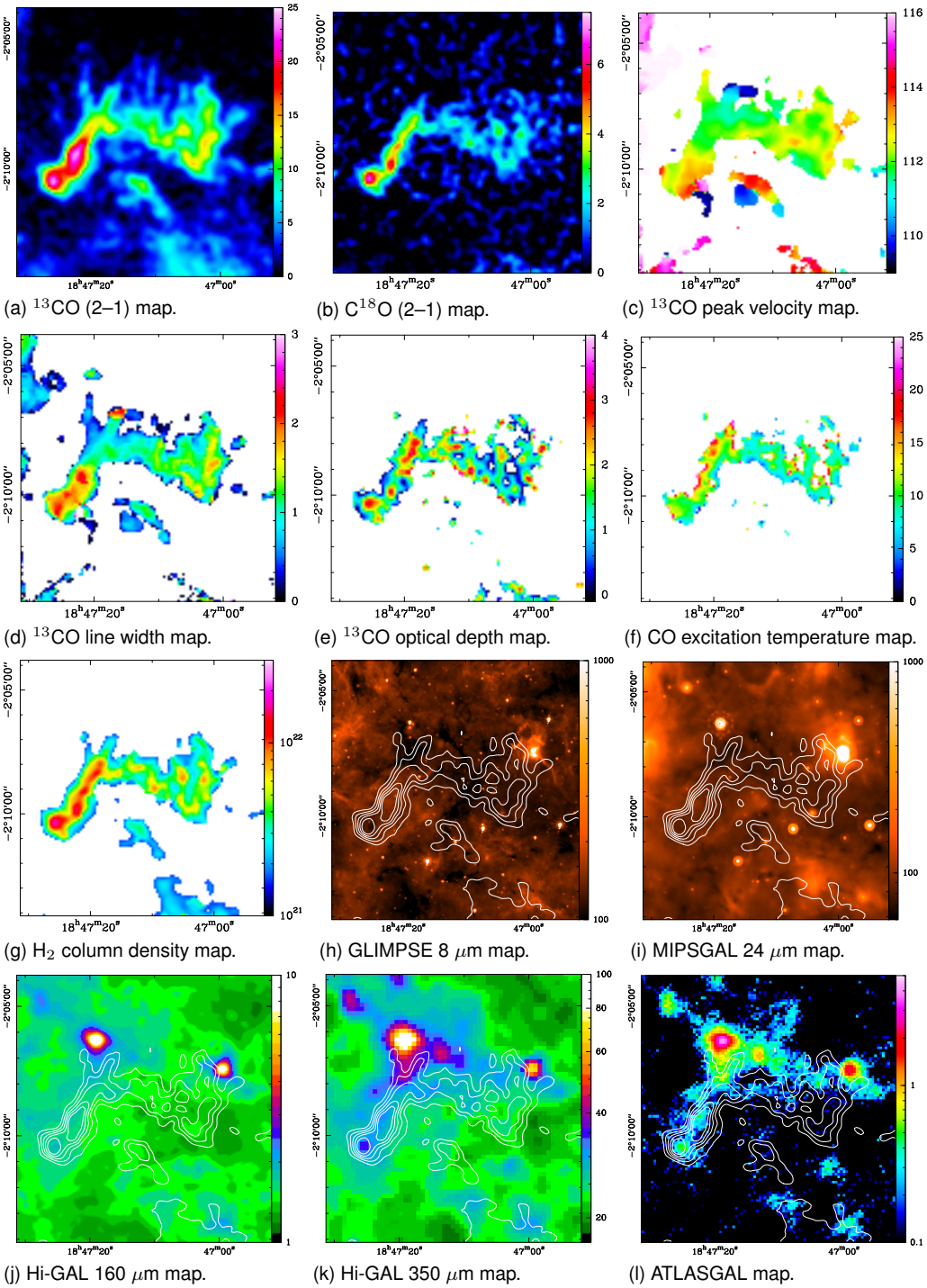

(a) ^{13}CO (2–1) map. (b) C^{18}O (2–1) map. (c) ^{13}CO peak velocity map.

(d) ^{13}CO line width map. (e) ^{13}CO optical depth map. (f) CO excitation temperature map.

(g) H_2 column density map. (h) GLIMPSE 8 μm map. (i) MIPSGAL 24 μm map.

(j) Hi-GAL 160 μm map. (k) Hi-GAL 350 μm map. (l) ATLASGAL map.

Fig. B.28: Several maps showing data and derived properties of source 28.

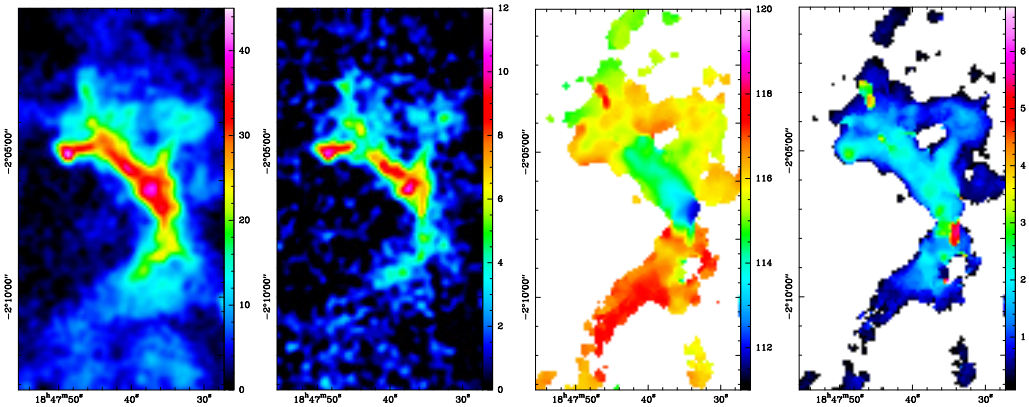

(a) ^{13}CO (2–1) map. (b) C^{18}O (2–1) map. (c) ^{13}CO peak velocity map. (d) ^{13}CO line width map.

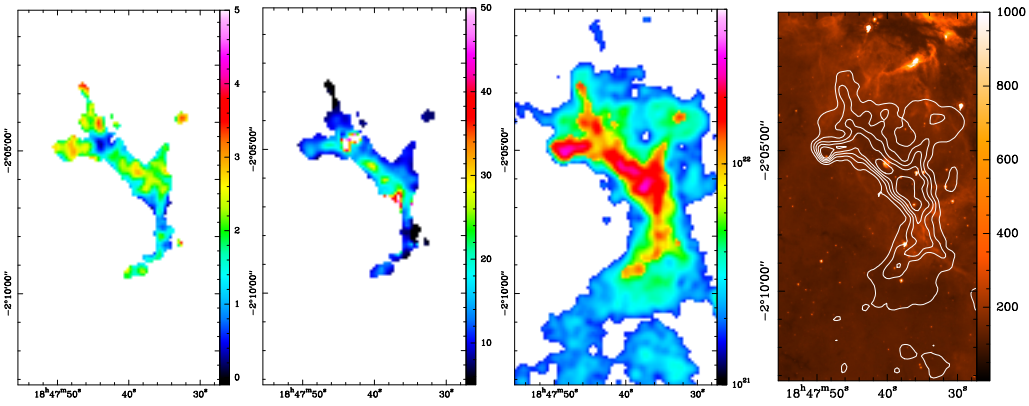

(e) ^{13}CO optical depth map. (f) CO excitation temperature map. (g) H_2 column density map. (h) GLIMPSE 8 μm map.

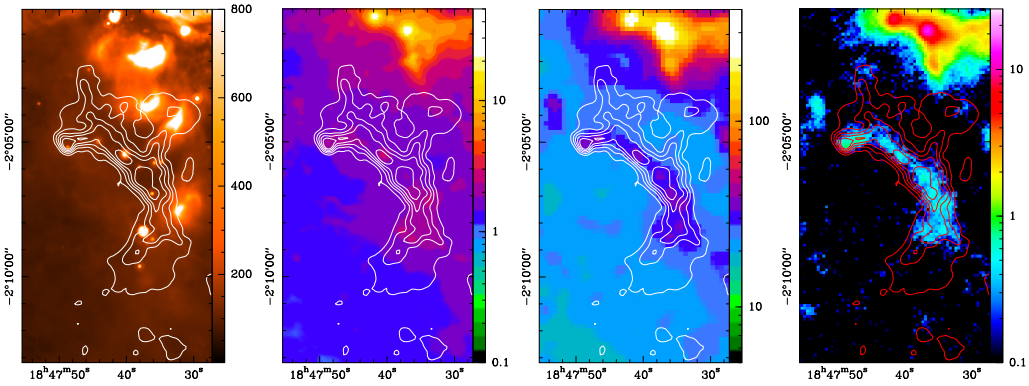

(i) MIPSGAL 24 μm map. (j) Hi-GAL 160 μm map. (k) Hi-GAL 350 μm map. (l) ATLASGAL map.

Fig. B.29: Several maps showing data and derived properties of source 29.

List of Figures

List of Tables

List of Acronyms

ACA Atacama Compact Array 24

ALMA Atacama Large Millimeter/submillimeter Array 2, 19, 24, 114, 138

AOS acusto-optical spectrometer 22, 87

APEX Atacama Pathfinder Experiment 4, 19, 69, 71, 90–92, 101, 106–108, 113, 135, 138, 190

ATLASGAL APEX Telescope Large Area Survey of the Galaxy 69, 71, 77, 78, 142–144

BIMA Berkeley Illinois Maryland Association 92

CARMA Combined Array for Research in Millimeter-wave Astronomy 4, 92, 93, 95–97, 101, 107, 109–111, 113, 121, 122, 125, 135–137

CCAT Cerro Chajnantor Atacama Telescope 21

CCD charge-coupled device 22

CLASS Continuum and Line Analysis Single-dish Software 33, 98

CMF core mass function 7, 8

CNM cold neutral medium 11–13

DAAD Deutsche Akademische Austauschdienst e. V. 190

DFG Deutsche Forschungsgemeinschaft 190

DisPerSE Discrete Persistent Structures Extractor 139

DLR Deutsches Zentrum für Luft- und Raumfahrt 190

ESA European Space Agency 86, 88, 89

ESO European Southern Observatory 2, 90

FTS Fourier-transform spectrometer 22

FWHM full width at half maximum 79, 105–108, 110, 111, 113, 141

GILDAS Grenoble Image and Line Data Analysis Software 33, 41, 50, 89, 91, 98

GLIMPSE Galactic Legacy Infrared Mid-Plane Survey Extraordinaire 68, 69, 78, 79, 83, 84, 127, 128, 142, 144

GMC giant molecular cloud 2, 6, 10, 133, 138

GOT C+ Galactic Observations of Terahertz C^+ 131

GreG Grenoble Graphic 33

HCHII hyper compact H II region 10

HEB hot electron bolometer 22, 87

HERA Heterodyne Receiver Array 31, 32, 34, 35

Hi-GAL *Herschel* infrared Galactic Plane Survey 15, 69, 71, 72, 74, 77, 78, 80, 87, 114, 127–129, 135, 142–144

HIFI Heterodyne Instrument for the Far Infrared 86–89, 100, 104, 105, 131, 135, 137, 190

HIM hot ionized medium 12

HIPE *Herschel* Interactive Processing Environment 89

HOBYS *Herschel* imaging survey of OB Young Stellar objects 72, 80

HPBW half power beam width 21, 31, 58, 84, 89, 91, 98, 101, 111, 138

HRS High Resolution Autocorrelation Spectrometer 87

HSO *Herschel* Space Observatory 4, 7, 14, 19, 86

HSpot *Herschel* Observation planning tool 88

IGM intergalactic medium 11

IMF initial mass function 6–8

IPAC Infrared Processing and Analysis Center 20

IRAM Institut de Radioastronomie Millimétrique 4, 29–31, 33, 34, 42, 63, 68–70, 74, 79, 80, 83–89, 91, 98, 100, 101, 103–114, 133, 135, 145, 190

IRAS Infrared Astronomical Satellite 10, 72

IRDC infrared dark cloud 15, 70, 127

ISM interstellar medium 1, 2, 5, 6, 9–13, 19, 24–26, 131

ISRF interstellar radiation field 127

JCMT James Clerk Maxwell Telescope 118, 190

LO local oscillator 22

LOFAR Low-Frequency Array 20

LTE local thermal equilibrium 117, 120

MHD magneto-hydrodynamics 15, 16

MIPS Multiband Imaging Photometer for *Spitzer* 71

MIPSGAL MIPS Galactic Plane Survey 68, 71, 127–129

MIRA Multichannel Imaging and Calibration Software for Receiver Arrays 33

MIRIAD Multichannel Image Reconstruction, Image Analysis and Display 94, 95

MPIfR Max-Planck-Institut für Radioastronomie 90

NASA National Aeronautics and Space Administration 6, 20, 86

NSF National Science Foundation 92

OSO Onsala Space Observatory 90

OTF on-the-fly 23, 32, 88, 91, 98

OVRO Owens Valley Radio Observatory 92

PACS Photodetecting Array Camera and Spectrometer 71, 87

PAH polycyclic aromatic hydrocarbon 12, 127, 128

PDF probability distribution function 6, 13, 75, 76, 135–137

PDR photodissociation region/photon-dominated region 4, 70, 122, 123, 125, 126, 129, 130, 136–139

pv position velocity 45, 50, 51, 104–107, 112, 134

rms root mean square 21, 34, 89, 92, 97, 98

SED spectral energy distribution 73, 126

SFR star formation rate 7, 71

SHS SuperCOSMOS Hα Survey 127, 129

SIS superconductor-insulator-superconductor 22, 87

SKA Square Kilometre Array 20

SMA Submillimeter Array 101

SMART Sub-Mm Array Receiver for Two frequencies 98, 111, 138

SOFIA Stratospheric Observatory For Infrared Astronomy 19, 90, 97, 139

SPIRE Spectral and Photometric Imaging Receiver 71, 87

STO Stratospheric Terahertz Observatory 19

SZA Sunyaev–Zel'dovich Array 93

THOR The HI/OH/Recombination line survey of the Milky Way 71, 72

UCHII ultra compact H II region 10, 33, 79

UKST UK Schmidt Telescope 127

VESPA Versatile Spectrometer Array 31, 33

VGPS VLA Galactic Plane Survey 48

VLA Very Large Array 19, 71, 72, 138

W43 HERO W43 Hera/EmiR Observations 29, 71, 85, 133, 136

WBS Wideband Spectrometer 87, 88

WIM warm ionized medium 11

WNM warm neutral medium 11–13, 131

YSO young stellar object 70, 79

List of Constants and Units

(1) Constant/Unit	(2) Value/Unit	(3) Name/Description
k_{B}	1.3806×10^{-23} J K^{-1}	Boltzmann constant
c	2.9979×10^{10} cm s^{-1}	speed of light in vacuum
h	6.6261×10^{-34} J s	Planck constant
G	6.6738×10^{-11} m^3 kg^{-1} s^{-2}	Gravitational constant
pc	3.0857×10^{18} cm	parsec
AU	1.4960×10^{13} cm	astronomical unit
ly	9.4607×10^{17} cm	light year
yr	3.1558 s	year
Jy	10^{-23} erg s^{-1} cm^{-2} Hz^{-1}	jansky
$M_\odot$	1.9891×10^{30} kg	solar mass
$L_\odot$	3.839×10^{26} W	solar luminosity
$R_\odot$	8.5 kpc	solar Galactic radius
$m(\mathrm{H_2})$	3.3474×10^{-27} kg	mass of molecular hydrogen
τ		optical depth
n_{X}	cm^{-3}	number density of X
$N(X)$	cm^{-2}	column density of X
λ	m	wavelength
ν	Hz	frequency
T	K	temperature
J		total angular momentum quantum number

Table B.1: List of constants, units, and variables, frequently used throughout this work.

List of Publications

Refereed

The APEX Telescope Large Area Survey of the Galaxy (ATLASGAL), Schuller, F.,... Carlhoff, P.,... et al., 2010, The Messenger, 141, 20

W43: the closest molecular complex of the Galactic bar?, Nguyen Luong, Q.,... Carlhoff, P.,... et al., 2011, Astronomy & Astrophysics, 529, A41

The onset of high-mass star formation in the direct vicinity of the Galactic mini-starburst W43, Beuther, H.,... Carlhoff, P.,... et al., 2012, Astronomy & Astrophysics, 538, A11

Low-velocity shocks traced by extended SiO emission along the W43 ridges: wittnessing the formation of young massive clusters, Nguyen Luong, Q., Motte, F., Carlhoff, P., et al., 2013, The Astrophysical Journal, 775, 88

Large scale IRAM 30m CO-observations in the giant molecular cloud complex W43, Carlhoff, P., Nguyen Luong, Q., Schilke, P., et al., 2013, Astronomy & Astrophysics, 560, A24

Non-refereed

Molecular cloud formation and filamentary structure in W43, Carlhoff, P., Nguyen Luong, Q., Schilke, P., et al., in prep.

The formation of the W43 complex: constraining its atomic-to-molecular transition and searching for colliding clouds, Motte, F.,... Carlhoff, P.,... et al., submitted to Astronomy & Astrophysics

Acknowledgements

Preparing this thesis has taken much time and effort. And although at some points I wondered if I was still on track, I had a really good time. I learned so much in these years, had so many interesting experiences, and met nice people that I would not miss this time for anything in the world. I am grateful to be part of this project and this institute, which posed so many opportunities, like working in Chile, Spain, France, and the US. This was beneficial not only on the scientific level, but also the personal one. Here, I want to express my gratitude to all people who contributed to this thesis, who helped me on my way to it, or whom I just met and who made this a great time. And my apologies to all those that I should have forgotten here.

First of all, I want to thank Prof. Schilke for supervising this thesis, for always helping me and giving advise in his friendly kind. He really is always there for his students and I learned a lot from him. Many thanks go to Prof. Stutzki for being my second supervisor and referee of this work. I especially want to emphasize the two weeks we worked together at the NANTEN2 telescope. I probably learned more about telescopes and instrumentation in these days than in the remaining years.

I am also thankful to Prof. Kiefer for taking over chairmanship of my PhD committee and who already was a pleasant supervisor of my Diploma thesis. Many thanks to Robert Simon for being reporter at my defense.

Frédérique Motte, Nicola Schneider and Quang Nquyen Luong were all closely involved in the W43 project and provided so much input and ideas, that I cannot list it in detail. Without Frédérique, this project would not have existed at all and I am happy about all the hard work and effort she put in it. And Nicola, I still remember my visit in Bordeaux, which was really nice. I also want to mention the rest of the W43 consortium, especially Friedrich Wyrowski, Henrik Beuther, and Frederic Schuller whom I had valuable discussions with and who helped a great deal finishing my paper.

It was really nice having a large work group of friendly colleagues that were always open for questions or discussions. I really liked the atmosphere in our institute. So I want to thank Robert Simon, Volker Ossenkopf, Markus Röllig, and Urs Graf for always being around and always being willing to help, no matter how

much work you had yourselves. Ronan and Alvaro, thank you again for spell-checking my thesis, that was a great help. Ed, Christian, Guan Xin, Christian, Zoltan, Pablo, Yoko, Silke, Michael, Oli, Timo, Norma, Anika, Thomas, Alvaro, and the rest of the group, thank you for the help, the chatting, hanging around, parties, going out, having fun, and everything else. I really had a great time.

Not to forget the staff of our institute who made everything run, and helped with administrative questions, Steffi Krämer, Bettina Krause, Marlies Selt, Tanja Bodendorf, Susanne Herbst, Maxi Limbach, and last but not least Frank Schlöder, who rescued my computers more than once.

Then, there are those people I met in Pasadena, and made my stay there a wonderful time, Thushara Pillai, Jens Kauffmann, Laura Perez, and Walter Max-Moerbeck. John Carpenter, Nikolaus Volgenau, Andrea Isella and the rest of the Caltech and CARMA crew form whom I learned so much. And of course Cedric Cocaud. Cedric, you were the best flat-mate I could imagine, thanks for that time.

I am much obliged to Carsten Kramer and the Rest of the IRAM team for helping me setting up and observing our project, especially Manuel Gonzalez, who was a great astronomer on duty at the 30m and spent countless nights, helping me with my observations.

Thanks to the HIFI and APEX teams for conducting my projects and help with the setup. Also, thanks to all those people who stayed at NANTEN2 with me, Reinhold Schaaf, Chandani Rajbahak, Matthias Justen, Jürgen Stutzki, Christian Glück, Guan Xin, Silke Andree, Pablo Garcia, and our Japanese and Chilean colleagues and the Astronorte staff. It was always instructive and interesting down there.

I further want to acknowledge Rene Plume and Toby Moore for giving me access to their JCMT ^{13}CO (3–2) data and letting me use it for this work.

Finally, I want to thank my parents, my brother and sister, and all my family and friends who supported me in all that time and who did not see much of me in the last months. Sorry for that, it will be better again, soon. And thank you Flora, you were my greatest help and support.

This project was carried out within the Collaborative Research Council 956, sub-project A4, funded by the Deutsche Forschungsgemeinschaft (DFG). From Oktober 2013 on it is funded by the Deutsches Zentrum für Luft- und Raumfahrt (DLR)
My stay at Caltech in Pasadena, California, was sponsored by the Deutsche Akademische Austauschdienst e. V. (DAAD).

Erklärung

Ich versichere, dass ich die von mir vorgelegte Dissertation selbstständig angefertigt, die benutzten Quellen und Hilfsmittel vollständig angegeben und die Stellen der Arbeit – einschließlich Tabellen, Karten und Abbildungen –, die anderen Werken im Wortlaut oder dem Sinn nach entnommen sind, in jedem Einzelfall als Entlehnung kenntlich gemacht habe; dass diese Dissertation noch keiner anderen Fakultät oder Universität zur Prüfung vorgelegen hat; dass sie – abgesehen von unten angegebenen Teilpublikationen – noch nicht veröffentlicht worden ist sowie, dass ich eine solche Veröffentlichung vor Abschluss des Promotionsverfahrens nicht vornehmen werde.

Die Bestimmungen der Promotionsordnung sind mir bekannt. Die von mir vorgelegte Dissertation ist von Prof. Dr. Peter Schilke betreut worden.

Nachfolgend genannte Teilpublikationen liegen vor:

Large scale IRAM 30m CO-observations in the giant molecular cloud complex W43, Carlhoff, P., Nguyen Luong, Q., Schilke, P., et al., 2013, Astronomy & Astrophysics, 560, A24

Ich versichere, dass ich alle Angaben wahrheitsgemäß nach bestem Wissen und Gewissen gemacht habe und verpflichte mich, jedmögliche, die obigen Angaben betreffenden Veränderungen, dem Dekanat unverzüglich mitzuteilen.

Köln, 18. November 2013

Philipp Carlhoff